3D Triply Resonant Sum Frequency Spectroscopy with applications towards biological molecules

By
Jonathan Daniel Handali

A dissertation submitted in partial fulfillment of
the requirements for the degree of

Doctor of Philosophy
(Chemistry)

at the
UNIVERSITY OF WISCONSIN - MADISON
2018

Date of final oral examination: July 24, 2018
This dissertation is approved by the following members of the Final Oral Committee:
John C. Wright, Professor, Analytical Chemistry
Randall Goldsmith, Professor, Physical Chemistry
Thomas Brunold, Professor, Inorganic Chemistry
John Berry, Professor, Inorganic Chemistry

Contents

List of Figures

List of Tables

Acknowledgments

There are so many people who have walked alongside me on this long journey that I would like to mention and thank.

Firstly, my mentor and advisor John Wright. John places a lot of trust in his students, trust perhaps that they do not even have in themselves. He is an absolute gentleman and respects our opinions and abilities. He considers himself responsible for our general well-being and he and his wife Carol take upon themselves the role of foster grandparents. He is a person whom I seek to emulate not only as a scientist but as a human being. I also want to thank the other members of my mentorship committee, Thomas Brunold and Randy Goldsmith. Thomas has been a willing collaborator on the cobalamin project, educating us non-experts and providing plenty of background, insight, and paper revisions. This project would be floundering without his expertise. Randy was my first mentor in graduate school as I TA'd under him in my first semester. He is a brilliant teacher and that semester teaching 109H along with Hannah Bowman stands out as the best teaching experience I've ever had. Randy is a tough committee member and does not hesitate to ask difficult questions that stretch my knowledge. I feel good whenever I get a compliment from Randy because I know it was well earned.

I want to thank my labmates and coworkers in the Wright Group. I truly hit the jackpot when I landed in this research group. The selflessness that begins with John is reflected in all members of the group. The Wright Group is a special collection of individuals with a high level of talent and a low level of ego. The camaraderie is contagious and I believe it has helped me develop into a much better team player. They are a strongly opiniated bunch and arguments over small things can last for hours, but their opinions stem from a desire to see the truth come to light and the world improve rather from from personal pride.

- Nathan - Thanks for reminding me that there are important and immediate problems outside the world of science
- Kyle - You are the exemplary happy computer nerd and I'm often astonished at all the things you know. The world needs for perfectionist people like you to exist, don't ever change.
- Emily - Thanks for bringing in much needed energy just as I was getting tired of it all. You were a great first year to train and your love for baking and podcasts is infectious. Thanks for bringing back the tradition of going to get ice cream!
- Dan - You are the perfect mentor. Whenever I ask you for help, you alway provide it in a way that both brilliantly solves the problem and makes me feel like I own the accomplishment.

- Blaise - There is no person I know who is more brilliant and intelligent but yet so humble and generous than you
- Darien - In 2050, there will be two kinds of people: those who work for robots and those who work for Darien Morrow. You are an absolute boss who leads from the front as well as from the back. I expect great things from you.
- Natalia - Our resident karate expert and artist, you bring refreshing enthusiasm and passion for science and life in general. I look forward to seeing Wright Toons take its rightful place online alongside xkcd and phd comics.
- Skye - My late night lab buddy, thanks for keeping me company streaming sports at 12 am.
- Erin and Paul - Thanks for teaching me that lasers only respect those who are respectful to them.
- My laser friends Tsunami, Spitfire Ace, and OPAs 1, 2, and 3 - they are like livestock: largely similar creatures and have the same basic design principles, maintainance and operation, but each individual unit has its own unique personality, likes and dislikes. Some are moody and temperamental, while others are steady and dependable. Find out what they want, consistently give them what they want, and they will treat you well.

I want to thank the people who befriended me and became part of my community outside the chemistry department. In particular, I want to thank the members of Permias Madison and the larger Indonesian community for taking me into their close family circle and giving me a home. Many of them are undergraduates who are quite a bit younger than me, but while they make me feel old, at the same time they make me feel young. There was always something going on over the weekend for me to look forward to during the week. Thanks to them, my life was never boring. My old roommates Jason, Praisten, and Davin helped me feel not alone during the darkest days of my academic struggles. Listening to teenagers complain about feelings and grades is always good medicine for times when nothing is working in the lab. Members of the Permias Madison Volleyball team: Donny, Handoy, Guan Hong, Gavin, Josmat, and Yuan Feng. Traveling to other schools to take part in sports tournaments and battling alongside my friends made me feel like I was back in high school. My Christian fellowship group: Grady, Velli, Vanessa, Ci Joyce, and Jessalyn, lent such patient ears to my problems every week and gave me endless words of encouragement and prayers. I have greatly enjoyed the company of the younger students who befriended me during the last couple of years in Madison including Harman, Bastian, Daniel, Young Min, Jimmy, and Victor to name a few. Thanks for keeping me in shape by dragging me to the basketball court every week. I am grateful to the Psyk family: Randy, Mary, Ben, Sam and Ethan, who have treated me like an adopted son and have been so generous to me, lavishing me with all kinds of goodies and good company whenever I needed it, as well as Terrell and the International Student Fellowship for taking care of me when I first arrived and made sure I got the full Wisconsin experience. The kindness shown to me on such a regular basis by these amazing people reminds me of the debt of kindness I owe to humanity.

I want to thank my family for always supporting me from a distance. During my struggles, my father often reminded me how much he struggled while pursuing his PhD. I am not sure what tactic of motivation he was going for, but knowing that struggling is normal and expected is often enough to persevere and endure it. My mother provided the calm I needed simply by being calm. Silly conversations with older sister Melody and my younger brother Paul kept me sane.

Finally I want to thank my fiancée Merly. We were together in Madison for a year and then long distance for two years. The highlight each day was waking up in the morning to a tiny and badly pixelated representation of your otherwise very attractive face. Thanks for waiting patiently for me to finally finish and for listening to me whine about every broken motor and unsightly looking spectrum. Thank you for your willingness to try to understand the strange problems I would bring up in conversation even though it was already midnight where you were. Thank you for the many words of encouragement and for motivating me to persevere with things that you did not even fully understand.

Abstract

Electronic transitions typical of transition metal complexes often appear in the UV-visible region of the absorption spectrum. If properly resolved, these electronic transitions can be tracked to provide insight into the chemical changes occuring around the metal ion during the course of a reaction, shedding light on the reaction mechanism. In natural catalysts of biological interest, such as cobalamin (Vitamin B_{12}) and the Oxygen Evolving Complex (OEC), however, congestion of spectral features obscures the electronic structure and prevents meaningful interpretation of the absorption spectrum. We develop a multidimensional technique called Three Dimensional Triply Resonant Sum Frequency Spectroscopy (3D-TRSF) to resolve the electronic structure. In 3D-TRSF, three pulses of light are used to excite a triple quantum coherence. The first two pulses excite vibrational modes while the third pulse causes a transition from the excited vibrational states to the electronic states which are coupled to these vibrational states. We characterize phase-mismatch artifacts which appear due to interference between the sample and sample cell window generated signal. Using the specificity of vibrational-electronic coupling, we show that the congested α/β region of the absorption spectrum of cyanocobalamin and aquacobalamin contains three distinct electronic states which are unresolvable using linear absorption techniques. We hope to develop 3D-TRSF along with other multidimensional techniques to study the reaction mechanisms of the Co-C bond cleavage in cobalamin and the water oxidation reaction in the OEC.

Chapter 1

Introduction

Coherent Multidimensional Spectroscopy has been developed to resolve spectra which are congested by overlapping states [8, 9, 10, 11, 12]. Multidimensional frequency spectra rely on coupling between related states. This dissertation describes my work developing a technique of CMDS, Three Dimensional Triply Resonant Sum Frequency Spectroscpy (3D-TRSF). TRSF measures the coupling between vibrational states and electronic states. The goal of my project was the decongestion of UV-vis absorption spectra of biological molecules taking advantage of the selectivity of vibrational-electronic coupling.

1.1 Limitations of linear absorption spectra

The absorption spectra of molecules in the UV-visible region contain signatures of transitions of electrons between occupied and unoccupied states. Transition metal compounds, which play a vital role in artificial and natural catalysts, have electronic transitions in this spectral region. The electronic structure and the possible transitions are strongly linked to the chemical structure of the molecule and UV-vis absorption spectra contain signatures of the chemical environments surrounding the orbitals. Properties of the metal species, such as oxidation states, ligand identities, and coordination number, cause changes to the electronic structure which are detectable in an absorption spectrum[13, 14]. For example, in the spectrum shown in Figure 1.1, the absorption spectrum of a Cr/Al_2O_3 catalysts was recorded as a

function of temperature. In the first scan, there are two strong CT transitions at 370 and 250 nm associated with Cr^{6+}. As T_{red} increases, the CT transitions die away while a feature at 800 nm grows. In the final scan, the absorption spectrum resembles that of $Cr^{2+/3+}$[1]. The clues about the electronic structure revealed by the absorption spectrum allowed the authors to quantify the change in oxidation state of the metal based on physical conditions. There are many examples of chemical reactions involving small molecules and well resolved electronic structures being detected by simple linear absorption spectroscopy[13].

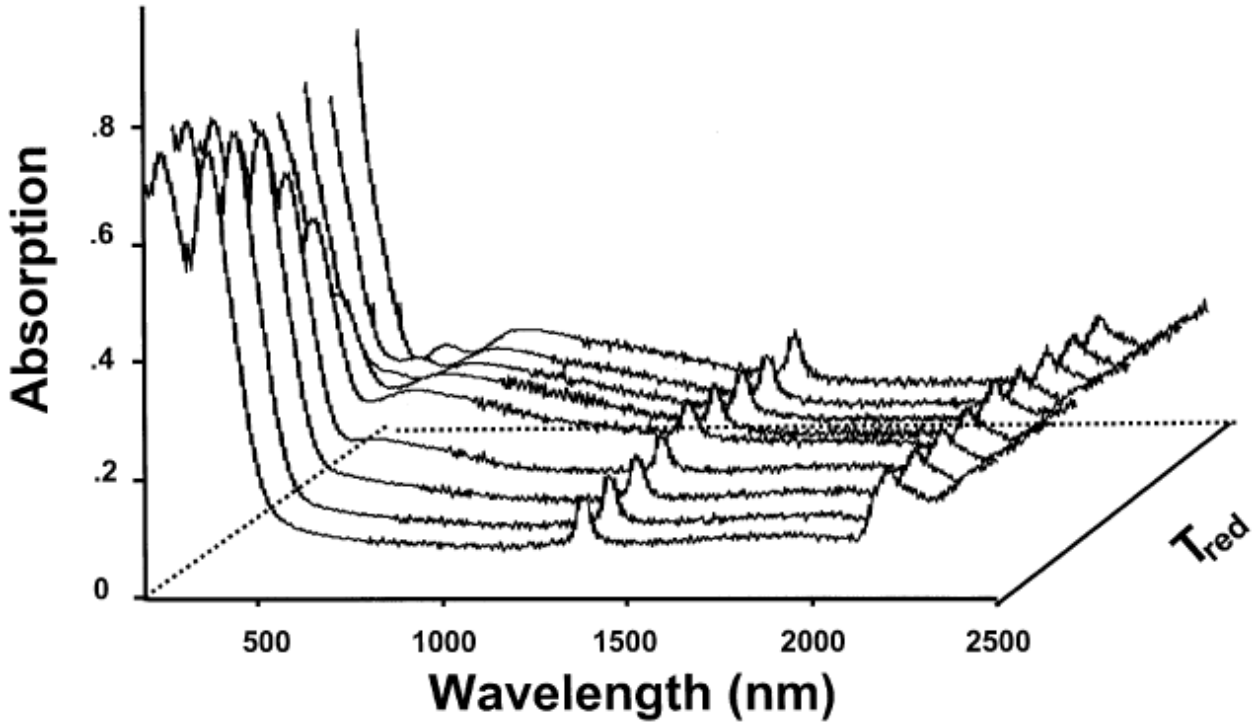

Figure 1.1: A series of absorption spectra of a Cr/Al_2O_3 catalyst showing the change in oxidation number reflected by changes in the absorption spectrum. Taken from reference [1]

In the natural world can be found some interesting catalysts which are responsible for vital reactions occurring within the human body and in plant tissues. Two such systems of interest to our group are cobalamin and the Oxygen-Evolving Complex (OEC). Cobalamins are a family of Co-corrinoid complexes that act as cofactors for enzymes which catalyze many reactions important to biology such as isomerase, methyl transferase, halogen transferase, and reduction dehalogenase reactions[15]. It is known medically that a deficiency of cobalamin in the body can lead to anemia and neurological problems, as well as poor growth and development in young children. Meanwhile the OEC is the Mn-based catalytic centre of the plant enzyme Photosystem II, which is responsible for splitting water molecules into oxygen and protons[16, 17]. The reaction takes place in a four step process known as the Kok cycle and 100 molecules of oxygen are generated per second per OEC. The metal centre is Mn, an earth abundant metal unlike the heavy rare-earth metals used in typical artificial catalysts. Unsolved problems include the electronic structure of cobalamin, and the reaction mechanism of the OEC.

The electronic structure of cobalamin problem has been tackled largely by a combination of experimental and theoretical techniques[18, 19, 3, 20, 21]. Following the x-ray diffraction breakthrough which mapped the dark state structure of the reaction centre[7, 22], a wide variety of experimental[23, 24, 7, 22] and theoretical techniques[25, 26, 27] have been used to study the reaction mechanism and structure of the OEC. Among the many approaches, however, electronic absorption spectroscopy quickly reached the limit of its usefulness. Metal ligand complexes are known to have transitions involving metal ion orbitals in the visible region. Observing how the transitions involving the Mn and Co ions are affected by chemical stimulation would give valuable insight into the reaction mechanism. The problem is that the electronic transitions of biological molecules tend to be complicated. The absorption spectra of cobalamins[3] and photosystem II[2], shown in Figure 1.2, are congested with many broad and overlapping states obscuring the true electronic structure. The spectrum of cobalamin contains several large bands of congested electronic states. The absorption spectrum of photosystem II is dominated by extraneous chlorophyll peaks, and the transitions related to the metal ions in the reaction centre are believed to be between 300 and 350 nm, buried beneath the strong pigment absorptions. The detection of chemical change relies on taking the difference between spectra of two different states which often involves identifying minuscule changes in large features[28]. At best, absorption can identify that a change has occurred but cannot shed any light on its nature. Similar difference measurements in the infrared region have

tentatively found changes to the vibrational structure related to catalytic reactivity[29, 30, 31, 32] but in an enzyme the size of PS II, which has thousands of bonds in the fingerprint region, such assignment is somewhat tenuous.

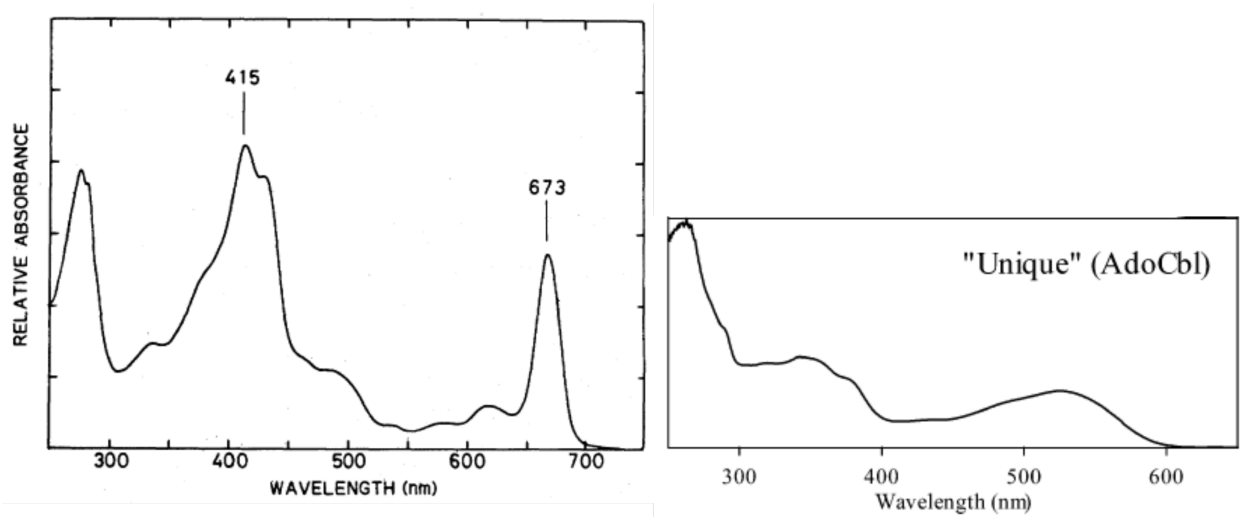

Figure 1.2: The absorption spectrum of the OEC and adocobalamin from references [2] and [3].

1.2 3D-TRSF for the decongestion of electronic structure

The strategy of the picosecond system of the Wright Group is to exploit the selectivity of vibrational-electronic coupling to reduce the number of states producing signal at any given set of frequencies. The absorption spectrum is congested because the ground state is coupled to numerous excited electronic states. In absorption, the probability of a transition taking place is related to the dipole transition moment between the ground and excited electronic states: $P \propto \mu_{eg}^2$. Vibronic transitions however, add an additional layer of specificity. The probability of a vibronic transition is related to the dipole transition moment of the vibrational mode to the electronic state: $P \propto \mu_{ve}$. Controlling the starting vibrational mode allows the coupling strength to be selected in a much more discriminatory manner. Our strategy rests on exciting electronic transitions not directly from the ground state, but rather through intermediate vibrational states. The diversion enhances transitions to coupled electronic states but suppresses transitions to uncoupled ones.

The strategy is similar to resonance Raman in that it relies on vibronic coupling for enhancement of vibrational modes, but takes an opposite approach in that it relies on vibrational intermediate states to suppress transitions to uncoupled electronic states. My project focused specifically on a particular technique called Three Dimensional Triply Resonant Sum Frequency Spectroscopy (3D-TRSF). Non-electronically-resonant versions of fully coherent 2DIR spectroscopy techniques like DOVE and TSF (Triple Sum Frequency) have been explored in the literature[33, 34, 35, 36, 37, 38, 39]. 3D-TRSF represents our first attempt to measure the strength of vibrational-electronic coupling as a function of electronic resonance.

In TRSF, excitation frequencies are in the IR but detection frequencies are in the visible. A triple pulse-sequence is used to induce a series of three excitations. Pulse 1 and 2 are in the mid-IR and have frequencies labeled ω_1 and ω_2. Pulse 3 is in the visible and has a frequency labeled ω_3. The detection frequency is at the sum of the excitation field frequencies ω_{TRSF}. On resonance, the excitation pulses stimulate three sequential transitions: ω_1 from the ground state g to fundamental state v, ω_2 from v to either combination band $v + v'$ or overtone state $2v$, and ω_3 from $2v/v + v'$ to the excited electronic/vibronic state e. The polarization created by the coherence eg creates an anti-stokes Resonance Raman transition and launches a fourth output photon with frequency ω_{TRSF}. The intensity

of the output pulse is measured as TRSF signal. Vibrational transitions are resonantly enhanced by the electronic transition, similar to resonance enhancement of Raman signal in resonance Raman. TRSF is sensitive to the detuning of each excitation field energy from resonance, the absorptivity of each individual transition, and the coupling strength between the states involved in each transition. TRSF is sensitive to IR active pathways, as opposed to resonance Raman which is only sensitive to Raman active pathways. The application of TRSF is illustrated in Figure 1.3, which shows three overlapping but separate electronic states, e_1, e_2, and e_3 (a) which are unresolvable in the linear electronic absorption spectrum (b). Each electronic state is coupled to a different vibrational state: e_1 to v_1, e_2 to v_2, and e_3 to v_3. Upon excitation of the vibrational modes by a TRSF pathway (c), the signal between coupled modes is strongly enhanced and allows for the resolution of the electronic structure along the vibrational frequency axis.

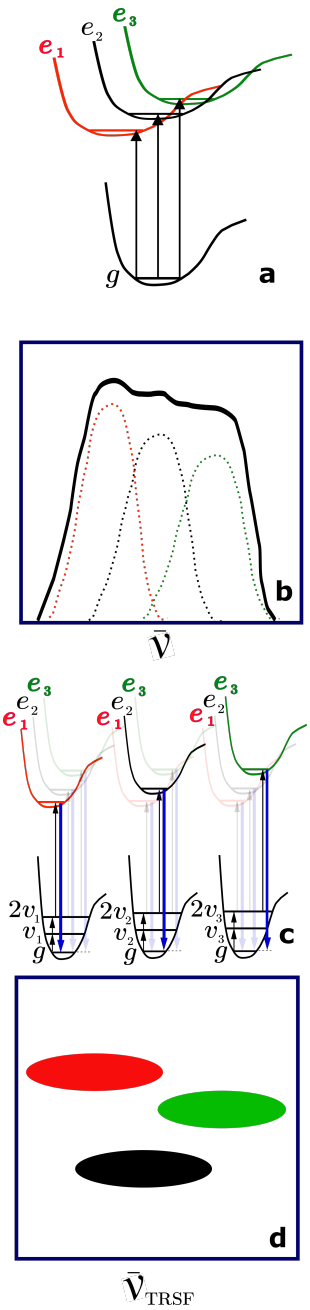

Figure 1.3: An illustration of the resolution provided by the vibrational-electronic coupling of a molecule using TRSF. (a) The electronic structure of the molecule, (b) the net absorption spectrum (solid black) and the underlying electronic states (dotted red, black, and green), (c) the energy level diagrams of the TRSF pathway, and (d) the TRSF spectrum.

When I joined the group, TRSF spectra were limited to 2D frequency scans of the two IR axes ω_1 and ω_2, while ω_3 was fixed at the frequency of the regenerative amplifier output. All spectra taken were either electronically non-resonant, or were of molecules with a convenient electronic resonance at the available sum frequency[4, 5, 6]. The work that I will describe in this dissertation largely comprises of transforming the instrumental system from a 2D to a 3D frequency system, and doing exploratory studies using the new system.

1.3 Summary of work

In Chapter 3, I describe my instrumentation work to upgrade the 2D system to the 3D system capable of doing experiments in which all three frequency axes are scanned. I provide a full description of the system and instructions on how to use it for TRSF experiments. Some example spectra are included showing the results of the additional third tunable frequency.

As frequency ranges became larger, I started to notice oscillations appearing in the spectra in regions where the output is expected to be uniform. The source of the oscillations was eventually identified to be the phase-mismatch effects occuring within the windows of the sample cell. Chapter 4 describes my efforts to characterize the oscillations using a non-resonant sample and model them using simple phase-mismatch theory. It also details measures I took to minimize the effect so as not to interfere with real signal on electronically resonant samples.

In Chapter 5, I describe the application of 3D-TRSF to cyanocobalamin (CNCbl) and deuterated aquacobalamin (D_2OCbl). I scanned the frequency region of the α/β band, a congested feature which is present in the absorption spectra of all major cobalamins. The electronic structure of this region is still a matter of debate in the literature. Models describing it as a vibronic structure and as a combination of several states have been proposed. I targeted the vibrational modes and detected selective coupling to the electronic states in the region. The three vibrational modes were each enhanced at different output frequencies in TRSF and are compared to the two competing electronic state models.

In Chapter 6, I describe my work with chlorophyll and my experience visiting the group of Petra Fromme at Arizona State University. The Fromme group specializes in protein extraction and cyrstallization and

the graduate students walked me through the extraction process and we discussed ideas on how to prepare the sample for multidimensional experiments. Chlorophyll is an integral part of Photosystem 2 and any sample of the OEC will contain chlorophyll molecules. It is necessary to characterize chlorophyll before any attempts are made of the OEC, as chlorophyll is likely to dominate the spectrum and cause confusion if not studied properly.

Chapter 2

Theory and Background

2.1 Triply Resonant Sum Frequency

The Wave Mixing Energy Level (WMEL) Diagram of Triply Resonant Sum Frequency (TRSF) spectroscopy is shown in Figure 2.1

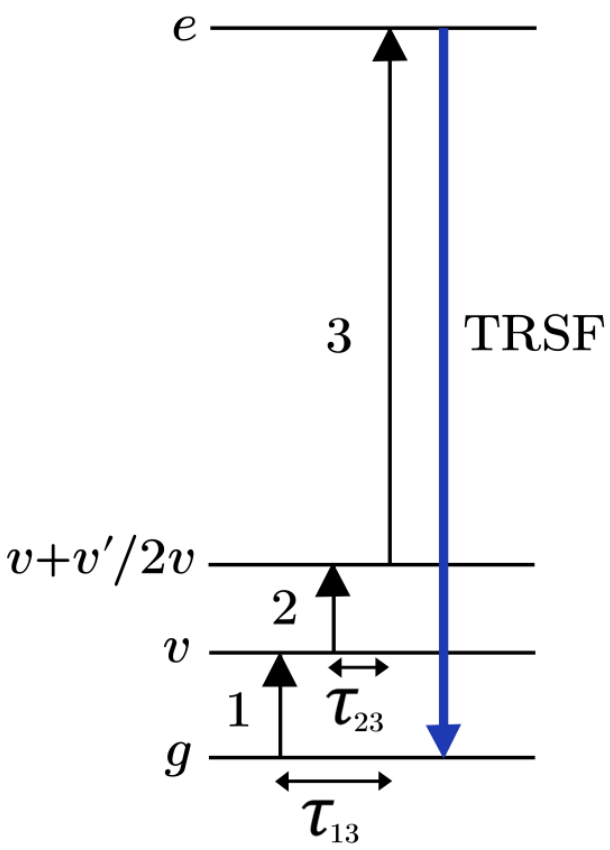

Figure 2.1: Wave Mixing Energy level diagram of TRSF.

When on resonance, pulse 1 creates a coherence vg between the ground state g and a fundamental vibrational mode v, pulse 2 creates a coherence $(v+v')g$ between g and a combination band or overtone state $(v+v')$, and pulse 3 creates a coherence eg between g and an excited electronic state e. The Liouville pathway for TRSF is:

$$gg \rightarrow vg \rightarrow (v+v')g \rightarrow eg \tag{2.1}$$

TRSF consists of three ket-side interactions to form the final coherence. Before interacting with pulse 1, the system is in the ground state ρ_{gg}. When pulse 1 is resonant with a fundamental vibrational mode v, it induces a ket side transition to form a coherence vg with density matrix element:

$$\rho_{vg} = \frac{\Omega_{vg}}{2\Delta_{vg}} \rho_{gg} e^{i(k_1 z - \omega_1 t)} \tag{2.2}$$

where

$$\Omega_{vg} = \frac{\mu_{vg} E_1^0}{\hbar} \tag{2.3}$$

$$\Delta_{vg} = \omega_{vg} - \omega_1 - i\Gamma_{vg} \tag{2.4}$$

Ω_{vg} is called the Rabi frequency, μ_{vg} is the transition dipole moment from state g to v, E_1^0 is the electric field amplitude of pulse 1, ω_1 is the excitation frequency of pulse 1, ω_{vg} is the resonance frequency of the fundamental vibrational transition, and Γ_{vg} is the dephasing rate of the vg coherence.

When pulse 2 is resonant with a transition from v to the overtone state or a combination band $v+v'$, it induces a ket side transiiton to form a coherence $(v+v')g$ with density matrix element:

$$\rho_{(v+v')g} = \frac{\Omega_{(v+v')v}}{2\Delta_{(v+v')g}} \frac{\Omega_{vg}}{2\Delta_{vg}} \rho_{gg} e^{i((k_1+k_2)z - (\omega_1+\omega_2)t)} \tag{2.5}$$

$$\Omega_{(v+v')v} = \frac{\mu_{(v+v')v} E_2^0}{\hbar} \tag{2.6}$$

$$\Delta_{(v+v')g} = \omega_{(v+v')v} - \omega_1 - \omega_2 - i\Gamma_{(v+v')g} \tag{2.7}$$

where μ_{vg} is the transition dipole moment from state v to $v+v'$, E_2^0 is the electric field amplitude of pulse 2, ω_2 is the excitation frequency of pulse 2, $\omega_{(v+v')v}$ is the resonance frequency of the fundamental to overtone/combination band transition, and $\Gamma_{(v+v')g}$ is the dephasing rate of the $(v+v')g$ coherence.

When pulse 3 is resonant with a transition from $v + v'$ to the electronic excited state e, it induces a ket side transition to form a coherence eg with density matrix element:

$$\rho_{eg} = \frac{\Omega_{e(v+v')}}{2\Delta_{eg}} \frac{\Omega_{(v+v')v}}{2\Delta_{(v+v')g}} \frac{\Omega_{vg}}{2\Delta_{vg}} \rho_{gg} e^{i((k_1+k_2+k_3)z-(\omega_1+\omega_2+\omega_3)t)} \tag{2.8}$$

$$\Omega_{e(v+v')} = \frac{\mu_{e(v+v')} E_3^0}{\hbar} \tag{2.9}$$

$$\Delta_{eg} = \omega_{eg} - \omega_1 - \omega_2 - \omega_3 - i\Gamma_{eg} \tag{2.10}$$

where μ_{eg} is the transition dipole moment from state $v + v'$ to e, E_3^0 is the electric field amplitude of pulse 3, ω_3 is the excitation frequency of pulse 3, $\omega_{e(v+v')}$ is the resonance frequency of the fundamental to overtone/combination band transition, and Γ_{eg} is the dephasing rate of the eg coherence.

2.1.1 TRSF Density Matrix

The density matrix element amplitude is labelled $\widetilde{\rho}_{eg}$ such that

$$\rho_{eg} = \widetilde{\rho}_{eg} e^{i((k_1+k_2+k_3)z-(\omega_1+\omega_2+\omega_3)t)} \tag{2.11}$$

$$\widetilde{\rho}_{eg} = \frac{\Omega_{e(v+v')}}{2\Delta_{eg}} \frac{\Omega_{(v+v')v}}{2\Delta_{(v+v')g}} \frac{\Omega_{vg}}{2\Delta_{vg}} \rho_{gg} \tag{2.12}$$

2.1.2 Polarization and output electric field

The three excitation fields create a nonlinear polarization

$$P^0 = D\chi^{(3)} E_1^0 E_2^0 E_3^0 \tag{2.13}$$

where P^0 is the polarization amplitude, $D = 6$ in the Maker-Terhune convention for excitation field permutations[40], and $\chi^{(3)}$ is the third order susceptibility. $\chi^{(3)}$ is defined explicitly later on.

The polarization created by an electric field is related to the transition dipole moment by

$$\vec{P} = NF\langle\vec{\mu}\rangle \tag{2.14}$$

where N is the chromophore concentration, F is the field enhancement factor, and $\vec{\mu}$ is the transition dipole moment. The polarization amplitude of the eg coherence is defined by

$$P^0 = 2NF_{net}\mu_{eg}\widetilde{\rho}_{eg} \tag{2.15}$$

The TRSF output field with amplitude E_4^0 is created by the nonlinear polarization P. Using Maxwell's scalar wave equation , the relationship between the polarization and the output field it creates can be described by

$$\frac{\partial E_4^0}{\partial z} + \frac{1}{c}\frac{\partial E}{\partial t} = \frac{2\pi i F_4\omega_4 P^0}{n_4 c}e^{i\Delta Kz} \tag{2.16}$$

where z is the pathlength, F is the field enhancement factor, ω_4 is the output field frequency, n_4 is the index of refraction of E_4^0, c is the vacuum speed of light, and ΔK is the complex wave-vector phase-mismatch term between the nonlinear polarization and the output electric field. Assuming steady state, Equation 2.16 simplifies to

$$\frac{\partial E_4^0}{\partial z} = \frac{2\pi i F_4\omega_4 P^0}{n_4 c}e^{i\Delta Kz} \tag{2.17}$$

To get the total electric output field, Equation 2.17 is integrated across the sample pathlength ℓ

$$E_4^0 = \int_0^\ell \frac{2\pi i F_4\omega_4 P^0}{n_4 c}e^{i\Delta Kz} \tag{2.18}$$

Assuming constant excitation field intensity across the pathlength

$$E_4^0 = \frac{2\pi i F_4\omega_4 P^0}{n_4 c}\frac{e^{i\Delta K\ell} - 1}{\Delta K} \tag{2.19}$$

Assuming short pathlengths ($\ell \sim 25\mu$ m), the phase-mismatch term is close to 1 and can be considered constant. However, this assumption does not always hold true even when the sample itself has a short pathlength. See section 2.2 for more details.

Inserting Equations 2.15 and 2.12 into Equation 2.19 yields the expression

$$E_4^0 = \frac{4\pi i F_4 \omega_4 2 N F_{net} \mu_{eg} \Omega_{e(v+v')} \Omega_{(v+v')v} \Omega_{vg} \rho_{gg}}{8 n_4 c \Delta_{eg} \Delta_{(v+v')g} \Delta_{vg}} \frac{e^{i\Delta K \ell} - 1}{\Delta K} \tag{2.20}$$

Inserting the expressions of the Rabi frequencies from Equations 2.3,2.6, and 2.9 into Equation 2.20

$$E_4^0 = \frac{\pi i F_4 \omega_4 N F_{net} \mu_{eg} \mu_{e(v+v')} \mu_{(v+v')v} \mu_{vg} \rho_{gg}}{4\hbar^3 n_4 c \Delta_{eg} \Delta_{(v+v')g} \Delta_{vg}} E_1^0 E_2^0 E_3^0 \left(\frac{e^{i\Delta K \ell} - 1}{\Delta K} \right) \tag{2.21}$$

Equation 2.13 relates the nonlinear polarization to the excitation field amplitude product by the third order susceptibility $\chi^{(3)}$, which is derived from Equation 2.21 to be

$$\chi^{(3)} = \frac{N F_{net} \mu_{eg} \mu_{gv} \mu_{v(v+v')} \mu_{(v+v')e} \rho_{gg}}{4 D \hbar^3 \Delta_{vg} \Delta_{(v+v')g} \Delta_{eg}} \tag{2.22}$$

Experimental signal as measured on the detector is the output signal intensity

$$I = E_4^{0*} E_4^0 \tag{2.23}$$

In this dissertation, the TRSF output signal is represented as the absolute value of the output amplitude

$$E_{TRSF} = \sqrt{I} = |E_4^0| \tag{2.24}$$

2.2 Phase mismatch in the sample and sample cell

TRSF is not a phase-matchable process in typical solvents. The index of refraction in most media tends to increase with frequency, such that the wave-vector term of the output field, k_4, is always larger than the sum of the input field wave-vectors $k_1 + k_2 + k_3$. As shown in Equation 2.19, the phase-mismatch effect causes the output signal to oscillate with sample length. The sample is intentionally restricted to very low pathlengths ($\sim$25μm) to mitigate the effects of phase-mismatch and disregard such effects in interpreting TRSF spectra. However, it was discovered that low intensity non-resonant signal from the sample cell windows, which are relatively thick, interfered with the resonant signal resulting in oscillatory

artifacts when scanning large frequency ranges. Here, phase-mismatch and the interference of resonant and non-resonant signal is described in more detail.

2.2.1 Wave-vector descriptions

The phase-mismatch term ΔK is defined as

$$\Delta K = K_4 - K_1 - K_2 - K_3 \tag{2.25}$$

In medium which partially absorbs the excitation or output fields, K_j can be defined as [41]:

$$K_j = k_j - ik''_j \tag{2.26}$$

where k_j and k''_j are the real and imaginary parts of k_j. k_j is calculated as

$$k_j = \frac{n(\omega_j)\omega_j}{c} \tag{2.27}$$

where n is the index of refraction of the medium at frequency ω_j and c is the speed of light.

$$k''_j = -\frac{\alpha_j}{2} \tag{2.28}$$

where α_j is the absorption coefficient at ω_j. The polarization wave-vector k'_4 is given by

$$\begin{aligned} K_4 &= k_4 + ik''_4 \\ &= (k_1 + k_2 + k_3) + i(k''_1 + k''_2 + k''_3) \\ &= (k_1 + k_2 + k_3) - i\frac{(\alpha_1 + \alpha_2 + \alpha_3)}{2} \end{aligned} \tag{2.29}$$

The wave-vector phase-mismatch is defined by

$$\begin{aligned}\Delta K &= K_4' - K_4 \\ &= (k_1 + k_2 + k_3) - k_4 - i(\frac{(\alpha_1 + \alpha_2 + \alpha_3 - \alpha_4)}{2}) \\ &= \Delta k - i\alpha_{net}\end{aligned} \tag{2.30}$$

2.2.2 Window and solvent signal interference

In our system, the sample is composed of a front window, a solvent, and a back window. Each component contributes to the net output signal E_{net}

$$E_{net} = E_{w1} + E_s + E_{w2} \tag{2.31}$$

$$E_{w1} = \int_0^{L_w} \frac{2\pi i F_4 \omega_4 P^0}{n_4 c} e^{i\Delta k_w z} dz \tag{2.32}$$

$$E_s = \int_{L_w}^{L_w+L_s} \frac{2\pi i F_4 \omega_4 P^0}{n_4 c} e^{i(\Delta K_s z + i\frac{\alpha_s}{2} + \phi_1)} dz \tag{2.33}$$

$$E_{w2} = \int_{L_w+L_s}^{2L_w+L_s} \frac{2\pi i F_4 \omega_4 P^0}{n_4 c} e^{i(\Delta k_w z + \phi_2)} dz \tag{2.34}$$

where $E_{w1,s,w2}$ are the output electric fields generated in the first window, solvent, and second window, and $L_{w,s}$, $\Delta k_{w,s}$, and $P_{w,s}$ are the patlengths, wave-vector phase mismatch terms, and non-linear polarizations created in the windows and solvent layers respectively. α_s is the solvent absorption coefficient at both excitation frequencies similar to α_{net} in Equation 2.30, and the windows are assumed to be completely transparent. The ϕ_1 and ϕ_2 terms are phase factors that describe the phase changes that accrue as the fields pass through the first and last windows respectively.

$$\phi_1 = i\Delta k_w L_w \tag{2.35}$$

$$\phi_2 = i(\Delta k_w L_w + \Delta k_s L_s + i\frac{\alpha_s}{2} L_s) \tag{2.36}$$

The effects of the interference of window and sample generated signal is explored in detail in Chapter 4.

2.3 Franck-Condon Factors and vibronic coupling

The transition probability of vibronic transitions can be estimated by the nuclear overlap of the initial and final state. According to the Born-Oppenheimer approximation, the motions of nuclei can be treated separately from those of electrons, such that the wavefunction can be written as a product of the nuclear and electronic wavefunction

$$\psi_{en}(x, r) = \psi_e(x)\psi_n(r) \tag{2.37}$$

where $\psi_e(x)$ is the electronic wavefunction with coordinates x and $\psi_n(r)$ is the nuclear wavefunction with coordinates r[42]. The transition probability P is given by

$$\begin{aligned} P &= |\int_{-\infty}^{\infty} \psi_{0n} * \mu\psi_{1m} dx dr|^2 \\ &= |\int_{-\infty}^{\infty} (\psi_0(x)\psi_n(r)) * \mu(\psi_1(x)\psi_m(r)) dx dr|^2 \\ &= M_e|\int_{-\infty}^{\infty} \psi_n(r) * \psi_m(r) dr|^2 \end{aligned} \tag{2.38}$$

where M_e is the transition dipole moment function characteristic of the electronic transition, n and m are the ground and excited state vibrational levels respecitively, and 0 and 1 are the electronic state levels[42, 43]. The square of the overlap integral is called the Franck-Condon factor[44, 42]. The Franck-Condon factors are directly related to the absorption intensity from the ground electronic and vibrational state to the vibrational levels of the excited electronic state. Meanwhile the TRSF transition probability is related to the overlap integral of the overtone vibrational state in the electronic ground state to the excited electronic state. The overlap integrals can be analytically solved by the following equations taken from Myers et al.[45]

$$\langle 0|0\rangle = \left(\frac{2}{1+R}\right)^{1/2} R^{1/4} exp\left[\frac{-\Delta^2}{2(1+R)}\right] \tag{2.39}$$

$$\langle m|0\rangle = \frac{\langle 0|0\rangle}{(2^m m!)^{1/2}} \left(\frac{R-1}{R+1}\right)^{m/2} H_m\left[-\left(\frac{R}{R^2-1}\right)^{1/2}\Delta\right] \tag{2.40}$$

$$\langle 0|n\rangle = \frac{\langle 0|0\rangle}{(2^n n!)^{1/2}} \left(\frac{R-1}{R+1}\right)^{n/2} H_n\left[\frac{\Delta}{(1-R^2)^{1/2}}^{1/2}\Delta\right] \tag{2.41}$$

$$\langle m|n\rangle = \langle 0|0\rangle^{-1} \sum_{k=0}^{min(m,n)} \left(\frac{2R^{1/2}}{1+R}\right)^{k} \frac{1}{k!} \left[\frac{m!n!}{(m-k)!(n-k)!}\right]^{1/2} \langle m-k|0\rangle \langle 0|n-k\rangle \tag{2.42}$$

where $|n\rangle$ and $|m\rangle$ are the ground and excited state vibrational levels, R is the ratio of the ground and excited vibrational state frequencies, H_m is the mth Hermite polynomial, and Δ is the excited state displacement. Equations 2.39,2.40,2.41 and 2.42 can be used to calculate the relevant Franck-Condon factors and TRSF Raman transition probability P_{TRSF}

$$FC = |\langle m|0\rangle|^2 \tag{2.43}$$

$$P_{TRSF} = \langle m|2\rangle \langle 0|m\rangle \tag{2.44}$$

The overlap integrals are used in the line-shape analysis of the TRSF spectrum of CNCbl and D_2OCbl in Chapter5.

Chapter 3

Picosecond Experimental System

3.1 Additions to the Picosecond system

Here I describe my contribution to the development of the picosecond system. The picosecond system was originally designed for 2dIR TRSF experiments with a fixed visible excitation field frequency. A schematic of the old picosecond experimental system is shown in Figure 3.1.

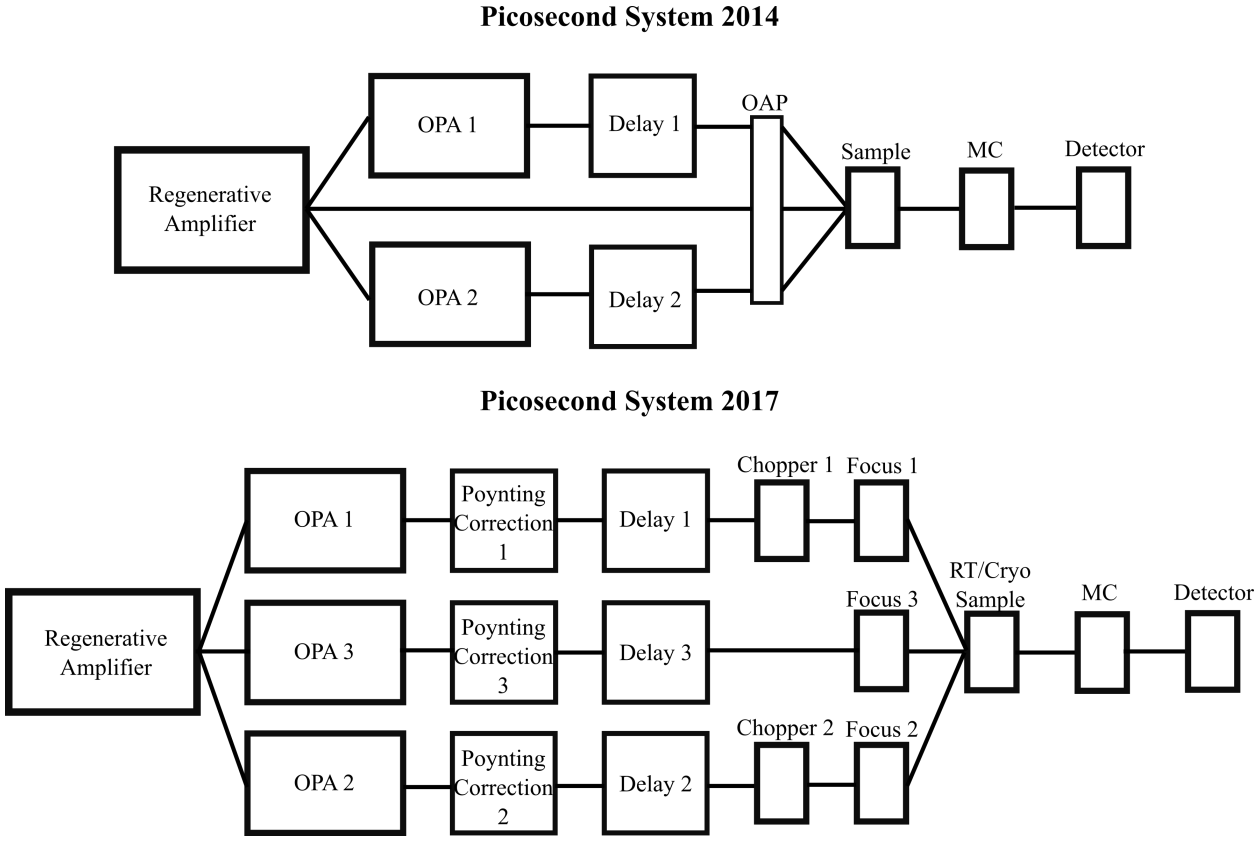

Figure 3.1: A comparison of the two frequency scannable picosecond system components in 2014, and the three frequency scannable picosend system componenets in 2017.

The system comprised of two mid-IR OPAs (OPA1 and OPA2), an 800 nm visible beam, two retroreflectors mounted on translation stages for delay correction, one Off-Axis-Parabolic mirror for overlapping and focussing the three excitation fields, and monochromator for output wavelength selection. Over the course of my graduate career, I have overseen the addition of a third tunable visible source, and the restructuring, streamlining, and optimization of the laser table to handle the challenges involved with 3D experiments. Notable hardware additions to the table include the third OPA (OPA3), OPA output Pointing Correction mirrors, choppers for noise reduction, a fixed sample position beam overlap pinhole, specialized focussing optics for each laser line for optimal focus and overlap, and the installation of the cryostat for experiments on cryogenic samples.

3.1.1 OPA3

OPA3 was added to provide a third fully tunable light source. OPA1 and OPA2 were already setup to produce mid-IR light so OPA3 was fitted with a Second Harmonic Signal BBO with the option to switch to a Sum Frequency signal BBO for higher energy output. I completely redesigned the table to accomodate OPA3, placing the OPA itself on the experimental table. The old table design can be found in Erin Boyle's dissertation. The new table design is illustrated in Figure 3.7.

3.1.2 Pointing Correction

I discovered that the beam output from each OPA changes direction as the frequency changes, an effect I suspect is due to spatial walk-off in the BBO and output crystals. While the angular changes are relatively very small, on the order of tenths of degrees, they are sufficient to affect the beam overlap at the sample position. Two scans of the same sample could appear different depending on what frequency combination the OPAs were set to while pulse overlap was maximized. The walk-off was not noticeable in smaller scale 2D experiments in which the vibrational features were narrow and scanning ranges were kept to around 500 cm^{-1}. Experiments with a fully tunable ω_3, however, scanned over almost 3000 cm^{-1} across broad electronic states as well as non-electronically resonant solvent signal, and the walk-off became obvious. Razor blade scans across the output beams of OPA1, OPA2, and OPA3 with respect

to frequency shown in Figures 3.2,3.3, and 3.4 show drifting output direction. In these scans, the OPA output beam was fed into a detector which a razor blade mounted on a translation stage was translated perpendicular to the beam to determine the center of the mode. While the y-axes in Figures 3.3 and 3.4 are labeled τ_{23} ann τ_{13} respectively, they actually represent the position of the motorized translation stages on which the razor blades were mounted. The razor blade was positioned close to and far away from the OPA exit to show that the beam was changing direction and not merely translating while remaining parallel.

To address the problem, motorized kinematic mirrors were purchased from Zaber for each laser line and were named the pointing correction mounts. They were integrated into PyCMDS by Kyle Sunden. The Pointing correction motors now act as an additional motor in the OPA tuning setup along with the grating, BBO, and Mixer motors. The generation of the Pointing correction motor curves is a process called Pointing tune. The beams are overlapped at the sample position using the pinhole, which is left in place while the appropriate detector is mounted on the monochromator. The ϕ and θ axes of the Zaber mirrors are scanned to find the mirror angles that correspond with the maximum throughput through the pinhole. In the 3D Pointing tune of ω_3 shown in Figure 3.5, OPA3 is sent to nine different set points in its tuning range while ϕ and θ are scanned. The 3D scan shows how the center of the mode migrates from left to right in θ and explains how overlap can be lost during a large frequency scan. The Zaber motors also provide us with an opportunity to view the mode structure at the sample position. As seen in Figure 3.5, the mode structure of ω_3 becomes inexplicably split into two peaks betwen 14,000 and 16,300 cm^{-1}. Typically, Pointing tunes are collected as a set of two one-axis calibration as shown in Figure 3.22.

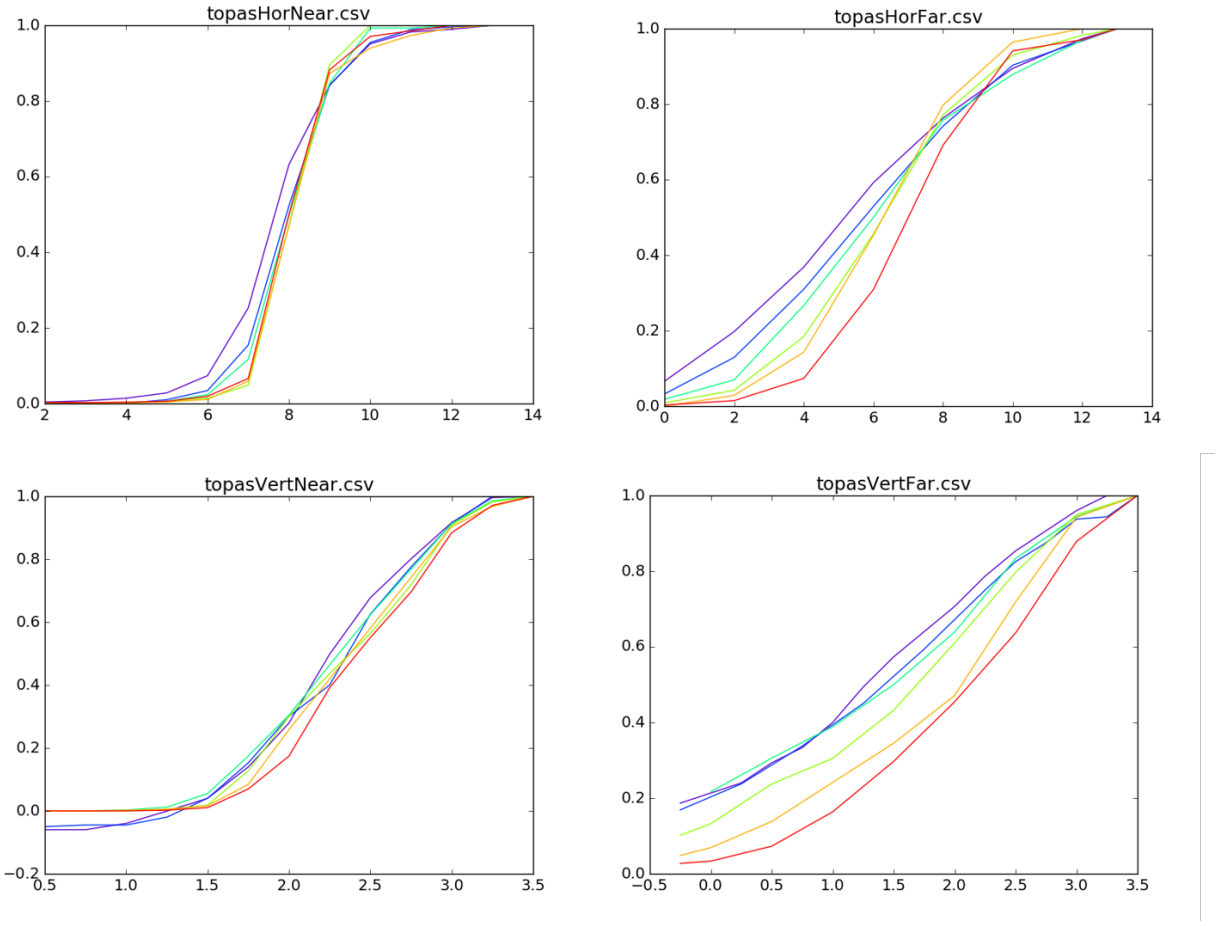

Figure 3.2: The spatial walkoff of the output beam of OPA1

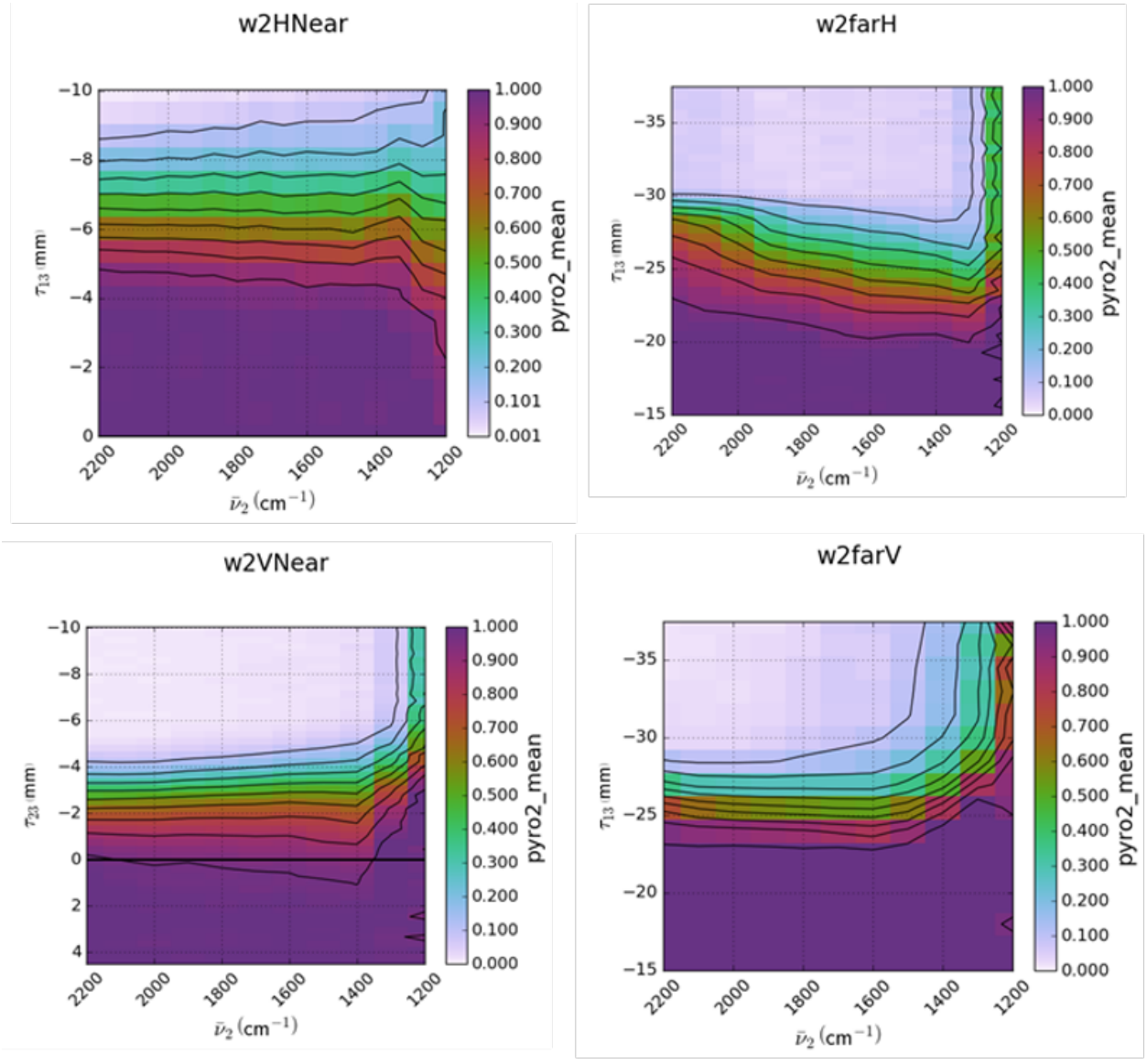

Figure 3.3: The spatial walkoff of the output beam of OPA2

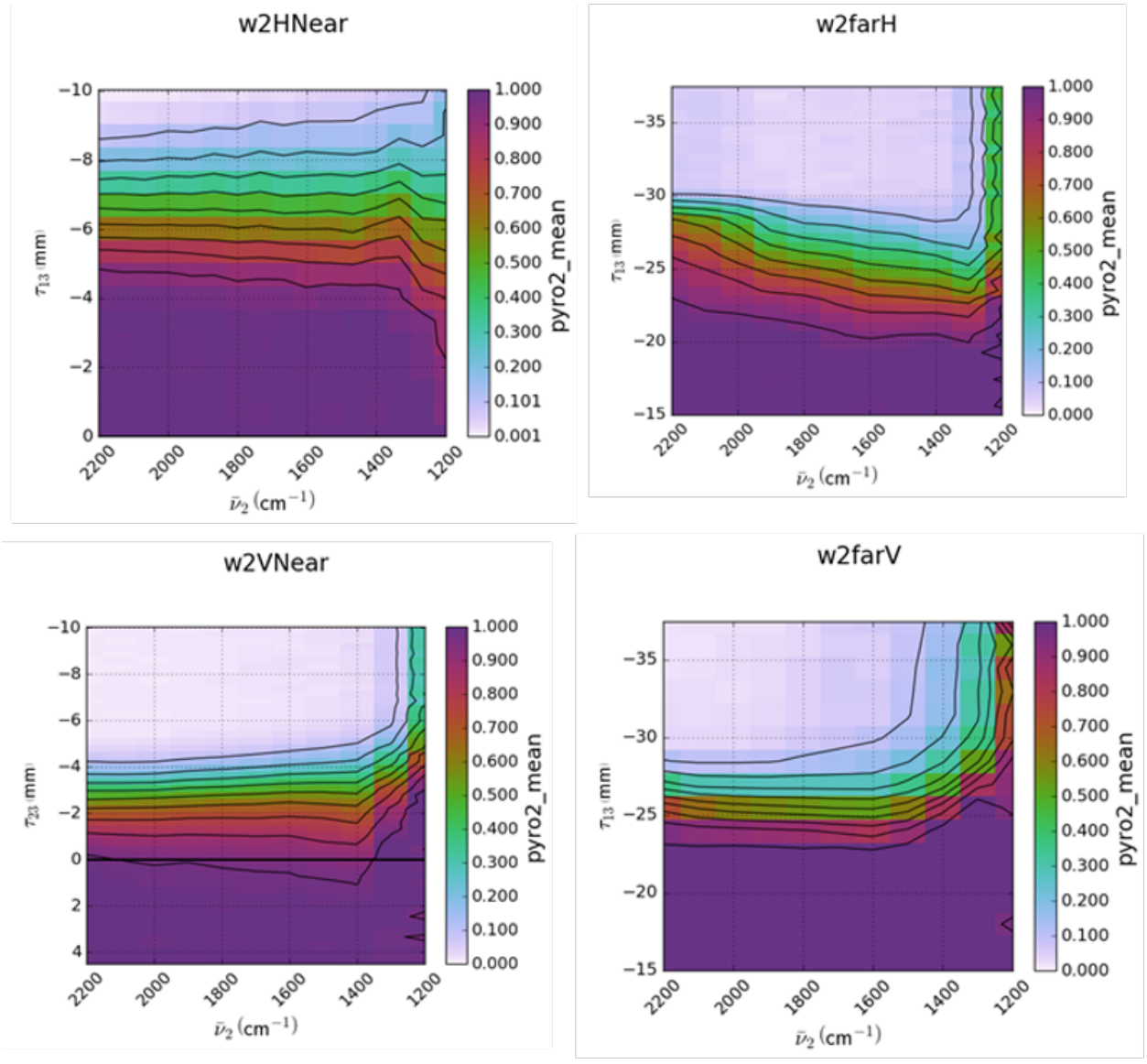

Figure 3.4: The spatial walkoff of the output beam of OPA3

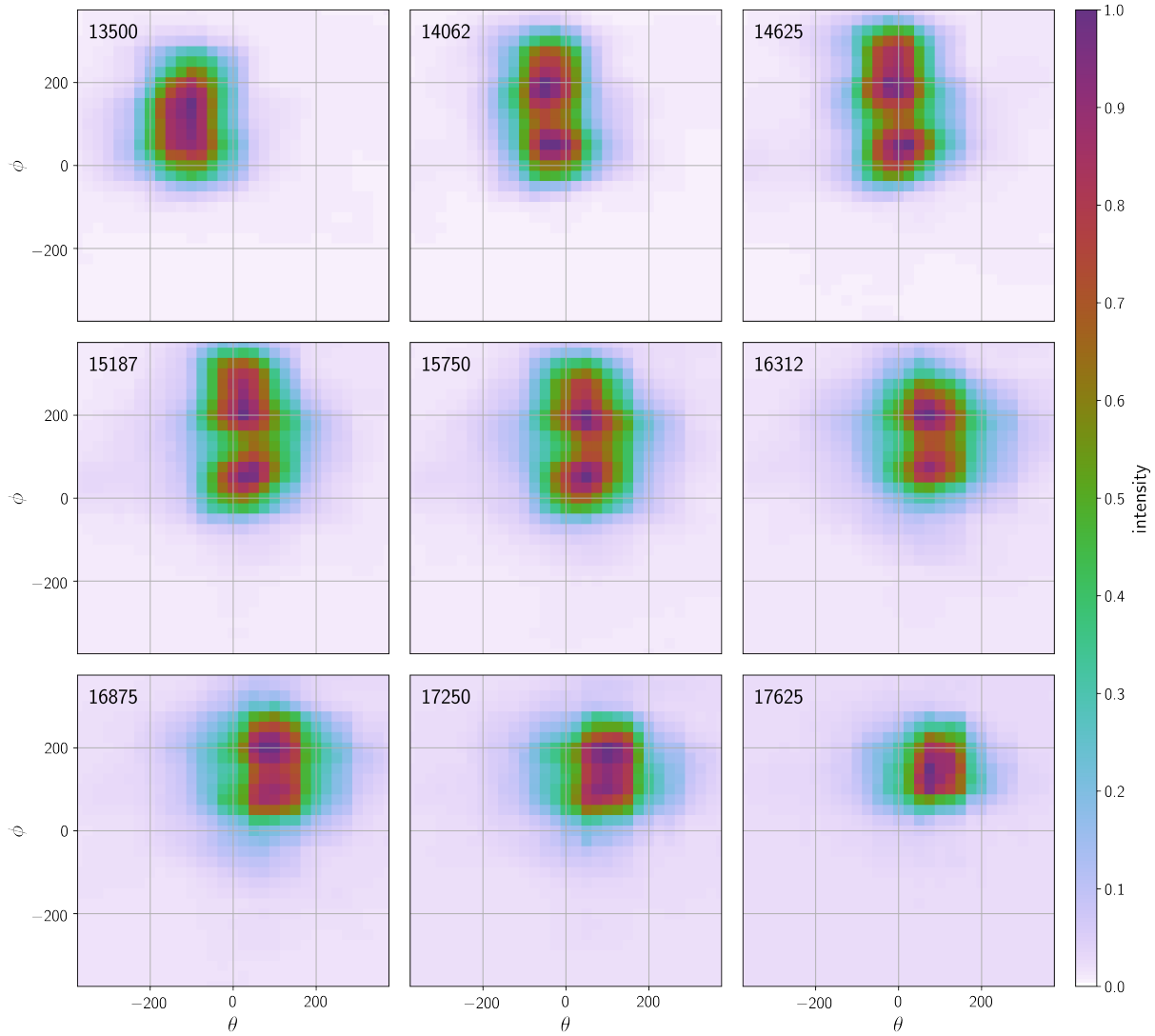

Figure 3.5: Frequency dependent drift of OPA3 output beam at the pinhole

3.1.3 Individual focusing optics setup

In the old system, all three beams were focused and overlapped at the sample by a single gold or silver Off-Axis Parabolic (OAP) mirror. While the single focusing optic provided a convenient and compact way to achieve both overlap and focus, the difference in wavelengths between the visible and IR beams meant that ω_3 was being focused to a beam waist 10 times narrower than ω_1 and ω_2. The output signal intensity depends on the intensity of the excitation fields and the number of oscillators, and is maximum when the three fields are equally intense with a similar beam waist. In order to have such conditions, each beam requires its own focussing optic of appropriate focal length. Along with Dan Kohler, I created a system of three concave mirrors: two gold mirrors of focal length 25 cm for ω_1 and ω_2, and a silver mirror of focal length 1 m for ω_3. ω_1 and ω_2 pass around the sides of the prism mirror and are then focused by their respective concave mirrors. ω_3 reflects off of the 1 m focal length silver mirror mounted above the height of the prism mirror, and then descends towards a flat silver mirror, passing over the prism mirror, before reflecting off the flat mirror and the prism mirror towards the sample. For ω_3, the beam begins to be focused 1.5 m before the sample. Figure 3.6 illustrates the setup from above (top), and the geometry of ω_3 from the side (below). We decided against using focusing lenses to avoid spherical aberrations.

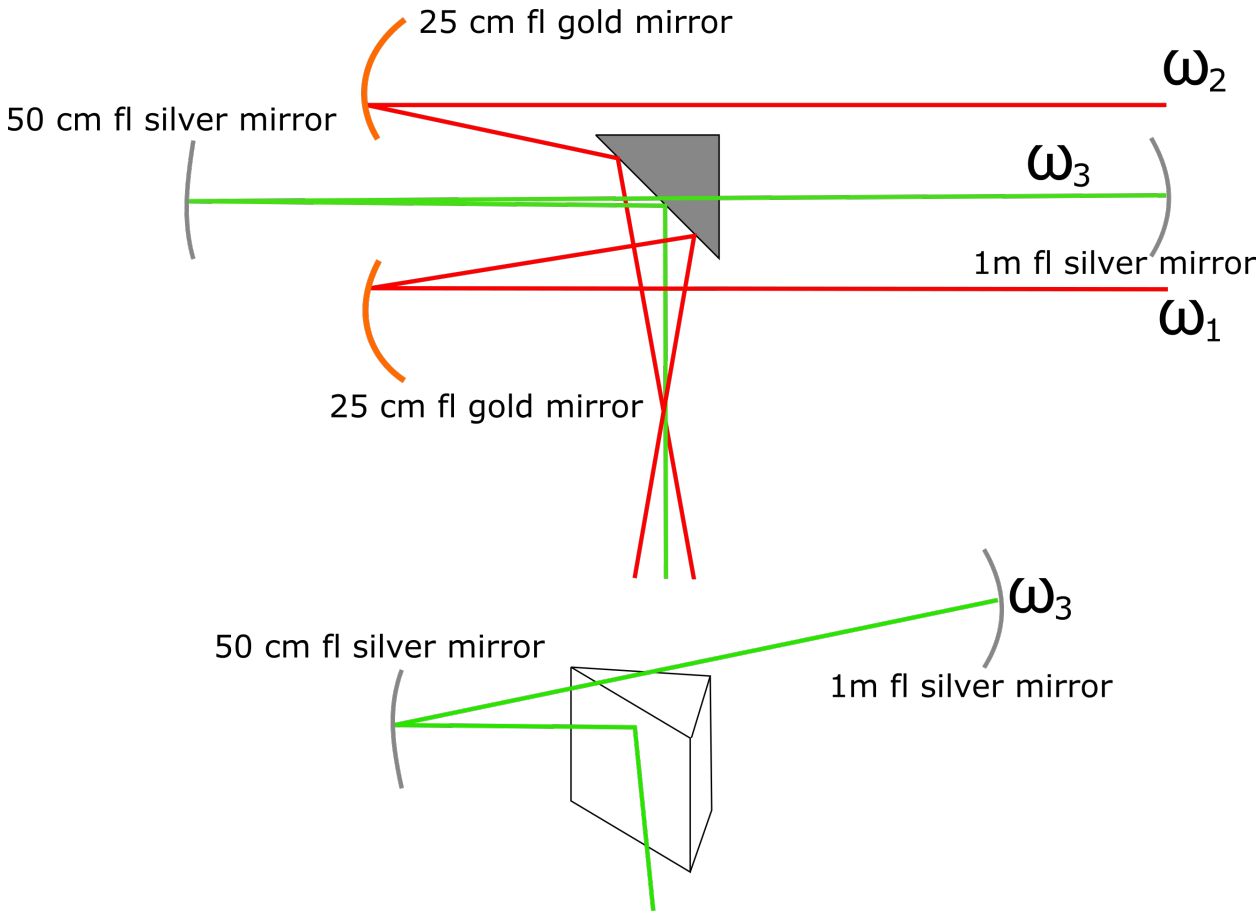

Figure 3.6: Individual focussing optics setup from above (top) and from the side (below)

3.1.4 Cryogenic sample cell

When I joined the group, the cryostat, described in more detail in the full description of the system, had been purchased but not implemented on the table. We plan to ultimately use the cryostat to hold OEC samples at 77 K while collecting multidimensional spectra of fixed intermediate states. I have constructed a modular sample staging area allowing for the user to easily switch between the alignment pinhole, room temperature samples, and cryogenic samples simply by placing and removing stages from magnetic mounts. The preparation area for the cryostat is on the Spitfire laser table. TRSF spectra on cryogenic samples are now relatively straightforward to perform.

3.2 Description of PS laser system

Here I describe the picosecond system. This chapter focuses on the layout and operation of the experimental system after the Regenerative Amplifier. For details about the Tsunami Oscillator and the Spitfire Regenerative Amplifier, see the Appendix.

3.3 Introduction

The Wright Group Picosecond system is an instrument designed to perform Coherent Multidimensional Spectroscopic (CMDS) experiments, in particular Four-Wave Mixing Experiments. Three tunable picosecond pulses are generated by three separate Optical Parametric Amplifiers (OPAs) powered by a picosecond regenerative amplifier. The OPAs can be tuned to produce pulses of whatever frequency the user requires from the UV to the mid-IR using variety of mixing crystals. The system overlaps the pulses at the sample spatially, using mirrors and focusing optics, and temporally, using retroreflectors as delay stages. The signal is separated from the excitation fields either spectrally, using cutoff filters, or spatially using an aperture to isolate the correct phase-matching. The output is further filtered by a monochromator and detected using a PMT. The OPAs, delay stages, and monochromator motors are computer controlled using PyCMDS. Data is acquired using a DAQ (National Instruments) and is recorded into data files using PyCMDS.

3.4 Layout

The scaled schematic of the laser table is illustrated in Figure 3.7. The ω_1 line is the pink trace, ω_2 is the purple trace, and ω_3 is the green trace. The holes on the breadboard are gridded and labeled numerically along the long and alphabetically along the short edge of the table.

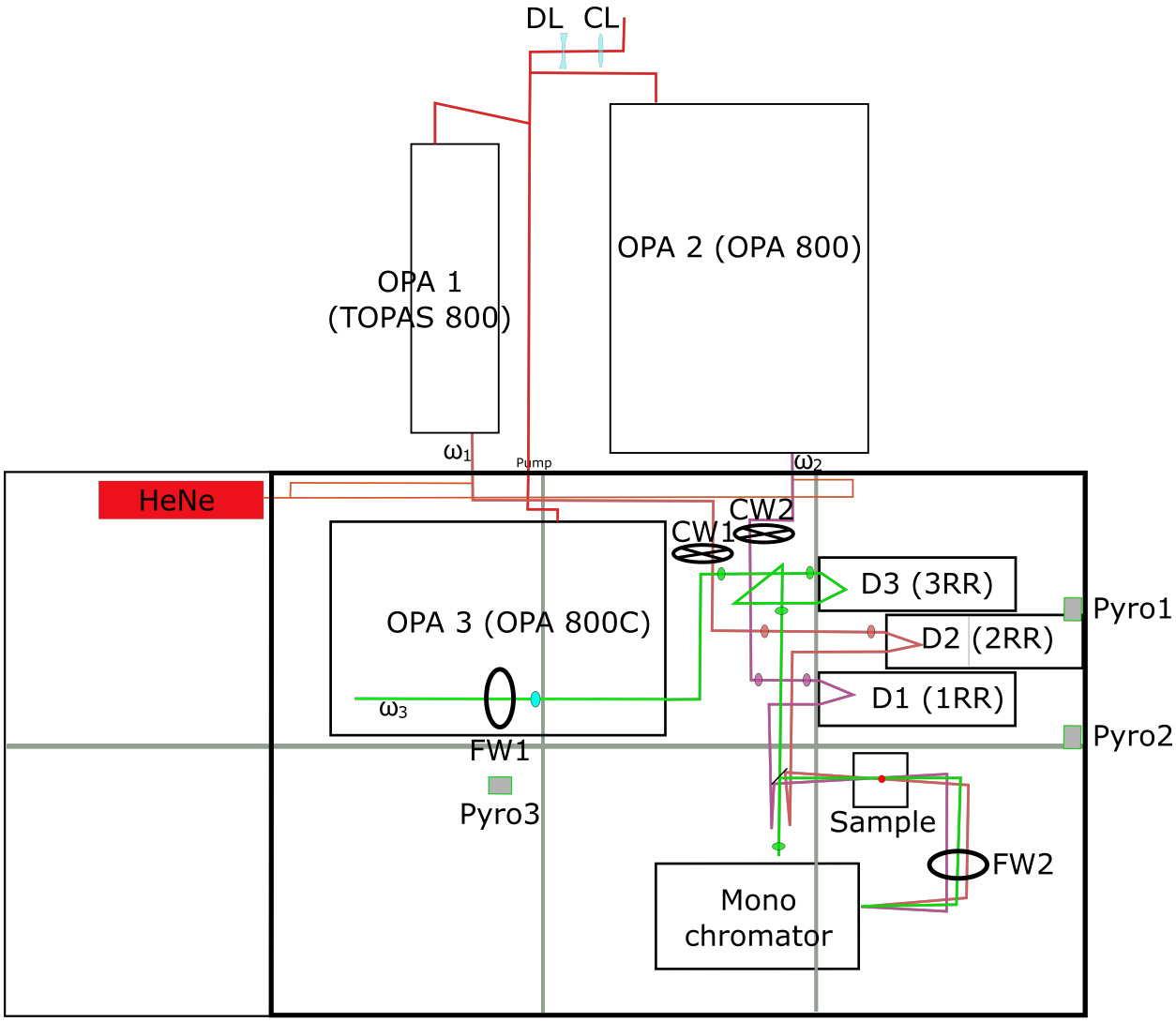

Figure 3.7: The picosecond experimental system drawn to scale

3.4.1 Pump distribution

The output of the Spitfire is split by transmissive/reflective beamsplitters to the OPAs (Figure 3.8). The output distribution to the OPAs is listed below

- CL- telescope that narrows the beam width from 10 mm to 6 mm, 75 mm FL converging lens.
- DL - 100 mm FL Diverging lens
- BS1 - 90/10 T/R beamsplitter, sends 0.5 W to power OPA2
- BS2 - 70/30 T/R beamsplitter, sends 1.4 W to power OPA1
- BS3 - 50/50 T/R beamsplitter, sends 1 W to power OPA3, dumps 1 W of excess power

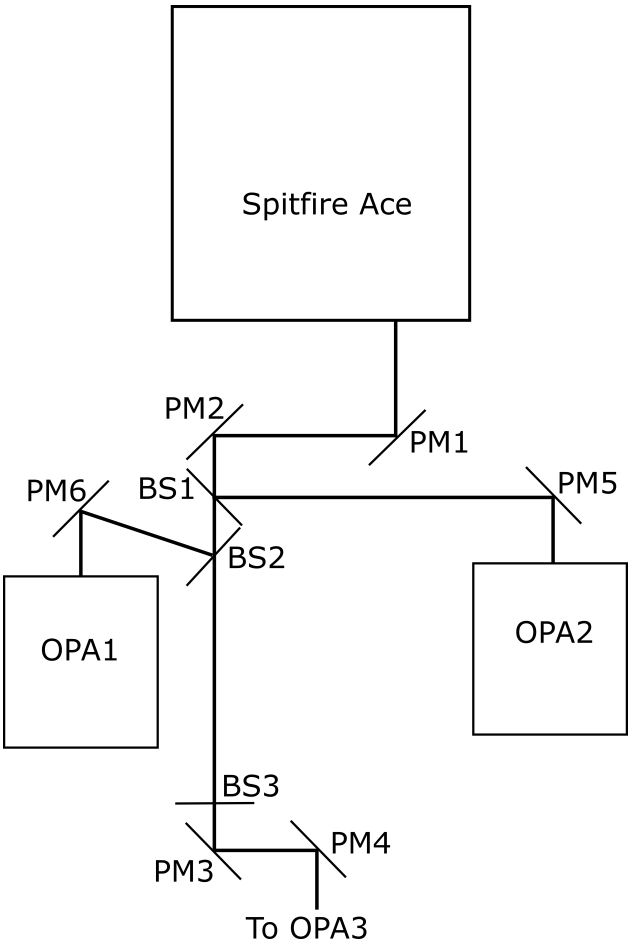

Figure 3.8: The pump distribution to the OPAs

3.4.2 ω_1

The first beam is generated by a TOPAS – 800 OPA from Light Conversion (OPA1). For current experiments (TSF, DOVE) ω_1 is near to mid – IR. The beam enters the table through a hole in the side of wall near A52. The path of ω_1 is as follows:

- 1M1: Plano gold mirror - C52
- 1M2: Plano gold mirror - C31
- 1M3: Plano gold mirror - P31
- 1AP1: Alignment Aperture post (14.5 cm) - P29
- 1AP2: Alignment Aperture post (14.5 cm) - P11
- 1RR: Gold retroreflector, mounted on motorized delay stage D1
- 1M4: Plano gold mirror - Q23
- 1CM: 25 cm FL gold concave mirror - EE23
- PM: Prism Mirror - BB24
- Sample - BB19

Additional components:

- 1CF1 - C37 – Calcium Fluoride window: set at 45 degrees to the optical axis, beam combiner for IR light from OPA1 (transmits) and visible tracking line from HeNe laser - C37
- 1CF2 - P14 – Calcium Fluoride window: set at 45 degrees to the optical axis, reflects 5% of the light to Pyro1
- Pyro1– Pyroelectric detector for OPA1 power monitoring

The beam is 14.5 cm above the table until reaching the retroreflector 1RR, after which the height is adjusted to 5". The beam path of ω_1 is illustrated in Figure 3.9

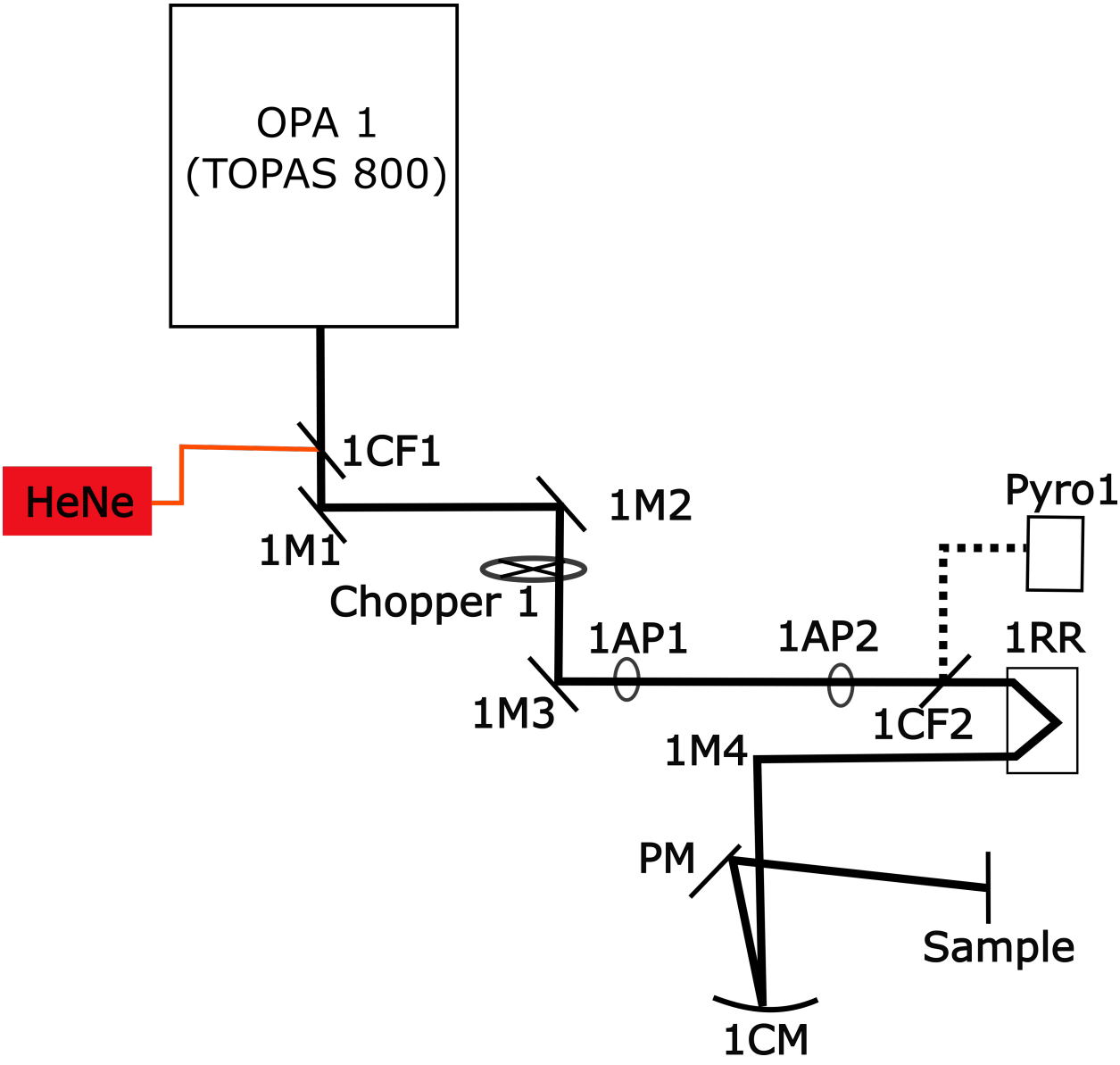

Figure 3.9: The beampath of ω_1

3.4.3 ω_2

The second beam is generated by an OPA 800 from Spectra Physics (OPA2). For current experiments (TSF, DOVE) ω_2 is near to mid - IR. The beam enters the table through a hole in side of the wall near A25. ω_2 follows the path:

- 2M1: Plano gold mirror - B25
- 2M2: Plano gold mirror - B28
- 2M3: Plano gold mirror - U28
- 2AP1: Alignment Aperture post (12 cm) - U27
- 2AP2: Alignment Aperture post (12 cm) - U21
- 2RR: Gold retroreflector, mounted on motorized delay stage D2
- 2M4: Plano gold mirror - V25
- 2CM: 25 cm FL gold concave mirror - EE25
- PM: Prism Mirror - BB24
- Sample - BB19

Additional components:

- 2CF1 - E28 – Calcium Fluoride window: set at 45 degrees to the optical axis, beam combiner for IR light from OPA1 (transmits) and visible tracking line from HeNe laser
- 2CF2 - U20 – Calcium Fluoride window: set at 45 degrees to the optical axis, reflects 5% of the light to Pyro2.
- Pyro2 – Pyroelectric detector for OPA2 power monitoring

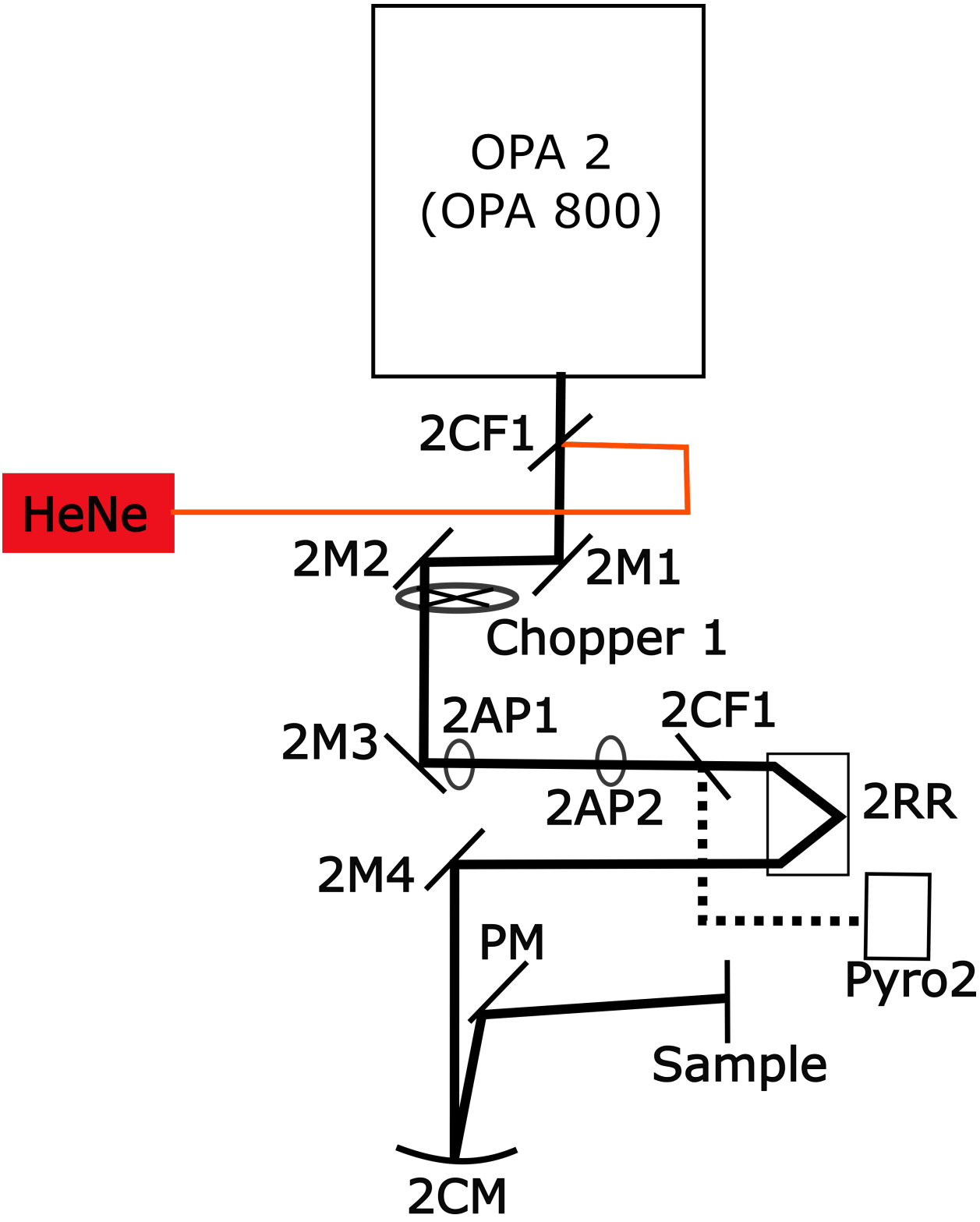

Figure 3.10: The beampath of ω_2

3.4.4 ω_3

The third beam is generated by an OPA 800C from Spectra Physics (OPA3). The OPA itself is on the main laser table. For current experiments (TSF, DOVE) ω_3 is visible to near-UV. Once the parametric output is generated, ω_3 follows the line:

- 3P1: Periscope mirror, Silver Plano mirror, raises the beam height from 12.5 to 16 cm above the table
- 3P2: Periscope mirror, Silver Plano mirror
- 3M1: Plano silver mirror - T33
- 3M2: Plano silver mirror - K33
- 3AP1: Alignment Aperture post (16.5 cm) - K31
- 3AP2: Alignment Aperture post (16.5 cm) - K22
- 3RR: Aluminium retroreflector, mounted on manual delay stage
- 3CM1: 1 m FL silver concave mirror - M28
- 3M3: Plano silver - J24
- 3AP3: Alignment Aperture (16.5 cm) - N24
- 3AP4: Alignment Aperture (12.7 cm) - II24
- 3CM2: 50 cm FL silver concave mirror - JJ24
- PM: Prism mirror - BB24
- Sample - BB19

Additional components:

- 3CF1 –Calcium Fluoride window: set at 45 degrees to the optical axis, reflects 5% of the light to Pyro3.

- Pyro3 – Pyroelectric detector for OPA3 power monitoring

The beam is 12.5 cm after the mixing crystal and is raised to 16.5 cm by 3P. After 3M3, the beam is angled downwards to a final height of 5" off the ground before hitting 3CM2.

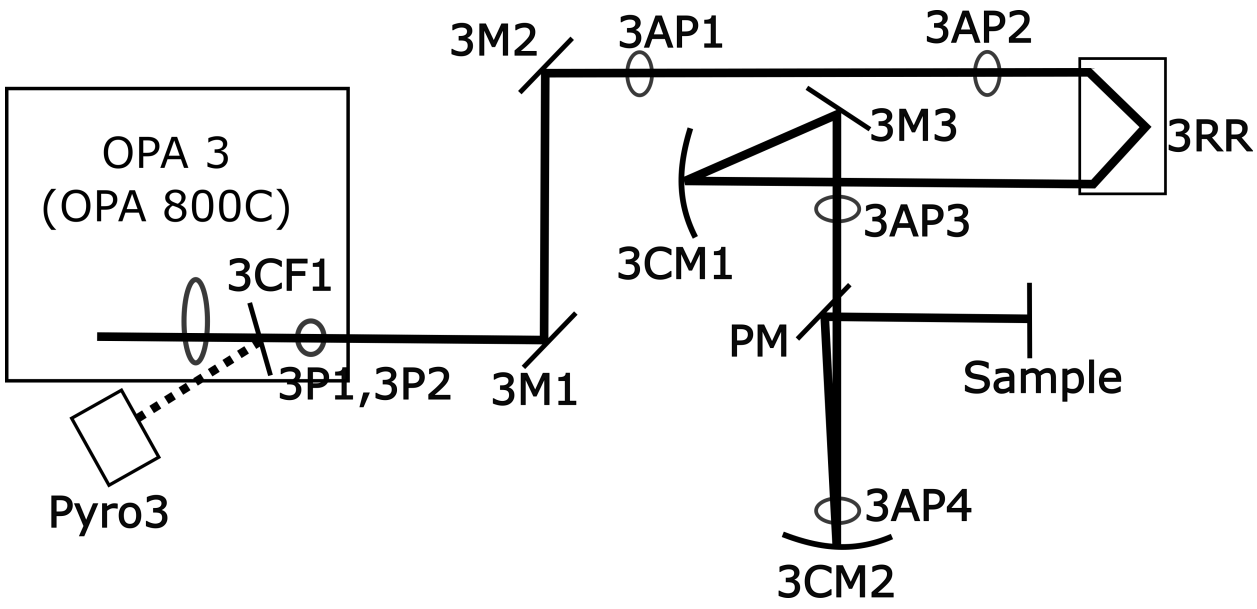

Figure 3.11: The beampath of ω_3

3.5 Components

3.5.1 TOPAS-800

The TOPAS-800 produces around 200 μJ/pulse of signal and idler, and is coupled to an NDFG box, also from Light Conversion, to output between 2 μJ to 20 μJ/pulse of IR light depending on the frequency. The power curve is somewhere on the computer. The input is 1.4 W of 800 nm light of pulse width 1 ps from the Spitfire. The NDFG box has a choice of a $AgGaS_2$(1,000 - 4,000 cm^{-1}) and $AgGaSe_2$(700 - 4,000 cm^{-1}) DFG mixing crystal. There are two modes of operation: non-collinear and collinear. In non-collinear mode, signal and idler are crossed at an angle such that DFG output can be spatially isolated, and in collinear mode, the signal and idler are collinear such that the DFG output must be spectrally isolated with a long-pass filter. We typically operate in collinear mode to simplify output Pointing. For complete documentation, see the TOPAS manual.

3.5.2 OPA-800

The OPA 800 from Spectra Physics produces around 75 μJ/pulse of signal and idler, and in DFG configuration outputs around 1 μJ/pulse of mid-IR light. For complete documentation, see the OPA 800 manual. The input is 0.55 W of 800 nm light of pulse width 1 ps from the Spitfire. The BBO is an 8 mm Type II crystal, and the DFG mixer a $AgGaS_2$ crystal.

3.5.3 OPA-800C

The OPA 800C from Spectra Physics produces around 120 μJ/pulse of signal and idler, and in SFG configuration outputs around 10 μJ/pulse of visible light with an output range of 14,000 - 18,000 cm^{-1}. For complete documentation, see the OPA 800C manual. The input is 1 W of 800 nm light of pulse width 1 ps from the Spitfire. The BBO is an 8 mm Type II crystal, and the SHS mixer a 4 mm Type I BBO crystal.

3.5.4 Delay Stages

Two motorized stages control the pathlengths of the ω_1 and ω_2 line and hence control the time at which the pulses arrive at the sample position. Retroreflectors 1RR and 2RR are mounted on the stages and movement of the stages corresponds to a change in the beam pathlength equal to twice the distance travelled by the stage. Delay stages are used to control the delay time between the pulses as well as to correct for delay changes as a result of OPAs changing frequency.

Zero delay correction

3.5.5 Pointing Correction Mirrors

The Pointing correction is performed by a T-MM series motorized mirror mount from Zaber Technologies. Each laser line has a Zaber mount located close to the OPA output port. The Zaber mounts are automated with RS-232 serial communication to the Picosend system computer and are fully implemented in PyCMDS which controls movement and homing. They can also be controlled manually, although the manual control feature is never used.

3.5.6 Monochromator

The monochromator is a MicroHR model from Horiba Jobin-Yvon. There are two available gratings. Grating 1 has 1200 grooves/mm and is blased for 630 nm and Grating 2 has 120 grooves/mm and is blased for 5000 nm. Grating 1 is used for visible processes like SHS tuning and TRSF experiments while Grating 2 is used for tuning the IR OPAs. Detectors are mounted onto the exit slit and are fastened using a clamp.

3.5.7 Detectors

Photodiode

From Thorlabs. General purpose detector for visible light measurement. Large active area so suitable for Pointing calibration.

MCT mid-IR detector

From Teledyne-Judson. The MCT IR Detector is used for tuning the IR OPAs. It is sensitive to wavelengths between 1500 – 20,000 nm. It requires LN_2 cooling.

Pyroelectric detectors

The Pyroelectric detectors (pyros) are used to monitor OPA output for tuning and power normalization purposes. A CaF_2 window is placed at 45° in each line diverting 5% of the output to the pyro elements. For Pyro1 and Pyro2, CaF_2 convergent lenses are used to focus down the beam onto the element and obtain maximum signal detection. Pyro3 does not require a lens.

PMT

From Hamamatsu. The PMT is used for experiments in which the signal intensities are very low, such as DOVE and TSF. It is not to be used for OPA tuning. It has a flat response over the wavelength range from 400 - 800 nm.

PbSe IR detector

The PbSe detector is used to locate and align the mid-IR OPA lines. PbSe is most sensitive to wavelengths between 1.0 and 4.8 μm, although it can detect down to 7μm. It is powered by an S-video 4

pin minidin connection and accepts ±15V. The detection area is small so care should be taken when using this detector for alignment.

3.5.8 Cryostat

The PS system cryostat is a Variable Temperature Pour Fill Liquid Nitrogen Cryostat: Sample in Vacuum Thermal Link Style from Cryo Industries of America. The operating temperature is 77K to 325 K and the dewar has a 0.4 L liquid nitrogen capacity. The full documentation is available on the Wright Group google drive under the folder Lab Logistics. Two of the windows are CaF_2 from International Crystal Labs and two of the windows are quartz. The CaF2 windows allow mid-IR pulses to pass for DOVE and TSF experiments. See section 3.6.5 for instructions on how to operate the cryostat and prepare a cryogenic sample.

3.5.9 Focusing setup

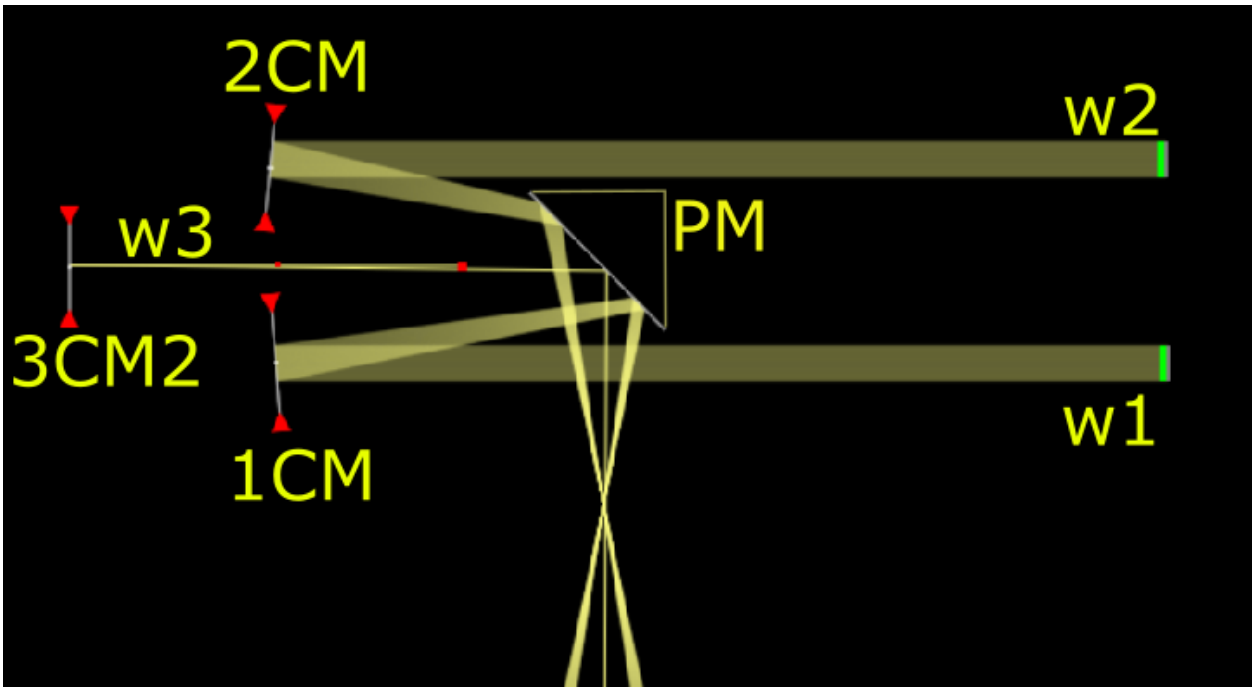

Figure 3.12: Focusing setup

3.5.10 Choppers

The picosecond system is equipped with dual-chopping with allows for the isolation of output signal which depends on all three pulses. This feature enables the removal of competing processes such as $2\vec{k_1}+\vec{k_3}$ and $2\vec{k_2}+\vec{k_3}$. ω_1 and ω_2 are the chopped lines. The choppers are controlled by control boxes located on the overhead platforms above the TOPAS. The choppers are phase-locked, with Chopper 1 the master and Chopper 2 the slave. For a full description of dual-chopping and shots processing, see Blaise Thompson's thesis. The chopped signal are represented in the software as:

- signal_mean: Average signal from all phases
- signal_diff: Processed signal from all three pulses

3.5.11 Polarization

Polarization of ω_3 is controlled by placing a half-waveplate in the post holders between 3M1 and 3M2. At this moment, only ω_3 is polarization-controlled.

3.5.12 Filters

Table 3.1 lists the commonly used filters for SHS TRSF experiments.

Table 3.1: Commonly used filters

Type	**Range/Cutoff (nm)**	**Manufacturer**	**OD**	**Location**
Short pass	610	Asahi	7	Filter Wheel 2
Notch	800	Thorlabs		Filter Wheel 2
Short pass	530	Asahi	7	Filter Wheel 2
Long pass		Corning		Pre - OPA3 Mixer
Long pass	630	Corning		Filter Wheel 1
Long pass	4000			Post - OPA2 Mixer
Long pass	4000			Post OPA1 Mixer

3.5.13 Data Acquisition Card

Table 3.2: Data Acquisition Breakout box channels

Physical Channel	Channel name
0	Signal
1	Pyro1
2	Pyro2
3	Pyro3
4	Chopper
5	PMT voltage

3.6 Operation

The scanning motors and detectors of the Picosecond system are computer controlled by the python program PyCMDS, while the tuning curve generation, fitting, and data workup are performed by the WrightTools python package, both created by Blaise Thompson[46]. For a full description of PyCMDS and WrightTools, see Blaise Thompson's dissertation. This section covers the operation of PyCMDS as required for preparing and running experiments on the Picosecond system.

3.6.1 OPA Alignment, Calibration, and Tuning

OPA1

Alignment

1. Using a power meter, measure the input power, ensure that it is around 1.4 mW
2. Use a white card to block the input beam at the entrance to the OPA
3. Place cards blocking the 4th and 5th passes reflecting from beam splitters BS1 and BS2 (internal).
4. Partially close aperture A1 and centre the input beam on it by adjusting BS2 (Note this is not the same BS2 and in the above step. See Figure 3.8). Use a fluorescent card and centre the airy disc pattern.
5. Open A1 all the way. BE SURE TO OPEN A1 ALL THE WAY BEFORE UNBLOCKING THE BEAM. Failure to do so could result in hot-spots and components could be damaged
6. Centre the beam on A2 using the pump mirror PM6 using a fluorescent card
7. Repeat steps 4-6 until beam is centred on both apertures
8. Remove cards blocking the 4th and 5th passes, observe the light at the exit of the OPA. the pink-red 800 nm mode as well as the signal-idler white-green mode; peak up the second pump mirror to make all beams collinear and maximize brightness

9. If no signal-idler mode is observed, carefully move the second pump mirror side to side and up and down until it is observed
10. Iterate between centering the mode on the first aperture using the first pump mirror and maximising the signal and idler using the second pump mirror
11. Allow the signal and idler to enter the NDFG box
12. Place a mid-ir low pass filter and a power metre at the exit of the NDFG box and use BS2 to maximize the DFG output
13. Place white card further down the TOPAS line; remove low pass filter and adjust PM6 to make the signal and idler leakage processes collinear
14. Iterate between maximizing output power using BS2 and enforcing collinearity using PM6

Calibration and Tuning Before beginning calibration and tuning, align the ω_1 line to the apertures as described in the general alignment section. Observe the DFG signal on Pyro1, and align ω_1 into the monochromator. Mount the MCT detector onto the monochromator as describe in section 3.5.7. Due to the stability of the tuning curve, the TOPAS motors are not individually calibrated. The tuning procedure for OPA1 is described below:

1. In PyCMDS set the monochromator to grating 2, set the mono frequency and OPA1 frequency to 2500 cm^{-1}
2. Set the entrance and exit slits to 500 μm
3. Observe the IR signal on the scope
4. Adjust the pointing of OAP 2 to maximize the signal on the scope
5. In the Devices tab on PyCMDS, set the DAQ to the MCT settings as described in section 3.5.7.
6. Place a scattering material (lens tissue, frosted glass, IR ND filters) in front of OAP 2 until the signal no longer saturates
7. Run a Tune test for OPA1 using PyCMDS

8. Load the new curve into the PyCMDS and repeat the tunetest until the tuning curve is satisfactory

Tune test procedure

1. In PyCMDS, enter the Somatic tab
2. Set queue name: w1tune
3. Make queue
4. Select Acquisition from the dropdown menu
5. Select Tunetest from the Acquisition dropdown menu
6. Select OPA1 from the OPA menu
7. Set the width to -250 wn and the number of points to 50
8. Select 'Signal' as channel to be processed
9. Add the acquisition to the queue and run the queue
10. Load the new curve into the PyCMDS and repeat the tunetest until the tuning curve is satisfactory

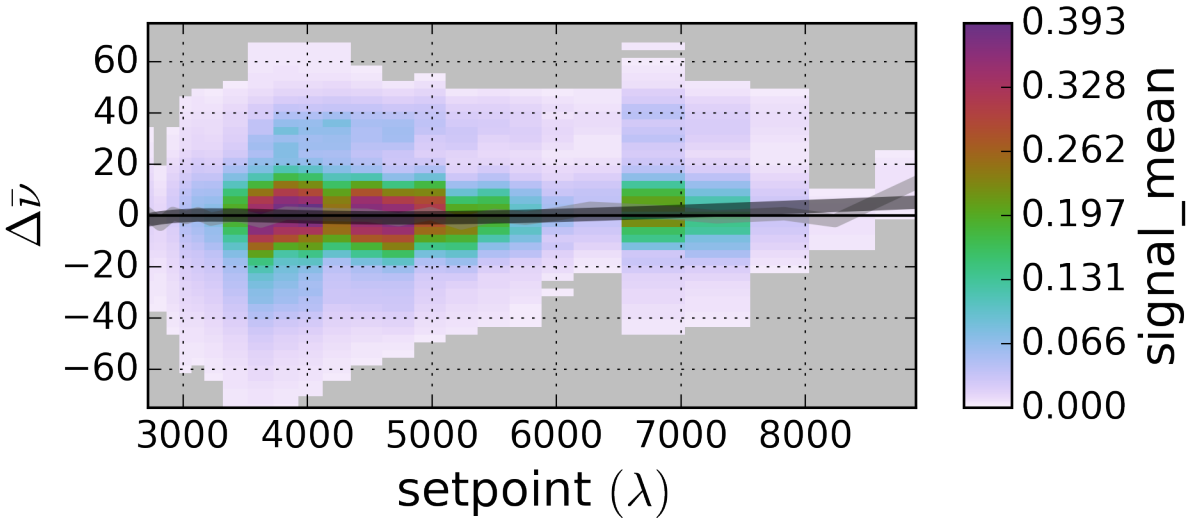

Figure 3.13: TOPAS 800 Frequency Calibration Scan using PyCMDS

OPA2

Alignment

1. Using a power metre, measure the input power and ensure that it is around 0.6 mW; if greater than 0.6 mW, attenuate using the entrance window aperture
2. Place a white card in front of the white light crystal
3. Place a fluorescent card after I1
4. Centre the beam on I1 using PM5
5. Close aperture 1 until an airy disc appears in the mode; adjust PM5 until the airy disc pattern is centred
6. Centre the beam on I2 using PS1
7. Repeat steps 4 and 5 until the beam is centred on both apertures
8. Place a white card after the beam splitter such that it blocks the second pass
9. Place the black alignment tool into the first set of set screws in the first pass
10. Centre the first pass on the alignment tool hole using BS2, then place the alignment tool into the second set of set screws and centre the first pass through the the alignment tool hole using D1
11. Repeat 9-10 until the first pass is aligned to the alignment tool
12. Unblock the white light crystal and adjust WLR1 and WLR2 to overlap the white light with the first pass at the two alignment positions
13. Observe the light after D2, a green-yellow mode (pump+signal and pump+idler) should be observable
14. Adjust the white light delay (Delay 1), the second pass delay (Delay 2), and the white light pointing mirrors (WLR1 and WLR2) to maximize the signal and idler and make them collinear
15. Centre mirror OR1 on aperture 3, and mirror OR2 on aperture 4

16. Near IR DFG might be observable on Pyro2
17. If not, remove the short pass filter and direct the signal and idler leakage onto the element of Pyro2
18. Adjust the degrees of freedom listed in 14 to peak up DFG signal

BBO and Mixer motor calibration

1. In PyCMDS, select the Somatic tab
2. Set queue name: w2tune
3. Create queue
4. Select Acquisition from the dropdown menu
5. Select Autotune from the Acquisition dropdown menu
6. Select OPA2 from the OPA menu
7. Uncheck the Spectrometer box from the motor types menu
8. Set the BBO motortune width to 0.5 mm and the number of steps to 21
9. Set the Mixer motortune width to 3.0 mm and the number of steps to 11
10. Set 'Pyro2' as the channel to be processed
11. Add the acquisition to the queue and run the queue

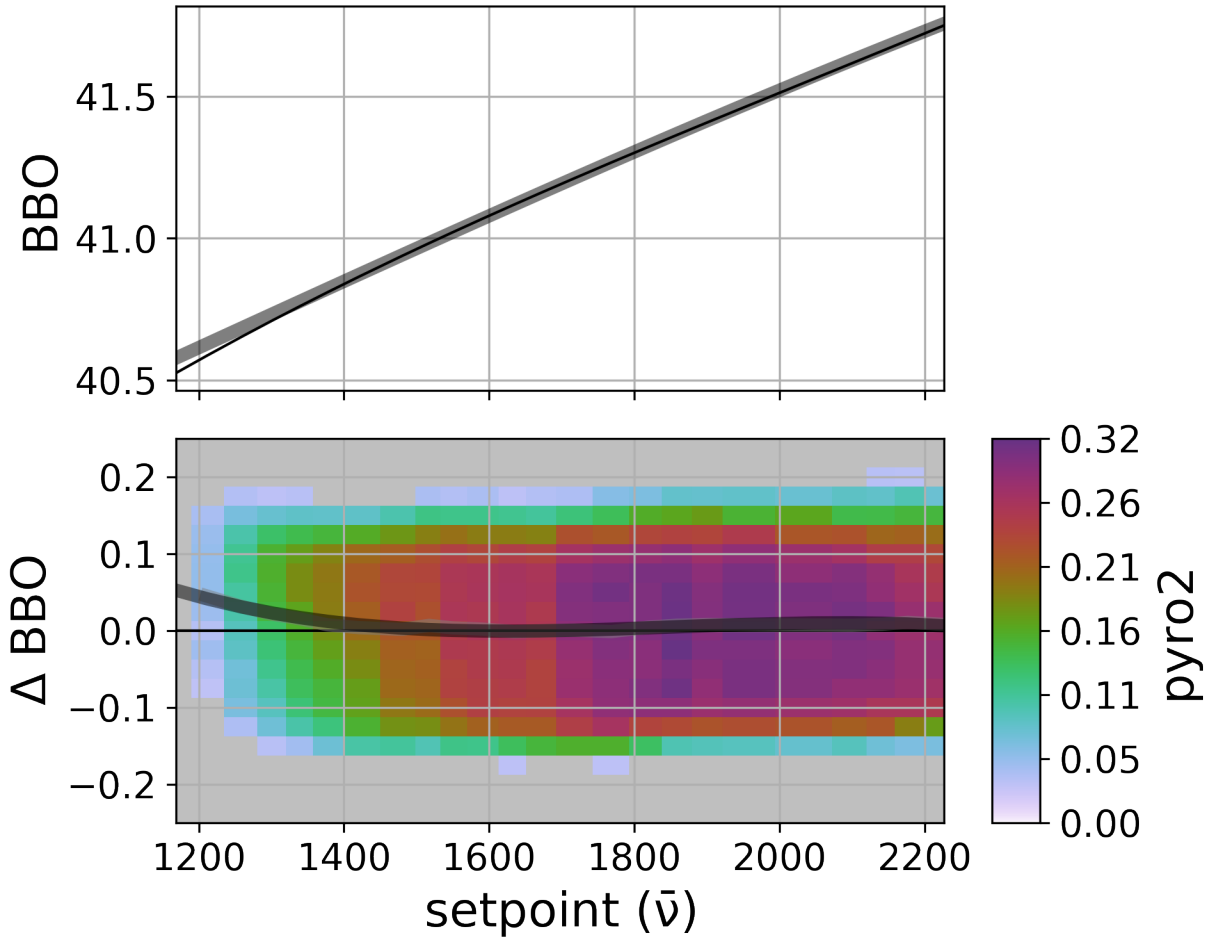

Figure 3.14: OPA 800 BBO Calibration Scan using PyCMDS

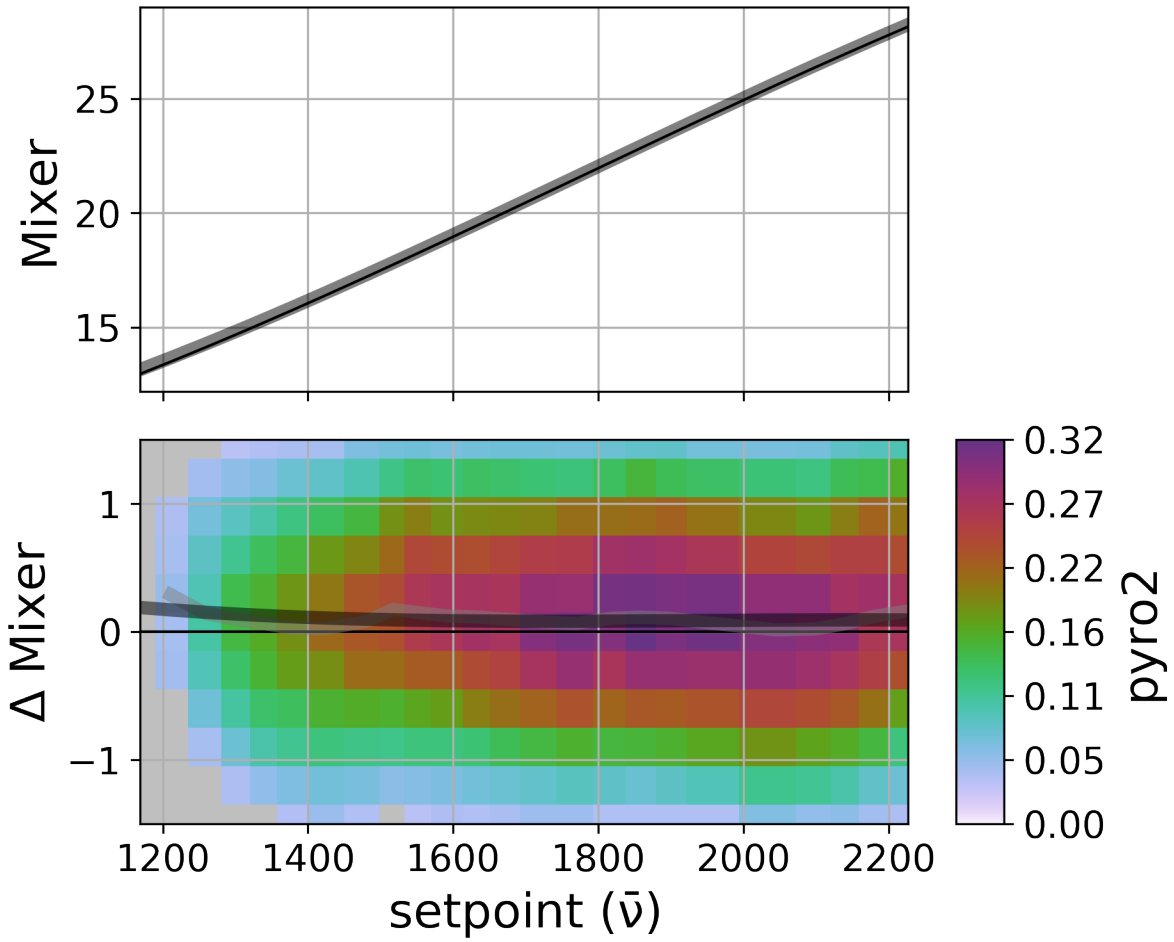

Figure 3.15: OPA 800 Mixer (SHS) Calibration Scan using PyCMDS

Tuning curves are automatically processed from the autotunes and the curve files are uploaded into PyCMDS. It is, however, good practice to manaully move these files to the OPA tuning curve file in PyCMDS rather than leaving them in the data folder.

Tuning

1. Align ω_2 to the line apertures as detailed in section 3.6.2.
2. Centre the HeNe trace of the beam on the entrance slit of the monochromator
3. Attach the MCT detector to the monochromator
4. In PyCMDS set the monochromator to grating 2, set the mono and OPA2 frequency to 2000 cm^{-1}
5. Set the entrance and exit slits to 500 μm
6. Observe the IR signal on the scope
7. Adjust OAP2 to maximize signal on the scope
8. If the detector saturates, place scattering material (filter paper, frosted glass, IR ND filters) in front of OAP 2 until the signal no longer saturates the detector
9. Run a Tune test using PyCMDS
10. Load the new curve into PyCMDS and repeat the tunetest until the tuning curve is satisfactory

Tunetest

1. In PyCMDS, select the Somatic tab
2. Use w2tune queue from Autotune
3. Select Tunetest from the Acquisition dropdown menu
4. Select OPA2 from the OPA menu
5. Set the width to -250 wn and the number of points to 50

6. Select ‘signal_mean’ as the channel to be processed

7. Add the acquisition to the queue and run the queue

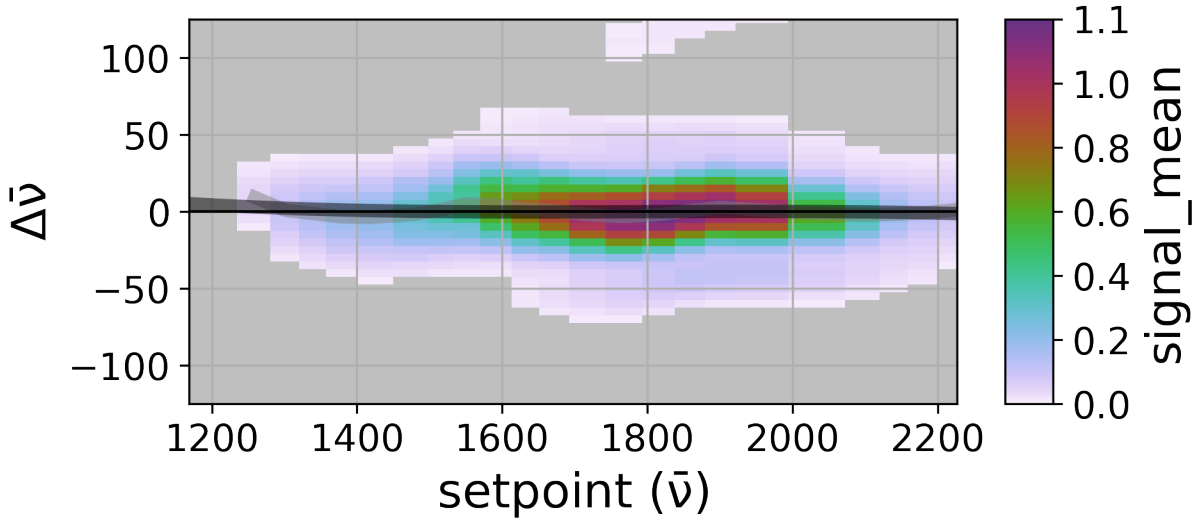

Figure 3.16: OPA 800 Frequency Calibration using PyCMDS

OPA3

Alignment

1. In PyCMDS, set the OPA3 frequency to 16,500 cm^{-1} if in SHS mode
2. Using a power metre, measure the input power and ensure that it is around 1 W
3. Place a white card in front of the white light crystal
4. Place a fluorescent card after aperture I1
5. Centre the beam on I1 using PM3
6. Close I1 until an airy disc appears in the mode; adjust PM3 until the airy disc pattern is centred
7. Centre the beam on I2 using PM4
8. Repeat steps 5 - 7 until the beam is centred on both apertures
9. Place a white card after the beam splitter such that it blocks the second pass
10. Place the black alignment tool against the guide plate in front of the BBO
11. Centre the first pass on the alignment tool hole using BS2, then place the alignment tool behind the BBO and centre the first past through the alignment tool hole using D1
12. Repeat 10 - 11 until the first pass is aligned to the alignment tool
13. Unblock the white light crystal and adjust WLR1 and WLR2 to overlap the white light with the first pass at the two alignment positions
14. Observe the light after D2, a red-white-blue mode should be observable
15. Adjust the white light delay, the second pass delay, and the white light pointing mirrors to maximize the signal and idler and make them collinear
16. Visible SFG might be observable on Pyro3

17. Align signal and idler leakage to aperture 3 and SFG output to 3AP1 using OR1 and OR2 respectively
18. Peak up the degrees of freedom listed in 14 to maximize the signal on Pyro3

After signal and idler generation, the beam is passed through an 800 nm low pass filter to remove pump+signal and pump+idler leakage processes, as well as leftover 800 nm light. After the SFG mixing crystal, the beam passes through a heat filter to remove signal and idler, and then through a long pass filter to remove higher order processes created in the mixing crystal.

BBO and Mixer calibration

1. In PyCMDS, enter the Somatic tab
2. Set queue name: w3tune
3. Create queue
4. Select Acquisition from the dropdown menu
5. Select Autotune from the Acquisition dropdown menu
6. Select OPA2 from the OPA menu
7. Uncheck the Spectrometer box from the motor types menu
8. Set the BBO motortune width to 0.5 mm and the number of steps to 21
9. Set the Mixer motortune width to 0.4 mm and the number of steps to 31
10. Set 'Pyro3' as the channel to be processed
11. Add the acquisition to the queue and run the queue

Tuning curves are automatically processed from the autotunes and the curve files are uploaded into PyCMDS. It is, however, good practice to manaully move these files to the OPA tuning curve file in PyCMDS rather than leaving them in the data folder.

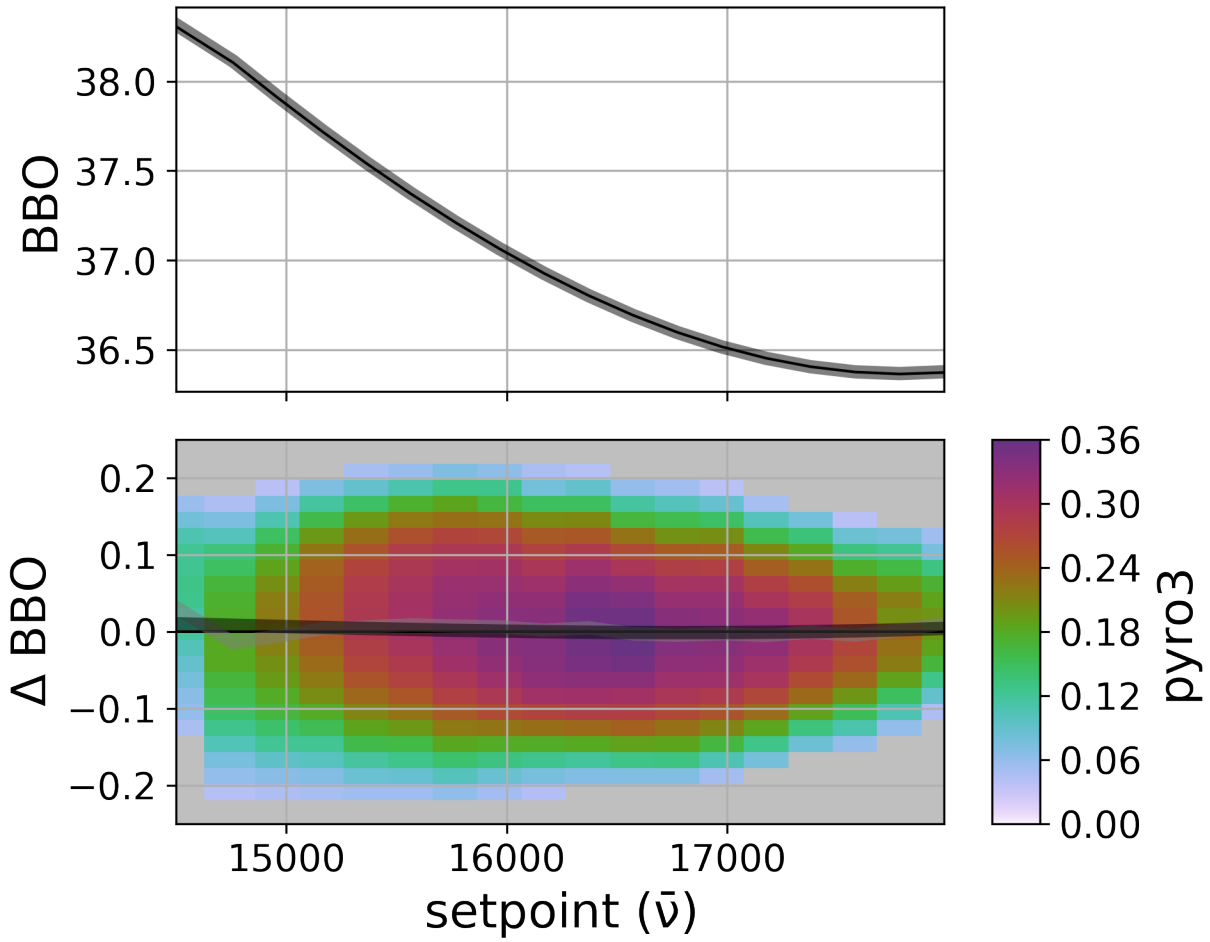

Figure 3.17: BBO autotune for ω_3

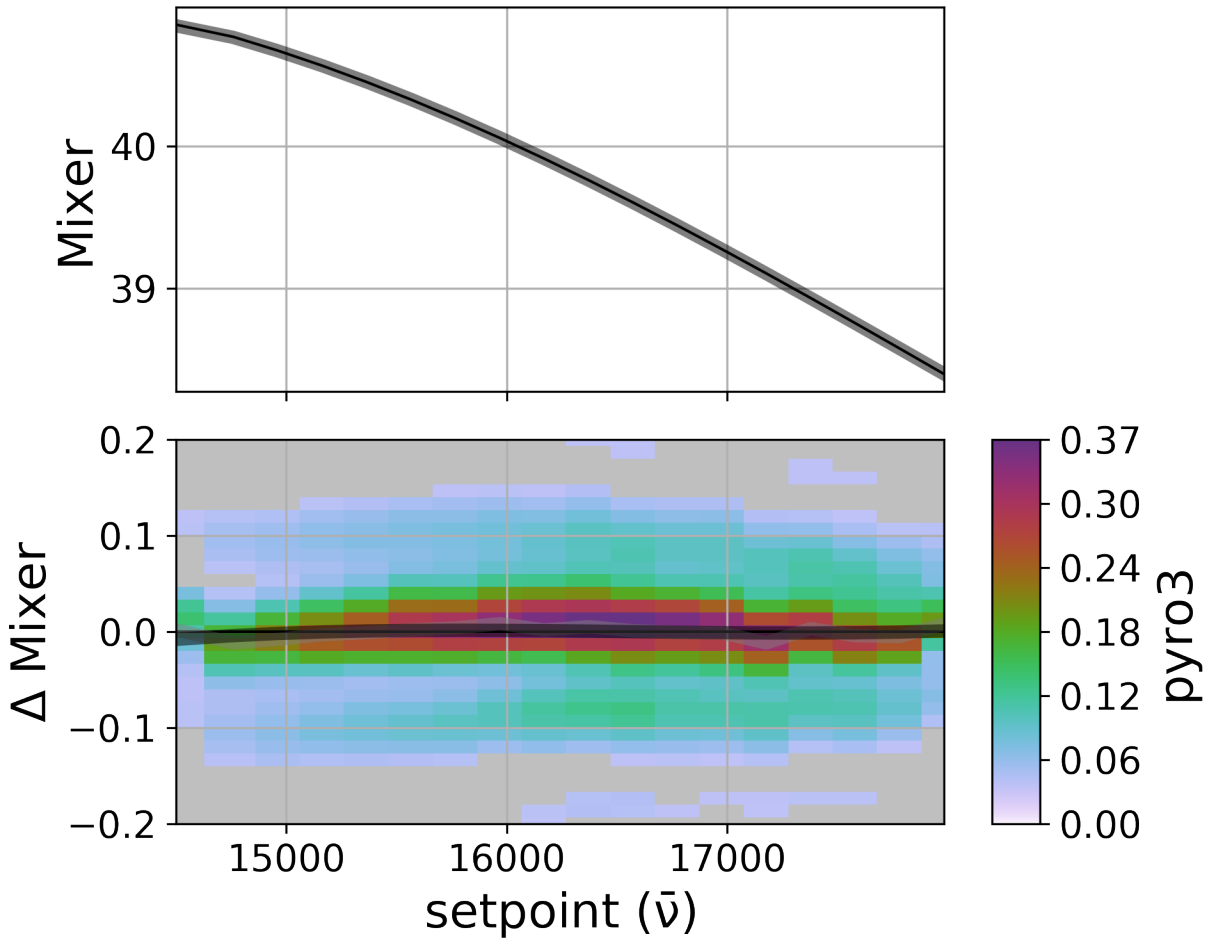

Figure 3.18: Mixer autotune for ω_3

Tuning

1. Align ω_3 to the line apertures as detailed in section 3.6.2
2. Centre ω_3 on the entrance slit of the monochromator
3. Mount the Thorlabs photodiode (detector number) to the monochromator
4. In PyCMDS set the monochromator to grating 1, and set the monochromator and OPA3 frequency to 16,500 cm^{-1}
5. Set the entrance and exit slits to 500 cm^{-1}
6. Observe the visible signal on the oscilloscope
7. If the detector saturates, place a ND filter in front of OAP 2 until no more saturation is observed
8. Run a Tune test using PyCMDS:
9. Load the new curve into PyCMDS and repeat the tunetest until the tuning curve is satisfactory

Tunetest

1. In PyCMDS, enter the Somatic tab
2. Use w3tune queue from Autotune
3. Select Tunetest from the Acquisition dropdown menu
4. Select OPA3 from the OPA menu
5. Set the width to -250 wn and the number of points to 50
6. Select 'signal_mean' as the channel to be processed
7. Add the acquisition to the queue and run the queue

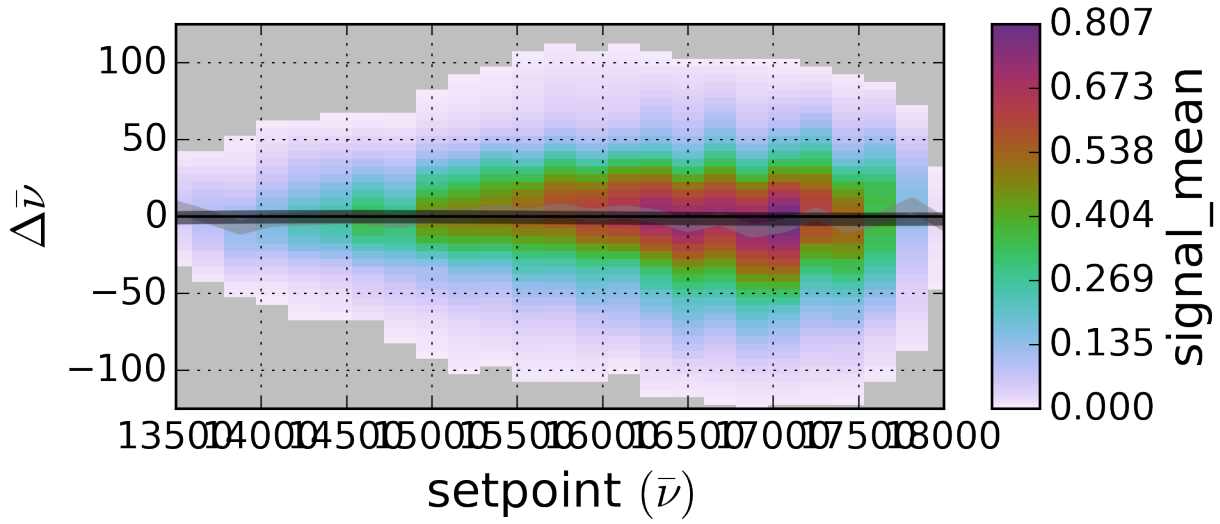

Figure 3.19: Tune test for ω_3

3.6.2 Table Alignment

After all three OPAs are producing parametric output, use the following steps to align the beams to the optics on the table.

1. ω_1: Center the beam to 1AP1 using 1M2, and to 1AP2 using 1M3. Move the aperture and post to the target postholder and maximize power on Pyro1.
2. ω_1 tracer: Center the HeNe tracer to 1AP1 using 1TM1, and to 1AP2 using 1CF1.
3. ω_2: Center the beam to 2AP1 using 2M2, and to 2AP2 using 2M3. Move the aperture and post to the target postholder and maximize power on Pyro2.
4. ω_2 tracer: Center the HeNe tracer to 2AP1 using 2TM1, and to 2AP2 using 2TM2.
5. ω_3: Center the beam to 3AP1 using 3P2, and to 3AP2 using 3M2.

At this stage, the three beams are aligned to their respective retroreflectors. Use the following steps to align the beams to the sample position.

1. Place the focussing alignment mirror against the guide plate at Z24
2. Close 1AP1 and 2AP1 until the iris just starts to clip the mode
3. Look for the back reflection of the ω_1 and ω_2 tracer on the reverse side of the closed apertures
4. Center the back reflection on 1AP1 using 1M4, and on 2AP1 using 2M4
5. Remove the mirror and place the magnetic alignment mask at Z24
6. Center the ω_1 and ω_2 tracers on the marked spots on the mask using the vertical translation adjustment on 1RR and 2RR, and the horizontal adjustment on the 1M4 and 2M4 translation stages respectively
7. Center ω_3 on 3AP1 using 3P1 and on 3AP2 using 3M2
8. Center ω_3 on 3AP3 using the horizontal and vertical adjustment stages of 3RR, and on 3AP4 using 3M3

9. Place the pinhole at the sample stage (the magnetic mount will snap into place)
10. Adjust 1M4, 2M4, and 3M3 to center the visible tracers of the three beams on the pinhole
11. Replace OAP1 from its magnetic mount with the PbSe detector behind the pinhole and maximize the two IR beam throughputs
12. Set up appropriate filters and process picking irises for output process and use OAP2 to center the output process onto the entrance slit of the monochromator

3.6.3 Pointing correction

This section provides instructions on how to correct output Pointing drift. Before Pointing correction is performed, each OPA must be completely tuned and the three beams must be focussed and overlapped at the pinhole. Example scans and curves are shown in Figures 3.20, 3.21, and 3.22.

1. Mount the MCT detector at the monochromator, open the slits completely, select grating 1, and set the grating position to 0 nm
2. Block ω_2 and ω_3
3. If the detector saturates, scatter the beam at the monochromator entrance slit using layers of lens tissue
4. In PyCMDS, create a queue named 'pt'
5. Select w1 and select phi by checking the box
6. Set the width at 2000 cm^{-1} and the number of points at 30
7. Append to the queue and run the scan
8. Repeat for theta
9. The Pointing curve is automatically generated and loaded, although you should still move the curve from the data folder into the Pointing curve folder located in the general calibration curves folder

10. Repeat the process for ω_2. It is likely that you will have to remove some layers of lens tissue to get an appropriate level of signal.

11. Mount the photodiode and repeat the process for ω_3. To prevent saturation, use ND filters rather than lens tissue.

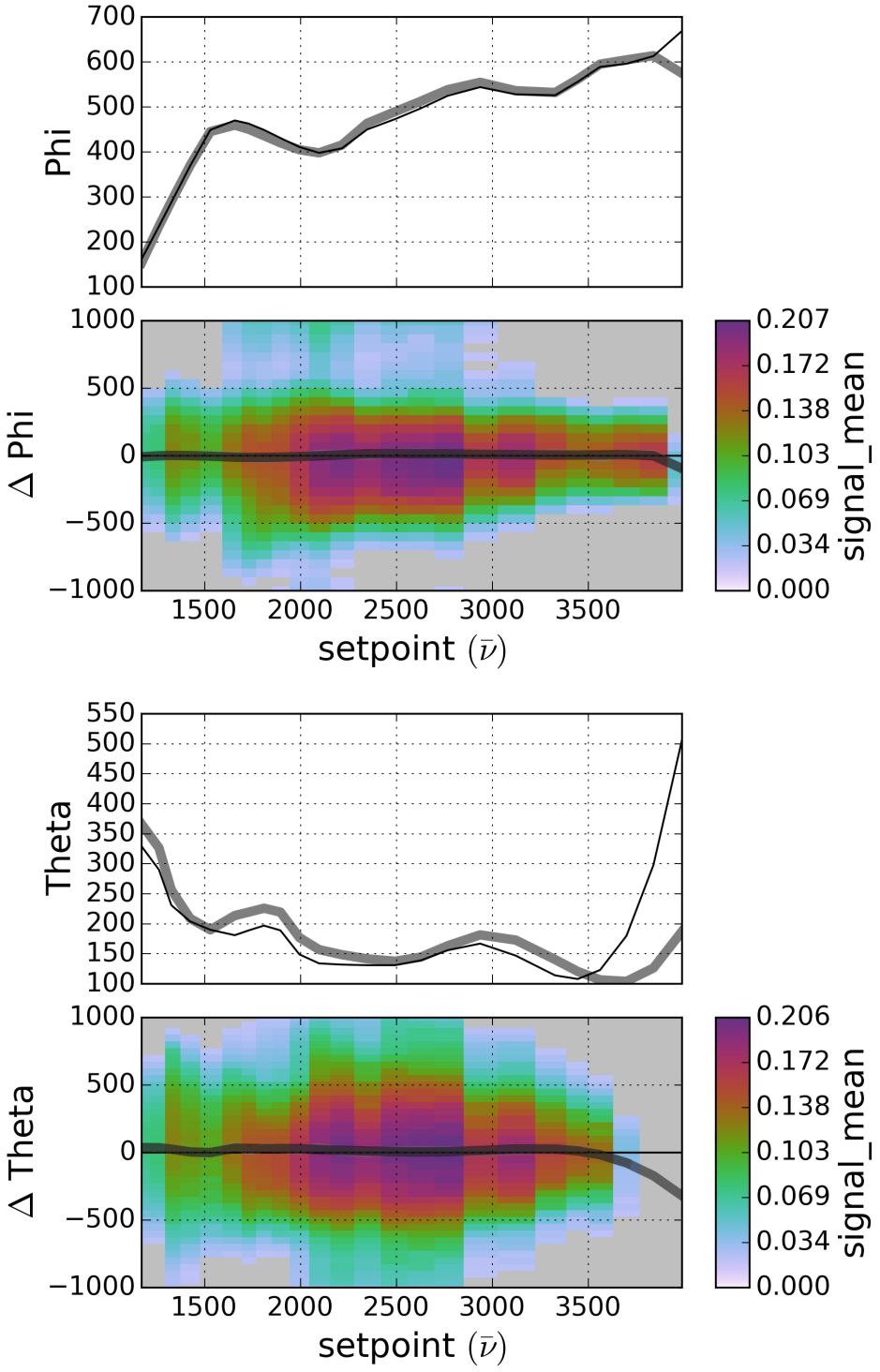

Figure 3.20: ω_1 Pointing Correction Calibration Scan using PyCMDS

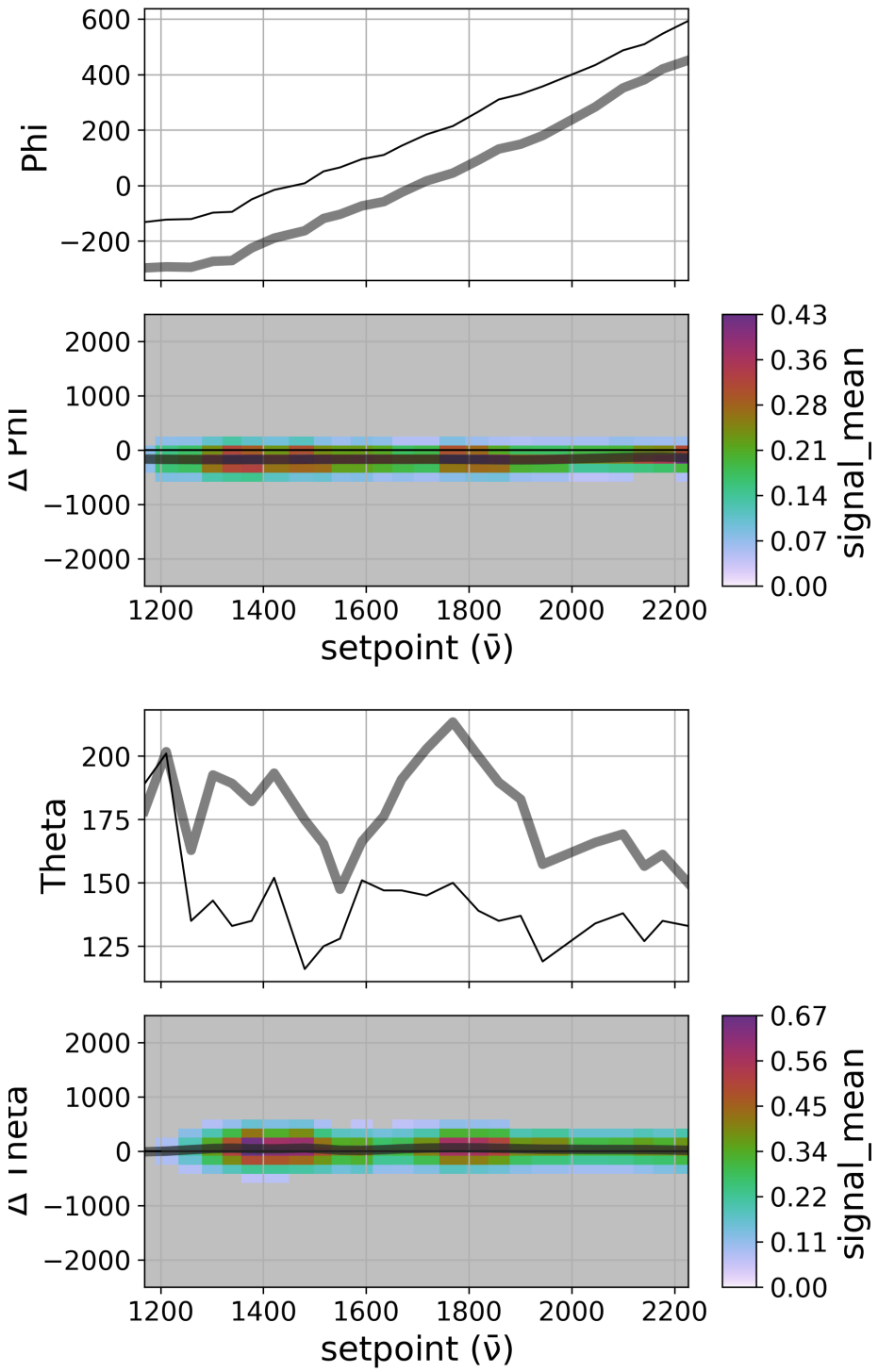

Figure 3.21: ω_2 Pointing Correction Calibration Scan using PyCMDS

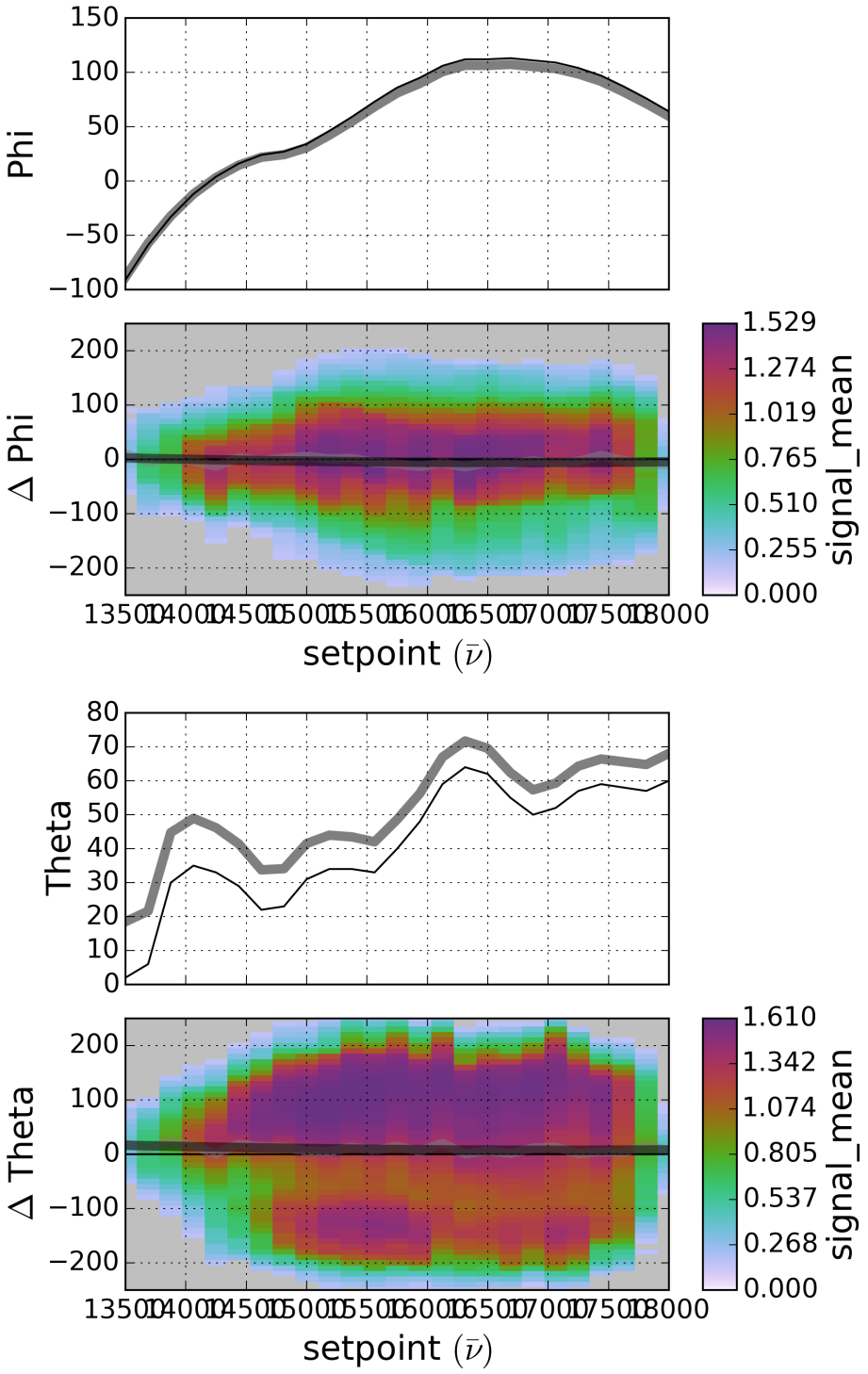

Figure 3.22: ω_3 Pointing Correction Calibration Scan using PyCMDS

3.6.4 Zero delay and Zero tuning

Finding Zero Delay

1. Place a workup material at the position of overlap between the three beams. The workup material for TSF and DOVE is a 1 mm ZnSe and 1 mm CaF_2 window respectively, but we have also used 25 μm pathlength D_2O in a CaF_2 window sample cell for tuning OPA3.
2. Switch off the room lights block the monochromator entrance slit
3. Place appropriate filters in the pathway of the signal in front of the monochromator (see Table 3.1)
4. Set the OPAs to a convenient frequency, for example, $\omega_1 = 1500$ cm^{-1}, $\omega_2 = 1500$ cm^{-1}, $\omega_3 =$ 15,000 cm^{-1} for ZnSe and CaF_2, and $\omega_1 = 2100$ cm^{-1}, $\omega_2 = 2100$ cm^{-1}, $\omega_3 = 16{,}000$ cm^{-1} for D_2O
5. Block ω_2
6. Set the monochromator to the sum frequency: $\omega_m = \omega_1 + \omega_1 + \omega_3$ such that it passes $2\vec{k}_1 + \vec{k}_3$
7. Turn up the PMT voltage to 300 mV
8. Unblock PMT, open up monochromator slits fairly wide (250 – 500 μm)
9. $2\vec{k}_1 + \vec{k}_3$ signal should be visible on the signal channel of the oscilloscope. If not, push on d1 or on the ω_3 retroreflector. If things are set up correctly, you should see signal (if no signal is seen, recheck monochromator settings, pulse overlap)
10. Set d1 to maximize output signal
11. Adjust sample z-position and (mirror number) to maximize TSF signal; adjust PMT voltage such that detector does not saturate. A maximum voltage of around 0.7 V is safe, do not pass 1.0 V
12. Block ω_1 and unblock ω_2
13. Set the monochromator to the sum frequency: $\omega_m = \omega_1 + \omega_2 + \omega_3$ such that it passes $2\vec{k}_2 + \vec{k}_3$

14. $2\vec{k}_2 + \vec{k}_3$ signal should be visible on the signal channel of the oscilloscope. If not, push on d2 or on the ω_3 retroreflector. If things are set up correctly, you should see signal (if no signal is seen, recheck monochromator settings and beam spatial overlap)

15. Set d2 to maximize output signal

16. Unblock ω_1

17. Set ω_1 to 1400 cm^{-1} and ω_2 to 1600 cm^{-1} while leaving ω_m fixed. Narrow the window of the process picking aperture (aperture no.) to isolate $\vec{k}_1 + \vec{k}_2 + \vec{k}_3$ signal

Zero-tuning As OPAs change frequency, the crystals change angle and the pathlengths of crystal material through which the light passes changes, resulting in the output pulse timing being frequency dependent. Zero-tune corrects for this frequency dependent timing behaviour. Before starting zero-tune, the OPAs must be fully tuned and the system must be fully aligned with all beams focussed and overlapped at the sample position. The following steps assume that OPA3 is set for SHS, although the procedure is very similar for other processes. Figures 3.23, 3.24, and 3.25 show examples of zero-tuning scans and the generated coset files. Note that the coset file for ω_3 is collected in two stages and the two curves are manually joined together.

1. Set ω_3 to an appropriate frequency. For SHS, $\omega_3 = 15500$ cm^{-1}

2. Set ω_1 and ω_2 to 2000 cm^{-1} and the monochromator to the sum frequency

3. Adjust the PMT voltage to avoid saturation

4. Enter the Somatic tab

5. Create queue and name it ‘zt’

6. Name the acquisition ‘w1’

7. Select SCAN from the Acquisition drop down menu

8. Add one Energy axis and one Delay axis

9. Energy axis: ω_1: 2200 – 1200 cm-1 15 points, d1: -3 – 3 ps 31 points (adjust the range of ω_1 according to the experimental requirements)
10. Block ω_2
11. Append to the queue and run the scan
12. Repeat for ω_2 and d2 with ω_1 blocked
13. Process both wigner scans and generate coset files using the process_wigner module. See Wright Tools documentation for details.
14. Move the coset files to the autonomic folder and load them into PyCMDS via the autonomic tab in the section labeled 'Delays'
15. Enable both coset files and set ω_1 and ω_2 to 2000 cm^{-1}
16. Changing frequency should now be followed by a delay correction
17. Replace the ZnSe crystal with a work-up material for the visible region. This is usually a sample cell filled with D_2O.
18. Setup a wigner with axes: Energy axes ω_3 14000 to 18000 cm^{-1}, d1 = d2 = -3 to 3 ps
19. This scan may need to be taken in two steps with a change of filter part of the way
20. Process each wigner individually and join the two coset files
21. Create two copies of the ω_3 coset file, one for d1 and one for d2. Appropriate headers are required.
22. Move the coset files to the autonomic folder, load them into PyCMDS, and enable them for both delay stages

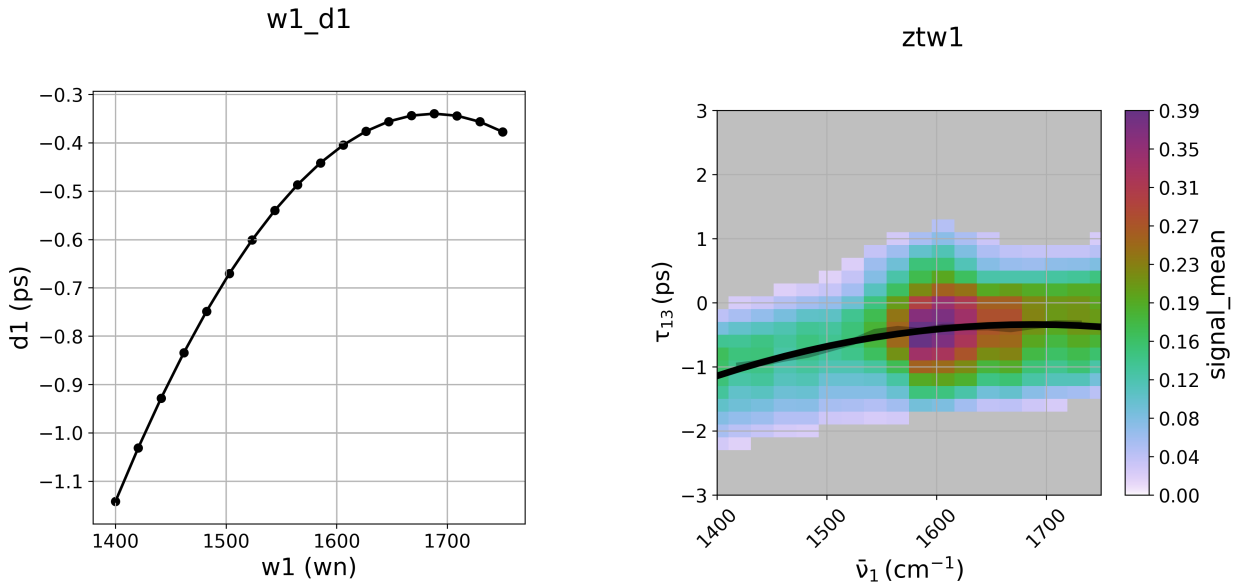

Figure 3.23: Zero tune scan for ω_1

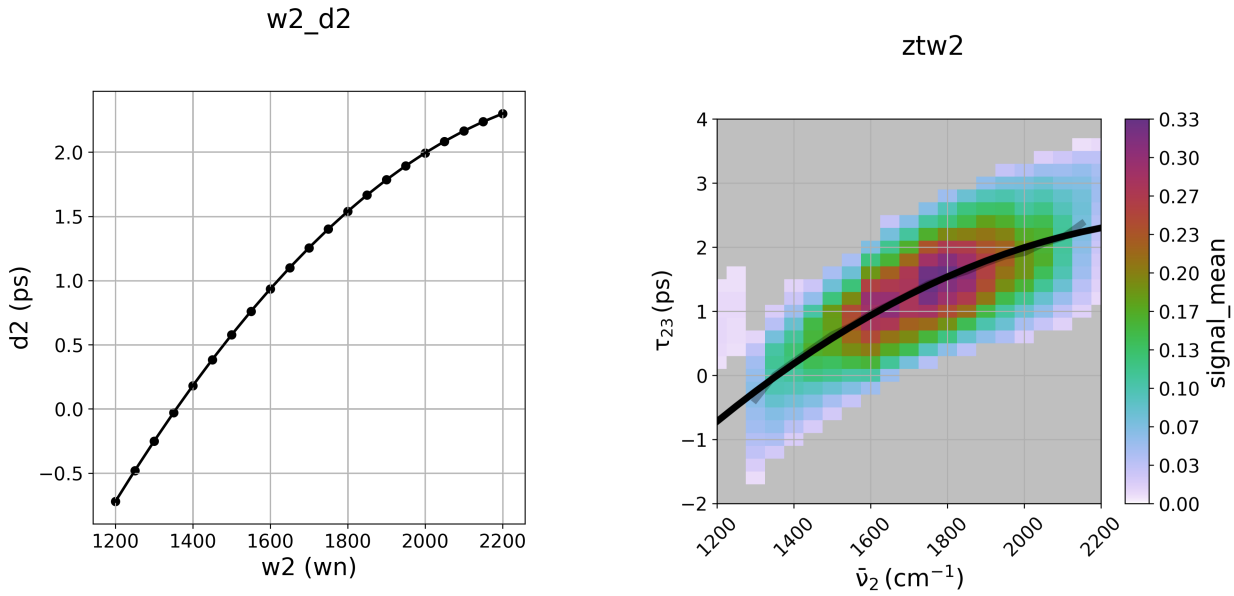

Figure 3.24: Zero tune scan for ω_2

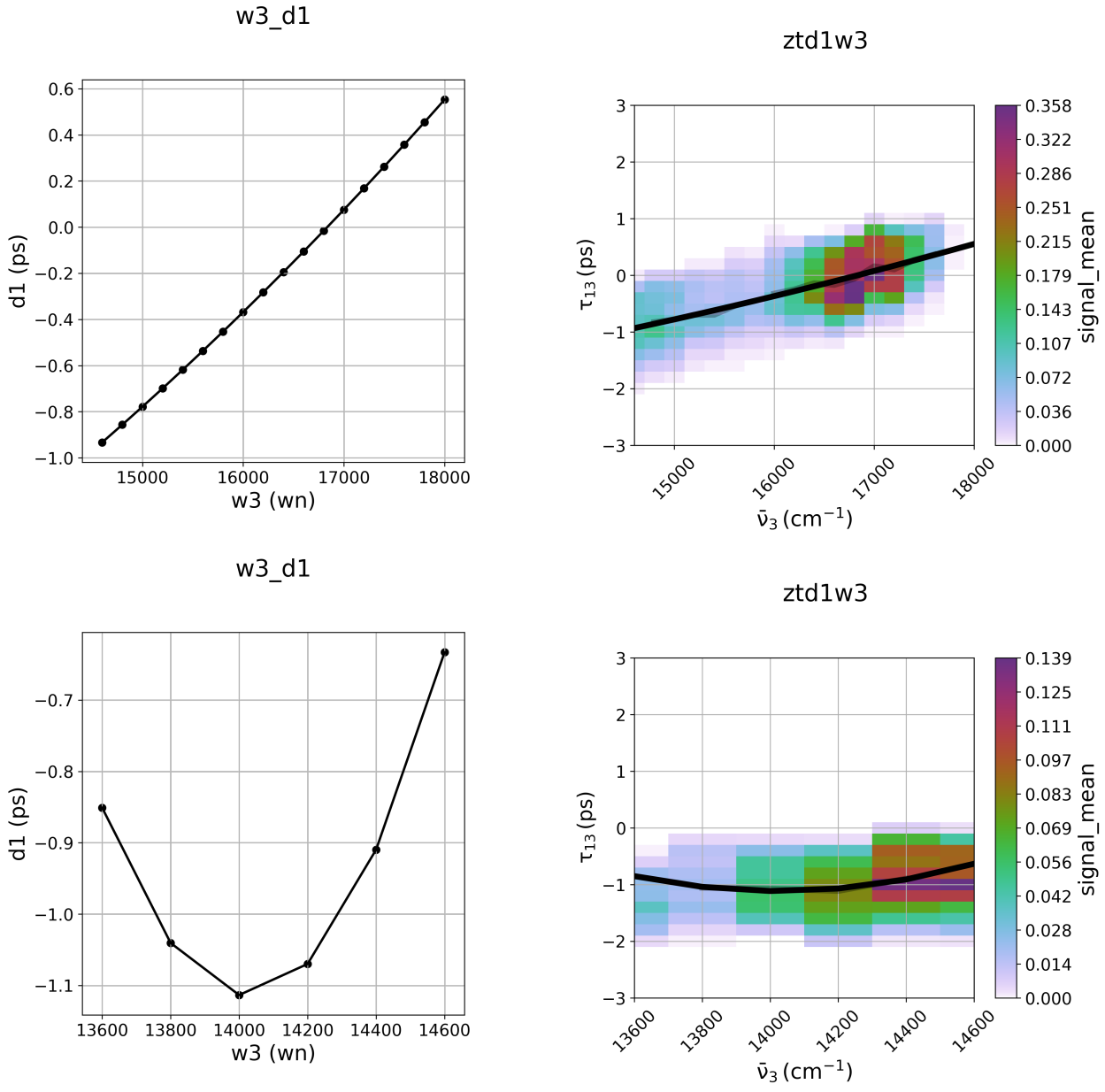

Figure 3.25: Zero tune scan for ω_3

3.6.5 Cryogenic sample preparation

The following steps provide instructions on preparing and using the cryostat for cryogenic experiments.

1. Attach the vacuum pump to the cryostat sidearm using the clamp and leave the Swagelok knob open
2. Mount the copper cell to the end of the cold finger
3. Start the vacuum pump
4. Immerse the sample directly into LN_2 and hold for 15 seconds
5. Quickly mount the top half of the cryostat onto the bottom half and fasten using the clamp
6. Ensure that the side arm is perpendicular to the input beam direction and facing to the right. The input beams pass through the CaF_2 windows
7. Monitor the pressure using the orange pressure gauge. The gauge is not calibrated and only to be used for measuring relative pressure.
8. Allow the reading on the gauge to drop to 0.3 torr
9. You will have seen frost buildup on the sample and the copper cell. Wait for the frost to evaporate and for the sample cell window to be clear before closing the valve
10. Close Swagelok to isolate the pump from the chamber and disconnect the hose from the sidearm
11. Add LN_2 to the dewar and secure the lid
12. Check LN_2 every hour or so

3.7 3D-TRSF example spectra

The experimental system described in this chapter enables the acquisition of three frequency dimensional spectra in which the two IR axes, ω_1 and ω_2, are scanned along with the TRSF output frequency axis,

ω_{TRSF}. We scan ω_{TRSF} rather that ω_3 since the output sum frequency corresponds to the frequency in an absorption spectrum. ω_3 is scanned indirectly by setting it to fulfill the relationship $\omega_{TRSF} = \omega_1+\omega_2+\omega_3$.

Three typical 2D representations of 3D TRSF data are presented in Figure 3.26. In 2DIR scans (Figure 3.26 left), ω_{TRSF} is kept fixed while ω_1 and ω_2 are scanned in the region of vibrational resonances. Meanwhile, ω_3 adjusts to keep the sum frequency fixed. In such scans, the vibrational overtone states appear as peaks along the diagonal line $\omega_1 = \omega_2$ (green and red features), while the vibrational combination bands appear as anti-diagonal peaks where $\omega_1 \neq \omega_2$ (unfilled features). The two other representations show the dependence of the electronic enhancement of the vibrational mode overtones and cross peaks on the electronic absorption. In IR-visible scans (Figure 3.26 middle), ω_2 is held fixed while ω_1 is scanned against ω_{TRSF}, and in (IR=IR)-Visible scans (Figure 3.26 right), $\omega_1 = \omega_2$ is scanned against ω_{TRSF}. The choice of representation depends on whether the feature of interest is vibrationl coupling or vibrational-electronic coupling.

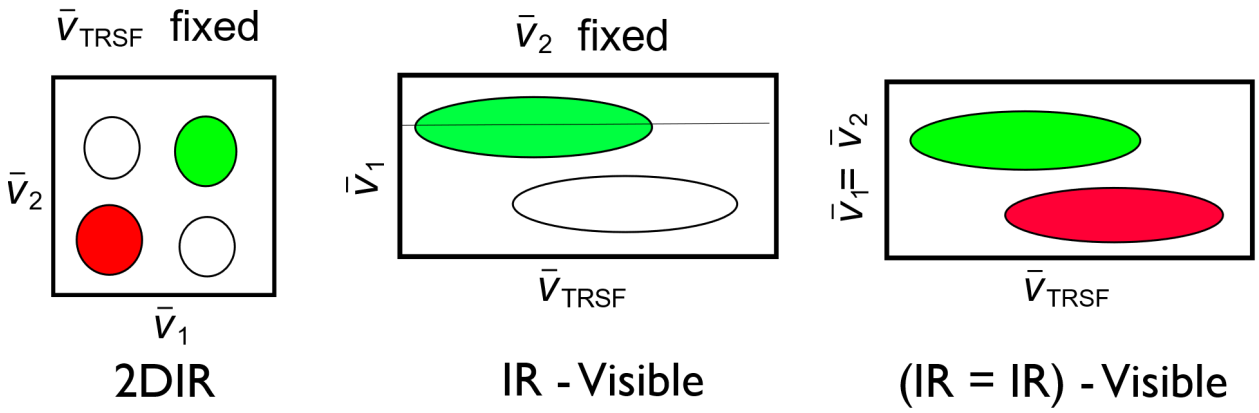

Figure 3.26: Types of 2D representations of 3D TRSF data

3.7.1 Previous 2dIR TRSF spectra

Prior to the addition of a tunable visible OPA, all TRSF spectra were purely of the 2DIR variety. Figure 3.27 shows the 2DIR TRSF spectra of benzene[4] (left), Styryl 9M[5] (middle), and Copper Phthalocyanine[6] (right). ω_3 was fixed at 800 nm (12,500 cm^{-1}) and it was therefore not possible to fix ω_{TRSF} at a particular frequency on the absorption spectrum.

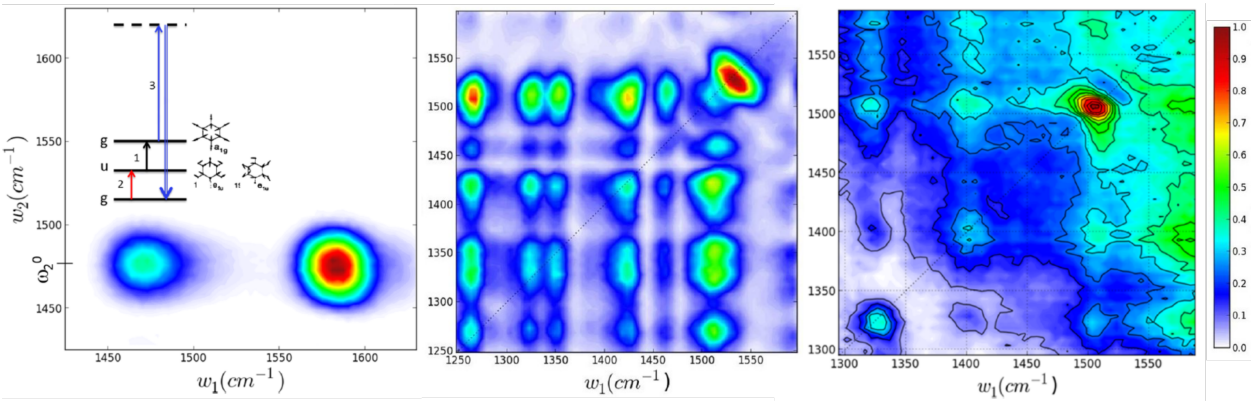

Figure 3.27: 2DIR TRSF spectra of benzene (left), styryl 9M (middle), and copper phthalocyanin (right). Taken from references [4],[5], and [6].

3.7.2 3D-TRSF spectra on Styrl 9M

Once OPA3 was installed and the table redesigned to incorporate three fully tunable light sources, it became possible to acquire 2DIR spectra at difference electronic resonance frequencies. A series of spectra of styryl 9M is shown in Figure 3.28 in which ω_{TRSF} is changed from 650 nm[5] (left), 550 nm (middle), and 520 nm. The similarity between the spectra show that the vibrational overtones and combination bands have equal and largely-unchanging relative coupling to the electronic state. These spectra are locally normalized and it is not possible to see the relative change in the strength of the output signal as ω_{TRSF} changes.

The IR-visible scan in Figure 3.29 shows the dependence of the output signal of a single vibrational mode at 1425 cm^{-1} on the output frequency. The signal is the strongest at ω_{TRSF} = 18,250 cm^{-1} at the peak of the absorption feature, and decreases as the output frequency is detuned towards the blue of the electronic resonance.

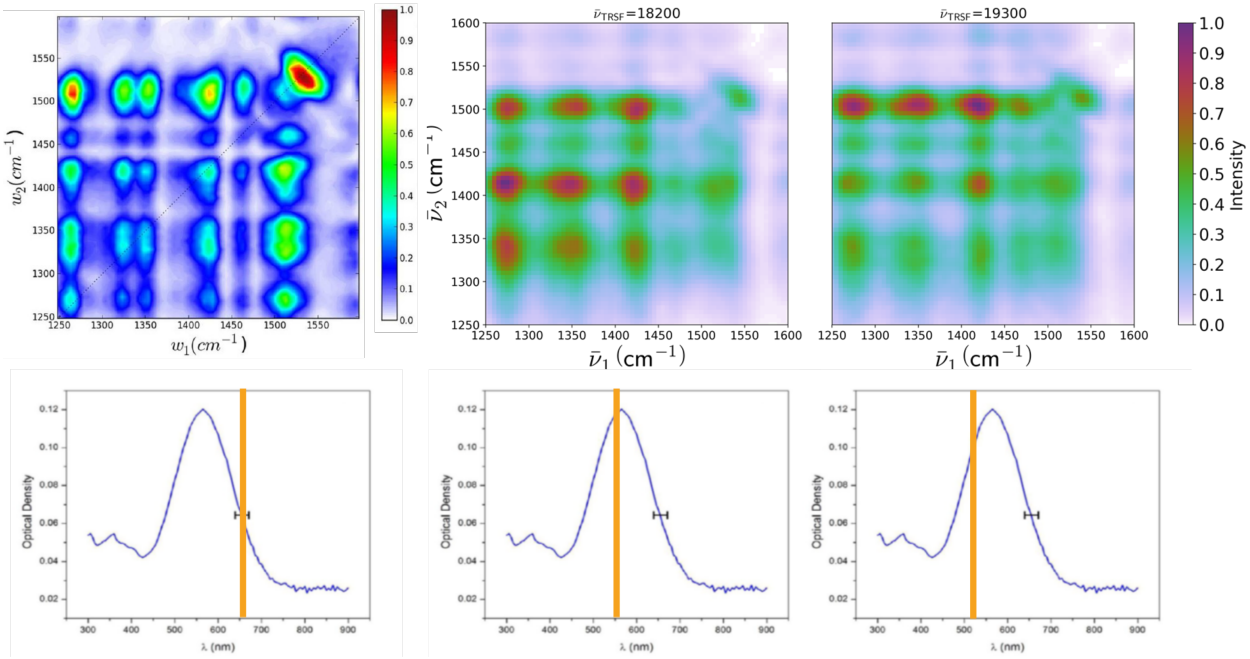

Figure 3.28: A series of 2DIR TRSF spectra of styryl 9M with $\omega_{TRSF} \sim$ 15,380 cm^{-1} (left) taken from Reference [5], ω_{TRSF} = 18,200 cm^{-1} (middle), and ω_{TRSF} = 19,300 cm^{-1} (right). The vertical orange bars on the corresponding absorption spectra (below) show ω_{TRSF} in relation to the electronic resonance.

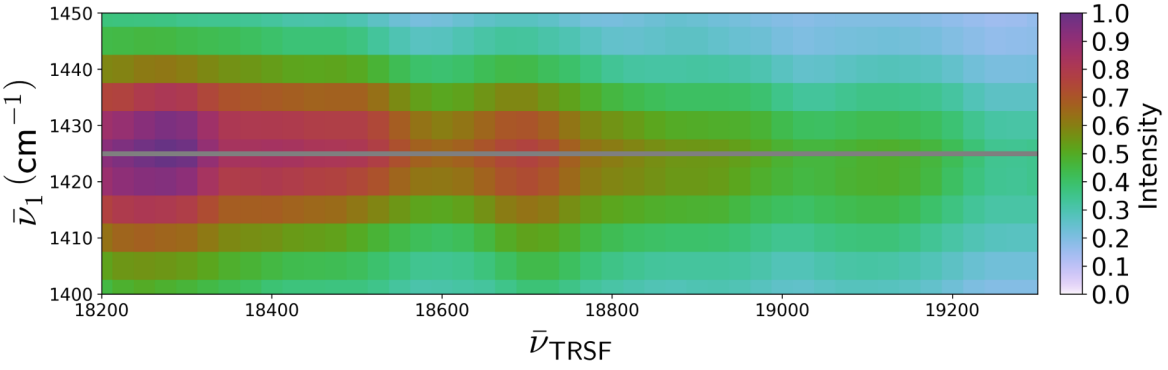

Figure 3.29: IR-visible spectra of styryl 9M in DeACN with ω_2 fixed at 1425 cm$-$1

Chapter 4

Phase Mismatch and Coherent Interference Effects

4.1 Summary

It was known since the beginning that TSF like pathways would suffer inherently from the inability to phase-match the output excitation field to the non-linear polarization. In non-resonant solvents and window materials, the index of refraction increases with frequency, meaning that the output field k-vector k_{TSF} is always larger than the sum of the input fields $k_1 + k_2 + k_3$, no matter the input field incident angles. It was assumed, however, that this problem was only relevant within the sample and that as long as the sample solution was kept to very small pathlengths ($\sim 25\mu$m), the phase-mismatch effect would be negligible. The CaF_2 windows were assumed to be completely transparent due to the absence of vibrational and electronic resonances in the scanning range. Over the course of 2dIR scans, the effect of phase-mismatch was indeed largely unnoticeable.

There was some evidence of this effect in the TRSF study of copper phthalocyanine[47]. The ω_1 versus ω_2 scan showed a rising background towards the blue corner of the scan which could not be explained by resonances. The rise was attributed to M-factors and largely ignored. The undeniable demonstration of the effect happened when a large IR-Visible diagonal scan was taken of CNCbl in D_2O across a frequency

region with no D_2O electronic resonances. The scan is shown in Figure 4.1. The infrared excitation field frequency range of 1500 - 2300 cm^{-1} falls in the region of the OD stretch of D_2O. CNCbl has no vibrational resonances in that region, and as such any TRSF output is due to non-electronically resonant solvent generated background signal. The output frequency range of 19,000 - 21,000 cm^{-1} is a region of complete transparency for D_2O. The non-resonant signal ought to be uniform across the ω_{TRSF} axis, but instead shows intense curved fringes across both the output and IR excitation field axes.

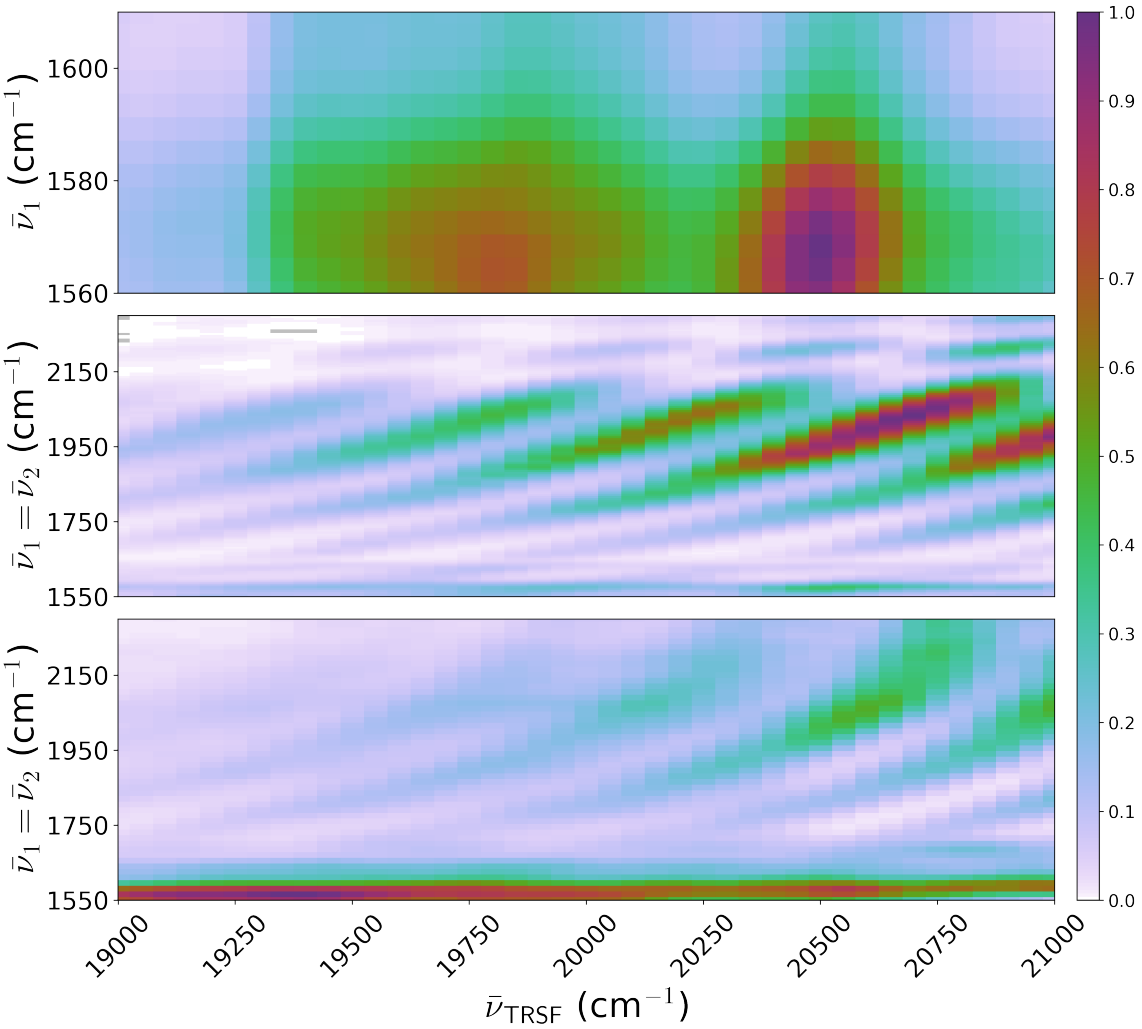

Figure 4.1: IR-visible TSF scan of CNCbl in D_2O in sample cell using 2 mm thick CaF_2O windows

It was necessary for us to understand, charaterize, and mitigate these effects. The rest of this chapter describes the experimental and computational work done to analyse the phase-mismatch effect in a paper titled: "Interference and phase mismatch effects in coherent triple sum frequency spectroscopy", published in Chemical Physics[1][48]. The contributors to this work were Jonathan Handali, Kyle Sunden, Emily Kaufman, and John Wright.

4.2 Body of paper

4.2.1 Abstract

Triply resonant sum frequency is a fully coherent method for multidimensional vibrational/electronic spectroscopy that creates cross-peaks between fundamental, overtone, and combination band vibrational states and electronic/vibronic states if they are coupled. It is also a methodology that cannot be phase matched. This paper explores the consequences of coherent interference and phase matching on the multidimensional spectra obtained in experiments performed in sample cells. Fringes appear in the multidimensional spectra and simulations show the character of the fringes depend on the refractive index dispersion, the thickness of different parts of the sample cell, the volume of the excitation region, and the relative third order susceptibility of the sample and the windows. It is suggested that the fringes provide a mechanism for determining the third order susceptibility and its multidimensional dispersion.

4.2.2 Introduction

Triply Resonant Sum Frequency (TRSF) is a fully coherent member of the Coherent Multidimensional Spectroscopy (CMDS) family of methods.[49, 4, 6] TRSF is a four wave process where three tunable excitation pulses resonantly excite different mixtures of vibrational and electronic states to form a three-quantum coherence with frequency $\omega_4 = \omega_1 + \omega_2 + \omega_3$ and a k-vector given by $\vec{k}_4 = \vec{k}_1 + \vec{k}_2 + \vec{k}_3$ where ω_i and $\vec{k}_i$ are the frequencies and wave vectors for the individual excitation pulses, respectively. Scanning the excitation pulse frequencies across different spectral regions while monitoring the output

[1] Jonathan D. Handali, Kyle F. Sunden, Emily M. Kaufman, John C. Wright. Interference and phase mismatch effects in coherent triple sum frequency spectroscopy. *Chemical Physics*, (2018)

intensity results in large multiplicative enhancements when the excitation frequencies become resonant with vibrational and/or electronic state resonances. The 2D-IR spectra contains diagonal and cross-peaks of the fundamental, overtone, combination bands,[49, 6] and Fermi resonance[4] modes that are coupled with each other. Resonance with an electronic state enhances the 2D-IR spectrum much like the electronic enhancements of resonance Raman spectroscopy.[6] TRSF is complementary to resonance Raman because the electronic resonances enhance asymmetric modes. The output frequency appears in the visible/ultraviolet region where there are excellent detectors. The output frequency is spectrally isolated from the excitation pulses so scatter from the excitation pulses can be spectrally rejected. Since the output intensity is created by a coherent ensemble of molecules within the excitation region, the emission is cooperative and scales quadratically with concentration if the wave vector of the nonlinear polarization created by the three excitation frequencies matches the wave vector of the output light field created by the nonlinear polarization. These characteristics make TRSF attractive for the study of resonance infrared vibrational spectroscopy.[9] Nonlinear spectroscopies are coherent and are subject to spectral interference effects that provide phase information about coherences but can also complicate the features created by quantum state resonances.[50, 51, 41, 52]

An important part of nonlinear spectroscopy is phase matching the spatial oscillations of the nonlinear polarization to the emitted light field. Typically, nonlinear spectroscopic methods match the wave vectors by focusing the excitation beams at angles so their projections shorten the nonlinear polarization wave vector until it matches the output light field wave vector.[53, 54] This approach fails for TRSF since $k_{NL} << k_{out}$. The phase mismatch constrains TRSF experiments to short sample path lengths. Normally, this constraint is not a limitation because the cooperative emission results in beams with high signal levels.[6, 49, 4]

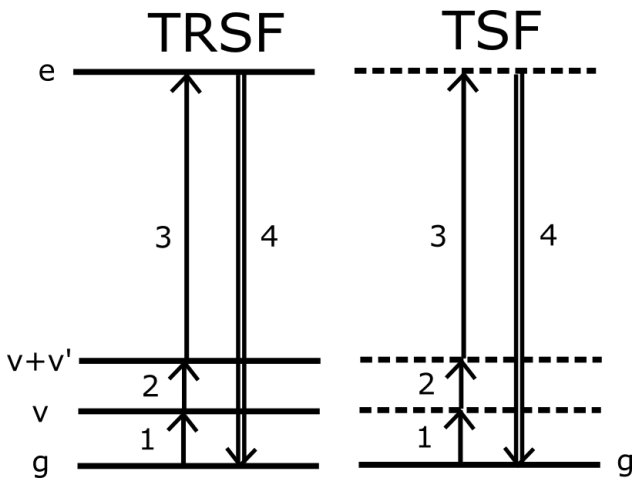

Figure 4.2: Wave Mixing Energy Level diagram of Triply Resonant Sum Frequency (TRSF) and nonresonant Triple Sum Frequency (TSF). g is the the ground state, v and $v + v'$ are the fundamental and combination vibrational states, and e is the electronic state. The dotted lines represent nonresonant virtual states.

This paper reports the results of nonresonant TRSF, or simply TSF (Triple Sum Frequency), experiments where the excitation pulses are temporally overlapped and the window thickness of the sample cell is large enough to create coherent interference effects that appear as multidimensional fringes. The Wave Mixing Energy Level diagram of nonresonant TSF is compared to that of TRSF in Figure 4.2.[55] In order to simplify the experiment, the spectral features of an empty sample cell are compared to those of a cell filled with D_2O. Under these conditions, the sample and the cell windows contribute a nonresonant nonlinear polarization and phase changes that constructively and destructively interfere with the resonant nonlinear polarization of the sample. Strong interference fringes are generated that distort the 2D spectra and create features that depend only on the phase mismatch and the relative nonlinearities of the window and sample. This paper describes the dependence of these features on the three excitation frequencies, and the window and sample thickness. It also describes how the simulations of the line shapes of these coherent interference effects can provide absolute quantification of the multidimensional third order susceptibility of the sample.

4.2.3 Theory

TRSF spectroscopy uses three excitation fields of electric field amplitude E_1, E_2, and E_3 to create a nonlinear polarization

$$P(z) = D\chi^{(3)}E_1(z)E_2(z)E_3(z) \tag{4.1}$$

where $D = 6$ in the Maker-Terhune convention[40] that accounts for the excitation field permutations in the definition of the third order susceptibility, $\chi^{(3)}$, and z is position along the axis of propagation. The overlap and focusing effects of the excitation electric fields are described in the Experimental section. The relationship between the non-linear polarization and the TSF output electric field can be described using Maxwell's scalar wave equation (assuming steady state, c.w. excitation fields, fixed group-velocity, and invoking the slowly varying envelope approximation)[40]

$$\frac{\partial E_4(z)}{\partial z} = \frac{2\pi i F \omega_4 P(z)}{n_4 c} e^{i\Delta k z} \tag{4.2}$$

where ∂E_4 is the amplitude of the TSF output electric field generated by the nonlinear polarization P over length ∂z, ω_4 is the output electric field frequency, F is a field enhancement factor, n_4 is the index of refraction of E_4, c is the vacuum speed of light, and Δk is the wave-vector phase-mismatch between the nonlinear polarization and the output electric field. The net electric output field is the integral of Equation 4.2 over the total pathlength L

$$E_{net} = \int_0^L \frac{2\pi i F \omega_4 P(z)}{n_4 c} e^{i\Delta k z} dz \tag{4.3}$$

Δk is defined as

$$\Delta k \equiv k_4 - k_1 - k_2 - k_3 \tag{4.4}$$

where k_i is the wave-vector of E_i. The wave vectors are related to the excitation frequencies by the refractive indices,

$$k_i = \frac{n(\omega_i)\omega_i}{c} \tag{4.5}$$

where $n(\omega)$ is the index of refraction of each material, calculated using the material's Sellmeier equation or direct measurement[56, 57, 58, 59], and ω_i is the excitation field angular frequency. To simplify calculations, we assume collinear excitation fields when calculating Δ_k.

When TRSF is used for molecular spectroscopy, the three excitation fields typically excite a multiple quantum coherence involving the ground state (g), two vibrational states (v and v'), and an electronic state e. The coherence between e and g is responsible for the nonlinear polarization that creates the output field. For this case, $\chi^{(3)}$ has three resonances[49, 4, 6]

$$\chi^{(3)} = \frac{N F_{net} \mu_{eg} \mu_{gv} \mu_{vv'} \mu_{v'e} \rho_{gg}}{4 D \hbar^3 \Delta_{vg} \Delta_{v'v} \Delta_{ev'}} \tag{4.6}$$

$$\Delta_{vg}(\omega_1) = \omega_{vg} - \omega_1 - i\Gamma_{vg}$$

$$\Delta_{v'v}(\omega_1, \omega_2) = \omega_{v'v} - \omega_1 - \omega_2 - i\Gamma_{v'g}$$

$$\Delta_{ev'}(\omega_1, \omega_2, \omega_3) = \omega_{eg} - \omega_1 - \omega_2 - \omega_3 - i\Gamma_{eg}$$

where N is the oscillator density, F_{net} is the local field enhancement factor, ρ_{gg} is the ground state

density matrix term, ω_i is the excitation field frequency, ω_{mn}, μ_{mn}, and Γ_{mn} are the resonance frequency, transition dipole moment, and dephasing rate of the mn coherence, respectively.

In this work, the sample contains only a nonresonant solvent in order to eliminate solute resonances and isolate coherent interaction effects, and the output is nonresonant TSF signal. The two windows of the sample cell and the sample all contribute nonlinear polarizations. They add to form the output field and each contribution is defined by its own phase matching

$$E_{net} = E_{w1} + E_s + E_{w2} \tag{4.7}$$

$$E_{w1} = \int_0^{L_w} \frac{2\pi i F \omega_4 P_w(z)}{n_4 c} e^{i\Delta k_w z} dz \tag{4.8}$$

$$E_s = \int_{L_w}^{L_w+L_s} \frac{2\pi i F \omega_4 P_s(z)}{n_4 c} e^{i(\Delta k_s z + i\frac{\alpha_s(\omega_1,\omega_2)}{2} + \phi_1)} dz \tag{4.9}$$

$$E_{w2} = \int_{L_w+L_s}^{2L_w+L_s} \frac{2\pi i F \omega_4 P_w(z)}{n_4 c} e^{i(\Delta k_w z + \phi_2)} dz \tag{4.10}$$

where $E_{w1,s,w2}$ are the output electric fields generated in the first window, solvent, and second window, and $L_{w,s}$, $\Delta k_{w,s}$, and $P_{w,s}$ are the pathlengths, wave-vector phase mismatch terms, and non-linear polarizations created in the windows and solvent layers, respectively. In the case of an empty solvent cell, $P_s = 0$. α_s is the solvent absorption coefficients at both excitation frequencies, and the windows are assumed to be completely transparent.[41] The ϕ_1 and ϕ_2 are phase factors that describe the phase changes that accrue as the fields pass through the first and last windows, respectively.

$$\phi_1 = i\Delta k_w L_w \tag{4.11}$$

$$\phi_2 = i(\Delta k_w L_w + \Delta k_s L_s + i\frac{\alpha_s(\omega_1,\omega_2)}{2} L_s) \tag{4.12}$$

The experimentally detected TSF output intensity I_{net} is proportional to the magnitude squared E_{net}

$$I_{net} \propto |E_{net}|^2 \tag{4.13}$$

4.2.4 Experimental

TSF spectra were obtained using two sample cells with 0.3 mm and 2.0 mm thick calcium fluoride windows. D_2O was purchased from Sigma Aldrich and used as purchased. A 1 kHz Spectra-Physics Spitfire Ace is used to pump three independently tunable Optical Parametric Amplifiers (OPA) along with mixing crystals. For these experiments, the sources labeled 1 and 2 are tuned between $\bar{\nu}_1$ and $\bar{\nu}_2$ = 1100 - 2200 cm^{-1} for the excitation of vibrational states and the source labeled 3 is tuned between ν_3 = 14,000 - 18,000 cm^{-1} for the excitation of electronic states. Note that the experimental frequencies are wavenumbers, not angular frequencies. The OPAs have a spectral width of 35 cm^{-1} fwhm, a temporal width of 1 ps, and a pulse energy of 1 - 5 μJ. The excitation fields are focused using spherical mirrors and spatially overlapped at the sample position using a pinhole. A retroreflector mounted on a motorized translation stage controls the delay times for each excitation pulse. Pulse temporal overlap is found using ZnSe as a nonresonant nonlinear medium. The changes in delay time and excitation beam direction resulting from changing the excitation frequencies are corrected throughout the scanning range using the delay stages and motorized kinematic mirror mounts.

The TSF output pulse is isolated and focused onto the entrance slit of a monochromator using a pair of off-axis parabolic mirrors. A short-pass filter spectrally rejects the excitation beam and the monochromator tracks the expected TSF output frequency at $\bar{\nu}_{TSF} = \bar{\nu}_4 = \bar{\nu}_1 + \bar{\nu}_2 + \bar{\nu}_3$ while eliminating other phase-matching processes. Dual chopping and spatial filtering, further isolates desired TSF output[60]. The TSF output is homodyne detected with a photomultiplier. The output signal is normalized to the excitation beam power. The tuning and scanning systems are entirely automated and computer controlled using locally developed Python Software PyCMDS for controlling motors and WrightTools for data processing, fitting, and plotting.[61, 62]

The simulations were performed using Python 3 scripts. The intensity of the TSF output signal I_{net} was calculated across the experimental scanning range of $\bar{\nu}_1 = \bar{\nu}_2$ and $\bar{\nu}_{TSF}$ and the simulated spectra were compared to experimental results. Experimental visible and mid-IR indices of refraction[] and absorption coefficients of CaF_2 and D_2O were obtained from literature and incorporated into the simulations.[56, 58, 59, 57]

The signal created in TSF spectroscopy depends on the size of the excitation region formed by the spatial and temporal overlap of the three tunable excitation fields in the focal volume. The nonlinear polarization P depends on the product of the three fields. The beams are on the same vertical plane and cross each other horizontally while the visible excitation field, E_3, propagates normal to the sample layer. The infrared excitation fields, E_1 and E_2, cross the visible excitation field, E_3, at 10^o from opposite sides. The intersection of the excitation fields creates an effective window thickness that is narrower than the thicker windows and modifies the phase matching conditions. The excitation field amplitudes along the direction of propagation z are described as symmetrical 2D Gaussian functions converging to a beam waist and overlapping at the sample position

$$E_i(x,y,z) = E_0 \frac{w_0}{w_z(z)} e^{(\frac{x-\mu_x}{w_0})^2} e^{(\frac{y-\mu_y(z)}{w_0})^2} \tag{4.14}$$

where E_i is the electric field amplitude, w_0 is the beam waist, and $w_z(z)$ is the spot size at z. The x, y, and z coordinates describe the Cartesian space at the sample cell with x as the vertical dimension, y as the horizontal dimension, z as the dimension along the optical axis, and μ_x and μ_y are the individual excitation field axis of propagation. The product of the excitation fields is integrated over x and y to obtain the excitation field value $E_1(z)E_2(z)E_3(z)$ in Equation 4.1

$$E_1(z)E_2(z)E_3(z) = \iint_{-\infty}^{\infty} E_1(x,y,z)E_2(x,y,z)E_3(x,y,z)\,dx\,dy \tag{4.15}$$

The geometry of the axes of propagation of the excitation fields are described by

$$\mu_y(z) = z\tan(\theta)$$

$$\mu_x(z) = 0$$

where θ is the beam crossing angle between $E_{1,2}$ with E_3. Diffraction determines the spot size

$$w_z(z) = w_0\sqrt{1+\left(\frac{z}{z_r}\right)^2}$$

where z_r is the Rayleigh range. Together, the geometry of the three overlapping beams defines the

excitation volume for the TSF spectra. Figure 4.3 shows the geometry of the electric field product in the excitation region of the two sample cells.

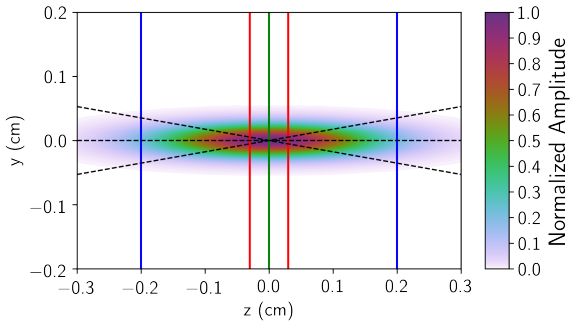

Figure 4.3: Cross section of sample and excitation field geometry. The dotted lines trace the optical axes of excitation fields. The blue and red vertical lines indicate the boundaries of the 2 mm and 0.3 mm sample cell windows, respectively, and the green vertical line represents the solvent layer. The color map shows the product of excitation fields $E_1E_2E_3(x, y, z)$.

In the case of an empty sample cell, the reflections of the excitation fields at the air to window interface create a Fabry-Pérot cavity within the air gap and cause a frequency dependent modulation of excitation field within the last window that is described by

$$E_{iw2} = E_i \frac{(1-R)^2}{1 - 2R\cos\delta + R^2} \tag{4.16}$$

where E_{iw2} is the excitation field within $w2$, R is the reflectance, and δ is round-trip phase difference given by

$$\delta = \frac{4\pi n_i L_s \cos\theta}{\lambda_i} \tag{4.17}$$

where n_i is the vacuum index of refraction, θ is the incident angle, and λ_i is the wavelength of excitation field E_i.

4.2.5 Results

The left hand column in Figure 5.11 shows the four 2D TSF spectra that were acquired for the two sample cells with CaF_2 windows of thickness 2 mm and 0.3 mm, and were either empty or filled with D_2O. The sample conditions are labeled 2 mm Empty, 2 mm D_2O, 0.3 mm Empty, and 0.3 mm D_2O for the sample cell window thickness and the fill. The spectra resulted from scanning the infrared frequencies so $\bar{\nu_1} = \bar{\nu_2}$ and the TSF output frequency $\bar{\nu}_{TSF} = \bar{\nu}_1 + \bar{\nu}_2 + \bar{\nu}_3$ and measuring the output beam intensity. Since the output intensity scales quadratically with concentration, the color bar defines the signal amplitude $\sqrt{I}$.

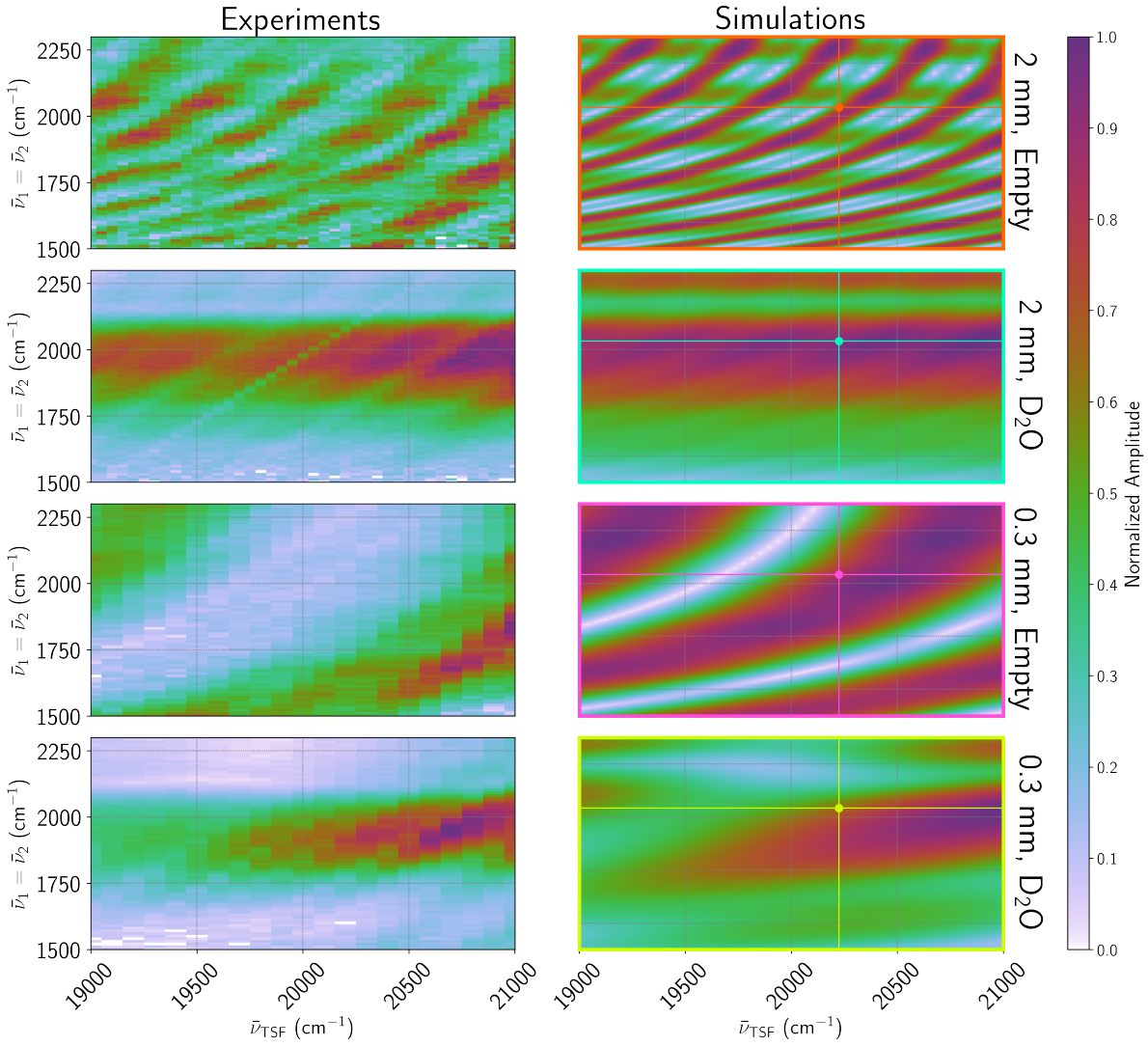

Figure 4.4: Left column: TSF spectra of an empty sample cell with CaF_2 window thickness 2 mm, D_2O in a sample cell with CaF_2 window thickness 2 mm and pathlength 25 μm, an empty sample cell with CaF_2 window thickness 0.3 mm, and D_2O in a sample cell with CaF_2 window thickness 0.3 mm and pathlength 25 μm. Right column: Simulations of the respective spectra on the left column using Eq 4.13. The crosshairs and colored circle indicate the excitation and output frequencies in the z-scan in Figs 4.7 and 4.8.

For the spectra of 2 mm Empty and 0.3 mm Empty in Figure 5.11 the nonlinear signal of CaF_2 is not resonant with any vibrational or electronic state so those signal modulations are completely dependent on the phase-mismatch term in Equation 4.4. The modulation periodicity changes with window thickness. The 2 mm and 0.3 mm thick windows correspond to a modulation periodicity of 200 and 1000 cm^{-1} respectively. The spectral features generated in the window have a curved modulation pattern, with each fringe starting out parallel to the x-axis at $\bar{\nu}_1 = \bar{\nu}_2 = 1500$ cm^{-1} and then curving up to become perpendicular to the x-axis at $\bar{\nu}_1 = \bar{\nu}_2 = 2{,}200$ cm^{-1}. The modulation periodicity also depends on $\bar{\nu}_1 = \bar{\nu}_2$, changing from 400 cm^{-1} near 2200 cm^{-1} to 600 cm^{-1} near 1500 cm^{-1} in Fig 5.11A. There are additional modulations along the $\bar{\nu}_1 = \bar{\nu}_2$ axis of constant frequency 200 cm^{-1} that result from etalon effects as the IR excitation beams pass through the cavity formed by the gap in the empty sample cell.

For the 2 mm D_2O and 0.3 mm D_2O spectra in Figure 5.11, the presence of D_2O changes the 2D spectrum. D_2O is a typical solvent used in vibrational CMDS because its vibrational resonances do not interfere with most vibrational modes. It contains only weak vibrational resonances in the fingerprint region and has the same solubility as water for many biologically relevant molecules. D_2O has a very strong O-D stretch mode at 2530 cm^{-1}, and a weaker bending mode at 1210 cm^{-1}. Even though the excitation fields are not resonant with the O-D stretch mode, there is still a large enhancement in the nonlinear signal in the region of these experiments. If the nonlinear signal is phase matched, the D_2O nonlinear polarization should be nearly constant across the spectral region of interest. The absorption from the O-D stretch mode will cause a distortion of the 2D spectrum and the complete loss of signal near the O-D stretch resonance but it will not cause the strong modulations observed in the spectra. The modulations are not uniform as a function of $\bar{\nu}_{TSF}$ and have a frequency dependent upon the excitation frequencies.

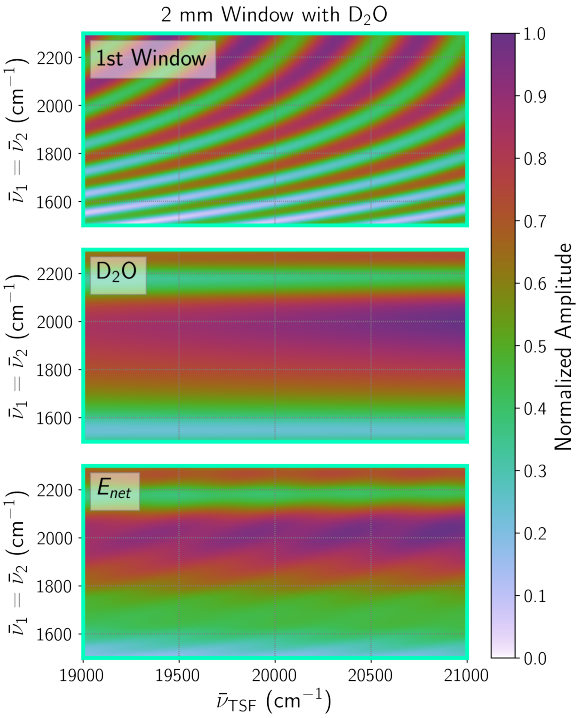

Figure 4.5: Simulations of the TSF output field generated in the first window (top), D_2O solvent layer (middle), and the net electric field E_{net} (bottom) for a 2 mm D_2O sample.

The simulated TSF spectra, shown in the right hand column of Figure 5.11, reproduce both the shape and periodicities of the window and solvent signal. The exception is the 0.3 mm Empty cell in which the simulated fringe periodicity does not match the experimental spectrum. The difference results from two effects that are not part of our simulation- a phase mismatch occurs in the air gap because the beams are not collinear and the slopes of the phase fronts change because of refraction at the window/air interface. The spectra were calculated using Equation 4.13 and account for the effects of phase matching, internal reflections, absorption, and nonlinear susceptibility. Figure 4.5 shows the relative contributions of the front window and the solvent, as well as the net electric field E_{net} for 2 mm D_2O. The curved modulations emerge from the contribution of the window terms while the band at $\bar{\nu}_1 = \bar{\nu}_2 = 2000$ cm^{-1} is due to the solvent contribution. The destructive interference in the window fringes is incomplete so modulations appear on a background signal. The 2000 cm^{-1} band is created by the resonance enhancement from the broad O-D stretch at 2530 cm^{-1}. When the excitation frequencies approach the O-D resonance, the strong absorption effects attenuate the excitation beams so the output intensity decreases. The absolute value of the sum of the output electric fields from each part of the sample cell is calculated to generate the spectrum of E_{net} in Fig 4.5. To reproduce the 2 mm Empty spectrum, the etalon effects described earlier were applied to the excitation fields.

The values of the window third order susceptibility, $\chi_w^{(3)}$, and the D_2O transition moment product in the sample third order susceptibility, $\chi_s^{(3)}$ (Equation 4.6), were adjusted to reproduce the experimental modulation effects on the solvent signal. The frequency and dephasing rates for the vibrational coherences are given in the Supporting Information. The ratios of the third order susceptibility terms are shown in Figure 4.6.

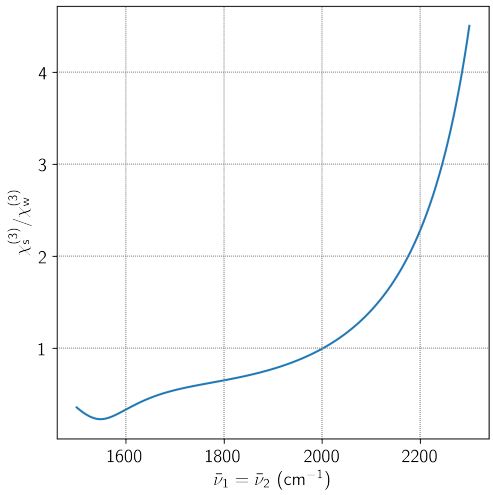

Figure 4.6: Ratio of the third order susceptibility of D_2O ($\chi_s^{(3)}$) and CaF_2 ($\chi_w^{(3)}$) for TSF across IR excitation frequencies.

We suggest that fitting the simulation to experimental TSF interference spectra can be used to derive absolute $\chi^{(3)}$ values for various solvents and molecules of interest. Note that the ratio becomes one at 2000 cm^{-1} so the D_2O $\chi^{(3)}$ is the same as the non-resonant $\chi^{(3)}$ of calcium fluoride at that frequency. Since the calcium fluoride non-resonant $\chi^{(3)}$ has been measured as 4.3x10^{-15} esu[51], Figure 4.6 could be scaled to reflect the dispersion of the multidimensional resonant $\chi^{(3)}$. As pointed out earlier, the capability of measuring absolute values of $\chi^{(3)}$ allows direct comparison of multidimensional spectra from different coherence pathways.

4.2.6 Discussion

The fringes observed in the experiment are defined by the phase-mismatch accumulated in the sample cell. To understand the cause of the frequency dependent fringe pattern, it is necessary to understand how the output electric field evolves as the excitation fields pass through the windows. Figure 4.7 shows a simulation of the output field strength along the axis of propagation z at a fixed excitation frequency combination ($\bar{\nu_1} = \bar{\nu_2} = 2030$ cm^{-1}, $\bar{\nu}_{TSF} = 20{,}245$ cm^{-1}) for 2 mm Empty, 2 mm D_2O, 0.3 mm Empty, and 0.3 mm D_2O is simulated and shown in Figure 4.7. The most important part of this figure is the realization that the output signal depends only on the very short path lengths near the window/sample interface. For reference, the simulated spectra in Figures 5.11 and 4.5 used the output field at the exit of the second window. The solvent layer begins at $z = 0$ cm and is represented by the colored layer.

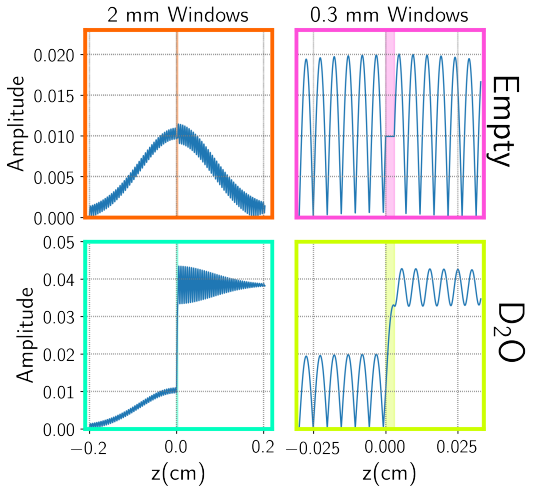

Figure 4.7: Evolution of TSF output electric field amplitude along the optical axis z for an empty (top) and D_2O filled (bottom) 2 mm (left) and 0.3 mm (right) thick windowed sample cell.

The driving fields for the 0.3 mm sample cell window enter the first window and generate a TSF output field. Due to the phase mismatch, the field created over the first 25 μm is destroyed by the output created over the next 25 μm, creating a cycle of creation and destruction of the output signal. The amplitude of the oscillations increases closer to the focal point of the excitation volume. The phase mismatch term $e^{i\Delta kz}$ in Equation 4.8 reproduces the observed oscillations. The modulation pattern is broken at the window/sample interface. For an empty sample cell, the output field remains unchanged through the air gap and continues the phase cycling in the second window. In the case of the D_2O-filled sample cell, however, there is a sharp increase in output field across the solvent region which continues as a constant field throughout the remainder of the cell. The size of the increase depends upon the phase of the field created in the window at the interface to the sample region. The phase mismatch causes large modulations in the amplitude of the solvent field over short distances and it defines its contribution to the field generated within the sample. It is this modulation that is largely responsible for the fringe pattern. Propagation within the sample does not experience the same phase oscillations since the phase mismatch in the sample is smaller and the sample path length is shorter. The field created by the sample adds to the field from the window so the field leaving the sample will depend on the constructive and destructive interference between the two fields. The propagation through the second window results in additional oscillations from the larger phase mismatch but the contribution from the sample persists. The field generated by the last window also decreases because of the lower excitation intensity as the beams near the exit. A similar behavior occurs for 2 mm windows, except the oscillations from the phase mismatch term continue throughout the thicker window before arriving at the solvent layer having cycled through many more periods (note: that the z axes scales are different).

The relative thickness of the excitation volume and the window has important effects on the output signal. The z-dependence of the field magnitude generated in the 0.3 mm Empty cell is almost constant because the excitation path length exceeds the window thickness whereas the field magnitude in the 2 mm Empty cell varies substantially and becomes a maximum at the sample position because the excitation volume is shorter than the window thickness (see Fig 4.3). The spatial dependence of the excitation fields causes incomplete destructive interference of the output field as it approaches the sample so the net field increases. When the sample cell is empty, the output field evolves in a reverse manner in the second window, where the excitation field product decreases from as z increases, destroying the

buildup from the front window. As a result, the maximum output field of 2 mm Empty is much weaker than that of 0.3 mm Empty, for which the excitation field overlap product is nearly constant across the path length. Incomplete phase cancellation in the thick windows is also responsible for the low contrast in the net electric field fringes of the empty sample cell in Figure 5.11.

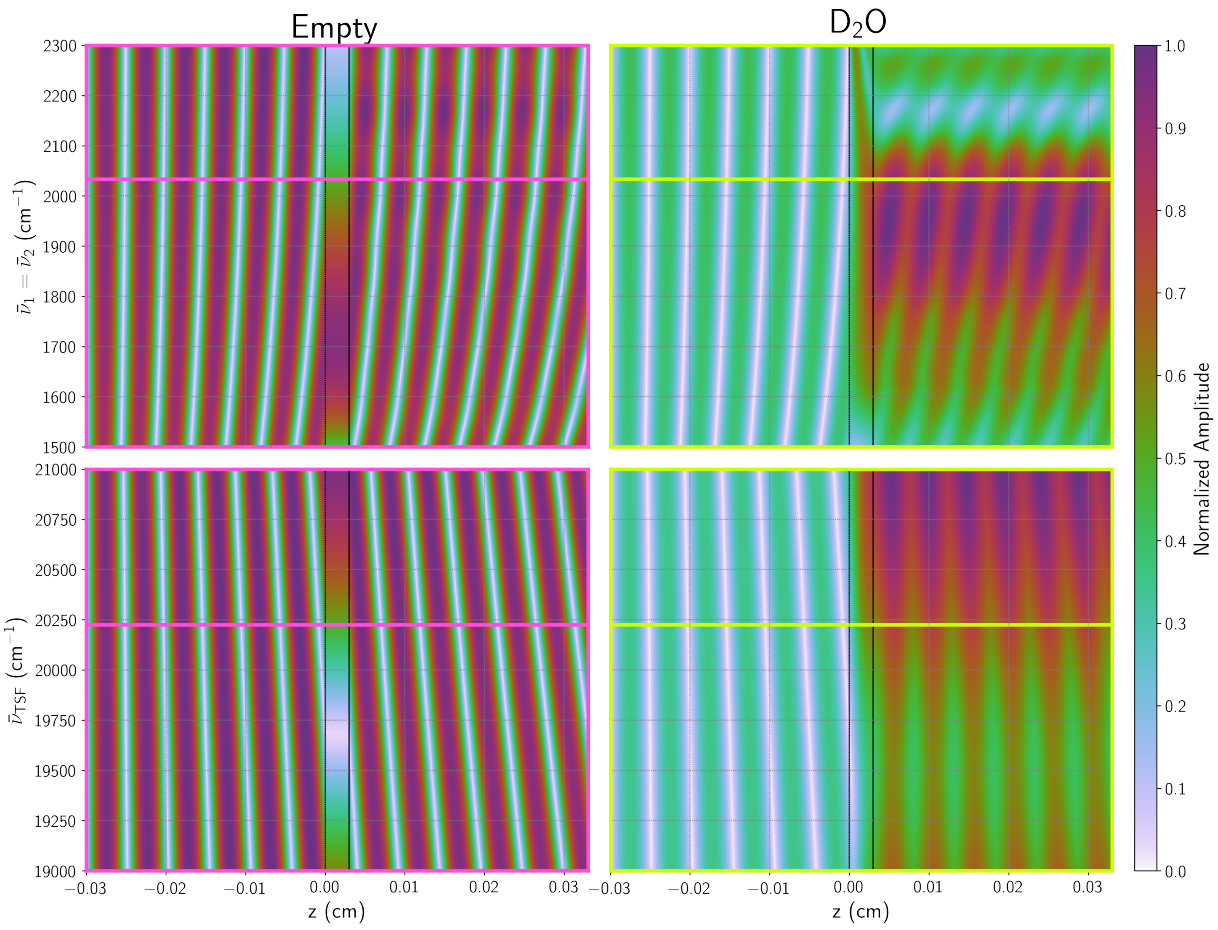

Figure 4.8: Simulation of the frequency dependence of TSF output electric field strength along the optical axis z across $\bar{\nu}_1 = \bar{\nu}_2$ (top) and $\bar{\nu}_{TSF}$ (bottom) for an empty (left) and D_2O-filled (right) sample cell of 0.3 mm window thickness. The magenta and lime horizontal lines indicate the fixed frequency of the static axis during the scanning of the other.

The period of the oscillations within the window depends on the frequency dependent phase mismatch Δk_w. Figure 4.8 shows the frequency dependence of the output field wave front evolution across z with respect to $\bar{\nu}_1 = \bar{\nu}_2$ and $\bar{\nu}_{TSF}$ for 0.3 mm Empty and 0.3 mm D_2O. Here, the net output field value is that of the last position along z at the exit of the second window. The wave fronts are initially independent of frequency but acquire increasing differences as they propagate, causing frequency dependent differences in the wave front at the window-sample interface. The frequency dependent slopes are positive as a function of $\bar{\nu}_1 = \bar{\nu}_2$ and negative as a function of $\bar{\nu}_{TSF}$. When the sample cell is empty, the window output field is constant across the air gap but its amplitude varies strongly as a function of the infrared and visible excitation frequencies. When the cell is filled with D_2O, the $\bar{\nu}_1 = \bar{\nu}_2$ frequency dependence of the phase fronts at the window-sample interface have little effect because the output field depends largely on the vibrational resonances of D_2O. The $\bar{\nu}_{TSF}$ frequency dependence of the phase fronts does cause a weaker output field from 20,000 to 19,000 cm^{-1}. Similarly, the graph for the 2 mm windows (see SI) shows the curvature of the fringes creates higher output fields at maxima in the slanted wave fronts intersecting the window-solvent border.

4.2.7 Conclusion

The role of phase matching is particularly important for TRSF experiments, especially those that involve sample cells where there is coherent interference effects between the nonlinear contributions from the windows and the sample. Optimum TRSF multidimensional spectra depend on having the thickness of the sample region short enough that $\Delta k L_s < 1$ so phase matching within the sample region is not important, the length of the excitation region is appreciably shorter than the window thickness, and the beam waists are centered at the sample position. Under these conditions, the fringes in the output signal depend on the coherent interference between the sample and the window contributions nearest the sample region. Simulation of the spectra can define the ratio of the third order nonlinear susceptibilities of the sample and window. If the window nonresonant susceptibility is known, the simulation can define the absolute non-resonant third order susceptibility of the sample's multidimensional spectra. This capability for measuring multidimensional frequency dependence of the absolute $\chi^{(3)}$ may be particularly useful in comparing the differences in coupling between quantum state features between multidimensional spectra of TRSF and other fully coherent methods such as Doubly Vibrationally Enhanced four wave mixing

and different coherent Raman methods.[63, 64, 65, 11, 66, 9, 67]

4.2.8 Acknowledgement

This work was supported by the National Science Foundation under grant CHE-1709060.

4.2.9 Supporting Information

The supporting information contains a simulation of the frequency dependence of TSF output electric field strength along the optical axis for the sample cell with a 2 mm window thickness. It also includes the details of how the simulations were created and instructions on how to access the original data, the data analysis tools, the simulation package, and run the programs.

4.3 Appendix

4.3.1 Additional simulations

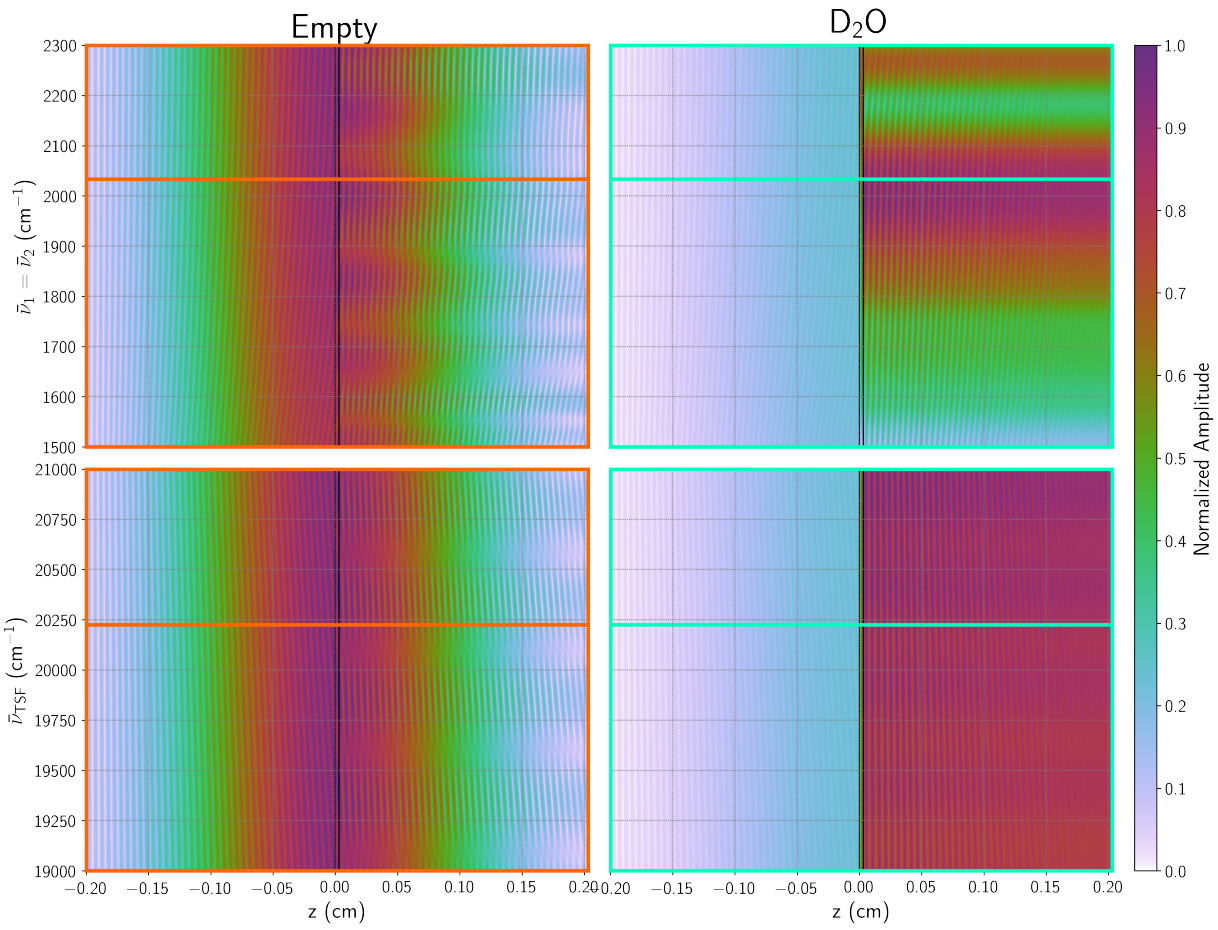

Figure 4.9: Simulation of the frequency dependence of TSF output electric field strength along the optical axis z across $\bar{\nu_1} = \bar{\nu_1}$ (top) and $\nu\bar{_{TSF}}$ (bottom) for an empty (left) and D_2O-filled (right) sample cell of 2 mm window thickness. The orange and cyan horizontal lines indicate the fixed frequency of the static axis during the scanning of the other.

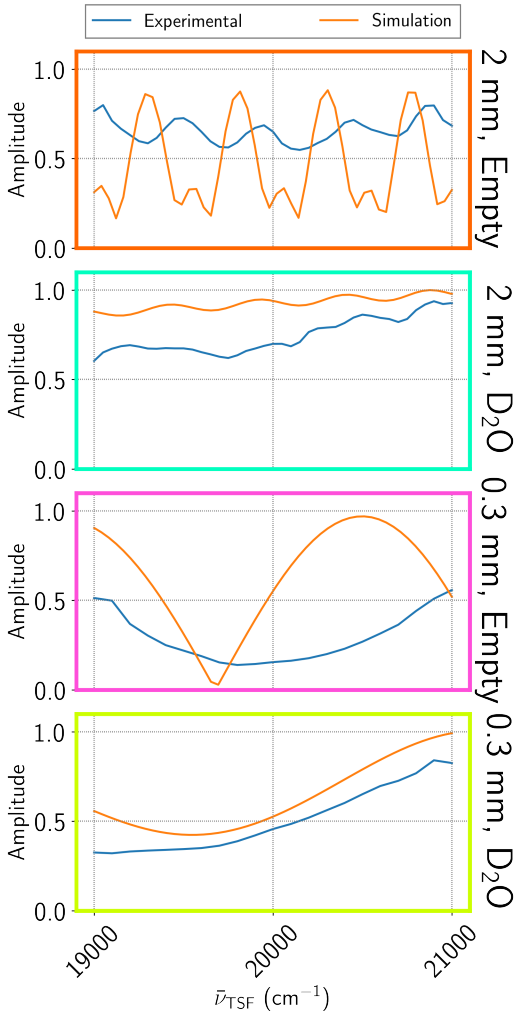

Figure 4.10: Comparison of $\nu\bar{T}SF$ slices of experimental and simulated data at fixed $\bar{\nu_1} = \bar{\nu_2} = 2030$ cm^{-1}. The slices are taken from the plots in Figure 3 from the main body text. Note that we are demonstrating that the periodicity of the oscillations matches reasonably. The precise phase of the oscillations is very sensitive to the exact thickness of the windows, and is subject to error.

4.3.2 Description of Simulation

The tools and raw data presented in this work are made publicly available. All supplementary information, including this document and the raw and processed data files are hosted on the Open Science Framework, DOI: 10.17605/OSF.IO/M9YCR.

Included are the raw data files, as collected from PyCMDS for the laboratory experiments. Our processing script generates `simulation.wt5`, a Hierarchical Data Format (HDF5) file with a structure specified at http://wright.tools/en/master/wt5.html. This file is completely compatible with the HDF5 specification by the HDF Group (https://www.hdfgroup.org), an can be viewed with any program which can view HDF5 files.

To view within Python, we recommend `h5py` (http://h5py.org) to access the data. Our own library, `WrightTools`, can also be used, and has some tools to more easily plot and manipulate the data.

Our libraries are maintained in an Open Source (MIT Licensed) repository hosted at https://github.com/wright-group. There you can find the latest versions of our libraries and data acquisition packages. `WrightTools` is additionally distributed via the Python Package Index (https://pypi.org/project/WrightTools/).

Computational Environment

Python version 3.6.4 was used to perform the computations. In order to best ensure reproducibility, the exact versions of `WrightTools`, and dependencies are as follows:

```
appdirs==1.4.3
cycler==0.10.0
h5py==2.7.1
imageio==2.2.0
kiwisolver==1.0.1
matplotlib==2.2.0
```

```
numexpr==2.6.4
numpy==1.14.2
Pillow==5.0.0
pyparsing==2.2.0
python-dateutil==2.7.0
pytz==2018.3
scipy==1.0.0
six==1.11.0
tidy-headers==0.2.0
WrightTools==3.0.0
```

HDF5 version 1.8.19 was installed when the simulations were performed.

Alternative versions of Python, modules, or external dependencies (particularly newer versions) may likely be substituted with no ill effect, however, this cannot be guaranteed. A virtual environment is recommended for running the simulations without needing to adjust installed Python packages on the host system. There are several tools available to create virtual environments, including `pipenv` (https://docs.pipenv.org/) and Conda (https://conda.io).

Simulations were performed on a computer running Solus with Linux kernel 4.15.17-65. There is nothing knowingly platform dependent in the code as written, however bugs in the Windows behavior of WrightTools were fixed in patch 3.0.1, so it is recommended to update.

Configuration File

The simulation is configured using an INI file. The entire contents of the configuration file are copied into the resulting HDF file, stored in the `attrs` dictionary with keys `"section:option"`.

```
[main]
dataname = 'sim'
```

The main section contains a single parameter, the name assigned to the resulting data object.

```
[window]
identity = 'CaF2'
sellmeier_b = [4.430595147e-1, 4.454624348e-1, 1.502595301e-1, 8.859807728]
sellmeier_c = [1.733873966e-3, 7.939087382e-3, 1.234337898e-2, 2.751117861e3]
length = .2
chi_constant = 1
```

The window section describes the window system. The first parameter (identity) is for human readability, it does not affect the simulation. Refractive indices are computed using the Sellmeier equation with constants given by sellmeier_b (dimensionless) and sellmeier_c (μm^2). The length field specifies the width of each window in cm. The final parameter, chi_constant, specifies the value of $\chi^{(3)}$ for the windows, which is assumed constant as the windows are assumed completely nonresonant.

```
[solvent]
identity = 'D2O'
resonance_positions = [2530, 1560, 1210]
resonance_weights = [49.5, 3.5, 3.5]
resonance_gamma = [60, 300, 25]
ir_offset = 0.02
ir_index_data = "ir_d2o.csv"
sellmeier_b = [-0.30637, 0.74659]
sellmeier_c = [-47.26686, 0.00893]
chi_constant = 20000
length = 25e-4 #cm
reflectance = 0.01
```

The solvent section describes the contents of the sample layer. As above, identity is for human readability, it does not affect the simulation. The next three parameters describe the position, relative

intensity, and breadth of peaks in the absorption spectrum in the infrared. The solvent is assumed to be transparent to visible wavelengths. These three lists must be the same length, and are used to compute absorbance and $\chi^{(3)}$. $\chi^{(3)}$ is additionally multiplied by `chi_constant`, which stands in for several constant terms. $\chi^{(3)}$ is also modeled by dividing the frequency dependant detuning terms, $\Delta_{vg}(\omega_1)$ and $\Delta_{v'v}(\omega_1, \omega_2)$. The electronic transition is considered nonresonant and is incorporated in `chi_constant`. These Δ terms use the same resonance positions and Γ values as the absorption specified by the three entries in the configuration file.

The index of refraction in the infrared can either be specified with an external data file `ir_index_data` or a constant `ir_index`. If using `ir_index_data` it should specify the path of a data file which is in Comma Separated Value format with two columns: the wavenumber in cm^{-1}, followed by the refractive index. An additional optional parameter `ir_offset` can be used to have a constant added to the numbers found in the data file.

The index of refraction in the visible region is calculated using the Sellmeier equation, the same as the windows above.

The `length` field specifies the width of the sample cavity in cm. Finally, `reflectance` controls the strength of the etalon effect. This should be set to 0. to remove the etalon completely.

```
[omega_1]
start = 1500
stop = 2300
shape = [1, 131]

[omega_2]
start = 1500
stop = 2300
shape = [1, 131]

[omega_out]
```

```
start = 19000
stop = 20800
shape = [37, 1]
```

These three sections describe the shape in frequency space to simulate. The user specifies the starting and stopping frequencies in each of ω_1, ω_2 and ω_4 (omega_out). ω_3 is computed from the other values. The simulation is flexible enough to handle 1-dimensional, 2-dimensional, or 3-dimensional frequency space acquisitions. Shown here is a 2D scan where the IR frequencies are scanned together. To select the dimensionality of the simulation, you change the shape field. These three fields **must** broadcast together. It is intended that each will have at most one value that is greater than 1. The points are distributed linearly in this dimension, with the number of points being given by the shape.

```
[spatial]
y_min = -0.5 #cm
y_max = 0.5 #cm
y_npts = 200

z_npts_window = 1000
z_npts_solvent = 200
focus_z = 0e-4 #cm
beam_waist = [0.03, 0.03, 0.03]
rayleigh_distance = 1.67
angle = [-10, 0, 10]
coeff = [1, 1, 1]
```

The final section, spatial, describes how the beams overlap. The first three fields y_min, y_max, and y_npts describe the parameters for numerically integrating the overlap region in the y dimension. The beams are assumed coplanar, and the integral in x is computed analytically.

beam_waist (cm), rayleigh_distance (cm), angle(°) describe the shape and geometry of the Gaussian beams. coeff describes the relative intensities of the beams. focus_z describes the position (in

z) where all three beams are focused. This position is relative to the first window/solvent interface, with the first window being negative, and the solvent and second window being positive.

Finally, `z_npts_window` and `z_npts_solvent` determine the number of integration steps to be performed in each window, and in the solvent cavity, respectively.

4.3.3 Running

The simulation may be run in several ways. All of the following assume your current working directory is the 'simulations' folder which includes `simulation.py`, `run_sims.py`, `plot.py` Further, the following assumes the tools listed in the Computational Environment section are present.

To run a single simulation from the command line:

```
$ python3 -i simulation.py [config.ini]
```

This will start an interactive python session with the `WrightTools` data object called `data`.

To run a simulation from within python (either interactive session or from a script):

```
import simulation
import WrightTools as wt
collection = wt.Collection()
data = simulation.main('config.ini', parent=collection)
```

Both parameters to `main` are optional, with the configuration file defaulting to `'config.ini'` and the parent defaulting to a new `WrightTools` Collection.

To run all of the simulations specific to this publication, creating the `simulation.wt5` file:

```
$ python3 run_sims.py
```

This will read in the experimental data from the `data_files` folder, as well as all `ini` files (except `config.ini`) and run the simulations. The result is `simulation.wt5`, which is expected for plotting.

Plotting

To plot, again, from within the `simulations` folder, and having already obtained `simulation.wt5`:

```
$ python3 plot.py
```

This will create all of the figures generated by Python for this publication. Individual figures may be selectively generated by passing command line arguments with the following keys:

```
thin_freq_vs_z
thick_freq_vs_z
z_slice
breakdown
experimental
chi
overlap
compare
```

4.3.4 D_2O Resonance Parameters

Table 4.1: The parameters for D_2O vibrational modes in the simulation

Resonace Center Frequency (cm^{-1})	Resonance Weight (A.U.)	Resonance Gamma (cm^{-1})
2530	24.5	60
1560	3.5	300
1210	3.5	25

Chapter 5

3D TRSF on cobalamins

5.1 Summary

In this chapter, I describe the 3D-TRSF studies we did on cyanocobalamin (CNCbl) and deuterated aquacobalamin (D_2OCbl). The chapter is divided into four sections.

The first section is the body of a paper soon to be submitted entitled "Three Dimensional Triply Resonant Sum Frequency spectroscopy reveals vibronic coupling in cobalamins: towards a probe of reaction coordinates". The authors of the paper are Jonathan Handali, Kyle Sunden, Blaise Thompson, Nathan Neff-Mallon, Emily Kaufman, Thomas Brunold, and John Wright. We focused on the α/β region of the two cobalamins which fell into the SHS tuning region of OPA3. We found coupling between three vibrational and three electronic states and showed that 3D-TRSF has the potential to resolve congested electronic spectra using the specificity of vibronic coupling. We also use our results in conjunction with resonance Raman and absorption to support a vibronic model for the α/β region.

In the last three sections, I present unpublished work on CNCbl including polarization effects, DOVE scans, and preliminary TRSF scans with SFS tuning targetting the D and E band region.

5.2 Three Dimensional Triply Resonant Sum Frequency spectroscopy reveals vibronic coupling in cobalamins: towards a probe of reaction coordinates

5.2.1 Abstract

Triply Resonant Sum Frequency (TRSF) spectroscopy is a fully coherent mixed vibrational-electronic spectroscopic technique that is ideally suited for probing the vibrational-electronic couplings that become important in driving reactions. We have used cyanocobalamin (CNCbl) and deuterated aquacobalamin (D_2OCbl^+) as model systems for demonstrating the feasibility of using the selectivity of coherent multidimensional spectroscopy to resolve electronic states within the broad absorption spectra of transition metal complexes and identify the nature of the vibrational and electronic state couplings. We resolve three short and long axis vibrational modes in the vibrationally congested 1400 - 1750 cm^{-1} region that are individually coupled to different electronic states in the 18,000 - 21,000 cm^{-1} region but have minimal coupling to each other. Double resonance with the individual vibrational fundamentals and their overtones selectively enhances the corresponding electronic resonances and resolves features within the broad absorption spectrum. This work demonstrates the feasibility of applying this new methodology to a broad range of transition metal complexes and their reaction mechanisms.

5.2.2 Introduction

Cobalamins are a family of Co corrinoid complexes that act as cofactors for enzymes that catalyze many reactions important to biology, such as isomerase, methyl transferase, halogen transferase, and reductive dehalogenase reactions[15, 68, 69]. The molecular structure of cobalamins is shown in Figure 5.1. These species contain a Co(III) cation at the center of a corrin ring, an upper axial ligand, which can be a CN, H_2O, OH, Me, or Ado group, and a dimethhylbenzimidazole lower axial tail group ligand that also attaches to the corrin ring[70]. The dominant vibrational modes and electronic states reflect the symmetry of the long and short axes (LA and SA) of the corrin ring indicated by the vertical and horizontal arrows in the figure. MeCbl and AdoCbl are the active species of cobalamin used by

human enzymes to initiate reactions by the heterolytic and homolytic cleavage of the Co-C bond, respectively[15]. CNCbl (Vitamin B_{12}) is a synthetic and photostable[71] form of cobalamin from which functional coenzyme derivatives are formed in the body.

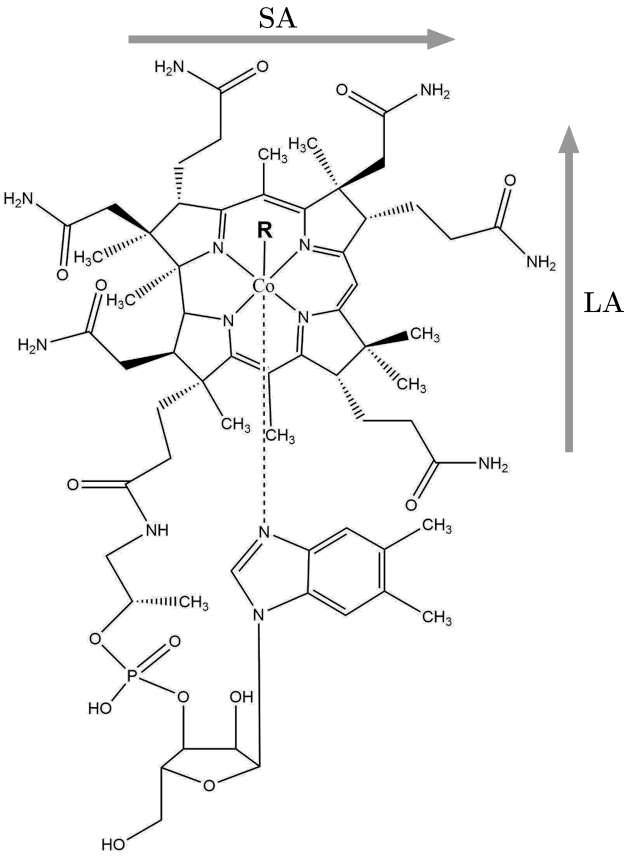

Figure 5.1: Structure of CNCbl (R = CN) and D_2OCbl^+ (R = D_2O). The gray arrows indicate the directions of the long axis (LA) and short axis (SA).

The visible absorption spectrum of cobalamin is sensitive to the electronic structure and contains signatures of the chemical environment. There are specific spectral features that are characteristic of the Co oxidation state and the identity of the upper axial ligand[20, 3, 72, 21, 73]. The absorption spectrum has been used in many studies to monitor oxidation state changes associated with enzyme turnover[74, 75, 76], cobalamin association with metals, cofactors and chaperones[77, 78, 79], and the synthesis of modified cobalamin forms and conjugates[80, 81, 82]. However, small changes in the electronic structure associated with cobalamin-dependent reactions are obscured by spectral congestion from multiple broad and overlapping peaks. Congested absorption spectra also provide little constraint for confirming particular electronic structure models of cobalamins. The accuracy of these models is important for computational studies of cobalamin reactivity[83, 84, 85, 86, 87, 88, 89, 90, 91, 92]. The α/β bands of CNCbl have been the subject of multiple spectroscopic and theoretical studies directed at understanding the nature of the electronic states associated with these bands. The Time Dependent Density Functional Theory (TD-DFT) calculated excited electronic state properties of CNCbl reported by Stich et al.[3], Andruniow et al.[18], and Ouyang et al.[93] are shown in Table 5.1. All three groups attribute the α band to a strong cor-π-HOMO$\rightarrow$cor-π*-LUMO transition in the corrin ring. However, there is disagreement over the nature of the β feature and shoulder peak.

Study	**State**	**Type**	**f**	**Energy (cm^{-1})**
Stich	$\alpha - v_1$	cor-π-HOMO $\rightarrow$ cor-π*-LUMO	0.1242	17,775
	Sideband		-	19,025
	Sideband		-	20,275
		cor-π - cor-π*-LUMO	0.0095	22,575
Andruniuw	α	cor-π-HOMO $\rightarrow$ cor-π*-LUMO	0.073	18,091
	β	cor-π+Co-3d_{yz} $\rightarrow$ Co-3d_{xy}+cor-N-σ	0.01	18,647
	Shoulder	cor-π+Co-3d_{yz} $\rightarrow$ Co-3d_{z^2}-axial-σ+cor-N-σ	0.003	19,502
Ouyang	α	cor-π-HOMO $\rightarrow$ cor-π*-LUMO	-	17,744
	Shoulder	cor-π-HOMO+Co-3d_{yz} $\rightarrow$ cor-π*-LUMO+Co-3d	-	20,164

Table 5.1: DFT calculated electronics states of CNCbl

Triply Resonant Sum Frequency (TRSF) spectroscopy is a fully coherent technique that simultaneously resolves vibrational and electronic resonances[5]. It is a member of a family of coherent multidimensional spectroscopies (CMDS) designed to deconvolute congested spectra along multiple frequency and temporal axes[10, 12, 94, 67, 39, 35]. TRSF employs three excitation pulses (two IR and one visible) to excite a triple quantum coherence that then emits frequency-resolved signal in the visible region. It has been described in several previous publications[37, 6, 5, 39, 63, 95]. TRSF has been shown to resonantly enhance signals from weak IR active vibrational modes via electronic coupling, to detect mechanical mode coupling (similar to 2D-IR spectroscopy[96, 97]), and to selectively enhance signal through coupling between vibrational modes and a single electronic state (similar to 2DEV spectroscopy[98]). Experiments with the highly symmetric copper phthalocyanine showed TRSF selectively enhances the infrared active modes, suppresses the Raman active modes, and serves as the infrared analogue to resonance Raman spectroscopy[6]. Each of these previous studies used two tunable IR light sources and a fixed visible source. In the present study, we report for the first time a TRSF experiment where all three excitation sources are scanned.

Previous work has defined our formalism for TRSF[39, 5, 6]. Briefly, pulses 1 and 2 have IR frequencies labeled $\bar{\nu}_1$ and $\bar{\nu}_2$ and pulse 3 has a visible-light frequency labeled $\bar{\nu}_3$. The triple quantum coherence emits the output signal at $\bar{\nu}_{TRSF} = \bar{\nu}_1 + \bar{\nu}_2 + \bar{\nu}_3$. The pathway is illustrated in the Wave Mixing Energy Level[99] (WMEL) diagram in Figure 5.2. When fully resonant, the excitation pulses stimulate three sequential transitions: $\bar{\nu}_1$ excites a vg vibrational coherence, $\bar{\nu}_2$ then excites a $(v + v'), g$ combination band/overtone double quantum coherence, and $\bar{\nu}_3$ excites the eg electronic output coherence. The polarization created by the eg coherence creates the output field at $\bar{\nu}_{TRSF}$, which corresponds to the frequency in the absorption spectrum. The strength of the output signal depends on the coupling strength between the vibrational and electronic states.

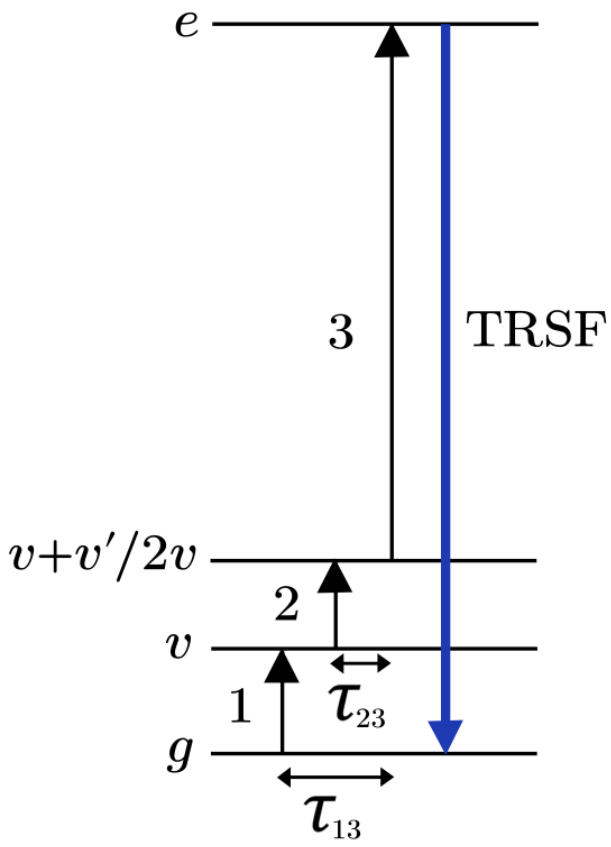

Figure 5.2: WMEL diagram of the Triply Resonant Sum Frequency Spectroscopy pathway. *g* represents the ground state, *v* and *v'* represent fundamental vibrational modes, *v+v'* or *2v* represents a combination/overtone state, and *e* represents an excited electronic state. τ_{13} and τ_{23} are the relative pulse delay times.

We have added a tunable visible light source allowing us to adjust $\bar{\nu}_3$ and scan $\bar{\nu}_{TRSF}$ to take advantage of the selectivity of vibrational-electronic coupling to resolve electronic states in congested absorption spectra. The four relevant frequencies are related by a single equation ($\bar{\nu}_{TRSF} = \bar{\nu}_1 + \bar{\nu}_2 + \bar{\nu}_3$), so the experiment can be fully parameterized by any three. We choose to scan $\bar{\nu}_1$, $\bar{\nu}_2$, $\bar{\nu}_{TRSF}$, while $\bar{\nu}_3$ is actively tuned to maintain the triple sum. The delay between pulse 1 and pulse 3 is labeled as $\tau_{13} \equiv t_3 - t_1$, and the delay between pulse 2 and pulse 3 is labeled as $\tau_{23} \equiv t_3 - t_2$, with positive delay indicating that pulse 3 arrives first.

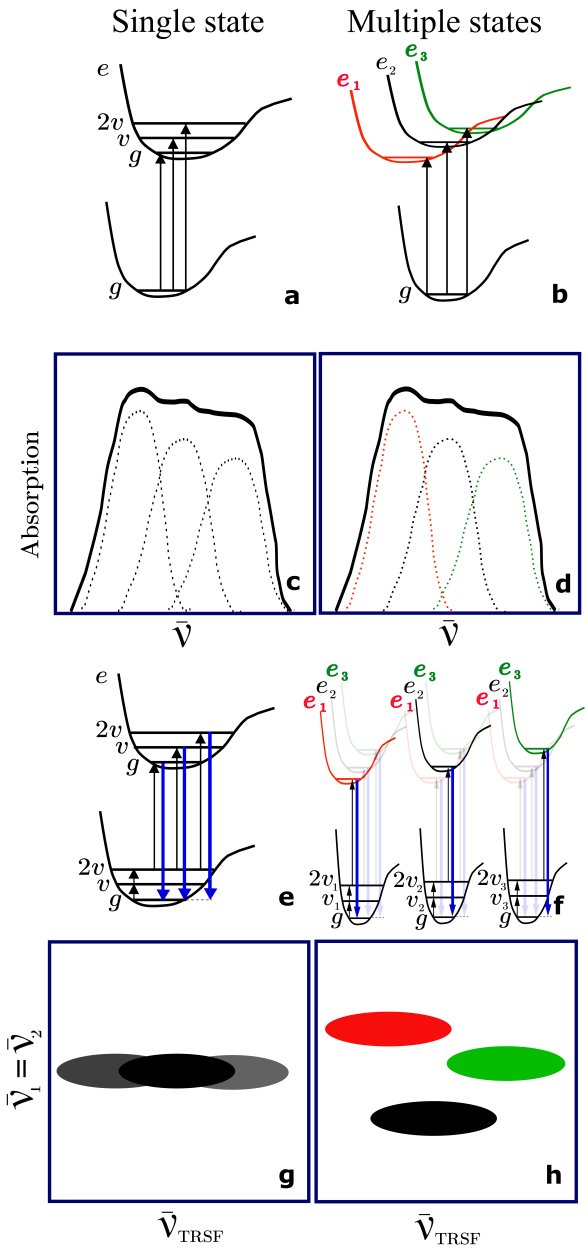

Figure 5.3: (a,b) Absorption energy level diagrams, (c,d) cartoon absorption spectra, (e,f) TRSF WMEL diagrams, and (g,h) cartoon TRSF spectra of a single electronic state vibronic structure (left) and a multiple electronic state structure (right).

We have applied 3D-TRSF to the α/β region of the cob(III)alamins cyanocobalamin (CNCbl) and deuterated aquacobalamin (D_2OCbl^+). Figure 5.3 illustrates how a congested electronic absorption spectrum can be resolved using the selective electronic enhancement of TRSF. Figures 5.3a and 5.3b show two different electronic structures that both produce the same absorption spectrum: (a) transitions to multiple vibronic states g, v, and $2v$ of a single electronic state e or (b) transitions to multiple electronic states e_1, e_2, and e_3. Absorption spectroscopy (Figures 5.3c and d) cannot distinguish between the two structures. Figures 5.3e and 5.3f show the same electronic structures interrogated using 3D-TRSF. Rather than stimulating a transition to the electronic state directly from the ground state, the triple-pulse sequence excites the fundamental (v) and overtone ($2v$) states of a vibrational mode and the Raman transition enhanced by the e state that is coupled to v. In the case of a single electronic state with multiple vibrational states (Figure 5.3e), the $\bar{\nu}_3$ Raman transition will be enhanced by each of the three vibronic transitions of e with a dipole moment determined by the Franck-Condon overlap factors. The resultant TRSF spectrum will have a vibrational peak along the $\bar{\nu}_1 = \bar{\nu}_2$ axis and a vibronic progression along the $\bar{\nu}_{TRSF}$ axis as illustrated in Figure 5.3g. In the case of different electronic states, $\bar{\nu}_3$ can only cause a transition to electronic states that are coupled to v_1. If v_1 couples only to e_1, TRSF signal is only enhanced when $\bar{\nu}_{TRSF}$ is resonant with e_1. Conversely, other vibrational modes v_2 and v_3 that couple to states e_2 and e_3, respectively, are enhanced at the e_2 and e_3 resonances. The resultant TRSF spectrum will have vibrational-electronic cross peaks at ($\bar{\nu}_1 = \bar{\nu}_2$, $\bar{\nu}_{TRSF}$) = (v_1,e_1), (v_2,e_2), and (v_3,e_3) as illustrated in Figure 5.3h.

In this study, we used TRSF to resolve the congested α/β region of the absorption spectrum for CNCbl and deuterated Aquacobalamin (D_2OCbl^+) taking advantage of the coupling between long and short axis corrin ring modes and the electronic states in the α/β region [100, 101, 20, 21, 102]. We collected 3D frequency spectra in an IR-IR-Visible TRSF experiment, and observe coupling between specific vibrational modes and electronic states in the α/β region. We compare the TRSF spectra to a single state vibronic progression and a multiple electronic state model to study the nature of the electronic structure.

5.2.3 Theory

TRSF is a four-wave-mixing process whose output intensity is defined by

$$I_{TRSF} \propto |\chi^{(3)}|^2 \ell^2 M I_1 I_2 I_3 \tag{5.1}$$

where ℓ is the path length, $\chi^{(3)}$ is the third order susceptibility, and I_i is the intensity of each excitation field.[39, 37] M is a correction factor for absorption and changes in phase-matching[5, 6, 41]. For a triply resonant process, the third-order susceptibility has the proportional relationship

$$\chi^{(3)} \propto \frac{N \mu_{vg} \mu_{(v+v'),v} \mu_{e,(v+v')} \mu_{ge}}{\Delta_1 \Delta_2 \Delta_3} \tag{5.2}$$

where N is the oscillator density, μ_{mn} is the transition dipole moment between states m and n, and Δ_j is the complex detuning factor for each excitation field:

$$\Delta_j = \delta_{mn} - i\Gamma_{mn} \tag{5.3}$$

where $\delta_{mn} = \bar{\nu}_j - \bar{\nu}_{mn}$ is the energy difference between the excitation $\bar{\nu}_j$ and mn transition frequencies, and Γ_{mn} represents the pure dephasing rate of the mn coherence.

Since the same transition moments and detuning factors occur in absorption and resonance Raman spectroscopies, equation 5.1 can also be written as

$$I_{TRSF} \propto \frac{\alpha^{(1)}_{g\to v} \alpha^{(2)}_{v\to v+v'} \sigma^{(3)}_{v+v'\to g} \ell^2 M}{\Gamma_{vg} \Gamma_{v'g}} \tag{5.4}$$

where $\alpha^i_{a\to b}$ is the absorption coefficient for the $a \to b$ transition at the $\bar{\nu}_i$ frequency, $\sigma^{(3)}_{(v+v')\to g}$ is the Raman cross section of the $v + v' \to g$ transition, and ℓ is the path length. The output signal is maximally enhanced when the two infrared pulse frequencies, $\bar{\nu}_1$ and $\bar{\nu}_2$, are resonant with vibrational transitions, and the visible frequency $\bar{\nu}_3$ is resonant with a coupled electronic/vibronic transition.

The presence of features in a multidimensional TRSF spectrum requires coupling between the vibrational and electronic states. If the vibrational transitions are allowed, the required coupling depends

on $\mu_{e,(v+v')}\mu_{ge}/\Delta_3$. These are the same factors that define the $v + v'$ resonance Raman combination band transition. These transition moments depend on the Franck-Condon and Herzberg-Teller coupling between the electronic and vibrational transitions. The coupling requires that the excited state potential energy surface is displaced relative to the ground state along both vibrational modes[103]. The ability of TRSF to reduce spectral congestion in complex samples rests on this coupling requirement.

5.2.4 Methods

Sample Preparation

CNCbl (Sigma Aldrich) was dissolved in D_2O (Sigma Aldrich) to make a saturated solution (approximately 5 mg/mL). Hydroxocobalamin acetate (Sigma Aldrich) was also dissolved in D_2O to make a saturated solution. Dilute DCl was added to reach a pD of 5. The sandwich sample cell consisted of two 300 μm thick CaF_2 windows with a 25 μm teflon spacer.

For the drop-casted sample, CNCbl was dissolved in methanol (both from Sigma Aldrich) with concentration 10 mg/mL. The solution was dropped onto a miscroscope slide (Fisher Scientific) and dried in a desiccator until a thin smooth layer of CNCbl was formed on the surface.

3D-TRSF Laser System

An 80 MHz Ti:sapphire ultrafast oscillator (Spectra-Physics Tsuanmi) was used to prepare $\sim$35 fs seed pulses. These seed pulses were amplified using a 1 kHz regenerative amplifier (Spectra-Physics Spitfire Ace). A mask was placed inside the amplifier to lengthen the output pulses to 1 ps. The 6 W amplifier output was split to pump three independently tunable motorized Optical Parametric Amplifiers (OPAs). OPA1 ($\bar{\nu}_1$) is a Light Conversion TOPAS-800 with an NDFG "DF1" mixer stage. OPA2 ($\bar{\nu}_2$) is a Spectra-Physics OPA-800 with a $AgGaS_2$ DFG mixing crystal. OPA3 ($\bar{\nu}_3$) is a Spectra-Physics OPA-800C with a BBO mixing crystal for signal doubling. A set of spectral filters removed the signal and idler as well as the higher order mixing processes. The grating and crystals within OPAs 2 and 3 have been motorized using 50 mm linear DC actuators (Ealing). In addition, each OPA was paired with a

motorized mirror mount (Zaber T-MM) to control output direction. For each OPA, the tunable output pulses had a spectral width of 35 cm^{-1} FWHM, a temporal width of 1 ps, and a pulse energy of 1-5 μJ.

Between the OPA and the sample, $\bar{\nu}_1$ and $\bar{\nu}_2$ each passed through a corner-cube retro-reflector which was moved to control relative pulse arrival time (delay). These delays were motorized using the same 50 mm linear actuators used inside of the Spectra-Physics OPAs.

Each pulse was focused to a 100 μm pinhole at the sample position using focusing mirrors of focal lengths 25 cm for $\bar{\nu}_1$ and $\bar{\nu}_2$ and 1 m for $\bar{\nu}_3$. The focal lengths were chosen to create a 200 μm beam waist for each beam. At the sample, the polarizations of $\bar{\nu}_1$, $\bar{\nu}_2$, and $\bar{\nu}_3$ were horizontal, horizontal, and vertical, respectively.

A pair of off-axis parabolic mirrors collimated and refocused the output signal onto a monochromator entrance slit. Spectral filters rejected the excitation beam and the monochromator tracked the expected TRSF output frequency and rejected light from other processes. Additionally, a combination of an aperture and dual-chopping was used to remove the processes with phase matching $2\vec{k}_1 + \vec{k}_3$ and $2\vec{k}_2 + \vec{k}_3$ and isolate $\vec{k}_1 + \vec{k}_2 + \vec{k}_3$. The TRSF output was homodyne-detected using a photomultiplier (Hamamatsu H7422-20).

System control, calibration, and data processing

The OPAs, direction control mirrors, delay stages, and monochromator are fully automated. Motor control and data collection are coordinated by home-built software PyCMDS[104]. Motors inside each OPA move to ensure phase matching and grating angles are appropriate for maximum conversion efficiency at each desired output wavelength. Motorized mirrors were used to ensure that OPA output direction is consistent. Delay stages were actively moved to ensure that optical path length remains consistent for different output colors.

We generated calibration or tuning curves for each motor prior to each experimental session. Pyroelectric detectors and a monochromator were used to measure OPA output power and spectrum respectively. A pinhole was used to measure OPA output direction. Four wave mixing within a ZnSe crystal was used to measure the relationship between OPA output color and optical path length. We have created fitting

routines that process these raw measurements to generate ideal calibrations and tuning curves. Curve generation, data collection, data processing, and plot generation were all carried out using WrightTools, a home-built general-purpose CMDS data processing package available for public download[46].

5.2.5 Results

Here we present the principal experimental results of this work. We show two dimensional frequency-frequency slices through our three dimensional frequency space, including IR-IR and IR-Visible scans. We also explore the dependence of our fully coherent signal on pulse delay.

Since TRSF is homodyne detected, the intensity scales quadratically as the third order nonlinear susceptibility, $|\chi^{(3)}|^2$ (5.2). We therefore plotted the square root of our measured intensity (the amplitude), to provide a linear relationship to $\chi^{(3)}$ and to other experiments like absorption spectroscopy.

Linear

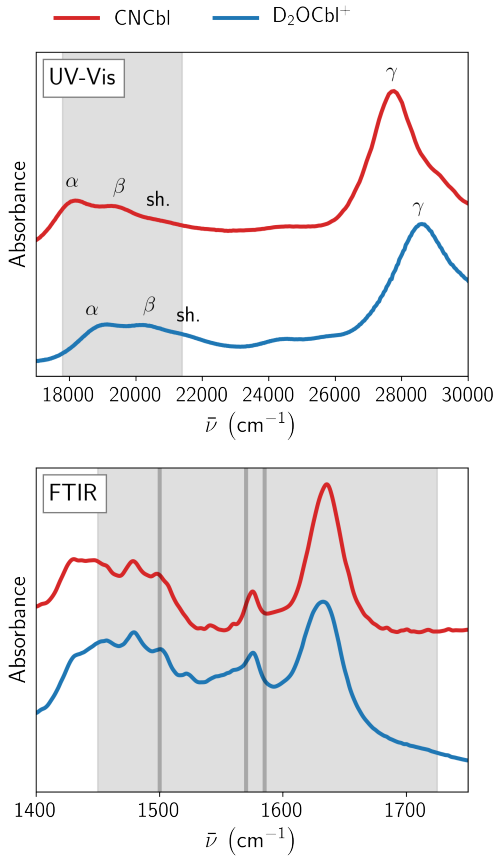

Figure 5.4: Room temperature linear spectroscopic data of CNCbl (red) and D_2OCbl^+ (blue) in D_2O. (Above) UV-vis absorption spectra showing the α, β, shoulder (sh.) and γ transitions. The scanning region in this work is marked by the gray area and extends across the α/β bands of both cobalamins. (Below) FTIR spectra with the electronically enhanced vibrational modes at 1500, 1570, and 1585 cm^{-1} marked by vertical gray lines. These same gray lines appear on all subsequent spectra. The spectra are offset for clarity.

The linear UV-vis and FTIR absorption spectra of the CNCbl and D_2OCbl^+ samples used in this work are shown in Figure 5.4. The electronic absorption spectra (Figure 5.4 top) have a broad multi-peaked feature in the visible region called the α/β bands, in which the lower-energy peak is the α-band and the middle peak is the β-band, along with a possible third higher-energy peak that appears as a shoulder. The α/β band electronic states are coupled to long-axis vibrational modes. There is also a strong feature to the blue called the γ-peak that is coupled to short-axis vibrational modes[3, 21]. The features in the visible absorption spectrum of D_2OCbl^+ are blue-shifted by $\sim$600 cm^{-1} from CNCbl. The TRSF frequency scanning range is highlighted in gray in Figure 5.4.

The FTIR spectrum identifies IR active vibrational modes that can act as intermediate vibrational states in the TRSF pathway (Figure 5.4, bottom). Park et al. labeled the 1500 cm^{-1} feature $\nu_s(\#1)$ and the 1580 cm^{-1} feature ν_{as}[21]. $\nu_s(\#1)$ was assigned to a totally symmetric corrin ring mode involving stetching motion along the long axis (LA, Figure 5.1) of the corrin ring, and ν_{as} was assigned to an asymmetric corrin ring stretching mode along the short axis (SA, Figure 5.1) of the corrin ring together with scissor and wagging motions of the outer ring methyl groups. The long axis mode $\nu_s(\#1)$ is hereafter referred to as ν_s(LA). The strong peak from 1600 - 1700 cm^{-1} has been tentatively assigned to a mode involving motion of the acetamide and propionamide groups on the outer corrin ring[105, 106]. The vertical lines in Figure 5.4 indicate the vibrational modes enhanced by TRSF: ν_s(LA) at 1500 cm^{-1} and unidentified modes at 1570 cm^{-1} and 1585 cm^{-1}. These same gray lines appear on all subsequent spectra.

IR-IR

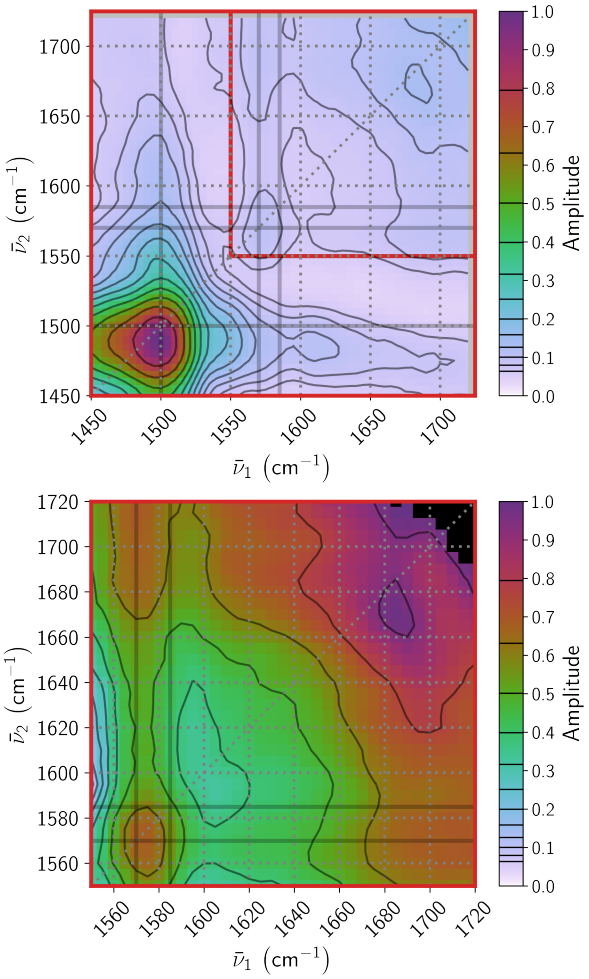

Figure 5.5: (Top) The TRSF spectrum of CNCbl scanning $\bar{\nu}_1$ and $\bar{\nu}_2$ with $\bar{\nu}_{TRSF}$ = 20,000 cm^{-1} at complete pulse overlap. (Bottom) The TRSF spectrum of the boxed region on the top plot focusing on the region around ν_{as}(SA). The bottom spectrum was collected seperately from the top spectrum. The signal above 1650 cm^{-1} is due to solvent. Black contour lines with logarithmic spacing highlight low-amplitude features. The black pixels in the top right corner of the lower figure show data points above the color bar upper limit. The vibrational modes at 1500, 1570, and 1585 cm^{-1} are marked in gray horizontal and vertical lines.

Figure 5.5 shows the 2D vibrational TRSF spectrum of CNCbl in D_2O with the output frequency fixed at 20,000 cm^{-1}. That frequency is higher than that of the α/β feature. As mentioned in the introduction, the visible pulse frequency, $\bar{\nu}_3$, was changed as well to maintain the relationship $\bar{\nu}_{TRSF} = \bar{\nu}_1 + \bar{\nu}_2 + \bar{\nu}_3$. All three pulses are overlapped in time with $\tau_{13} = \tau_{23} = 0$ ps. There is an intense feature along the diagonal ($\bar{\nu}_1 = \bar{\nu}_2$) in Figure 5.5 at 1500 cm^{-1}. Because the dynamic range of our data is large, we draw black contour lines with logarithmic spacing to highlight low-amplitude features. The lower panel of Figure 5.5 shows the same 2D vibrational region, collected seperately, with the spectral range constrained to avoid the intense feature at 1500 cm^{-1}. Two new on-diagonal features can be seen in this higher-energy region: a cobalamin vibrational mode at 1570 cm^{-1} and a feature at 1680 cm^{-1} that we attribute to D_2O solvent (see Supporting Information).

The 2D-TRSF vibrational spectrum identifies the IR modes that are coupled to each other and coupled with an electronic resonance at $\bar{\nu}_{TRSF}$. Features along the diagonal ($\bar{\nu}_1 = \bar{\nu}_2$) correspond to vibrational overtone states with one IR pulse exciting the fundamental mode, v, and the other IR pulse exciting the overtone, $2v$. Cross-peaks ($\bar{\nu}_1 \neq \bar{\nu}_2$) correspond to combination bands where v and $v + v'$ are excited. As seen in Figure 5.5, TRSF signal is observed at IR frequencies corresponding to the overtones of the 1500 cm^{-1} symmetric stretch ν_s(LA) and the 1570 cm^{-1} mode, indicating coupling between the overtone of these vibrational modes and an electronic state at 20,000 cm^{-1}. The amplitude of the peak at 1500 cm^{-1} is 10$\times$ greater than that of the peak at 1570 cm^{-1}, which is in agreement with the resonance Raman intensities of these modes at a similar excitation frequency[21]. No cross peaks are seen between the 1500 and 1570 cm^{-1} modes showing that those two modes are not coupled in this pathway.

Note that the spectrum does not include a feature from the carbonyl stretch at 1630 cm^{-1} or from the states in the congested region below 1500 cm^{-1} in the FTIR spectrum. The absence of these features is attributed to the lack of electronic coupling to these vibrational modes. The electronic excitations involving molecular orbitals localized on the carbonyl moieties occur in the UV[107], and the modes in the congested low energy region are also not coupled to electronic states in this region. The absence of uncoupled vibrational peaks allows for the deconvolution of congested vibrational spectra using resonance enhancement, as shown in previous studies[6].

IR-IR-delay

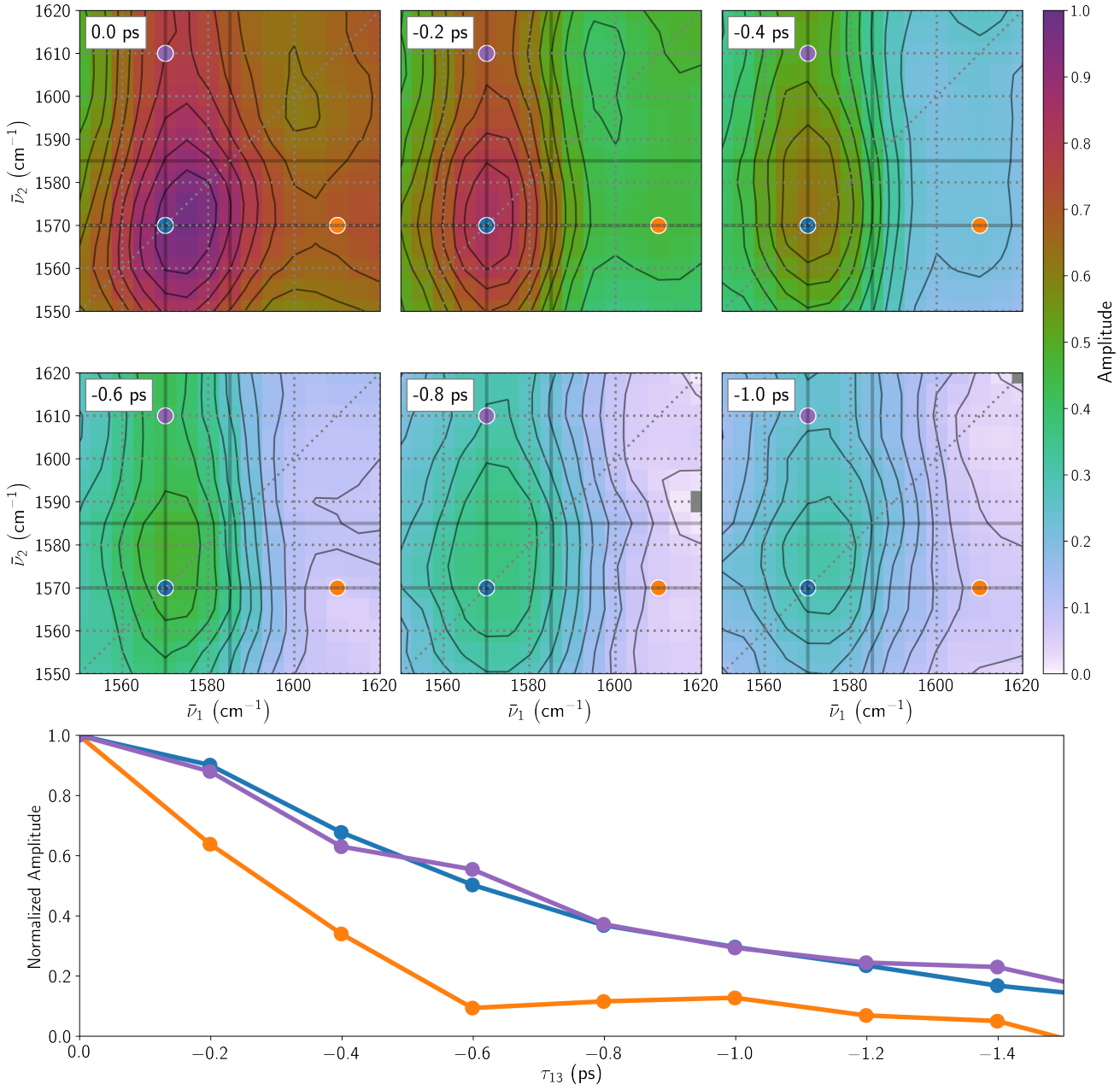

Figure 5.6: (Top) The TRSF spectrum of the region of the 1570 cm^{-1} mode of CNCbl along a 2DIR axis scanning τ_{13} from 0 to -1 ps showing the evolution of the line shape as a function of coherence dephasing, with $\bar{\nu}_{TRSF}$ fixed at 20,000 cm^{-1}. (Bottom) The time evolution of normalized amplitude at $\bar{\nu}_1, \bar{\nu}_2$ = 1570,1570 cm^{-1} (blue), $\bar{\nu}_1, \bar{\nu}_2$ = 1610,1570 cm^{-1} (orange), and $\bar{\nu}_1, \bar{\nu}_2$ = 1570,1610 cm^{-1} (purple).

Measurement of the coherent dynamics provides more insight into the nature of the spectral features in Figure 5.5. Figure 5.6 shows how the IR-IR spectrum changes as delays between the excitation pulses are scanned. In this figure, τ_{13} is the delay time between pulses 1 and 3 (See Figure 5.2). It was scanned from 0 to -1 ps while $\tau_{23} = 0$. Negative time delays indicate that pulse 1 arrives first, followed by pulses 2 and 3. Since $\bar{\nu}_1$ targets the fundamental mode frequency of the 1570 cm^{-1} mode, τ_{13} probes the dephasing dynamics of the single quantum coherence involving the fundamental mode. $\bar{\nu}_2$ measures the overtone/combination band frequency. The lower graph shows the transients at the excitation frequencies defined by the colored dots. The amplitude of the overtone peak (blue dot) and the off-diagonal feature at $\bar{\nu}_1, \bar{\nu}_2$ = 1570,1610 cm^{-1} (purple dot) both decay more slowly than the amplitude at $\bar{\nu}_1, \bar{\nu}_2$ = 1610,1570 cm^{-1} (orange dot). This difference results because the transients of the diagonal feature and the off-diagonal feature at $\bar{\nu}_1$ = 1570 cm^{-1} decay at the dephasing rate of the vibrational coherence created by $\bar{\nu}_1$ while the amplitude at $\bar{\nu}_1$ = 1610 cm^{-1} decays within the temporal width of the excitation pulse width. This result shows that the initially excited coherence dephasing rate at the cross peak (orange dot) is faster than the excitation pulse. This rapid dephasing is consistent with a fully driven non-resonant polarization. The vibrational coherence lifetime of the 1570 cm^{-1} mode is derived from the transient signal to be 0.61$\pm$0.05 ps (see Supporting Information)[108].

(IR=IR)-Visible

We now explore coupling between vibrational and electronic states. Figure 5.7 shows the 2D (IR=IR)-Visible TRSF spectra of CNCbl and D_2OCbl^+ in D_2O solvent with temporally overlapped excitation pulses. Here, $\bar{\nu}_1 = \bar{\nu}_2$ such that only the vibrational overtone states are excited. Figure 5.7 is equivalent to taking diagonal slices along the 2D vibrational spectrum in Figure 5.5 and scanning against $\bar{\nu}_{TRSF}$. This representation covers the α/β-bands and the three vibrational modes of interest (gray lines). For comparison, the absorption and FTIR spectra are reproduced above and to the right of the 2D (IR=IR)-visible plots so the TRSF spectrum can be easily compared with the vibrational and electronic absorption spectra.

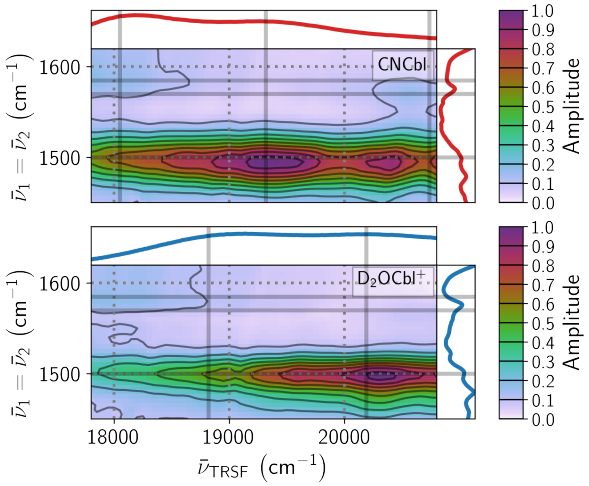

Figure 5.7: TRSF spectra of CNCbl (top) and D_2OCbl^+ (bottom) along the (IR=IR)-visible axis. $\bar{\nu}_1 = \bar{\nu}_2$ is scanned against $\bar{\nu}_{TRSF}$ with $\bar{\nu}_3$ tracking such that $\bar{\nu}_1 + \bar{\nu}_2 + \bar{\nu}_3 = \bar{\nu}_{TRSF}$. The UV-Vis and FTIR absorption spectra are plotted above and on the right. The vibrational modes at 1500, 1570, and 1585 cm^{-1} are marked by gray horizontal lines, and the α and β electronic transitions are highlighted by gray vertical lines.

In the CNCbl TRSF spectrum (Figure 5.7, top), ν_s(LA) at 1500 cm^{-1} is strongly enhanced across the α/β region. It is most intense at 19,400 cm^{-1}. Due to the limitations of the scanning range, only the lower-energy portion of the α/β region of the D_2OCbl^+ TRSF spectrum (Figure 5.7 bottom row) was accessible. ν_s(LA) at 1500 cm^{-1} is strongly enhanced and appears to be most intense at 20,300 cm^{-1}. In each species, ν_s(LA) is strongly and broadly enhanced across the α/β region, peaking at the β band, and mimicing the blue shift of the α/β band in the corresponding absorption spectra.

3D-TRSF scans of the ν_{as}(SA) region

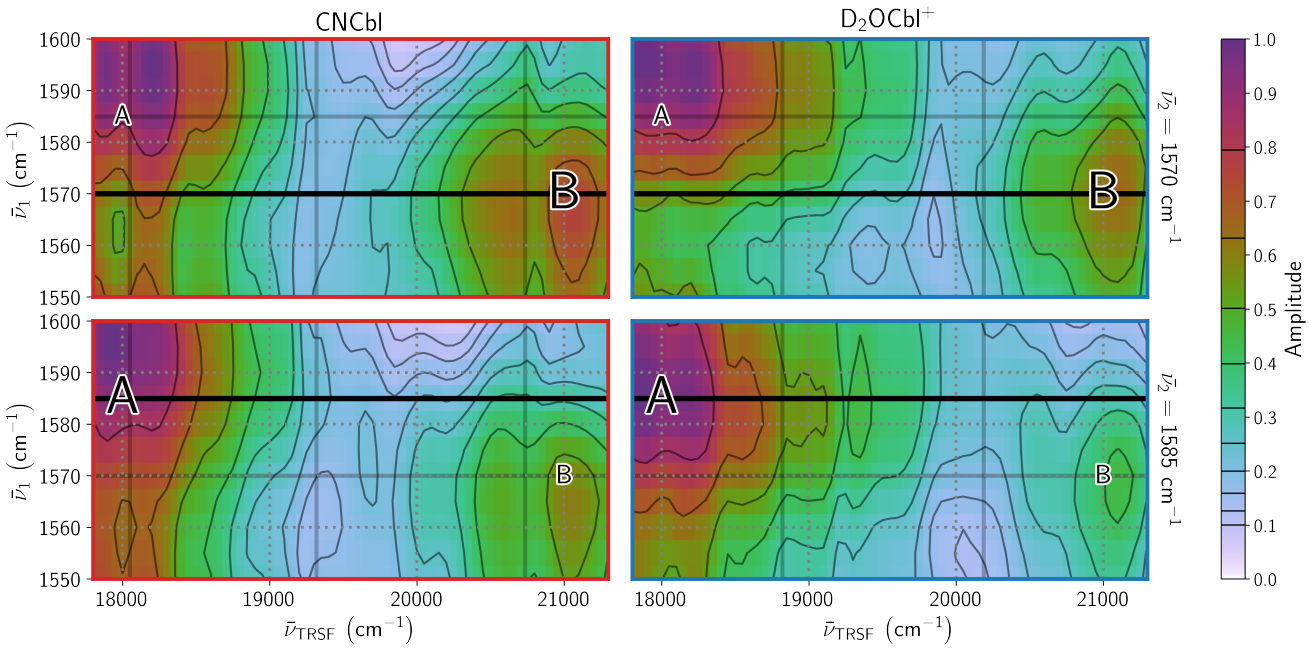

Figure 5.8: TRSF spectrum of CNCbl (left) and D_2OCbl^+ (right) along the IR-visible axis with $\bar{\nu}_1$ scanned against $\bar{\nu}_{TRSF}$. $\bar{\nu}_2$ is fixed at 1570 cm^{-1} (top) and 1585 cm^{-1} (bottom), as indicated by the black horizontal line, to excite the fundamental mode of ν_{1570}. The gray vertical lines show the α, β, and shoulder peaks, and the horizontal lines show the 1570 and 1585 cm^{-1} vibrational modes. The color bar is normalized to the strongest feature of each plot.

In addition to the dominant feature at ν_s(LA), there are two other vibrational-electronic cross peaks in the 3D frequency spectra of each sample with vibrational resonances at 1570 cm^{-1} and 1585 cm^{-1}. Both modes fall in the region where resonance Raman experiments identified a short axis mode, although neither of them occur at the asymmetric stretch frequency of 1580 cm^{-1}[21]. We label the unassigned modes as ν_{1570} and ν_{1585}.

Figure 5.8 omits the intense ν_s(LA) feature and focuses on the region where these two other cross peaks appear. Here, $\bar{\nu}_1$ and $\bar{\nu}_{TRSF}$ are scanned with $\bar{\nu}_2$ being fixed at 1570 cm^{-1} (top) and 1585 cm^{-1} (bottom) in order to resonantly enhance the two unassigned modes. The fixed value of $\bar{\nu}_2$ is represented by the black horizontal line. The scan range of $\bar{\nu}_{TRSF}$ is expanded compared to Figure 5.7.

Neither ν_{1570} nor ν_{1585} is coupled to the electronic state at 19,400 cm^{-1} (or 20,200 cm^{-1} in D_2OCbl^+) where ν_s(LA) is most strongly enhanced. ν_{1585} is coupled to an electronic feature at $<$18,500 cm^{-1}. We label this cross peak feature A. ν_{1570} is coupled to an electronic feature at $>$20,300 cm^{-1}. We label this cross peak feature B. Neither feature is fully captured over the available spectral range so the peak frequency may lie somewhat outside the scan range and the peak widths cannot be directly observed. Also, due to the limited scanning window, we cannot say whether these electronic states are shifted in D_2OCbl^+ compared to their CNCbl counterparts.

Because ν_{1570} and ν_{1585} are so close in frequency, the four 2D spectra in Figure 5.8 all contain some signal from both features. Feature A is the most intense feature, regardless of whether $\bar{\nu}_1$ and $\bar{\nu}_2$ are resonant with the two vibrational modes. Despite this congestion, the separate electronic enhancement profiles of ν_{1570} and ν_{1585} can clearly be seen by comparing the top and bottom rows of Figure 5.8. The labels of the resonant feature in each subplot have been enlarged to guide the eye. The detection of features A and B demonstrates the ability of TRSF to selectively enhance vibrational modes coupled to specific electronic transitions.

Phase-mismatch and filter etalon effects

The 3D-TRSF and (IR=IR)-visible spectra contain artifacts due to phase-mismatch within the sample cell windows, which result in a rising background towards the blue and red ends of the $\bar{\nu}_{TRSF}$ axis, and

a dip in the middle of the spectrum ($\bar{\nu}_{TRSF}$ ~19,500 cm^{-1}). These effects are described in greater detail in a separate publication.[48] Additionally, there are etalon effects in spectral filters that result in ~300 cm^{-1} oscillations along $\bar{\nu}_3$. The etalon oscillations create the appearance of substructure such as a shoulder peak at ($\bar{\nu}_1 = \bar{\nu}_2$, $\bar{\nu}_{TRSF}$) = (1500, 20,400) cm^{-1} (Figure 5.7) and double peaks in the feature at (1570, >20,300) cm^{-1} in CNCbl, and a progression of narrow peaks at ($\bar{\nu}_1 = \bar{\nu}_2$, $\bar{\nu}_{TRSF}$) = (1570, >20,800) cm^{-1} and (1585, <19,100) cm^{-1} (Figure 5.8) in D_2OCbl^+. The oscillations are clearer in the 1D slice representation across $\bar{\nu}_{TRSF}$ at fixed IR excitation frequencies in Figures 5.9 and 5.10. The artifacts have minimal impact on the interpretation of the spectra and are discussed further in the Supporting Information.

5.2.6 Discussion

Here we discuss the implications of this 3D-TRSF experiment for the assignment of electronic transitions within the α/β region of cob(III)alamins. Mirroring the Results section, we first focus on the intense feature coupled to the ν_s(LA) mode. We then describe the behavior of the higher-energy ν_{1570} and ν_{1585} modes. Finally, we discuss possible models of cob(III)alamin electronic structure that are consistent with our entire three-dimensional experimental data.

ν_s(LA)

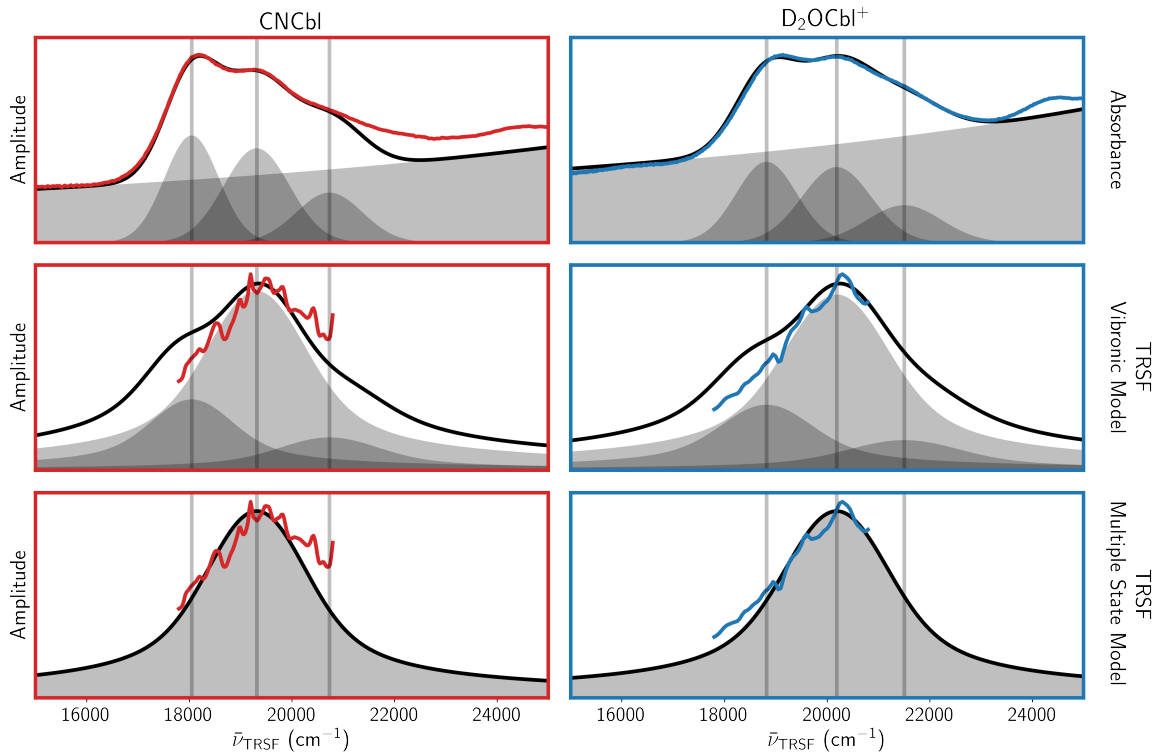

Figure 5.9: A comparison of the vibronic model and multiple state model against the absorption spectra (top row) and TRSF electronic enhancement spectrum of the vibraitonal mode ν_s(LA). The experimental TRSF spectra are compared to the simulated TRSF spectra of the vibronic model (middle) and multiple state model (bottom). CNCbl is shown in the left column and D_2OCbl^+ is shown in the right column. The red (CNCbl) and blue (D_2OCbl^+) traces show the experimental data, the black traces show the simulated spectra, and the gray-filled Gaussians show the vibronic/electronic states. The absorption spectra include a rising background to account for the cumulative effects of detuned high energy states.

Here we discuss the electronic dependence of ν_s(LA). Previous resonance Raman studies have found that ν_s(LA) is coupled to the π-HOMO$\rightarrow$ π*-LUMO transition in the α/β region[3, 21]. Using TRSF, we observe this same enhancement and measure its line shape with higher resolution compared to resonance Raman spectrum. We consider the two electronic structure models to explain the multiple features within the α/β bands: a vibronic progression model[3] and a multiple electronic state model[18, 93]. Figure 5.9 compares each model to the $\bar{\nu}_{TRSF}$ trace with $\bar{\nu}_1 = \bar{\nu}_2$ resonant with ν_s(LA).

We start our analysis by fitting the absorption spectrum to three Gaussian-shaped transitions (top row). An off-set Lorentzian is used to account for the rising absorptive background. The relative integrated amplitudes of our three Gaussians agree with a Franck-Condon vibronic progression with excited state offset $\Delta = 1.47$ for CNCbl and $\Delta = 1.50$ for D_2OCbl^+. The center and FWHM of each transition was chosen to provide best agreement with the absorption spectrum. We use these same three Gaussian transitions to model the TRSF line shape.

Given the peak positions and Δ from the absorption spectrum, there are several necessary steps to calculate the TRSF spectrum. First, the Franck-Condon overlap integrals are not the same between absorption and TRSF. In absorbance, the overlap scales according to the transitions $g \rightarrow e, g \rightarrow e + v, g \rightarrow e + 2v$, etc. The $g \rightarrow e$ transition at the α transition is the strongest. In contrast, TRSF involves an anti-Stokes Raman-like transition which starts at $g + 2v$. The TRSF Franck-Condon overlap scales according to the transitions $g + 2v \rightarrow e, g + 2v \rightarrow e + v, g + 2v \rightarrow e + 2v$, etc followed by the transitions returning to the ground state. The TRSF Franck-Condon overlap is highest at the β transition. This gives good agreement to our expermental result, as shown in the second row of Figure 5.9. Second, the TRSF line shape is also complicated by the homodyne-detected nature of the experiment. The three resonances must be allowed to interfere on the amplitude level before the magnitude is taken. See the Supporting Information for a description of this analysis, including all extracted parameters. Notably, the peak widths broaden with each subsequent transition from the α to the shoulder peak.

The TRSF slice also agrees quite well to the β state alone, as shown in the bottom row of Figure 5.9. The peak position and line width are unchanged from the absorption analysis. This is consistent with a model in which the three transitions are derived from three separate electronic states, of which

only the β transition couples to ν_s(LA). However, resonance Raman excitation profile experiments on H_2OCbl^+ by Stich et al.[3] show the 1500 cm^{-1} mode is most strongly enhanced in the region of the α band. This single-β transition model, which requires the 1500 cm^{-1} mode to be coupled solely to the β band transition, is therefore not reconcilable with resonance Raman results, which shows maximum enhancement at the α band.

It is clear that ν_s(LA) is most strongly coupled to the β feature, which is consistent with both the vibronic and multiple state model. By comparing the two models to the TRSF spectrum alone, we are unable to distinguish between the vibronic model or the multiple state model shown in Figure 5.3. However, the vibronic model is consistent with both TRSF and resonance Raman results, while the single-β state model contradicts published resonance Raman data. The differences between the two models would become clearer by expanding the visible scanning range to include the tails of the features.

ν_{1570} & ν_{1585}

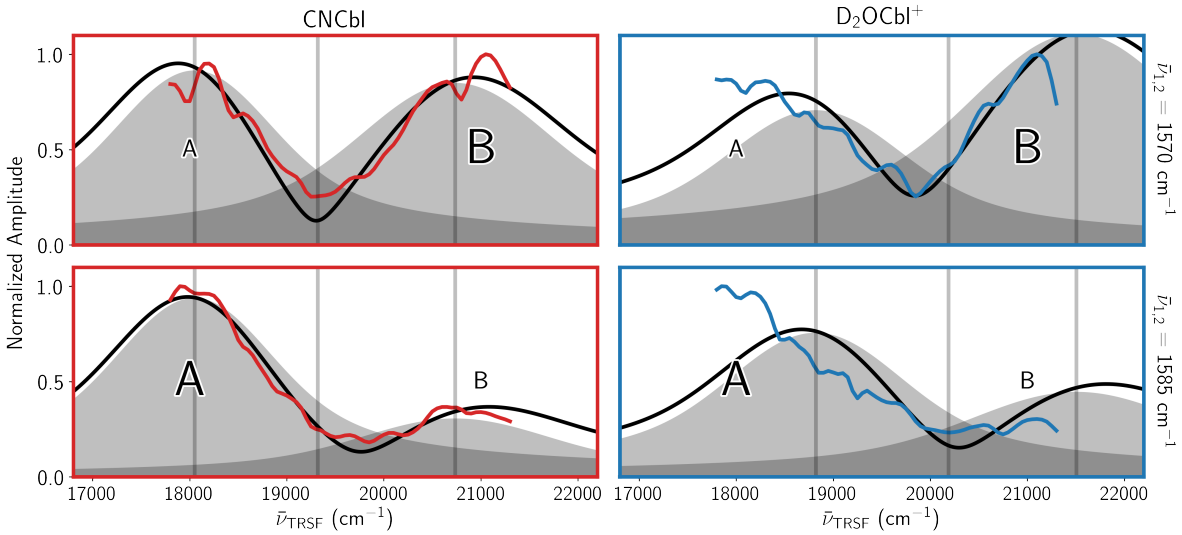

Figure 5.10: The electronic coupling of ν_{1570} (top) and ν_{1585} (bottom) to features A and B in CNCbl (left) and D_2OCbl^+ (right). The gray vertical lines show the α, β, and shoulder peaks. The gray peaks show the TRSF simulation of the shoulder peak (top) and the α peak (bottom).

The electronic coupling of the vibrational peaks in the region around ν_{1570} is shown in Figure 5.10 for both CNCbl and D_2OCbl^+. The top row shows the electronic coupling of ν_{1570}, resonant with feature A. The bottom row shows the electronic coupling of ν_{1585}, resonant with feature B. The horizontal black line within each subplot in Figure 5.8 marks the trace within the corresponding subplot in Figure 5.10. For each trace, $\bar{\nu}_1 = \bar{\nu}_2$ as in Figure 5.9.

Feature A is more intense than feature B in both samples. The two cross peaks are very close in vibrational frequency such that both features intersect both slices (see Figure 5.8). We assume that ν_{1570} is coupled only to the high energy electronic feature (B), and ν_{1585} is coupled only to the low energy electronic feature (A), as labeled in Figure 5.10. The labels of the resonant feature in each subplot have been enlarged to guide the eye. In each subplot, $\bar{\nu}_{TRSF}$ is the same as in Figure 5.8. The fast oscillations across $\bar{\nu}_{TRSF}$ are due to the filter etalon effects mentioned at the end of the Results section.

As we did with ν_s(LA), we compare the experimental TRSF spectra of ν_{1570} and ν_{1585} to three Gaussian transitions derived from the absorption spectrum in Figure 5.9 (top). The A and B cross peaks are not explained by a lone vibronic electronic state model which predicts a TRSF maximum at the β peak. We therefore compare each cross peak to the Gaussian transition that best agrees: feature A to the α peak, and feature B to the shoulder peak. We include both peaks in our model in Figure 5.10 due to the spectral overlap of the two vibrational modes. The amplitudes are chosen so that the sum (Figure 5.10 black line) best agrees with the TRSF result. Destructive interference between the two transitions "deepens" the valley between them, as can be seen when the black line dips below the gray filled regions.

Both features A and B in CNCbl and feature B in D_2OCbl^+ are consistent with the assignments of α to feature A and the shoulder to feature B. However, feature A of D_2OCbl^+ fits poorly to this model. This disagreement can be seen in both the D_2OCbl^+ slices in Figure 5.10, and in the 3D-TRSF spectra of D_2OCbl^+ in Figure 5.8. While the TRSF simulation does fit reasonably to most of the features in these slices, we do not scan over a wide enough range to make a definitive determination. We cannot experimentally determine the peak center and overall line shape for features A and B. The phase-mismatch effects create a rise in the background (see Supporting Information) towards the red and blue edge of the spectrum which obscures the line shapes and peak frequencies, and the etalon

oscillations further obscure the character of the peak envelope. The rising background affects the low intensity features A and B much more than the high intensity ν_s(LA)[48].

α/β Band Electronic Structure

In discussing our 3D-TRSF measurements, we considered several possible models of the α/β band structure. In Figure 5.9, we fit the absorption spectrum of each species to three Gaussian features, and compared the electronic enhancement spectrum of ν_s(LA) to a vibronic progression. We then compared these features to the electronic enhancement spectra of the three vibrational modes in the 3D-TRSF spectra (Figures 5.9 and 5.10).

Our results seem roughly consistent with a multiple electronic state model of the α/β band, where each of the three vibrations are coupled to a separate electronic state: ν_{1585} to α, ν_s(LA) to β, and ν_{1570} to shoulder. Refer to Figure 5.3 for a diagram of this model. Our electronic enhancement measurements are also consistent with an vibronic progression in the α/β region coupled to the 1500 cm^{-1} mode. The 1500 cm^{-1} mode that we resolve most cleanly is most enhanced by β, which is consistent with both models (see Figure 5.9). However, we retain a preference for the vibronic model due to previous resonance Raman experiments which disagree with the single-β transition model[3]. The high energy modes are clearly not coupled to a vibronic progression, but they may also be coupled to buried or heretofore unobserved electronic states rather than the α/β bands. In all three cases, our analysis cannot be definitive primarily because of the known artifacts and the available tuning range.

5.2.7 Conclusion

The ability of fully coherent multidimensional spectroscopies like TRSF to selectively enhance coupled vibrational and electronic/vibronic states provides new capabilities for resolving individual features within congested vibrational and electronic spectra. In this work, we have demonstrated this capability in CNCbl and D_2OCbl^+ where three vibrational states have been selectively enhanced by establishing electronic resonances within the α/β region of the electronic absorption spectrum. Similarly, three electronic and/or vibronic states have been selectively enhanced by establishing resonances with vibrational states. Work

continues on expanding the range of accessible vibrational and electronic states. CMDS methodologies such as TRSF spectroscopy, complementary techniques like Doubly Vibrationally Enhanced (DOVE) spectroscopy[109, 110, 67, 63, 35, 111, 12], and higher order methodologies[112, 113, 114], are likely to have wider application in the identification of reaction pathway potential energy surfaces that involve coupling between multiple vibrational and electronic states.

5.2.8 Acknowledgments

This work was supported by the National Science Foundation Division of Chemistry under Grant No. CHE-1709060 and Grant No. CHE-1710339 to T.C.B.

5.2.9 Appendix

Methods

Absorbance Measurements

UV-VIS absorbance experiments were performed using a Cary 50 benchtop spectrometer (Varian). FTIR absorbance was done using a Tensor 27 benchtop spectrometer (Bruker). All measurements were performed at room temperature with D_2O solvent.

TRSF system details

OPA1 ($\bar{\nu}_1$) is a Light Conversion TOPAS-800 with an NDFG "DF1" mixer stage. OPA2 ($\bar{\nu}_2$) is a Spectra-Physics OPA-800 with a $AgGaS_2$ DFG mixing crystal. OPA3 ($\bar{\nu}_3$) is a Spectra-Physics OPA-800C with a BBO mixing crystal (6mm thick, $\theta = 38^\circ$, $\phi = 0^\circ$, CASIX) for signal doubling. Within OPA3, prior to the mixing crystal long pass filters (Corning Glassworks 7-57) were used to isolate IR light. After mixing, a heat filter (Thorlabs NENIR550B) was used to reject remaining IR light after mixing, and a 550 nm long pass filter (Thorlabs FEL0550) was used to reject undesired mixing pathways.

After the sample and before the monochromator entrance slit, an 800 nm notch filter, a 610 nm (Asahi XVS0610) and either a 530 nm (Asahi XVS0530) reflective short-pass or 542 nm bandpass filter (50 nm width) filter spectrally reject the excitation beam. The monochromator tracks the expected TRSF output frequency and rejects light from other processes.

Data Processing

Once collected, TRSF data was processed and plotted using WrightTools, a general-purpose CMDS data processing package[46]. WrightTools is built on top of the Scientific Python ecosystem[115], and relies especially on numpy[116], scipy[115], h5py[117], and matplotlib[118]. These same tools were used for simulations and fitting work presented in this publication. The raw data and all associated processing, fitting, and simulation scripts used in this publication are available for public download.

5.2.10 Spectral artifacts

Solvent background

The spectrum in Figure 5.11 is the background signal that results from the third order susceptibility the sample cell windows and the D_2O. The background scan shows the non-resonant signal is a minimum at 19,500 cm^{-1}, rising continuously towards the red edge of the spectrum until 17,800 cm^{-1}. There is a minimum of the signal in the region near 20,100 cm^{-1} and the signal rises in both directions as a function of $\bar{\nu}_{TRSF}$. The background is constant as a function of $\bar{\nu}_1$.

A full IR-IR-visible scan of the solvent D_2O shows that the non-resonant signal generated by the solvent and windows rises towards the red and blue end of the spectrum and dips in the middle at $\sim$ 19,500 cm^{-1}. This effect is due phase-mismatch in the CaF_2 windows of the sample cell which interferes with and either amplifies or suppresses the solvent and cobalamin generated signal. The changes result because the TRSF process cannot be phase matched so the wave length of the nonlinear polarization is shorter than the wave length of the field that it creates. The phase mismatch creates fringes within the sample cell that oscillate with a spatial period that is longer than the sample thickness but shorter

than the window thickness. The intensity variation in the figure results from the changing interference effects between the phase mismatch in the windows and the sample. These effects are described in greater detail in a separate publication.[48]

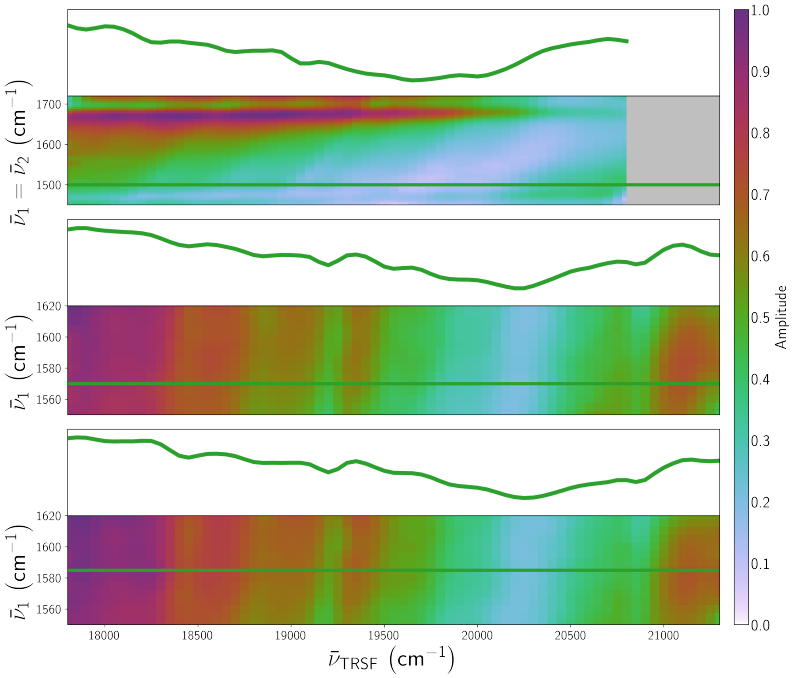

Figure 5.11: TRSF spectrum of D_2O along the IR-visible axis. Top: $\bar{\nu}_1 = \bar{\nu}_2$ is scanned across the IR frequency region against $\bar{\nu}_{TRSF}$. Middle: $\bar{\nu}_1$ is scanned in the region around ν_{as}(SA) against $\bar{\nu}_{TRSF}$ with $\bar{\nu}_2 = 1570$ cm^{-1}. Bottom: $\bar{\nu}_1$ is scanned in the region around ν_{as}(SA) against $\bar{\nu}_{TRSF}$ with $\bar{\nu}_2 = 1585$ cm^{-1}. The sideplots show slices of the 2D spectra along the horizontal green lines. In each spectrum, $\bar{\nu}_3$ tracking such that $\bar{\nu}_1 + \bar{\nu}_2 + \bar{\nu}_3 = \bar{\nu}_{TRSF}$, and $\tau_{13} = \tau_{23} = 0$ ps. The sample pathlength is 25 μm and the sample cell windows are 300 μm thick.

550 lp filter

The TRSF spectra of both CNCbl and D_2OCbl show fast oscillations with a periodicity of about 300 cm^{-1} across the $\bar{\nu}_{TRSF}$ axis, resulting in the features appearing to have shoulder peaks. Examples of such features include the double peak at 20,600 and 21,100 cm^{-1} at $\bar{\nu}_1 = \bar{\nu}_1 = 1570$ cm^{-1} for both CNCbl and D_2OCbl^+ (Figure 8 of the main text), and the shoulder peaks at 18,700 and 20,400 cm^{-1} at $\bar{\nu}_1 = \bar{\nu}_1 = 1500$ cm^{-1} for CNCbl (Figure 7 of the main text). These oscillations are artifactual and due to interference effects caused by étalon effects in the dielectric films of long and short pass filters used to reject higher order processes produced in OPA3. The absorption spectra of the filters in the scanning region in Figure 5.12 show that the transmissivity modulates with frequency.

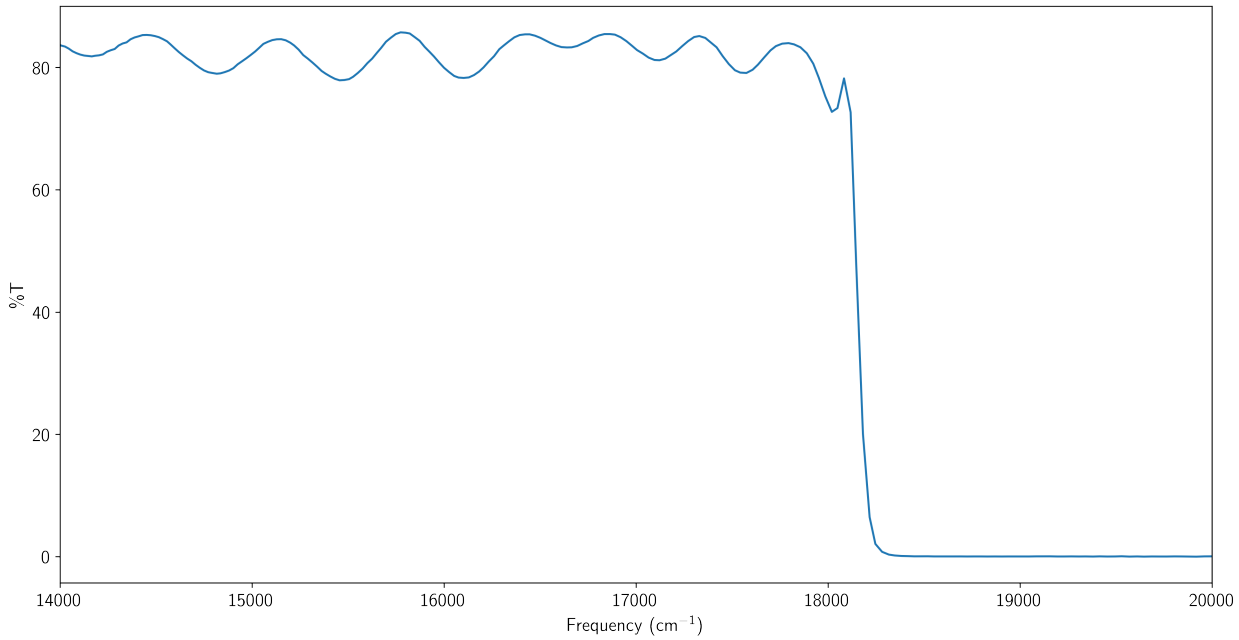

Figure 5.12: The absorption spectrum of the 550 nm long pass filter (550LP) used to reject higher order processes from the visible excitation field Pulse 3. The oscillatory behaviour in transmissivity is due to étalon effects in the dielectric coating of the filter. While the effects of coating on the ultrafast pulses are not straightforward, we can attribute the fast oscillations across $\bar{\nu}_{TRSF}$ to the filter as removal of the filter also removes the oscillations.

Glass background

Figures 5.13 and 5.14 show non-resonant background scans of the same frequency regions plotted along the $\bar{\nu}_{TRSF}$ output axis and the $\bar{\nu}_3$ visible excitation axis respectively. The background scans demonstrate the reproducibility of the fast oscillations regardless of the sample and show they correlate to $\bar{\nu}_3$.

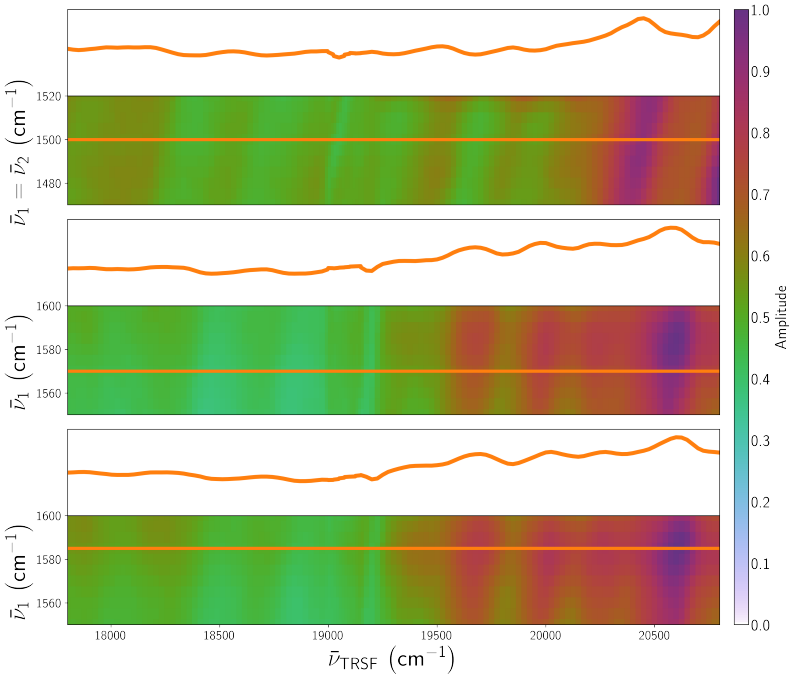

Figure 5.13: The non-resonant TRSF spectrum of a mid-IR absorbant glass slide along the IR-visible output axis. Top: $\bar{\nu}_1 = \bar{\nu}_2$ is scanned in the region around ν_s(LA) against $\bar{\nu}_{TRSF}$. Middle: $\bar{\nu}_1$ is scanned in the region around ν_{as}(SA) against $\bar{\nu}_{TRSF}$ with $\bar{\nu}_2 = 1570$ cm^{-1}. Bottom: $\bar{\nu}_1$ is scanned in the region around ν_{as}(SA) against $\bar{\nu}_{TRSF}$ with $\bar{\nu}_2 = 1585$ cm^{-1}. The sideplots show slices of the 2D spectra along the horizontal orange lines. In each spectrum, $\bar{\nu}_3$ tracking such that $\bar{\nu}_1 + \bar{\nu}_2 + \bar{\nu}_3 = \bar{\nu}_{TRSF}$, and $\tau_{13} = \tau_{23} = 0$ ps. These spectra show that the fast oscillations seen in the cobalamin spectra are due to instrumental response effects.

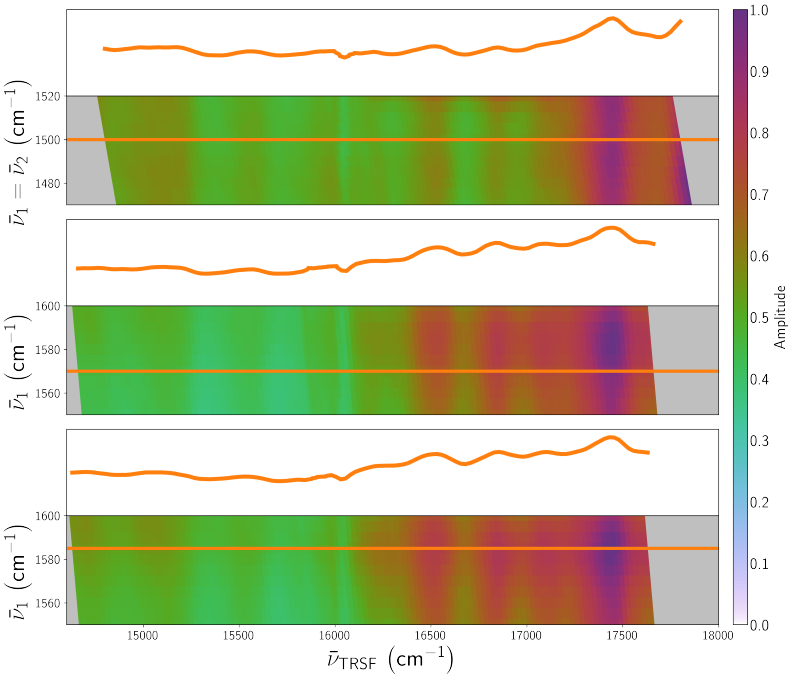

Figure 5.14: The non-resonant TRSF spectrum of a mid-IR absorbant glass slide transformed along the IR-visible excitation frequency ($\bar{\nu}_3$) axis. Top: $\bar{\nu}_1 = \bar{\nu}_2$ is scanned in the region around ν_s(LA) against $\bar{\nu}_{TRSF}$. Middle: $\bar{\nu}_1$ is scanned in the region around ν_{as}(SA) against $\bar{\nu}_3$ with $\bar{\nu}_2 = 1570$ cm^{-1}. Bottom: $\bar{\nu}_1$ is scanned in the region around ν_{as}(SA) against $\bar{\nu}_3$ with $\bar{\nu}_2 = 1585$ cm^{-1}. The orange horizontal lines mark the fixed $\bar{\nu}_2$. In each spectrum, $\bar{\nu}_3$ tracking such that $\bar{\nu}_1 + \bar{\nu}_2 + \bar{\nu}_3 = \bar{\nu}_{TRSF}$, and $\tau_{13} = \tau_{23} = 0$ ps. These spectra show the instrumental response function in the absence of resonant enhancement or phase-mismatch effects and show that the fast oscillations originate from the visible excitation pulse $\bar{\nu}_3$.

Thin layer Cobalamin

Figure 5.15 shows a 3D frequency scan of the same frequency region a thin layer of dry CNCbl on a mid-IR absorbant glass slide that was taken when all three excitation pulses were temporally overlapped. The peak positions of the CNCbl solution in a sample cell are almost identical to those of a thin layer of solid CNCbl on a glass slide in Figure 5.15. The glass slide is non-transmissive across the mid-IR region, such that the IR excitation fields are completely absorbed and produce no non-linear signal, thus removing the phase-mismatch effects. The similarity of the CNCbl spectrum with and without the phase-mismatch background effects shows that the TRSF spectrum in the region around 1570 cm^{-1} is minimally affected by the sample cell window related artifacts.

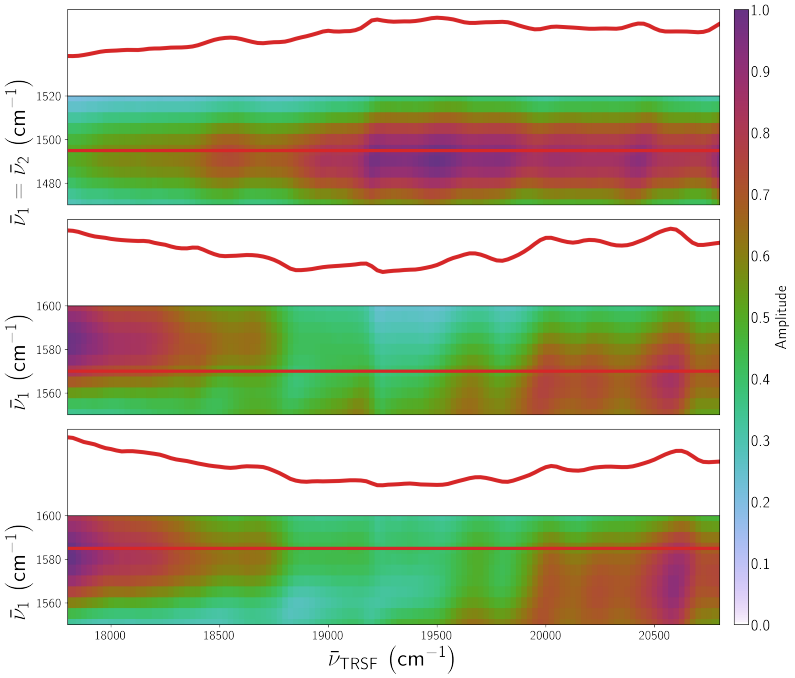

Figure 5.15: TRSF spectrum of a thin layer of dry CNCbl on a mid-IR absorbant glass slide along the IR-visible axis. Top: $\bar{\nu}_1 = \bar{\nu}_2$ is scanned in the region around ν_s(LA) against $\bar{\nu}_{TRSF}$. Middle: $\bar{\nu}_1$ is scanned in the region around ν_{as}(SA) against $\bar{\nu}_{TRSF}$ with $\bar{\nu}_2 = 1570$ cm^{-1}. Bottom: $\bar{\nu}_1$ is scanned in the region around ν_{as}(SA) against $\bar{\nu}_{TRSF}$ with $\bar{\nu}_2 = 1585$ cm^{-1}. The sideplots show slices of the 2D spectra along the horizontal red lines. In each spectrum, $\bar{\nu}_3$ tracking such that $\bar{\nu}_1 + \bar{\nu}_2 + \bar{\nu}_3 = \bar{\nu}_{TRSF}$, and $\tau_{13} = \tau_{23} = 0$ ps. The electronic and vibrational resonance frequencies of states A, B, and C do not change from the solution phase spectra of CNCbl.

5.2.11 Fitting

Delay

The data presented in this section is the same data presented in Figure 6 in the main body, showing an alternative representation and displaying the model used to find the coherence lifetime, τ.

Wigner Scan

The 3D data set can be integrated along $\bar{\nu}_2$. Figure 6 of the main text shows that the diagonal and off-diagonal traces at $\bar{\nu}_1 = 1570$ cm^{-1} have identical relative lifetimes. This view shows a clear resonance centered at $\bar{\nu}_1 = 1570$ cm^{-1} which has a a much longer lifetime than the non-resonant signal. Note that a resonance is not seen at $\bar{\nu}_1 = 1585$ cm^{-1} because it is not coupled to the electronic transition, 20,000 cm^{-1}.

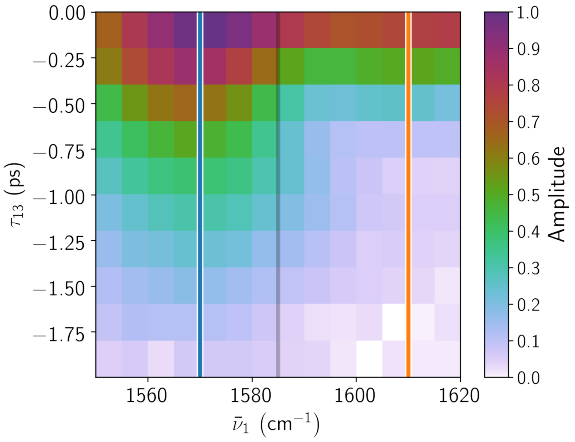

Figure 5.16: Three dimensional IR-IR-Delay dataset, integrated along $\bar{\nu}_2$, the temporally static IR axis. Blue and orange lines show the positions of the traces used in Figure 5.17. The blue and gray vertical lines show the positions of the resonances found in CNCbI.

Transient Deconvolution

In order to extract the coherence lifetime, the resonant and non-resonant traces were fit to a model. The non-resonant simulation is a convolution of a Gaussian peak with its square (as pulses $\bar{\nu}_2$ and $\bar{\nu}_3$ are not moving relative to each other). The resonant simulation is the same, with an additional convolution of an exponential decay function times a Heaviside step function.

In all, there were three parameters allowed to fit the model: the FWHM of the incident laser pulses, the offset of the peak of the non-resonant simulation relative to the point called zero-delay in the experiment, and the lifetime of the exponential decay function. A fourth parameter, controlling the proportion of non-resonant signal to be added to the resonant simulation, was considered but found to always go to the minimum allowed value (or negative, which is non-physical). That parameter was therefore dropped, but may be important in similar models with more data points.

The offset parameter was needed because the crest of the peaks were not observed in the original data. If we assume that the non-resonant peak is at experimental zero, its points can be reasonably fit, however the resultant resonant simulation is not well fit, as shown in the first panel of Figure 5.17. A pulse width of 0.5 ps is required to fit the data without an offset. This width does not reasonably agree with our excitation sources. For this reason, the model allows for the calibration of the zero point to be offset by a constant.

Note that, in part due to the data not capturing both sides of the peak, there is a wide range of values for which a reasonably good fit can be made using this model. We incorporate external knowledge of the pulse width of our lasers to select a range deemed plausible for the fit parameters. The lasers used are nominally 1 ps FWHM. The overall best fit for the model is at 1.01 ps, in close agreement with the expected value. The range for τ of 0.61 +/- 0.05 ps was determined by selecting a cutoff for the 1/cost function which encapsulated the uncertainty in pulse width. This range is slightly asymmetric about 0.61 ps, spanning 0.57 to 0.66 ps, thus the larger of the two deviations was chosen as the reported uncertainty.

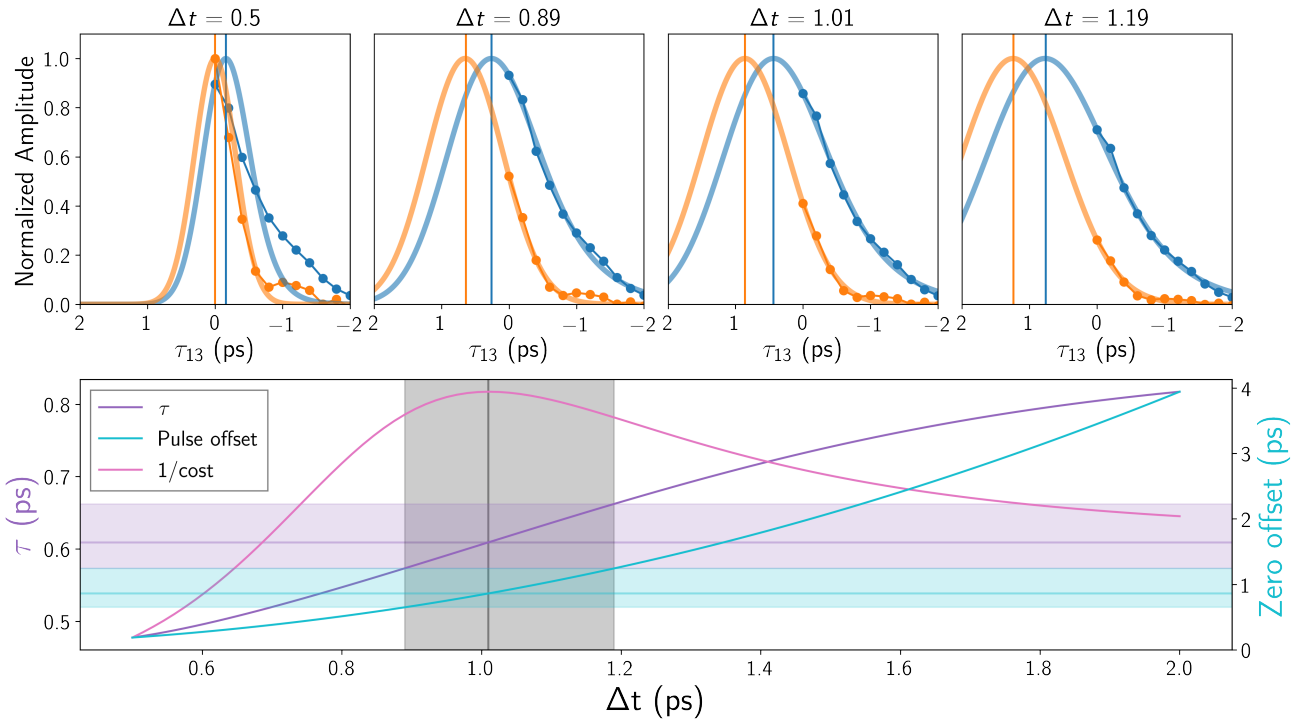

Figure 5.17: Deconvolution of coherence lifetime of v_{as}(LA). The solid blue and orange dots are the experimental time evolution of normalized amplitude at $\bar{\nu}_1 = 1570$ cm^{-1} (Resonant signal, blue), $\bar{\nu}_1 = 1610$ cm^{-1} (Non-resonant signal, orange). The points are taken from the wigner integrated along $\bar{\nu}_2$, as shown in Figure 5.16. The corresponding smooth lines are the simulated resonant and non-resonant transient amplitude signals. The resonant signal is the convolution of a Gaussian function and exponential decay function representing the excitation field pulse and the coherent lifetime transient, while the non-resonant signal is purely the Gaussians of the excitation pulses convolved together. The coherence lifetime is found to be 0.61 +/- 0.05 ps. The lifetime was derived from a three parameter fit, the bottom plot shows two of the parameters, τ (the coherence lifetime, left axis) and Zero offset (position of the non-resonant peak, right axis), as a function of the third, the pulse width (FWHM). Also shown on arbitrary scaling is 1/cost (pink), a measure of how well the fit matches the data. A gray vertical line shows the best overall fit, shown in the third plot above at $\Delta = 1.01$. The endpoints of the spans are shown above on either side. The leftmost plot above shows the result of holding Zero offset at Zero.

Frequency

Absorbance

We performed second derivative analysis of UV-VIS absorption spectra to extract peak centers for the principle transitions of cyanocobalamin and deuterated aquacobalamin. Figure 5.18 shows the absorption spectrum of each molecule (top row), and its second derivative (bottom row). The α, β, shoulder, and γ peaks were each found as local minima in the second derivative spectrum (vertical grey lines in Figure 5.18). See Table 5.2 for the exact values.

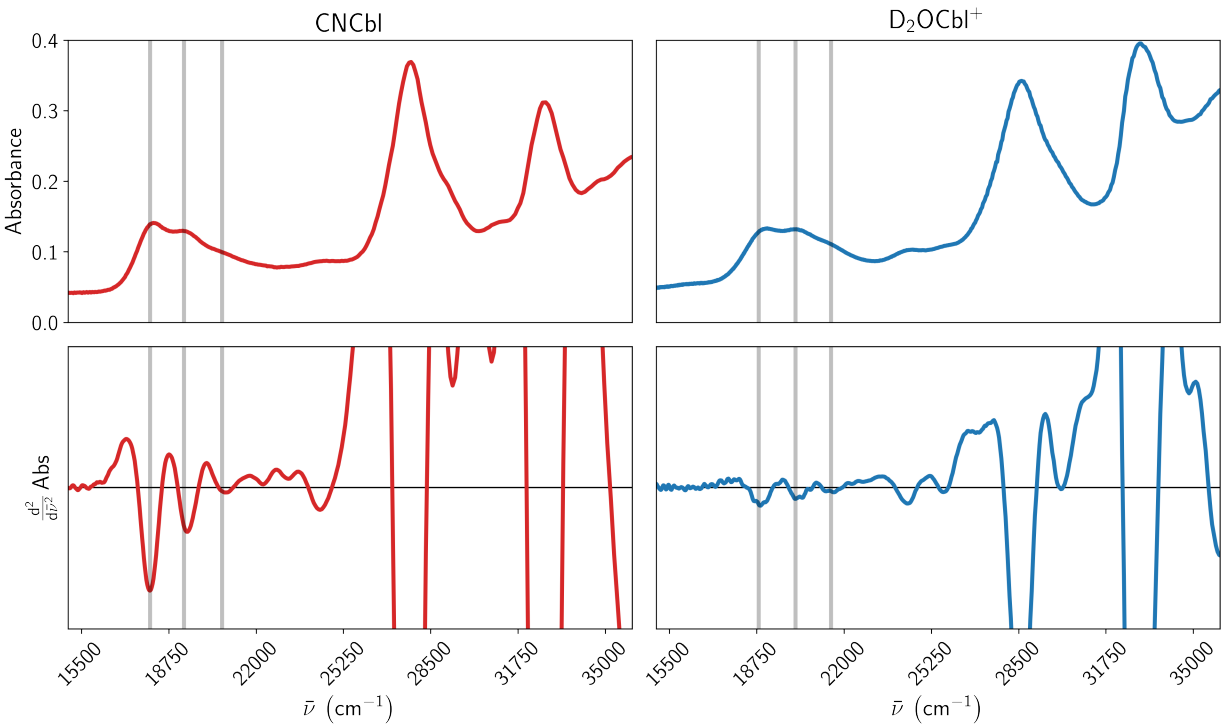

Figure 5.18: Absorption spectra of cyanocobalamin (left) and deuterated aquacobalamin (right), and second derivatives thereof (bottom row). Peak assignments made to local minima of second-derivative spectra shown as vertical grey lines.

	CN	AQ
α	18,050	18,920
β	19,456	20,178
shoulder	20,834	21,620
γ	27,702	28,577

Table 5.2: Peak centers, in wavenumbers, extracted from second-derivative analysis of UV-VIS absorption spectra.

Rising absorptive background

To properly model the three features within the α/β band, it is necessary to account for the rising absorptive background that the band rests upon. We chose to model this rising background as the tail of a large, far-off Lorentzian transition. This Lorentzian is shown in full within Figure 5.19. We emphasize that this single-Lorentzian model probably does *not* correspond to a single real transition. It is meant to roughly account for many transitions whose tails appear in the region of the α/β band. The single Lorentzian was chosen because it has reasonable agreement with the changing baseline over the entire range of our absorption spectra, as can be seen in Figure 5.19.

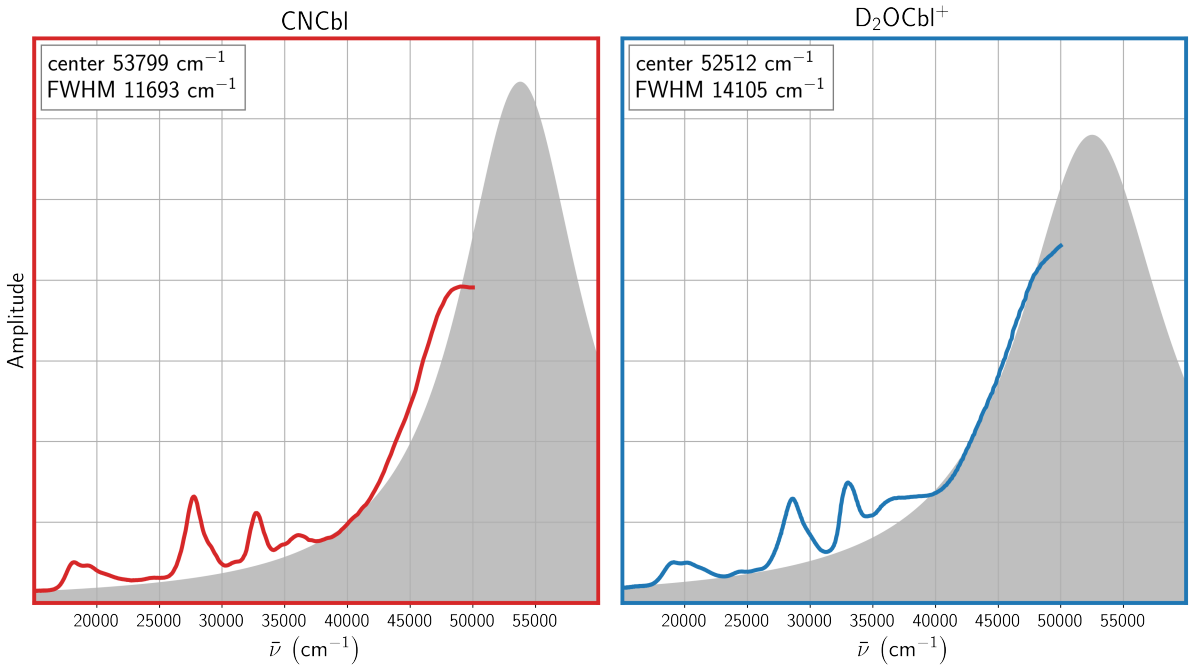

Figure 5.19: Comparison of absorption spectra with large Lorentzian used to account for rising background. The Lorentzian is shown as a filled gray peak, with peak center and FWHM inset. Each species is labeled above the corresponding plot.

Causality

As a homodyne-detected spectroscopy, TRSF does not distinguish between absorptive (imaginary) and refractive (real) portions of the resonant response. Figure 5.20 explains the contributions of each phased component within our simulation. The large upper plot shows the complex response of a single Gaussian resonance with an absorptive FWHM (purple) normalized to one. It is easy to see that the magnitude response is much broader—a disadvantage of TRSF. The lower two plots show the same phenomenon for our best-fit simulations of aquacobalamin and cyanocobalamin. The individual states are shown as filled shaded regions, while the sum is an open thick line. Note that the real component is signed such that adjacent states destructively interfere.

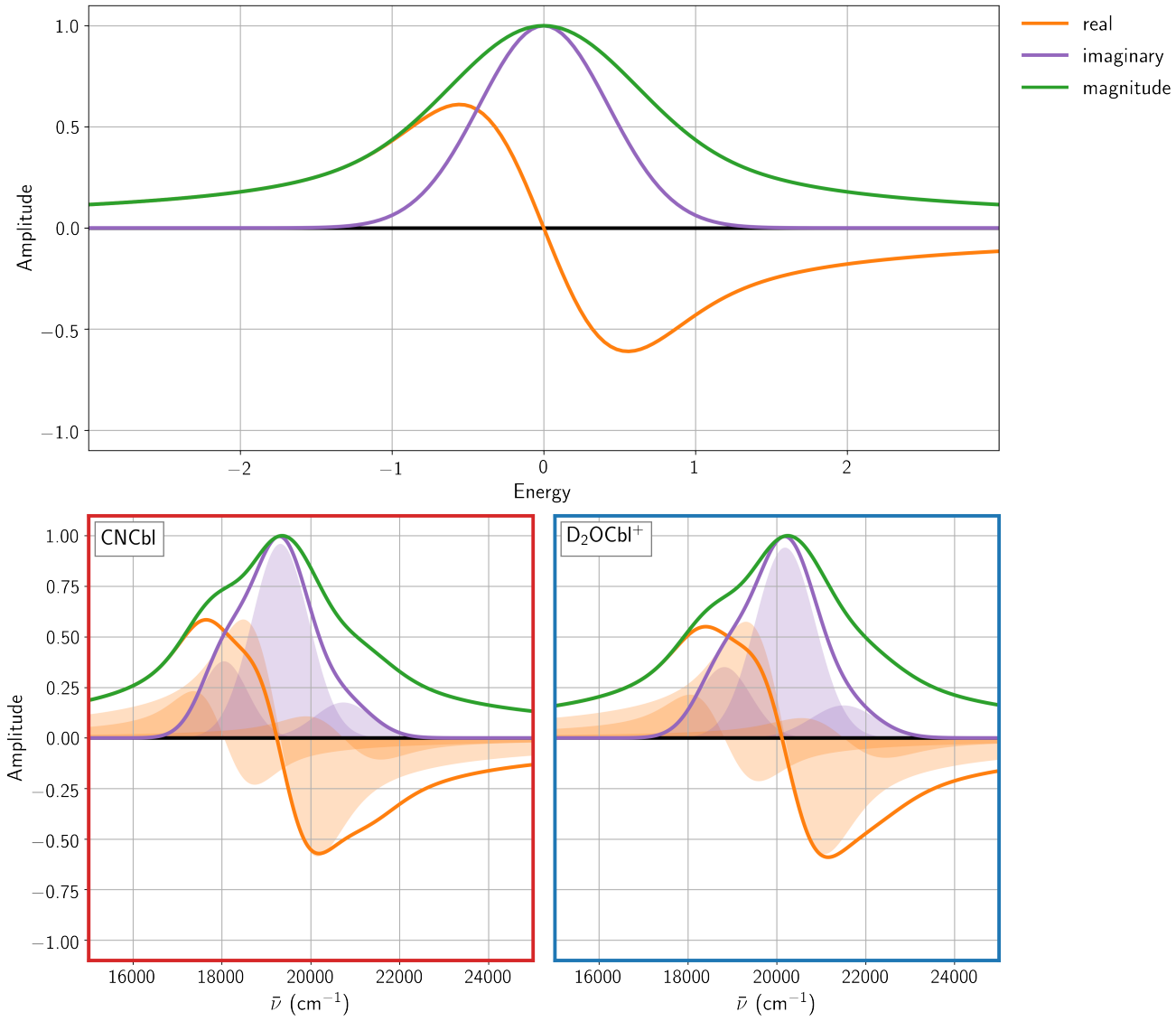

Figure 5.20: Complex TRSF resonance response shown as real and imaginary components. Phase of each component corresponds to legend in uppper right. Upper: single resonance with absorptive FWHM of one. Lower: three-state TRSF simulation of cyanocobalamin (left) and aquacobalamin (right). Single state responses are shown as filled shaded regions, sum is shown as thick solid line.

Franck-Condon Analysis

We modeled the $\bar{\nu}_{TRSF}$ traces at $\bar{\nu}_1 = \bar{\nu}_2 = 1500\,\mathrm{cm}^{-1}$ as a Franck-Condon vibronic progression. We used the equations in Reference [45] used to calculate the vibronic strength based on the excited state offset Δ. Δ was derived from the fit to the absorption spectrum.

Summary

Table 5.3 contains the assignments extracted from our Franck-Condon analysis.

		CN	AQ
Δ		1.47	1.50
α	center	18050	18820
	FWHM	1244	1394
β	center	19318	20118
	FWHM	1506	1591
shoulder	center	20735	21506
	FWHM	1516	1713
fudge	center	53799	52512
	FWHM	11693	14105

Table 5.3: Peak centers, in wavenumbers, extracted from second-derivative analysis of UV-VIS absorption spectra.

Raw data and workup scripts

All raw data, processing, fitting, and plotting scripts are freely available at the Open Science Foundation repository: https://osf.io/x4w2p/ (DOI: 10.17605/OSF.IO/X4W2P).

Raw data

Raw data is held within the `data` folder, organized by linear (FTIR, UV-Vis) and TSF subdirectories. Many of the TRSF spectra were collected in smaller pieces, so raw data has separate files for each. The Python script `workup.py` generates `data.wt5`, a WrightTools [46] data file, which is built on top of the Hierarchical Data Format (HDF5) file format, and can be inspected with any tool designed to work with HDF5 files.

That script goes through the following steps:

- Read raw data files
- Create collections for processed data
- Copy linear data into processed collection
- Background subtract CNCbl FTIR data (D_2OCbl^+ was already background subtracted by the instrument)
- Adjust FTIR baseline
- Scale the relevant channel of raw TRSF data to facilitate joining
- Join the raw TRSF data, placed in processed folder (some higher dimensionality data is removed in this step).
- Copy TRSF data that did not require joining (`cn_delay`, `cn_ir2d`)
- Normalize TRSF data to Pyroelectric monitors of input electric fields
- Normalize TRSF data to range of 0-1

- Convert to consistent units of cm^{-1}
- Smooth data with a Kaiser window of width 2
- Integrate and renormalize `cn_delay` for plotting Wigner (Figure 5.16).
- Save the data file

Once created, this data file is accessed by fitting and plotting routines.

Fitting scripts

Each fitting stage has its own Python source file. These fits take data as generated by the `workup.py` script, and apply some model. Parameters either input or extracted are written to human-readable/writable `.ini` files. Array outputs of the models are written to their own `.wt5` files, to be read by the plotting routines. Common functionality is located in `fitlib.py`. See above sections for specifics on each model.

Figures directory

The figures directory contains images for each figure, including the source to generate them. Most figures are generated using Matplotlib [118] and Python source files are provided. These source files read data from the `data.wt5` file and the files created by fitting and produce `.png` image files at double scale from expected printed dimensions. Each source file can be run directly to regenerate the figure (`$ python3 <file>.py` where `<file>` is the name of the desired figure. Common functionality is shared via `figlib.py`. Two figures (`intro_wmels` and `tsf_wmel`) were not made using Python, and the `.svg` source files are available.

Structure directory

This directory contains several representations of generalized cobalamin structure in ChemDraw coordinates and image representations.

LaTeX files

The LaTeX source files and PDFs that they generate are located in the root of the repository. The two files are `paper.tex` and `SI.tex` which hold the source for the manuscript and supporting information, respectively.

References are held in `references.bib`. The `library` directory holds a helper file for building the PDFs from python function calls.

Computational Environment

The Python scripts in the repository expect Python 3.6 with the following packages installed:

```
Package         Version
--------------- -------
cycler          0.10.0
docutils        0.14
h5py            2.8.0
imageio         2.3.0
kiwisolver      1.0.1
matplotlib      2.2.2
numexpr         2.6.5
numpy           1.14.5
Pillow          5.1.0
pip             10.0.1
pyparsing       2.2.0
python-dateutil 2.7.3
pytz            2018.5
scipy           1.1.0
setuptools      39.2.0
```

```
six             1.11.0
tidy-headers    0.3.0
wheel           0.31.1
WrightTools     3.1.0
```

While exact versions of dependencies may be able to vary, especially for newer releases, the versions listed here are known to work. It is known that versions of `WrightTools` prior to 3.1.0 will not build everything in this repository. A `Pipfile` and `Pipfile.lock` are provided and can be used to create a suitable virtual environment with a tool such as `pipenv` [119].

In addition to the Python libraries, LaTeX is required for both rendering figures and the final PDF documents. A slightly less polished version of the figures can be rendered without LaTeX by commenting out the line `wt.artists.apply_params("publication")` in `figlib.py`.

Building from scratch

A Python script is provided to perform all necessary building, from data workup all the way to LaTeX rendering. This script, `build.py`, is located in the root of the repository. It can be run using `$ python build.py`. By default, it will perform all steps. Additional arguments can be provided to limit which stages are performed:

```
data
fits
figures
documents
```

Note that each stage expects the outputs of the previous stages to be present. Multiple stages can be specified and they will be run in the proper order. Users are advised to remove the extra output files generated by LaTeX if problems occur.

5.3 Polarization studies

The relative strengths of the 1500 cm^{-1} and 1570 cm^{-1} mode are dependent on the polarizations of the excitation fields. Figure 5.21 shows two wigner scans, one taken with input polarizations HHV (ω_1, ω_2, ω_3), and the other HHH. It is clear that the 1500 cm^{-1} signal is many times stronger when ω_3 is oppositely polarized to the two IR beams, while the 1570 cm^{-1} appears to be polarization agnostic. We know that the change in signal intensity is not simply a matter of the monochromator being more efficient at a particalar output polarization, as the signal would decrease uniformly if that were the case. Figure 5.22 shows how the weaker vibrational mode signal slowly grows with respect to the strong mode as the angle between the two input polarizations is increased from 0 to 90°. We have not yet properly analyzed the potential implications of the polarization dependence.

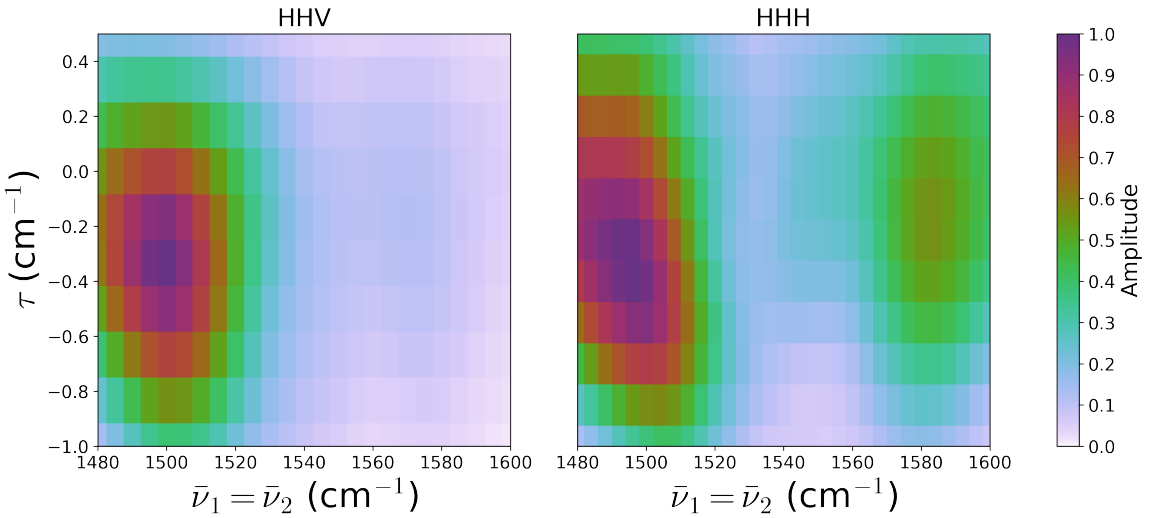

Figure 5.21: Wigner scans of CNCbl taken with HHV and HHH excitation field polarizations.

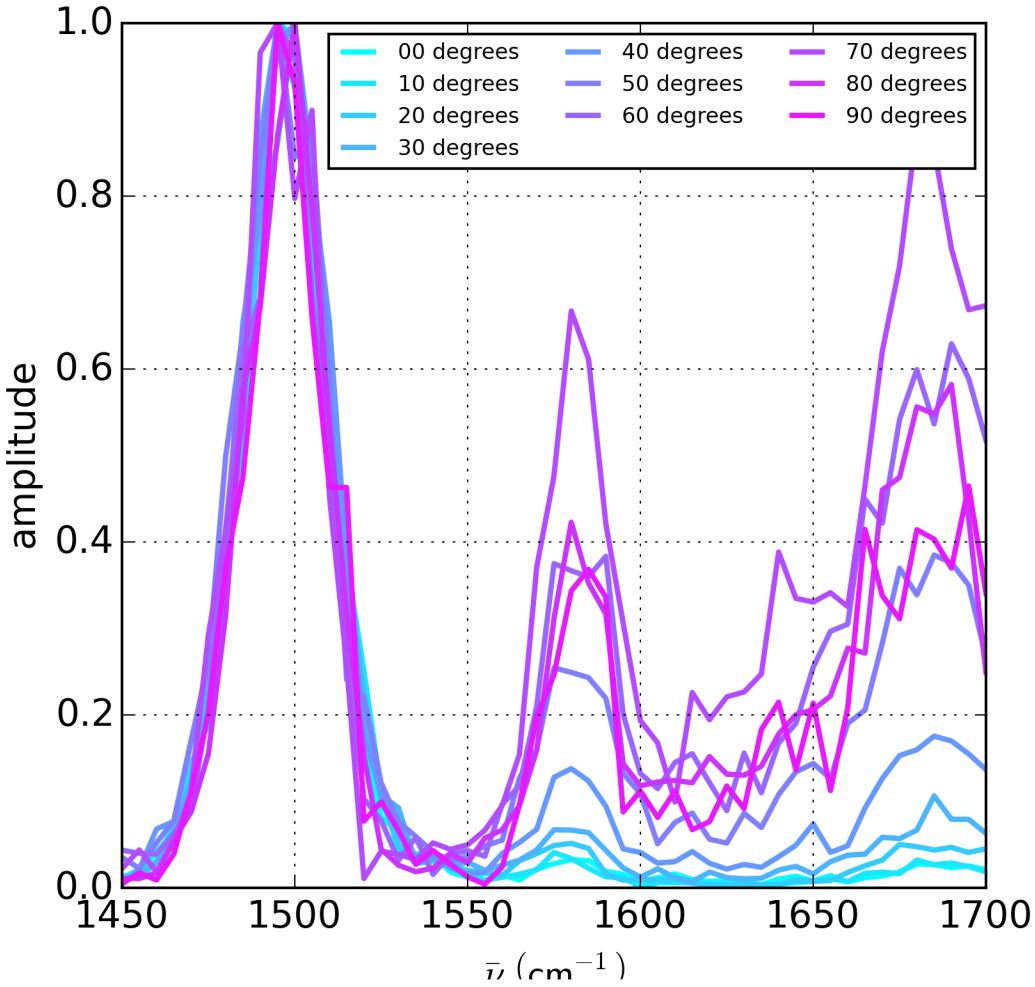

Figure 5.22: The change in relative signal between the 1500 and 1570 cm^{-1} mode in CNCbl as the angle between the input polarizations is scanned from HHH (0°) to HHV (90°).

5.4 DOVE scans on Cobalamin

While TRSF was the focus of most of my efforts, I also collected some preliminary DOVE scans on CNCbl. DOVE is a phasematchable process and non-resonant signal from the windows is very bright, so I used dry CNCbl on a mid-IR absorbant glass slide as my sample. The DOVE scans were taken with ω_3 fixed at 16,400 cm^{-1}. ω_1 was scanned over the overtone and combination band region and ω_2 was scanned over the fundamental mode region, and the scans were collected at zero delay. Figure 5.23 shows the DOVE scans with HHV and HHH polarization. The DOVE scans are fairly devoid of features except for a bright cross-peak at ω_1,ω_2 = 3050,1580 cm^{-1}. When the axes are transformed to $\omega_1 - \omega_2$,ω_2 as shown in Figures 5.24 and 5.25, the cross peak appears to show coupling between the 1585 and 1500 cm^{-1} modes. The overtone peaks, which are so dominant in TRSF, are completely missing. Also missing is the cross peak corresponding to the fundamental 1500 cm^{-1} mode and the 1500+1580 cm^{-1} combination band.

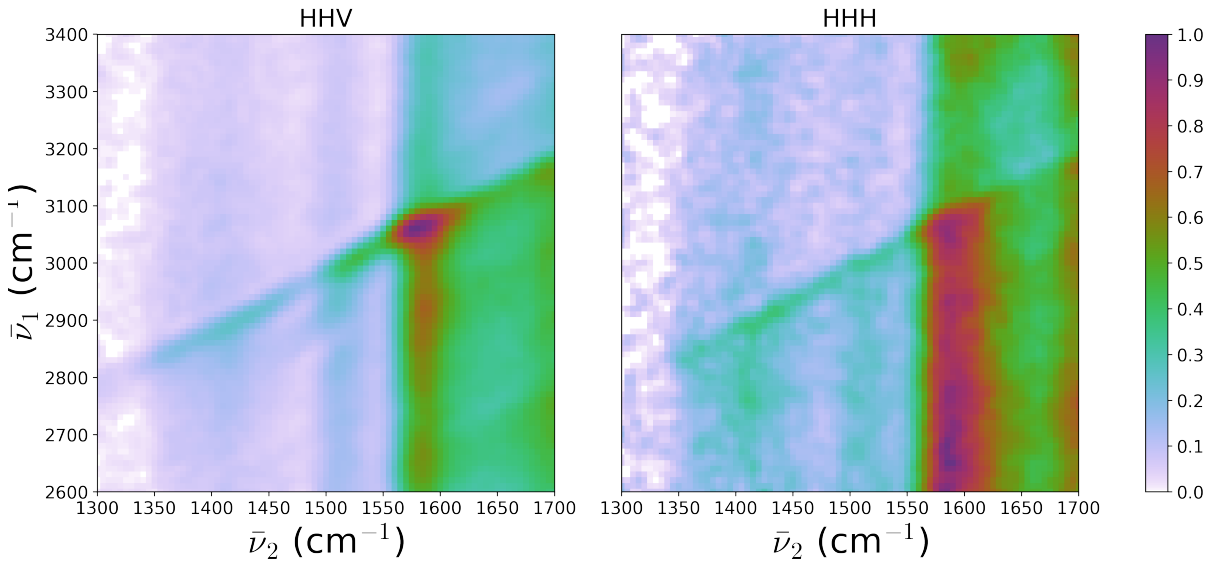

Figure 5.23: DOVE on Cobalamin

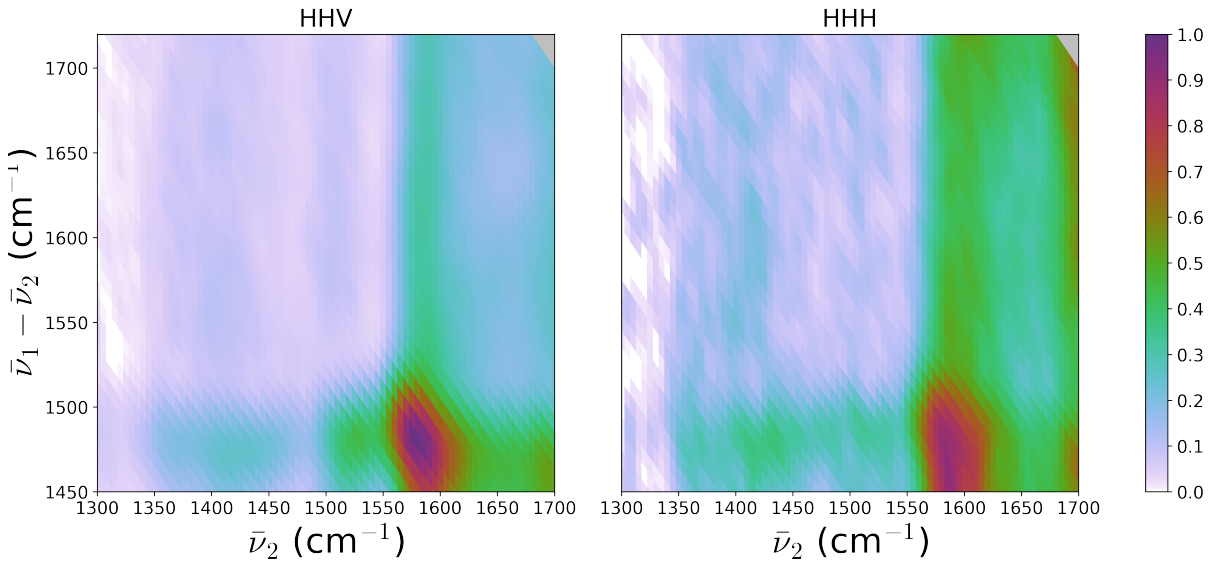

Figure 5.24: DOVE on Cobalamin Transformed axes zoomed

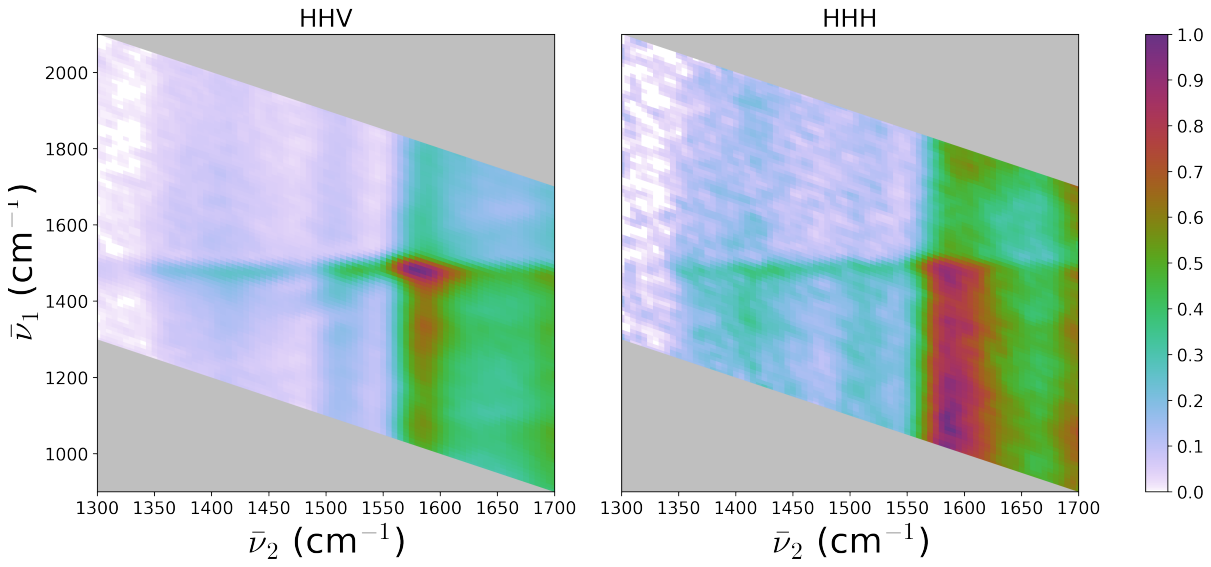

Figure 5.25: DOVE on Cobalamin Transformed axes

5.5 TRSF scans of Cobalamin above 21,000 cm^{-1}

One of the weaknesses of the published work was the limited scanning range which prevented us of observing the full electronic profiles of the features. The flexibility of the OPA allows us to switch to different processes to access a much larger scanning region than any one process can on its own. Figure 5.26 shows TRSF scans of a dry CNCbl sample (top) and a solution phase sample (middle and bottom) using the Sum-Frequency Signal (SFS) mixing process instead of SHS to access the region between 22,000 and 24,000 cm^{-1}. The excitation field polarizations are labeled on figure subtitles. The high energy TRSF scans show that both the 1500 and the 1570 cm^{-1} modes are still present in the region of the D and E bands. The 1500 cm^{-1} appears to be weaker in this region than in the α/β region. The scans in this figure are disrupted by the short-pass 450 nm cutoff filter which blocked all TRSF output below 22,200 cm^{-1}. We have since found a 500 nm shortpass filter that can be used for the red half of this spectrum. Ultimately, we want to target the region of the γ band at 30,000 cm^{-1} but will require the installation of a second BBO mixing crystal to produce fourth harmonic signal to access that region.

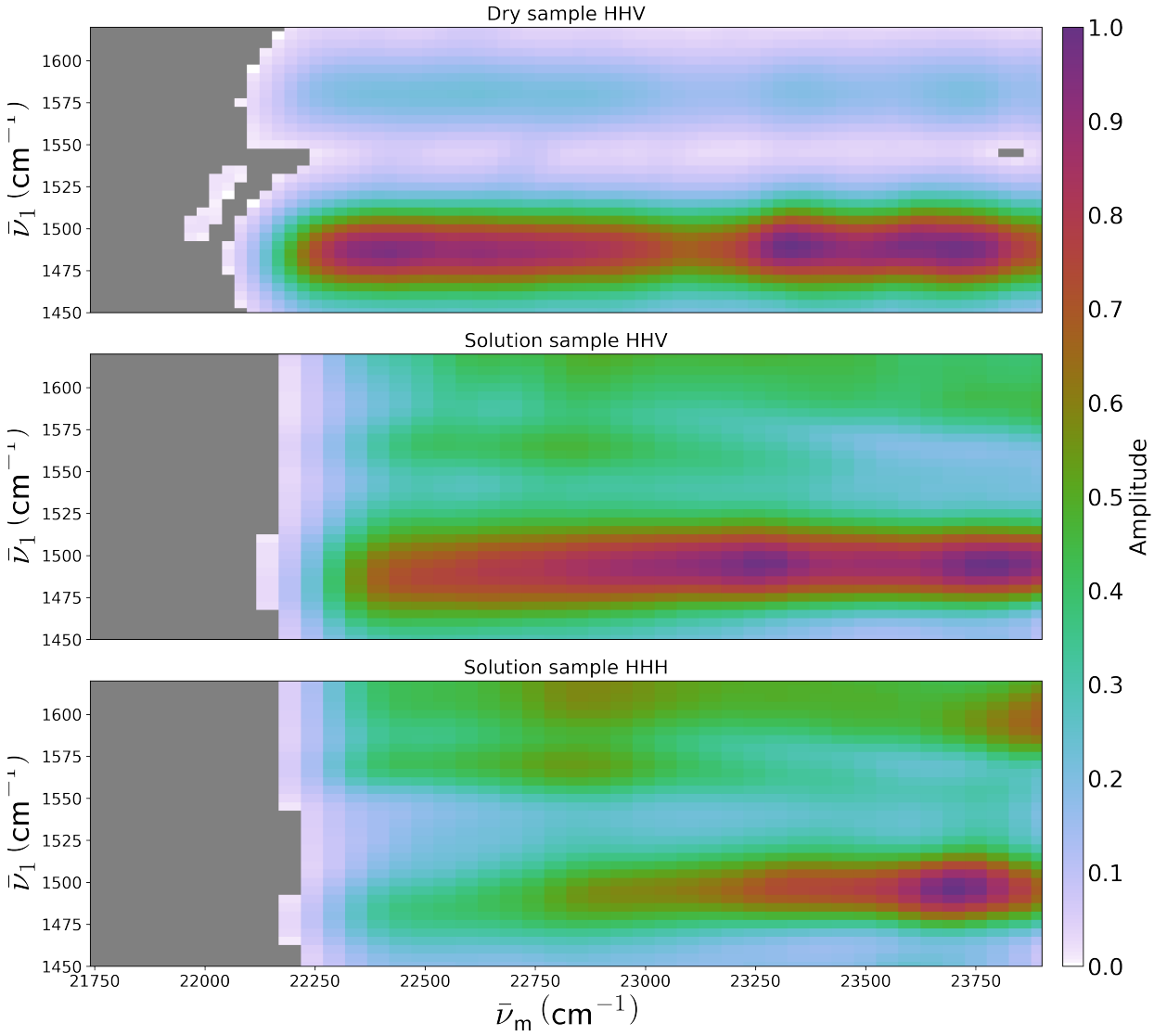

Figure 5.26: TRSF on CNCbl on the D and E band region

Chapter 6

Unpublished Work

6.1 Chlorophyll

In the scope of the project, chlorophyll is an important molecule to study primarily because it is a highly light absorbing pigment which is widely present in Photosystem II. The X-ray crystal structure by Umena et al[7] revealed that there are 35 chlorophyll a molecules within the reaction centre itself, not including the $\sim$ 140 chlorophyll molecules in the Light Harvesting Complex II (LHC II)[120]. As stated in the Introduction, the UV-Vis absorption spectra of Photosystem II contain mainly chlorophyll a features as seen in Figure 1.2. Pace et al[28] collected difference absorption spectra and measured changes in absorption in the region around 300 nm, as shown in Figure 6.1. It is believed that these absorption changes are due to changes in the Mn ion electronic states as a result of a chemical reaction. Chlorophyll a has large absorption bands in the region around 400 nm but nevertheless has significant absorption in the region where Mn ion states are expected to be found. It is not possible to remove the OEC from the chlorophyll a pigments within without significantly altering its behaviour and structure. Since chlorophyll a is a strong chromophore, it is expected that chlorophyll signal will be observed in multidimensional studies of the OEC.

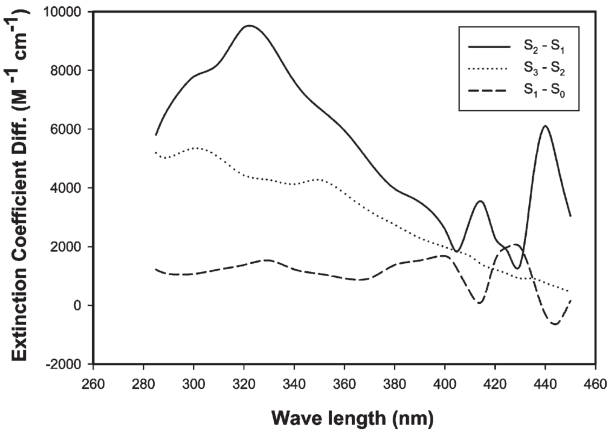

Figure 6.1: Absorption difference spectra of the Photosystem II reaction center.

Taking TRSF spectra of chlorophyll a has therefore been on the agenda for a long time. I have faced two major difficulties in obtaining good chlorophyll a spectra: time and expense. Chlorphyll a is in very high demand and suppliers such as Sigma Aldrich typically take months if not years to deliver a small amount at high expense. Furthermore, it is a light sensitive compound when removed from the protein network that binds it within the leave. Prolonged exposure to light causes the denaturing of chlorophyll a to pheophytin, chlorophyll a lacking the Mg ion. In one experiment, I observed that TRSF signal of a chlorophyll sample decreased over the course of a single scan (about 10 minutes). I decided that it was not economically feasible to use store-bought chlorophyll while our ability to perform the experiment was still being perfected. I decided to extract and purify my own chlorophyll from spinach leaves purchased at the local market place.

In this section, I describe the extraction process, show some early TRSF spectra of chlorophyll on samples extracted in our own lab versus some older spectra using store-bought samples, and describe my strategy for successfully collecting a full TRSF spectrum without photo-damage.

6.1.1 Extraction

I based my extraction procedure on the method described in Iriyama et al[121].

Lab conditions

Before beginning, I covered all the windows in the Wright Group wet lab with zinc foil to block out a majority of the outside light. I notified the group about the light sensitive extraction taking place and stuck a warning sign on the outside of the door. As soon as the pigments are removed from the leaves, they are sensitive to light damage and extra care must be taken to minimize the light in the room (the lights in the room turn on automatically so they must be manually switched off to ensure they stay off). For light, I covered a small portable orchestra light with two layers of green film. Chlorophyll is not damaged by green light as it reflects it. While the leaves are still intact, it is okay to have the room lights on, but as soon as the leaves are in the blender, all lights must be switched off.

Spinach preparation

For a typical chlorophyll a extraction, I purchased spinach from the local market place (Madison Fresh Market near 333 East Campus Mall, Madison WI). I either used the spinach immediately, or stored it in the freezer. Keeping the leaves in the refrigerator tended to result in lower yields. This is probably due to the protein structure being deconstructed by enzymes in the rotting process, which is not sufficiently slowed down in regular refrigerator temperatures. After about one week, the spinach is completely unusable and rotting can be observed and smelled very clearly. I used only the soft and dark leaves and left the stems out. I removed the stems and weighed out about 10 g of leaf. The original procedure recommends 100 g of leaf but I found it easier and more manageable to scale everything down.

Extraction and purification

I added the spinach leaves and 50 mL of methanol to a Waring blender (found in the top shelf of the glass windowed cabinet in the wet lab). I blended the mixture for about three minutes. I folded a piece of filter paper into a cone and slowly filtered the mixture into an Erlenmeyer flask. At this stage, the chlorophyll is in the solution. I collected the solid gunk in the filter paper and discarded it. The resultant supernatant is a dark green solution. The original procedure recommends centrifuging the solution to completely remove all solid impurities, but I found this to be unnecessary.

Next I added 7 mL of dioxane and about 8 - 10 mL of distilled water to the Erlenmeyer flask. I added the dioxane immediately, but added the distilled water drop-wise, constantly swirling and watching for the solution to turn from clear to turbid. It is hard to see this change in low light conditions and I occasionally went closer to the window and exposed the solution to a little more light. As soon as the solution turned turbid, I stopped adding water. Adding too much water prevents the chlorophyll from precipitating. On one occasion, I overshot and added water well after the solution had turned turbid, and was unable to obtain any chlorophyll product. In addition to solution turbidity, I could see the chlorophyll aggregates as small dark spots near the bottom of the flask. I wrapped the Erlenmeyer flask in zinc foil and placed it in the freezer for one hour to allow further precipitation. After freezing, the aggregates were even more clearly visible.

At this point, the chlorophyll was in the precipitate and the supernatant needed to be removed. I divided the suspension into equal portions and distributed it among four centrifuge tubes. I wrapped each tube in aluminium foil and centrifuged them at 3000 rpm and 5 °C in the Keck Center centrifuge (5th floor, Matthews building). After returning to the dark lab, I decanted the supernatant and was left with the chlorophyll pellets. I added small amounts of methanol to dissolved the pellets and remove them from the centrifuge tubes and collect all the product in a single vial. I placed the vial under a constant flow of dry air until the solution had dried and the chlorophyll solid was left. If the chlorophyll is left in solution, the rate of denaturing increases. The original procedure recommends performing a dioxane and distilled water extraction twice to obtain greater purity. I have found a single extraction to be good enough.

The product obtained by this procedure is a mixture of chlorophyll a, chlorophyll b, pheophytin, and some carotenoids. While it is desirable to remove these other pigments, chlorophyll a is by far the majority product. Additionally, TRSF should allow the spectral separation of a the pigment mixture since each pigment absorbs at different frequencies of light.

Summary

- Weigh out 10 g of spinach leaves
- Blend spinach leaves with 50 mL of methanol for 3 minutes
- Filter out solid waste using filter paper
- Add 7 mL of dioxane and 8-10 mL of distilled water dropwise until solution turns turbid
- Cover flask in aluminium foil and freeze for one hour
- Centrifuge, discard supernatant
- Collect pellets and dry solvent
- Store chlorophyll in freezer

Column chromatography

I attempted to separate the pigments obtained from the spinach extraction using column chromatography. I based the column separation on the original procedure by Iriyama et al[122]. The column used was ordered at the glass shop and is stored in the burets drawer in the wet lab. The column diameter is X cm wide and its length is X cm. The column was covered in aluminium foil for the duration of the separation, except to observe. I used confectionary sugar as the packing material, and petroleum ether as the eluent. I added steel wool and sand to the column and packed them using a long steel rod. After drying the sugar in the oven overnight at 70 °C, I passed it through a sieve to further remove any lumps. I added petroleum ether to the sugar to create a slurry. I set up the column in the fume hood and slowly poured the slurry into the column, adding small amounts at a time to allow the packing material to settle. When the column was full, I added extra petroleum ether and opened the stop cock to allow the eluent to further pack the column. The packing material must never be allowed to dry to prevent cracks. Once the column cracks, it must be redone. The solvent level was reduced until only a little bit of excess solvent remains. I added the chlorophyll mixture to the column and allowed the pigments to absorb into the column. Once all the pigments were absorbed, I filled the column to the top with solvent. The column has a round bottomed flask welded at the top to contain extra solvent. I kept the stop cock open and waited for the pigments to separate. The pigments separated into four main bands. The first band is yellow and contains the carotenes, the second is yellow-green and contains pheophytin, the third is darker green and contains chlorophyll a, and the fourth is blue-green and contains chlorophyll b. I collected the band eluents into vials and took the UV-Vis spectrum of each vial to confirm the identity of the pigments. In many cases however, small cracks in the column caused the bands to not separate correctly.

Chromatography turned out to be very difficult to do and columns cracked frequently. The amount of effort required ended up being too much for the additional purity. I settled on extraction and purification, leaving the purchased chlorophyll a for work I was intending to publish.

6.1.2 TRSF spectra

Erin Boyle had collected TRSF spectra of store-bought chlorphyll a samples and a visible excitation beam of 800 nm, targetting the lower energy absorption band. The 2D spectra can be found in her dissertation. I collected a TRSF spectrum of a self-extracted chlorophyll sample with the visible beam fixed at 500 nm targetting the higher energy absorption band. I include an IR-IR diagonal slice of both the 800 nm and 500 nm TRSF scans in Figure 6.2. The two scans are largely similar. The major peaks are observed at the same frequencies, although the relative intensities differ considerably. The peaks in the 800 nm scan are also narrower, which is due to the pulses being spectrally narrower ($\sim$25 cmc^{-1}) in the old system. These scans show that the extraction process described above can produce high enough quality chlorophyll samples for TRSF.

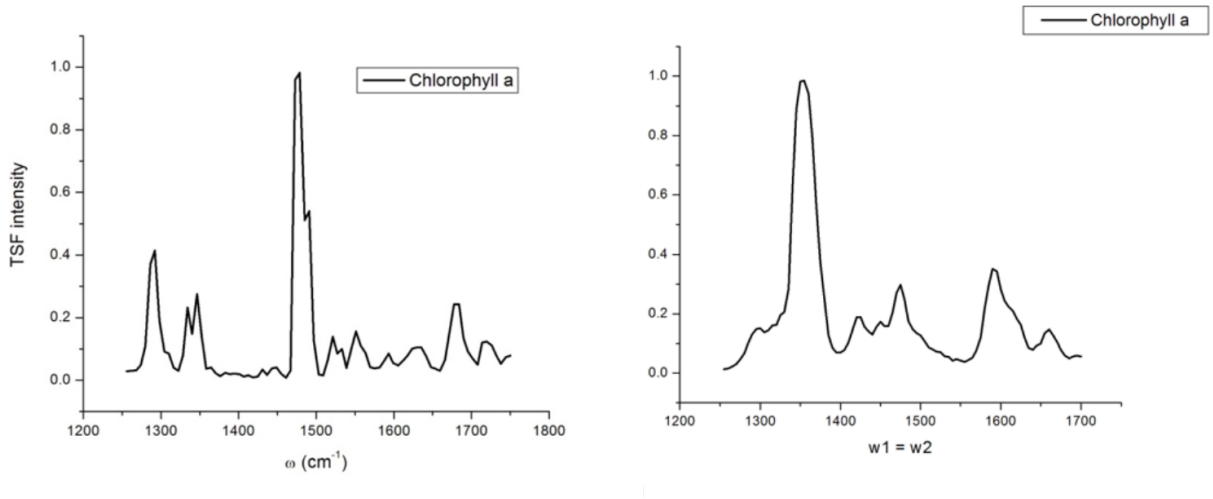

Figure 6.2: TRSF spectra of store-bought chlorophyll a with $\bar{\nu}_3 = 800$ nm (left), and an in-house extracted chlorophyll mixture with $\bar{\nu}_3 = 500$ nm (right).

6.1.3 Strategies for collecting TRSF spectra of Chlorophyll a

There are two major barriers that stand in the way of TRSF studies on chlorophyll. The first barrier is the delicate and light sensitive nature of the sample, which tends to be damaged in the time required for even a relatively quick scan. The second barrier is its lack of solubility in a solvent that is convenient for a mixed IR-visible technique. The solvent must be transparent in both the visible and fingerprint mid-IR region of the spectrum. The only available solvent that covers the entire range is deuterated acetonitrile. Chlorophyll is not soluble in acetonitrile, nor in water or D_2O. Deuterated methanol and ethanol both have vibrational resonances near those of chlorophyll.

My plan for a successful TRSF study of chlorophyll involves a dry and cryogenically cooled chlorophyll sample. While working with cobalamin, I found that placing a few drops of solution on a glass slide and allowing the volatile solvent to dry in a dessicant produced a smooth and uniformly thin layer of sample on the substrate. The thickness of the sample could be adjusted by adding fewer or more drops at a time. The glass substrate absorbed in the mid-IR, preventing the generation of non-resonant signal and removing the interference patterns observed with sample cell windows. The resultant spectra were very similar to those of solution phase samples, but were much cleaner. The drop-cast samples of cobalamin were also shown to survive in the cryostat vacuum and produced spectra similar to room temperature experiments.

My plan is to dissolve chlorophyll in small amounts of methanol and drop the sample on a mid-IR absorbant window, allowing the solvent to evaporate. The thin sample layer will then be mounted on the sample compartment of the coldfinger and directly immersed in LN_2 and sealed into the cryostat as normal. My belief is that the cryogenic temperatures will prevent thermal damage and prolong the lifetime of the sample. The cryostat is mounted on a three dimensional stage to allow suitable spot on the sample to be studied.

6.2 PS II

UV-vis studies of PS II have revealed that the electronic transitions of the manganese ions lie in the region around 300 nm[28]. Additionally, difference FTIR studies have assigned features in the fingerprint region to vibrations that can be assigned to the vibrations of the amino acids surrounding the OEC, as well as the metal-ligand modes[29, 32, 31, 30, 123, 124]. X-ray diffraction studies have determined the structure of the OEC at the dark-stable state S1[7, 22] and to some extent the intermediate states S2[125] and S3[126], although there is still debate about the intermediate states in the literature. Previous studies have used a visible nanosecond pulse to trigger the reaction into the intermediate, followed by a femtosecond x-ray pulse whose diffractogram is then subtracted from the ground state diffractogram to get a difference crystal structure[125, 24]. X-ray absorption[127, 23, 128] and EPR studies[129] have determined the oxidation states of the Mn ions during the mechanism. In addition to experiments, computational work using methods such as DFT[25, 26, 27] and QM/MM[130, 126, 131] have modeled the different steps in the reaction mechanism.

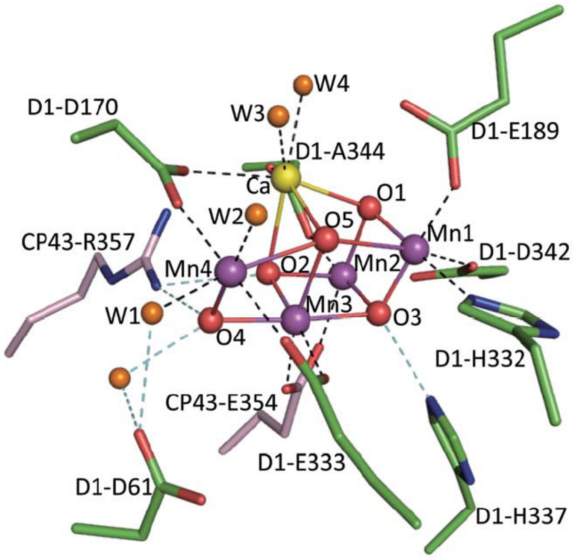

Figure 6.3: X-ray structure of the OEC complex in Photosystem II[7]

The X-ray structure of the OEC is shown in Figure 6.3. Our strategy relies on the sensitivity of the electronic structure of the Mn-ion based electrons on the immediately surrounding chemical environment. The electronic structure of the four Mn ions is slightly different due to the unique environment of each ion in the asymmetric cubane structure, and therefore should present a unique and identifiable absorption signature. Shifts in the electronic transitions that are assigned to particular Mn-ions can be used to track chemical changes in the complex such as the making and breaking of particular bonds over the course of a reaction. The absorption spectrum of the OEC has the potential to shed great insight into the complex's catalytic mechanism. The limitation of absorption spectroscopy is its resolution. Electronic transitions are broad and tend to have much overlap with other transitions. It is difficult to resolve between electronic transitions, particularly when there are multiple transitions with similar resonance frequencies, as in the case of the Mn-ions in the OEC. Failure to resolve the electronic structure makes detecting and interpreting changes in the absorption spectrum impossible.

Using FWM-CMDS techniques such as TRSF, DOVE, and CARS, our strategy is to derive a response from electronic transitions by way of vibrational states. In TRSF, for example, the first two pulses excite a set of vibrational coherences and the third pulse stimulates a transition from the vibrational state to the resonant electronic state. The inclusion of the vibrational excitations in the pathway restricts the TRSF output such that output is only emitted when the vibrations are coupled to the electronic state. Since each Mn-ion is coupled to a unique set of bonds, such as bonds to the bridging oxygen atoms and to the surrounding amino acids as seen in Figure 6.3, the combination of vibrational and electronic enhancement in the form of IR-visible cross-peaks can resolve the electronic transitions of each Mn-ion and allow detection of structure changes over the course of the catalytic cycle. The first challenge is to obtain a multidimensional spectrum of the complex and resolve the ground state electronic structure of the Mn-ions. Our strategy comprises of flashing followed by instantaneous freezing to cryogenic temperatures to fix the complex in place, after which CMDS spectrum are to be taken of the frozen sample. The cross-peaks are to be identified in each state and changes in the cross-peaks resonance frequency or line shape are to be compared against current mechanism theories.

The Wright Group Picosecond system is to be used to take CMDS spectra on PS II crystals extracted by the group of Petra Fromme at Arizona State University. The details of the extraction process and thoughts on sample preparation for CMDS experiments are written below.

6.3 Preparations of Photosystem II for CMDS experiments

6.3.1 Sample prep and protein extraction

Starting material: frozen cyanobacteria cells stored in liquid nitrogen. The cyanobacteria cells are grown in a cell culture (very classically named Medusa)

Buffer was heated using hot water from the tap. The hot water bath was used to melt the frozen cyanobacteria.

Prep 1: removal of contaminants

Mix Prep 1 with the cells, force the cells to dissolve in the buffer (resuspension) using a paint brush while keeping the suspension on ice. Centrifuge the suspension to separate contaminants from the bacteria cells. The bacterial cells form the pellet and the supernatant containing the contaminants is removed. Repeat the wash in the buffer.

Prep 2: Microfluidisation and purification

The pellet cells are resuspended in Prep 2, a buffer similar to Prep 1 but which contains Manatol. The suspension is homogenized (using a homogenizer) to break up chunks. The suspension is then passed through a microfluidiser, a narrow tube through which the suspension is forced at high pressure causing a shear force that rips open the bacterial cell membranes and releasing the proteins into the solution.

After microfluidization, the target proteins currently contained in the thylakoid membrane are dissolved in the solution. Centrifugation removes the heavier particles, including those cells which were not lysed. These unlysed cells form a pellet which is then resuspended and passed through the microfluidizer again. Only around 60% of the cells are lysed with each pass. The process is repeated until the majority of cells are lysed. The supernatants of the centrigation are kept each time. The supernatants are consolidated and multiple washes are performed to remove unwanted material like broken cell membrane.

Solubalization: Removing proteins from thylakoid membrane

A solution of β -DDM detergent is prepared to be added to the protein suspension. Small aliquots of protein mix are dissolved in acetone to extract the chlorophylls, the absorption of which is measured and used to estimate the concentration of PS in the supernatant. The detergent solution is prepared according to the results of the concentration calculation, and the detergent solution is added to the protein suspension and allowed to mix. The proteins are solubalized. Once that is complete, the mixture is centrifuged at very high acceleration (50,000 rpm for 1 and 1/2 hours) to separate the membrane and other unwanted material from the now soluble protein.

HPLC Column separation

The columns used are connected to HPLC pumps. The columns are about 10 cm in diameter and 1 meter in length. I do not remember what the packing material is. Two solutions are used in the separation process: AO and B. AO is Prep 3 solvent, and B is Prep 3 with $MgSO_4$ dissolved in it. $MgSO_4$ acts as a supplier of ions which stick to the polar sites on the packing material, causing all polar sites to be occupied and forcing the fractions to detach from the packing material and quickly elute down the column once the layers have been separated. The solubalized protein solution is inserted onto the top of the column and allowed to separate down the column. Unwanted proteins and carotenoids elute first, followed by PS1, followed by PS2, which stays at the top of the column. An elution method is implemented and the fractions containing PS2 are consolidated and stored in a freezer.

Crystallisation

Polyethylene Glycol (PEG) solution is added to the PS2 solution using a micro-pipette. PEG acts as the precipitation agent, causing the nucleation and slow growth of PS2 crystals as dissolved PS2 collect around the nucleation sites from the buffer solution and stick to the crystals. When the crystal becomes heavy, it drops to the bottom of the test tube. If the crystals are removed from the PEG containing solution, they will re-dissolve. If they are allowed to dry, they will fall apart and therefore must be kept wet, unless at cryogenic temperatures. There are two ways to add the PEG to the solvent:

- Batch method: Divide your intended total PEG solution into 4-8 aliquots. Add each aliquot to the protein solution and pipette mix each time.
- Drop method: Drop your PEG solution into the protein solution and allow the more viscous PEG to settle on the bottom forming a phase on the bottom of the test tube.

Jesse recommends using the batch method. I will have to email him at some later point to get the exact recipe and concentrations of PEG solution, as well as the buffer solution.

6.3.2 Solvents and buffers

Prep 1: Water at pH 6.4

Prep 2: Water at pH 6.4 with Manatol sugar to prevent the proteins from lysed cells from undergoing shock and self destructing once the cell wall has been ripped apart in the microfluidiser. Also contains PMSF serine protease inhibitor.

Prep 3: Water pH 7.0, contains no PMSF, no Manatol. PS2 dissolved in this post solubalization.

PMSF: Serine protease inhibitor. It stops the proteins from self-destructing by inhibiting destructive enzymes from ripping the proteins apart once they sense that they are in a foreign environment outside the cell. Hazardous to humans as it inhibits important proteases.

β-DDM: Maltoside, a detergent that allows the proteins to exist in an aqueous environment outside the safety of the thylakoid membrane. The detergent forms micelles around the proteins creating an hydrophobic environment and preventing the proteins from disintegrating. The detergent molecules replace the lipids of the cell membrane and allow the proteins to dissolve in water.

Vitamin E, tekoferol: A radical scavenger which prevents radicals formed by chlorophyll interaction with stray light in the room to cause damage to the extracted proteins. This is added to the solution at some point during the extraction, I do not really remember at which stage however.

Polyethylene Glycol (PEG): Crystallization agent. Polymer chain with OH groups on either end and CH_2 groups in between.

6.3.3 Sample mounting strategies

Considerations

- PS2 crystals have to be frozen at cryogenic temperatures if they are to be removed from the solvent.
- The buffer solution (Prep 3) used in the extraction contains PEG, water, and β-DDM detergent. Water absorbs everywhere in the mid-IR region, PEG contains OH groups and CH groups, and β-DDM contains OH groups and CH groups. The final PS2 solution is initially in Prep 3 buffer solvent.
- In vacuum, the PS2 crystals have to be protected otherwise they will be sucked away by the vacuum.
- Cryo-preservatives: Before freezing, glycerol is added to the solution to create defects in the water network preventing them from forming ice crystals inside the protein. If glycerol is not added, upon freezing the water will form ice and the protein will be ripped apart.

Sample handling

The samples are frozen to liquid nitrogen temperatures and stored inside a dewar. The samples are placed inside a puck, which is attached to a rack, which is inserted into the mouth of the dewar. The rack consists of two long steel bars to which the pucks are clipped and arranged one on top of the other until you get a stack of pucks. The top of the bars are hooked such that as the stack is inserted into the mouth of the dewar, the hooks attach to the lips and hold the stack in place. The dewar is then filled with LN_2. For shipping, the samples are frozen and stored in an empty dewar. The samples can last at least a couple of days, but upon receiving the dewars, they are to be immediately filled with LN_2.

Premounting sample prep

We think it would be a good idea to remove as much of the water as possible and replace it with D_2O to allow for a cleaner IR space. Our rudimentary FTIR attempt ended in utter failure, water signal was so dominant that we could see nothing underneath it. Before crystallization, we intend to perform the following prep steps:

- Insert the solution into a protein concentrator sieve tube. The solvent will pass through the holes in the sieve but the protein will be trapped.
- Repeat until all the protein you wish to use has been trapped in the sieve.
- Remove the protein sludge from the sieve and dissolve it in D_2O.
- Repeat the process several times until most of the water in the protein has been replaced by D_2O.

Mounting strategy

The Fromme group often uses teflon micro-loops, a very small loop of teflon in which a crystal can sit held within the loop by the surface tension of the solvent in which it sits. The crystal floats in the tiny droplet of solvent in the middle of the loop. We plan to try the following strategy:

- Attach the teflon loop to the coldfinger of the cryostat.
- Dip the loop into the crystals until some crystals have been trapped in the loop.
- Freeze the droplet by dunking into LN_2.
- Insert the coldfinger containing the loop into the cryostat and perform normal experiments.

We would have to figure out a way to attach the little teflon loop and needle onto the coldfinger. Also, we should consider that teflon is non-conductive and might not transfer the cold from the coldfinger to the droplet that well. Also, we do not know how long an unprotected droplet of D_2O will survive in vacuum before it starts getting sucked away. We need to experiment with that first.

Perhaps what we could do is use a copper "eye-of-a-needle" rather than a teflon loop. It might make it much more difficult to get the crystal into the loop in the first place, but once it is in there, it would be much more conductive and more likely to keep the glass cold enough.

6.3.4 Sample flashing strategy

This part I am still rather unclear about. The flash-then-freeze procedure will work at least for the S_1 to S_2 transition, for which the lifetime is on the order of seconds. Dr Fromme even suggested that we can keep the PS2 frozen in its S_1 state and still flash it to the S_2 state. She said using a flash-lamp should be fine, although I do not have the exact numbers yet. We can worry about that when we actually see signal on the dark state. The S_2 to S_3 transition will be more difficult because the S_3 state will retreat to the S_2 state within around 300 νs. We will need to double flash the PS2 and then completely freeze it within 300 νs of the second flash. Such a thing would have to be automated. Also, it take some time for the cold from the liquid nitrogen to permeate the entire solution, during which time the PS2 could slip back into the dark state. We have a long way to go before we are ready for this step. The Fromme group side steps this problem by flashing the sample right before probing it, all at room temperature. We do not have that luxury, unless we want to implement large changes to our system to include an independently triggered 50-100 ns laser and do all our experiments at room temperature.

6.3.5 Ambiguities and possible pitfalls

- The UV-vis spectrum of PS2 contains a lot of chlorophyll, and other pigments such as carotenoids. We were not able to see any kind of obvious peak at 300 nm, where Ron Pace says the Mn states are. Dr Fromme said that carotenoids also have an absorption in the 300 nm region (I have checked the literature and found that that is indeed the case), so we have to be really really sure that the Mn states are actually there. Can we get a hold of some manganese oxide and just take a simple UV-vis spectrum? I cannot seem to find a simple one in the literature. Everyone is looking at the k-edge x-ray spectrum instead.
- FTIR absorption spectrum was a disaster. The solvent, buffer, chlorophyll, and other materials all cluttered up the spectrum so much that we basically could not see anything. Replacing water

with D_2O might help, using the method I have described above.

- Are we worried about the PS2 crystals scattering our light too much? I know we worry about our light being scatter by water forming crystalline ice, would this be an issue for PS2 crystals? Especially if they are randomly oriented?

Appendix A

Maintenance of upstream light sources

A.1 Tsunami

For detailed notes on the Tsunami, see Paul Hebert's dissertation. A complete alignment and maintenance procedure is available in the Tsunami user manual. Here, I provide a brief guide on how to align the Tsunami after power decreases and mode-locking becomes either difficult or impossible to achieve using common tricks.

Tsunami maintenance is typically required every 4 - 5 months or so, depending on the weather conditions and seasonal changes. The PS system is more robust to changes in Tsunami performance than the FS system. Loss of power occurs slowly over time, although there is a suspicious correlation between intense weather systems passing through and deterioration in pulse quality. The normal modelocked output power from the Tsunami is 480 - 520 mW which corresponds to 7 - 8 bars on the internal photodiode reader. The photodiode output reader is on the AOM control box.

Sometimes, modelocking is lost even when output power is still relatively high. Such occurences are typically accompanied by partial CW breakthrough, evident by an intense narrow peak overlaid on the broadband spectrum recorded by the Ocean Optics spectrometer. In such instances, it is usually sufficient to reduce the Millenia input power until the CW breakthrough disappears. The Millenia power can be adjusted using the Millenia control box. Care should be taken to lower the pump power only as

much as necessary. Once CW breakthrough occurs, it is an indication that the system health descent has begun and a full realignment is only being postponed.

Modelocking typically becomes difficult when the power has dropped to around 300 mW. When power is this low, the oscillator must be opened and realigned from within. Here, I list the steps I usually take to get the Tsunami back to operating condition including details and nuances that might be helpful to the service personel.

1. **Measure the Millenia output power using the 407A power meter**: This power is traditionally maintained at 4 W, although it has been raised to 4.2 W to compensate for lower Tsunami output power.

2. **Record the Millenia set point, Millenia Diode 1 and Diode 2 temperatures and currents, Tsunami mode locked and CW output power, internal photodiode counter, and width and wavelength knob positions**: Typical measurements are recorded on google drive. Watch the Millenia diode temperatures and currents as these tend to drift over time as the laser tries to compensate for loss of conversion efficiency by decreasing the temperature and increasing the currents. At one time, the temperatures had been driven so low that ice was forming in the control box below the laser table. Contact Spectra Physics if this ever happens.

3. **Reinsert the dust tube and unfasten the Tsunami cover locks**: Try to not break you fingers undoing some of the difficult to reach locks.

4. **Observe the lasing mode on mirrors M4 and M5**

5. **Lower the wavelength selector all the way down by turning the wavelength knob clockwise**: The blades will interfere with the cavity alignment. Bring these back in at the end of the alignment process.

6. **Centre the mode on M4 using M3, on M5 using M4, and on M10 using M5. Then peak to output power using M1 and M10. Iterate until no improvement is seen. When the cavity condition is good, M5 can be adjusted by maximizing the internal photodiode bars**: Changes to the cavity mirrors need to be made slowly. Lasing can only be maintained when the

changes are made in small increments. Many iterations might be required before the lasing mode is centred on all of the main mirrors in the cavity. When the lasing mode is centred on M4, M5, and M10, the cavity is as well aligned as it can be to the input pump.

7. **Place the 407A power meter aside and observe the output on the spectrometer**: At this point, the output is purely CW.

8. **Activate the AOM to trigger modelocking by pressing the black button on the AOM box**: If the cavity is in decent shape, it will modelock and the bandwidth will increase to around 60 nm FWHM. If no modelocking is observed, try gently tapping on the side of the cover. You can also adjust the AOM phase. The fine adjustment is the round knob on the front panel and the course adjustment is the round switch on the circuit inside the box. If no modelocking is observed, the input pump Poynting needs to be corrected. Once the cavity is modelocking, press the button again to deactivate the AOM. Modelocking should persist.

9. **Lower the Millenia set point to 1 W**: The pump needs to be lowered to a more manageable power to facilitate alignment. Too much power makes the scatter so bright that it saturates the eye. In addition, as the input Poynting is adjusted, scatter on the crystal can sometimes increase suddenly which represents a danger to the user. Protective eye-wear is counterproductive as it completely blocks out the very light the user is using to complete the alignment.

10. **Center the pump mode onto P2 using P1, and onto M3 using P2**: It is easy to horizontally center the pump onto M3, but it is difficult to do so vertically due to the angle. I have found that aiming for the upper half of the mirror tends to increase the output power but decrease modelocking stability. Conversely, aiming for the lower half of the mirror decreases output power and increases stability. There is a sweet spot in the middle that achieves both power and stability. If power is good but no modelocking is observed, or if modelocking is unstable, lower the mode on M3 using P2. Make small adjustments to the pump input Poynting mirrors. Lasing will be lost and large adjustments make it difficult to get it back.

11. **Find lasing**: Assuming only small adjustments were made to the pump mirror, the cavity should be very close to lasing. Place a card after M4 and observe the two red squares caused by the forward propagating and the back reflected fluorescence. Adjust M1 to overlap the two squares.

Adjust M4 to center the square on Pr1, slightly clipping on the top of the prism. Adjust M5 to center the square on the AOM. Place a card at the exit at maximize the throughput. Place a card between M4 and Pr1 and look for the back reflection from M10. Adjust M10 to overlap the forward and backward propagating light. At this point, if you observe the mode at the exit, you should see a rough overlap of three modes that each respond as you adjust M1 and M10. Make small adjustments to the two end mirrors until the cavity lases. Repeat the alignment steps to match the cavity to the new input Poynting and look for signs of stable modelocking. Repeat the pump correction step until satisfied with the mode stability and output power.

12. **Test for modelocking stability**: Lower the prism assembly to increase the spectral width of the mode. The mode must be stable up to a width of 60 nm FWHM. Drop a ball driver on the table next to the Tsunami. Modelocking must survive the drop of the ball driver from a height of at least half an inch. If the stability is bad, the spitfires will be in danger of damage. Return to the pump adjustment step and try tricks like lowering the reflection of P2 on M3.

13. **Raise the wavelength selector and return it to its original position**

14. **Close the Tsunami lid and adjust the width and wavelength knobs to mimic the master spectrum**: There is an air current that causes the cavity to be unstable when the lid is off. Close the lid before doing additional stability tests.

15. **Allow the Tsunami to equilibrate overnight**

16. **Readjust the wavelength and width knobs if the spectrum shifts during equilibration**

Additional notes: When the cover is open, dust tends to settle on the horizontal surfaces. Pr1, Pr4, M6, and M9 are particularly susceptible. If you find that power is low even though you are centered on all the mirrors and power was good just a few minutes ago, it might be due to dust. You should be able to see scatter on the guilty surface. Shutter the pump, wipe the dust off the surface with a methanol soaked lens tissue held by a haemestat, and wait for 30 seconds for the solvent to dry. Every now and then, dust will settle on the AOM. To access the AOM surface, unscrew the metal cover, fold a sheet of lens tissue twice, cut off the edges around the haemestat, and carefully wipe in a single downward motion.

The vertical and horizontal adjustment knobs of M1 and M10 suffer from hysteresis. You might find you only get maximum power when approaching from one direction and not from the other.

A.2 Spitfire Ace

Details on Spitfire alignment can be found on google drive and in the Spitfire Ace users manual. Here, I provide a brief guide on how to switch on and align the Spirfire after a system shutdown. I use the same part numbers as the Spitfire Ace manual. At the start of the process, it is assumed that the Tsunami is well aligned, the Empower is off, and the Spitfire control boxes are also switched off. The Spitfire is expected to produce 6 - 6.1 W when seeded. The optimal switch-out time of Channel 3 is usually 281 - 291 ns.

The first section informs how to turn on the electronics.

1. **Shutter the Spitfire output port**
2. **Switch on the three boxes above the Spitfire**: The three boxes are ps EMPOWER, ps TDG, and ps TCU control boxes. Leave the High Voltage switch off for the moment. Wait for the Humidity and Communications lights to turn green.
3. **Open the Spitfire Ace software**: Communication might take a while. Ensure that all three boxes are on otherwise the computer will not be able to communicate with the Spitfire.
4. **Open the TCU tab and switch on TEC**
5. **In the Empower tab, set the current to 5 A and turn the Empower on**: Hold down the Empower button for three seconds and wait for the beep. This will trigger Xtal cooling.
6. **Wait until the Xtal temperature has settled at -10 $^\circ$ C**
7. **Switch the key on the ps TDG control box to enable High Voltage**
8. **Switch on the high voltage using the software**: The High Voltage lights will turn green.

This next section deals with seed alignment.

1. **Align the seed to the entrance apertures**: The two entrance apertures are found on either side of the Faraday isolator at the seed entrance into the Spitfire. Align to the first aperture using the external mirror, and to the the second aperture using the first internal mirror. The internal mirror require a 3/32 allen wrench to turn and it is difficult to reach the hex holes. I recommend using one of the shorter allen wrenches marked with red tape.

2. **Align the seed to the A-hole of the green alignment tool at the two marked positions in the stretcher using mirrors SM2 and SM3**: Markings on the benchtop show the position and orientiation of the alignment tool as well as which hole to align to. Access to the hex holes is difficult in this spot. Use the short-handle allen wrenches.

3. **Using the Find-R-Scope, observe the pattern on the stretcher grating and adjust SM3 such that the two circles are vertically aligned**: See Figure A.1 for an illustration of the grating pattern.

4. **Ensure that both detectors on the bandwidth detector are lit and stable**: Reset the bandwidth detector by clicking on yellow button labelled "Reset BWD" on the software front panel. Tap the wall of the Spitfire around the region of the bandwidth detector. If the either of the detectors trip, the Spitfire will shut off. Carefully reposition the bandwidth detector until both detectors are stable and do not trip upon vibration. Use the Find-R-Scope to aid with repositioning.

5. **The first iteration of seed alignment is complete**

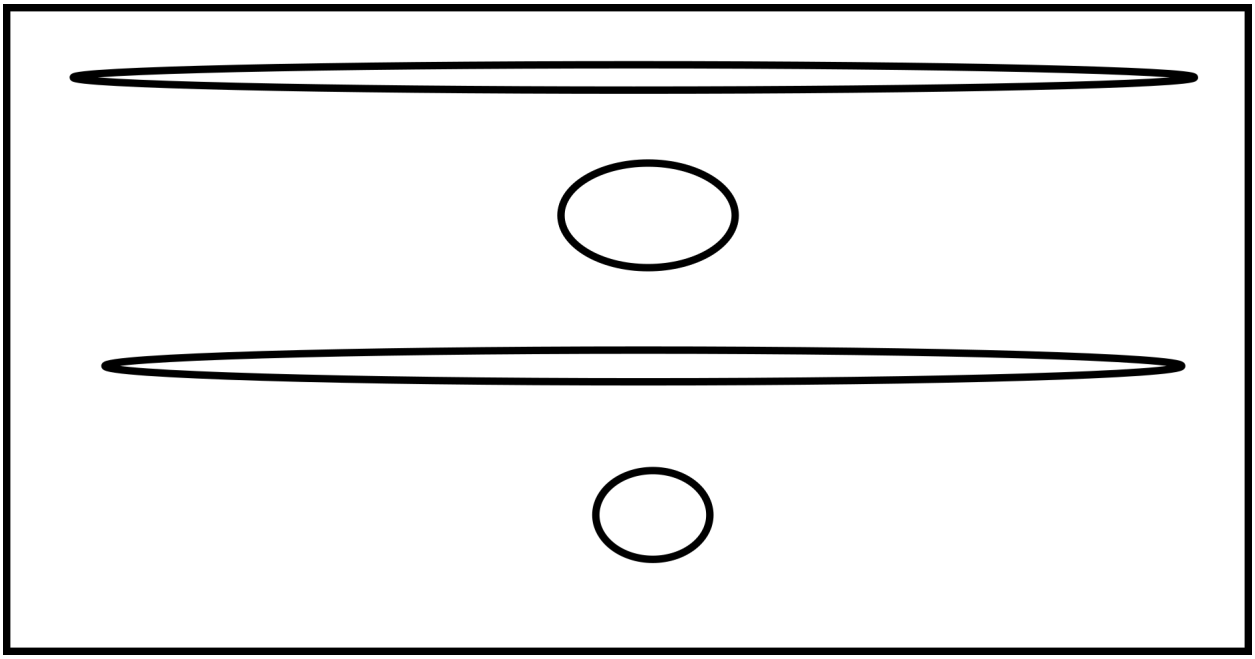

Figure A.1: Pattern on stretcher grating as viewed on the Find-R-Scope. Upon initial alignment, the two circles usually need to be vertically aligned.

This next section deals with cavity alignment. In steps 11 and above, it is assumed that the input pump does not require alignment. See the next section for pump alignment steps.

1. **Block the seed at the exit to the stretcher**: The Spitfire is now in Q-switched or unseeded mode. The expected output power is still 6 W.
2. **Place the 407A power meter in front of the entrance hole to the compressor**
3. **Leave the Pockel cells off for the moment**
4. **Increase the Empower set current to 20.5 A**: It is helpful to record a power curve of the Empower every now and then. The 407A head measures the pump power at entrance to the cavity.
5. **Wait for two hours for the Empower to equilibrate**
6. **Open the shutter to allow the pump into the cavity**
7. **In the Regen tab, set Channel 3 to 200 ns**: This step causes the exit Pockel cell to fire with a delay of 200 ns. The optimum Channel 3 delay in Q-switched mode is 310 - 320 ns. When the Pockels Cell switches out too early, as in this case, the intensity within the cavity is low and it is safe to align.
8. **Measure the output power and increase the Channel 3 delay time to 320 ns**: If the cavity is well aligned, the output power will immediately rise to 6 W. I have found that the power usually settles at around 5.7 W.
9. **If the power is slighly less that 6 W, WAIT. DO NOT TOUCH THE CAVITY**: The system requires time to equilibrate after shutting down. Often, it is sufficient to merely turn everything on and wait for about two hours for the system to recover and produce the expected output power.
10. **If the power is much less than 6 W, of if you have waited for two hours and the power has not increased, measure the Empower output**: Often, low power at a particular Empower set current is responsible for low Spitfire output power. If the Empower output is low, increase the set current until the output is 6 W.

11. **Set the Channel 3 delay to 200 ns and unblock the seed**
12. **Increase the switch-out time until you measure around 0.5 W of output**
13. **Maximize the overlap between the seed and the pump using the seed periscope mirror and the corner mirror to peak to power**
14. **Increase the switch-out time to 281 ns**: The Spitfire should be producing around 6 W of output power.

If the steps listed above do not succeed, then the pump input Poynting and the cavity end mirrors need to be aligned.

1. **Block the seed**
2. **Place a non-magnetic post-holder between CM2 and PM3 to block the back reflection**
3. **Lower the Channel 3 delay time until the output power is around 0.5 W**: This will probably occur at around 240 ns.
4. **Maximize power using PM2**: This step optimizes the pump input Poynting.
5. **Maximize power using CM5**: This step optimizes the cavity end mirror.
6. **Iterate between optimizing the pump input Poynting and the cavity end mirror until no more improvement is seen**
7. **Unblock the back reflection and maximize the output power by adjusting CM5**
8. **Unblock the seed and repeat the seed alignment steps from the previous section**

The following steps cover the alignment of the stretched output into the compressor.

1. **Remove the power meter, place the green alignment tool in the position and orientation marked on the benchtop at the entrance to the compressor, and the black alignment tool to the marked hole inside the compressor**

2. **Lower the switch-out time to 240 ns**

3. **Align to the H-hole of the green tool using M6 and to the A-hole of the black tool using TM**

4. **Align the back reflection to the B-hole of the black tool using M7**: The hex holes are very difficult to reach. I have found success by inserting the long end of the appropriate allen key into the hole holding the wrench between my index and middle fingers. Gloves must be worn.

A.3 OPA-800C additional process leakage

The alignment and operation of the OPAs are detailed in chapter 3. The OPAs actually output many different mixing processes in addition to the intended phase-matching. While the additional leakage processes are much weaker than the main process, they are nevertheless stronger than non-linear signal generated in the sample and in many cases tend to coincide with TRSF output frequencies making them a potential nuissance if not properly taken care of. The appropriate filters are tabulated in chapter 3. The known leakage processes are captured in the scan shown in Figure A.2.

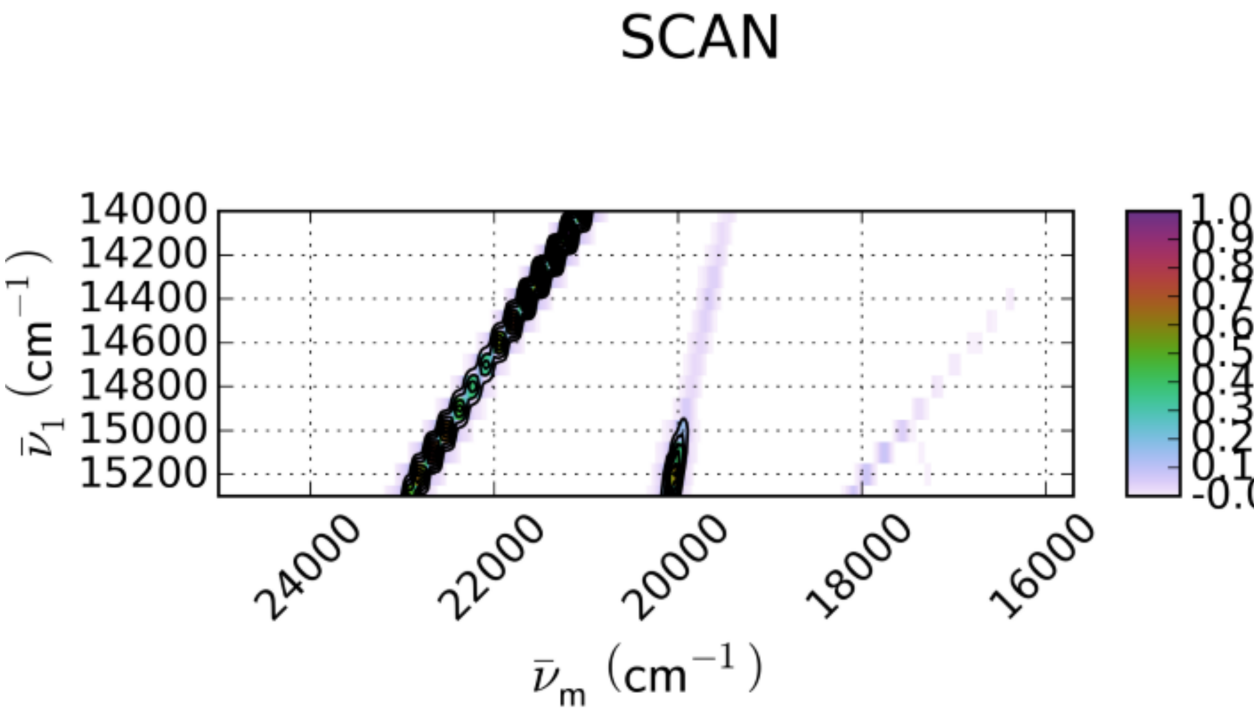

Figure A.2: Leakage processes from an OPA-800C when outputting SHS. The y-axis shows the SHS output frequency while the x-axis shows the monochromator detection frequency in the region around where TRSF output is expected.

Bibliography

[1] Bert M. Weckhuysen and Robert A. Schoonheydt. Recent progress in diffuse reflectance spectroscopy of supported metal oxide catalysts. *Catalysis Today*, 49(4):441–451, mar 1999.

[2] Osamu Nanba and Kimiyuki Satoh. Isolation of a photosystem ii reaction center consisting of d-1 and d-2 polypeptides and cytochrome b-559. *Proceedings of the National Academy of Sciences of the United States of America*, 84(1):109–112, 1987.

[3] Troy A. Stich, Amanda J. Brooks, Nicole R. Buan, and Thomas C. Brunold. Spectroscopic and computational studies of co3+-corrinoids: spectral and electronic properties of the b12cofactors and biologically relevant precursors. *Journal of the American Chemical Society*, 125(19):5897–5914, may 2003.

[4] E. S. Boyle, A. V. Pakoulev, and J. C. Wright. Fully coherent triple sum frequency spectroscopy of a benzene fermi resonance. *Journal of Physical Chemistry A*, 117(27):5578–5588, 2013.

[5] Erin S. Boyle, Nathan A. Neff-Mallon, and John C. Wright. Triply resonant sum frequency spectroscopy: Combining advantages of resonance raman and 2d-IR. *The Journal of Physical Chemistry A*, 117(47):12401–12408, nov 2013.

[6] E. S. Boyle, N. A. Neff-Mallon, J. D. Handali, and J. C. Wright. Resonance ir: a coherent multidimensional analogue of resonance raman. *J Phys Chem A*, 118(17):3112–9, 2014.

[7] Yasufumi Umena, Keisuke Kawakami, Jian-Ren Shen, and Nobuo Kamiya. Crystal structure of oxygen-evolving photosystem II at a resolution of 1.9 a. *Nature*, 473(7345):55–60, apr 2011.

[8] J. C. Wright. Coherent multidimensional vibrational spectroscopy. *International Reviews of Physical Chemistry*, 21:185–255, 2002.

[9] J. C. Wright. Analytical chemistry, multidimensional spectral signatures, and the future of coherent multidimensional spectroscopy. *Chemical Physics Letters*, 662:1–13, 2016.

[10] John C. Wright. Applications of the new family of coherent multidimensional spectroscopies for analytical chemistry. *Annual Review of Analytical Chemistry*, 10(1):45–70, jun 2017.

[11] Andrei V. Pakoulev, M. A. Rickard, K. A. Meyers, K. Kornau, N. A. Mathew, D. C. Thompson, and J. C. Wright. Mixed frequency/time domain optical analogues of heteronuclear multidimensional nmr. *Journal of Physical Chemistry A*, 110:3352–3355, 2006.

[12] Andrei V. Pakoulev, Mark A. Rickard, Kathryn M. Kornau, Nathan A. Mathew, Lena A. Yurs, Stephen B. Block, and John C. Wright. Mixed frequency-/time-domain coherent multidimensional spectroscopy: Research tool or potential analytical method? *Accounts of Chemical Research*, 42(9):1310–1321, sep 2009.

[13] Bert M. Weckhuysen, Israel E. Wachs, and Robert A. Schoonheydt. Surface chemistry and spectroscopy of chromium in inorganic oxides. *Chemical Reviews*, 96(8):3327–3350, jan 1996.

[14] Martin Gouterman. Spectra of porphyrins. *Journal of Molecular Spectroscopy*, 6:138–163, jan 1961.

[15] Ruma Banerjee and Stephen W. Ragsdale. The many faces of vitamin b12: Catalysis by cobalamin-dependent enzymes. *Annual Review of Biochemistry*, 72(1):209–247, jun 2003.

[16] Junko Yano and Vittal Yachandra. Mn4ca cluster in photosynthesis: Where and how water is oxidized to dioxygen. *Chemical Reviews*, 114(8):4175–4205, mar 2014.

[17] James P. McEvoy and Gary W. Brudvig. Water-splitting chemistry of photosystem II. *Chemical Reviews*, 106(11):4455–4483, nov 2006.

[18] Tadeusz Andruniow, Pawel M. Kozlowski, and Marek Z. Zgierski. Theoretical analysis of electronic absorption spectra of vitamin b12 models. *The Journal of Chemical Physics*, 115(16):7522–7533, oct 2001.

[19] Tadeusz Andruniow, Marek Z. Zgierski, and Pawel M. Kozlowski. Vibrational analysis of methylcobalamin. *The Journal of Physical Chemistry A*, 106(7):1365–1373, feb 2002.

[20] Troy A. Stich, Nicole R. Buan, and Thomas C. Brunold. Spectroscopic and computational studies of co2+corrinoids: Spectral and electronic properties of the biologically relevant base-on and base-off forms of co2+cobalamin. *Journal of the American Chemical Society*, 126(31):9735–9749, aug 2004.

[21] Kiyoung Park and Thomas C. Brunold. Combined spectroscopic and computational analysis of the vibrational properties of vitamin b12 in its co3+, co2+, and co1+ oxidation states. *The Journal of Physical Chemistry B*, 117(18):5397–5410, apr 2013.

[22] Michihiro Suga, Fusamichi Akita, Kunio Hirata, Go Ueno, Hironori Murakami, Yoshiki Nakajima, Tetsuya Shimizu, Keitaro Yamashita, Masaki Yamamoto, Hideo Ago, and Jian-Ren Shen. Native structure of photosystem II at 1.95 a resolution viewed by femtosecond x-ray pulses. *Nature*, 517(7532):99–103, nov 2014.

[23] N. Cox, M. Retegan, F. Neese, D. A. Pantazis, A. Boussac, and W. Lubitz. Electronic structure of the oxygen-evolving complex in photosystem II prior to o-o bond formation. *Science*, 345(6198):804–808, aug 2014.

[24] Jesse Coe, Christopher Kupitz, Shibom Basu, Chelsie E. Conrad, Shatabdi Roy-Chowdhury, Raimund Fromme, and Petra Fromme. Crystallization of photosystem II for time-resolved structural studies using an x-ray free electron laser. In *Methods in Enzymology*, pages 459–482. Elsevier, 2015.

[25] Per E. M. Siegbahn. Substrate water exchange for the oxygen evolving complex in PSII in the s1, s2, and s3 states. *Journal of the American Chemical Society*, 135(25):9442–9449, jun 2013.

[26] Per E.M. Siegbahn. Water oxidation mechanism in photosystem II, including oxidations, proton release pathways, o—o bond formation and o2 release. *Biochimica et Biophysica Acta (BBA) - Bioenergetics*, 1827(8-9):1003–1019, aug 2013.

[27] Xichen Li and Per E. M. Siegbahn. Alternative mechanisms for o2 release and o–o bond formation in the oxygen evolving complex of photosystem II. *Physical Chemistry Chemical Physics*, 17(18):12168–12174, 2015.

[28] Ron J. Pace, Lu Jin, and Rob Stranger. What spectroscopy reveals concerning the mn oxidation levels in the oxygen evolving complex of photosystem II: X-ray to near infra-red. *Dalton Transactions*, 41(36):11145, 2012.

[29] T NOGUCHI. Fourier transform infrared analysis of the photosynthetic oxygen-evolving center. *Coordination Chemistry Reviews*, 252(3-4):336–346, feb 2008.

[30] Takumi Noguchi. Fourier transform infrared difference and time-resolved infrared detection of the electron and proton transfer dynamics in photosynthetic water oxidation. *Biochimica et Biophysica Acta (BBA) - Bioenergetics*, 1847(1):35–45, jan 2015.

[31] Taishi Nishimura, Chihiro Uno, Kunio Ido, Ryo Nagao, Takumi Noguchi, Fumihiko Sato, and Kentaro Ifuku. Identification of the basic amino acid residues on the PsbP protein involved in the electrostatic interaction with photosystem II. *Biochimica et Biophysica Acta (BBA) - Bioenergetics*, 1837(9):1447–1453, sep 2014.

[32] Chihiro Uno, Ryo Nagao, Hiroyuki Suzuki, Tatsuya Tomo, and Takumi Noguchi. Structural coupling of extrinsic proteins with the oxygen-evolving center in red algal photosystem II as revealed by light-induced FTIR difference spectroscopy. *Biochemistry*, 52(34):5705–5707, aug 2013.

[33] Paul M. Donaldson, Rui Guo, Frederic Fournier, Elizabeth M. Gardner, Laura M. C. Barter, Chris J. Barnett, Ian R. Gould, David R. Klug, D. Jason Palmer, and Keith R. Willison. Direct identification and decongestion of fermi resonances by control of pulse time ordering in two-dimensional IR spectroscopy. *The Journal of Chemical Physics*, 127(11):114513, sep 2007.

[34] Frédéric Fournier, Elizabeth M. Gardner, Rui Guo, Paul M. Donaldson, Laura M.C. Barter, D. Jason Palmer, Chris J. Barnett, Keith R. Willison, Ian R. Gould, and David R. Klug. Optical fingerprinting of peptides using two-dimensional infrared spectroscopy: Proof of principle. *Analytical Biochemistry*, 374(2):358–365, mar 2008.

[35] Frederic Fournier, Rui Guo, Elizabeth M. Gardner, Paul M. Donaldson, Christian Loeffeld, Ian R. Gould, Keith R. Willison, and David R. Klug. Biological and biomedical applications of two-dimensional vibrational spectroscopy: Proteomics, imaging, and structural analysis. *Accounts of Chemical Research*, 42(9):1322–1331, sep 2009.

[36] Lays Rezende Valim, Julia A. Davies, Karina Tveen Jensen, Rui Guo, Keith R. Willison, Corinne M. Spickett, Andrew R. Pitt, and David R. Klug. Identification and relative quantification of tyrosine nitration in a model peptide using two-dimensional infrared spectroscopy. *The Journal of Physical Chemistry B*, 118(45):12855–12864, nov 2014.

[37] Minhaeng Cho. Theoretical description of two-dimensional vibrational spectroscopy by infrared-infrared-visible sum frequency generation. *Physical Review A*, 61(2), jan 2000.

[38] Kyungwon Kwak, Sangyob Cha, Minhaeng Cho, and John C. Wright. Vibrational interactions of acetonitrile: Doubly vibrationally resonant IR–IR–visible four-wave-mixing spectroscopy. *The Journal of Chemical Physics*, 117(12):5675–5687, sep 2002.

[39] Erin S. Boyle, Andrei V. Pakoulev, and John C. Wright. Fully coherent triple sum frequency spectroscopy of a benzene fermi resonance. *The Journal of Physical Chemistry A*, 117(27):5578–5588, jul 2013.

[40] P. D. Maker and R. W. Terhune. Study of optical effects due to an induced polarization third order in the electric field. *Physical Review*, 137:A801, 1965.

[41] R. J. Carlson and J. C. Wright. Absorption and coherent interference effects in molecular four wave mixing. *Applied Spectroscopy*, 43:1195–1208, 1989.

[42] Edward U. Condon. Nuclear motions associated with electron transitions in diatomic molecules. *Physical Review*, 32(6):858–872, dec 1928.

[43] Roland L. Dunbrack. Calculation of franck-condon factors for undergraduate quantum chemistry. *Journal of Chemical Education*, 63(11):953, nov 1986.

[44] J. Franck and E. G. Dymond. Elementary processes of photochemical reactions. *Transactions of the Faraday Society*, 21(February):536, 1926.

[45] Anne B. Myers, Richard A. Mathies, David J. Tannor, and Eric J. Heller. Excited state geometry changes from preresonance raman intensities: Isoprene and hexatriene. *The Journal of Chemical Physics*, 77(8):3857–3866, oct 1982.

[46] Blaise J. Thompson, Kyle F. Sunden, Darien J. Morrow, Nathan Andrew Neff-Mallon, Kyle J. Czech, Daniel D. Kohler, Tom Parker, and Rachel Swedin. Wrighttools.

[47] Erin S. Boyle, Nathan A. Neff-Mallon, Jonathan D. Handali, and John C. Wright. Resonance IR: A coherent multidimensional analogue of resonance raman. *The Journal of Physical Chemistry A*, 118(17):3112–3119, apr 2014.

[48] Jonathan D. Handali, Kyle F. Sunden, Emily M. Kaufman, and John C. Wright. Interference and phase mismatch effects in coherent triple sum frequency spectroscopy. *Chemical Physics*, jun 2018.

[49] E. S. Boyle, N.A. Neff-Mallon, and J. C. Wright. Triply resonant sum frequency spectroscopy: Combining advantages of resonance raman and 2d-ir. *Journal of Physical Chemistry A*, 117(047):12401–12408, 2013.

[50] M. D. Levenson and N. Bloembergen. Dispersion of nonlinear susceptibilities of organic liquids and solutions. *Journal of Chemical Physics*, 60:1323–1327, 1974.

[51] M. D. Levenson and N. Bloembergen. Dispersion of the nonlinear optical susceptibility tensor in centrosymmetric media. *Physical Review B*, 10:4447–4463, 1974.

[52] Darien J. Morrow, Daniel D. Kohler, and John C. Wright. Group- and phase-velocity-mismatch fringes in triple sum-frequency spectroscopy. *Physical Review A*, 96(6), dec 2017.

[53] A.C. Eckbreth. Boxcars: Crossed-beam phase-matched cars generation in gases. *Applied Physics Letters*, 32(7):421–423, 1978.

[54] W. M. Tolles, J. W. Nibler, J. R. McDonald, and A. B. Harvey. Review of theory and applications of coherent anti-stokes raman spectroscopy. *Applied Spectroscopy*, 31:253–271, 1977.

[55] D. Lee and A. C. Albrecht. *Advances in Infrared and Raman Spectroscopy*, volume 12. Wiley-Heyden, Chichester, 1st edition, 1985.

[56] I. H. Malitson. A redetermination of some optical properties of calcium fluoride. *Applied Optics*, 2(11):1103–1107, 1963.

[57] J. E. Bertie, M. K. Ahmed, and H. H. Eysel. Infrared intensities of liquids .5. optical and dielectric-constants, integrated intensities, and dipole-moment derivatives of h2o and d2o at 22c. *Journal of Physical Chemistry*, 93(6):2210–2218, 1989.

[58] P. P. Sethna, K. F. Palmer, and D. Williams. Optical-constants of d2o in infrared. *Journal of the Optical Society of America*, 68(6):815–817, 1978.

[59] S. Kedenburg, M. Vieweg, T. Gissibl, and H. Giessen. Linear refractive index and absorption measurements of nonlinear optical liquids in the visible and near-infrared spectral region. *Optical Materials Express*, 2(11):1588–1611, 2012.

[60] Koichi Furuta, Masanori Fuyuki, and Akihide Wada. Cross-term selective, two-pulse correlation measurements by phase-shifted parallel modulation for analysis of a multi-photon process. *Applied Spectroscopy*, 66(12):1475–1479, dec 2012.

[61] Blaise J. Thompson, Kyle F. Sunden, and Nathan Andrew Neff-Mallon. Pycmds 0.8.0, 2018.

[62] Blaise J. Thompson, Kyle F. Sunden, Darien J. Morrow, Nathan Andrew Neff-Mallon, Kyle J. Czech, Daniel D. Kohler, and Rachel Swedin. Wrighttools 3.0.0, 2018.

[63] Nathan A. Neff-Mallon and John C. Wright. Multidimensional spectral fingerprints of a new family of coherent analytical spectroscopies. *Analytical Chemistry*, 89(24):13182–13189, nov 2017.

[64] N. A. Mathew, L. A. Yurs, S. B. Block, A. V. Pakoulev, K. M. Kornau, and J. C. Wright. Fully coherent and partially coherent pathways in multiply enhanced odd-order wave-mixing spectroscopy. *Journal of Physical Chemistry A*, 114(2):817–832, 2009.

[65] K. A. Meyer, D. M. Besemann, and J. C. Wright. Coherent two dimensional spectroscopy with triply vibrationally enhanced infrared four wave mixing. *Chemical Physics Letters*, 381(5-6):642–649, 2003.

[66] M. A. Rickard, A. V. Pakoulev, K. Kornau, N. A. Mathew, and J C.. Wright. Interferometric coherence transfer modulations in triply vibrationally enhanced four-wave mixing. *Journal of Physical Chemistry A*, 110:11384–11387, 2006.

[67] Wei Zhao and John C. Wright. Doubly vibrationally enhanced four wave mixing: The optical analog to 2d NMR. *Physical Review Letters*, 84(7):1411–1414, feb 2000.

[68] John M. Pratt. The b12-dependent isomerase enzymes; how the protein controls the active site. *Chemical Society Reviews*, 14(2):161, 1985.

[69] Maciej Giedyk, Katarzyna Goliszewska, and Dorota Gryko. Vitamin b12 catalysed reactions. *Chemical Society Reviews*, 44(11):3391–3404, 2015.

[70] DOROTHY CROWFOOT Hodgkin, JENNY Pickworth, JOHN H. Robertson, KENNETH N. Trueblood, RICHARD J. Prosen, and JOHN G. White. Structure of vitamin b12 : The crystal structure of the hexacarboxylic acid derived from b12 and the molecular structure of the vitamin. *Nature*, 176(4477):325–328, aug 1955.

[71] Joseph J. Shiang, Allwyn G. Cole, Roseanne J. Sension, Kun Hang, Yuxiang Weng, Jenna S. Trommel, Luigi G. Marzilli, and Tianquan Lian. Ultrafast excited-state dynamics in vitamin b12 and related cob(iii)alamins. *Journal of the American Chemical Society*, 128(3):801–808, 2006. PMID: 16417369.

[72] Dennis G. Brown. The chemistry of vitamin b12 and related inorganic model systems. In *Progress in Inorganic Chemistry*, pages 177–286. Wiley, mar 2007.

[73] R V Banerjee and R G Matthews. Cobalamin-dependent methionine synthase. *The FASEB Journal*, 4(5):1450–1459, mar 1990.

[74] James T. Drummond and Rowena G. Matthews. Nitrous oxide degradation by cobalamin-dependent methionine synthase: Characterization of the reactants and products in the inactivation reaction. *Biochemistry*, 33(12):3732–3741, mar 1994.

[75] Celia W. Goulding and Rowena G. Matthews. Cobalamin-dependent methionine synthase from escherichia coli: Involvement of zinc in homocysteine activation. *Biochemistry*, 36(50):15749–15757, dec 1997.

[76] Matthew D. Liptak, Angela S. Fleischhacker, Rowena G. Matthews, and Thomas C. Brunold. Probing the role of the histidine 759 ligand in cobalamin-dependent methionine synthase. *Biochemistry*, 46(27):8024–8035, jul 2007.

[77] Halina Y. Neujahr and Leif Bertilsson. Methylation of mercury compounds by methylcobalamin. *Biochemistry*, 10(14):2805–2808, jul 1971.

[78] David M. Hoover, Joseph T. Jarrett, Richard H. Sands, William R. Dunham, Martha L. Ludwig, and Rowena G. Matthews. Interaction of escherichia coli cobalamin-dependent methionine synthase and its physiological partner flavodoxin: Binding of flavodoxin leads to axial ligand dissociation from the cobalamin cofactor. *Biochemistry*, 36(1):127–138, jan 1997.

[79] J. Kim, C. Gherasim, and R. Banerjee. Decyanation of vitamin b12 by a trafficking chaperone. *Proceedings of the National Academy of Sciences*, 105(38):14551–14554, sep 2008.

[80] Claudia C. Smeltzer, Michelle J. Cannon, Patrick R. Pinson, John D. Munger, Frederick G. West, and Charles B. Grissom. Synthesis and characterization of fluorescent cobalamin (CobalaFluor) derivatives for imaging. *Organic Letters*, 3(6):799–801, mar 2001.

[81] Pradip M. Pathare, D. Scott Wilbur, Shannon Heusser, Edward V. Quadros, Patricia McLoughlin, and A. Charles Morgan. Synthesis of cobalamin-biotin conjugates that vary in the position of cobalamin coupling. evaluation of cobalamin derivative binding to transcobalamin II. *Bioconjugate Chemistry*, 7(2):217–232, jan 1996.

[82] Joshua D. Bagnato, Alanna L. Eilers, Robert A. Horton, and Charles B. Grissom. Synthesis and characterization of a cobalamin-colchicine conjugate as a novel tumor-targeted cytotoxin. *The Journal of Organic Chemistry*, 69(26):8987–8996, dec 2004.

[83] Nicole Dölker, Feliu Maseras, and Agustí Lledós. Density functional study on the effect of the trans axial ligand of b12 cofactors on the heterolytic cleavage of the co-c bond. *The Journal of Physical Chemistry B*, 107(1):306–315, jan 2003.

[84] Nicole Dölker, Feliu Maseras, and Per E.M. Siegbahn. Stabilization of the adenosyl radical in coenzyme b12 – a theoretical study. *Chemical Physics Letters*, 386(1-3):174–178, mar 2004.

[85] Nicole Dölker, Antonio Morreale, and Feliu Maseras. Computational study on the difference between the co–c bond dissociation energy in methylcobalamin and adenosylcobalamin. *JBIC Journal of Biological Inorganic Chemistry*, 10(5):509–517, jun 2005.

[86] H.M. Marques, B. Ngoma, T.J. Egan, and K.L. Brown. Parameters for the amber force field for the molecular mechanics modeling of the cobalt corrinoids. *Journal of Molecular Structure*, 561(1-3):71–91, apr 2001.

[87] Kasper P. Jensen and Ulf Ryde. Conversion of homocysteine to methionine by methionine synthase: A density functional study. *Journal of the American Chemical Society*, 125(46):13970–13971, nov 2003.

[88] Kasper P. Jensen and Ulf Ryde. How the co-c bond is cleaved in coenzyme b12 enzymes: A theoretical study. *Journal of the American Chemical Society*, 127(25):9117–9128, jun 2005.

[89] Kasper P. Jensen and Ulf Ryde. Cobalamins uncovered by modern electronic structure calculations. *Coordination Chemistry Reviews*, 253(5-6):769–778, mar 2009.

[90] Renata A. Kwiecien, Ilja V. Khavrutskii, Djamaladdin G. Musaev, Keiji Morokuma, Ruma Banerjee, and Piotr Paneth. Computational insights into the mechanism of radical generation in b12-dependent methylmalonyl-CoA mutase. *Journal of the American Chemical Society*, 128(4):1287–1292, feb 2006.

[91] Marek Freindorf and Pawel M. Kozlowski. A combined density functional theory and molecular mechanics study of the relationship between the structure of coenzyme b12 and its binding to methylmalonyl-CoA mutase. *Journal of the American Chemical Society*, 126(7):1928–1929, feb 2004.

[92] Karen S. Conrad, Christopher D. Jordan, Kenneth L. Brown, and Thomas C. Brunold. Spectroscopic and computational studies of cobalamin species with variable lower axial ligation: Implications for the mechanism of co–c bond activation by class i cobalamin-dependent isomerases. *Inorganic Chemistry*, 54(8):3736–3747, apr 2015.

[93] L. Ouyang, L. Randaccio, P. Rulis, E.Z. Kurmaev, A. Moewes, and W.Y. Ching. Electronic structure and bonding in vitamin b12, cyanocobalamin. *Journal of Molecular Structure: THEOCHEM*, 622(3):221–227, mar 2003.

[94] Andrei V. Pakoulev, Stephen B. Block, Lena A. Yurs, Nathan A. Mathew, Kathryn M. Kornau, and John C. Wright. Multiply resonant coherent multidimensional spectroscopy: Implications for materials science. *The Journal of Physical Chemistry Letters*, 1(5):822–828, feb 2010.

[95] Maksim Grechko, Taisuke Hasegawa, Francesco D'Angelo, Hironobu Ito, Dmitry Turchinovich, Yuki Nagata, and Mischa Bonn. Coupling between intra- and intermolecular motions in liquid water revealed by two-dimensional terahertz-infrared-visible spectroscopy. *Nature Communications*, 9(1), feb 2018.

[96] Megan C. Thielges and Michael D. Fayer. Protein dynamics studied with ultrafast two-dimensional infrared vibrational echo spectroscopy. *Accounts of Chemical Research*, 45(11):1866–1874, mar 2012.

[97] Junrong Zheng, Kyungwon Kwak, and M. D. Fayer. Ultrafast 2d IR vibrational echo spectroscopy. *Accounts of Chemical Research*, 40(1):75–83, jan 2007.

[98] Nicholas H. C. Lewis and Graham R. Fleming. Two-dimensional electronic-vibrational spectroscopy of chlorophyll a and b. *The Journal of Physical Chemistry Letters*, 7(5):831–837, feb 2016.

[99] Duckhwan Lee and Andreas C. Albrecht. A unified view of raman, resonance raman, and fluorescence spectroscopy (and their analogues in two-photon absorption. In R. J. H. Clark and R. E. Hester, editors, *Advances in infrared and Raman Spectroscopy*, chapter 4, pages 179–213. London; New York, 1 edition, 1985.

[100] E Mayer, D Gardiner, and R Hester. Resonance raman spectra of vitamin b12 and dicyanocobalamin. *Biochimica et Biophysica Acta (BBA) - General Subjects*, 297(2):568–570, feb 1973.

[101] J. Nestor, T. G. Spiro, and G. Klauminzer. Coherent anti-stokes raman scattering (CARS) spectra, with resonance enhancement, of cytochrome c and vitamin b12 in dilute aqueous solution. *Proceedings of the National Academy of Sciences*, 73(10):3329–3332, oct 1976.

[102] F. Galluzzi, M. Garozzo, and F. F. Ricci. Resonance raman scattering and vibronic coupling in aquo- and cyano-cobalamin. *Journal of Raman Spectroscopy*, 2(4):351–362, aug 1974.

[103] Tohru Azumi and Kazuo Matsuzaki. WHAT DOES THE TERM "VIBRONIC COUPLING" MEAN? *Photochemistry and Photobiology*, 25(3):315–326, mar 1977.

[104] Blaise J. Thompson, Kyle F. Sunden, Darien J. Morrow, and Nathan Andrew Neff-Mallon. Pycmds, March 2018.

[105] Alex R. Jones, Henry J. Russell, Gregory M. Greetham, Michael Towrie, Sam Hay, and Nigel S. Scrutton. Ultrafast infrared spectral fingerprints of vitamin b12 and related cobalamins. *The Journal of Physical Chemistry A*, 116(23):5586–5594, jun 2012.

[106] Graham Eaton, Martyn C. R. Symons, and Pushti P. Rastogi. Spectroscopic studies of the solvation of amides with n—h groups. part 1.—the carbonyl group. *Journal of the Chemical Society, Faraday Transactions 1: Physical Chemistry in Condensed Phases*, 85(10):3257, 1989.

[107] Subhajit Bandyopadhyay and Saswata Roy. Determination and comparison of carbonyl stretching frequency of a ketone in its ground state and the first electronic excited state. *Journal of Chemical Education*, 91(11):1995–1998, aug 2014.

[108] Daniel D. Kohler, Blaise J. Thompson, and John C. Wright. Frequency-domain coherent multidimensional spectroscopy when dephasing rivals pulsewidth: Disentangling material and instrument response. *The Journal of Chemical Physics*, 147(8):084202, aug 2017.

[109] Wei Zhao and John C. Wright. Measurement of $\chi^{(3)}$ for doubly vibrationally enhanced four wave mixing spectroscopy. *Physical Review Letters*, 83(10):1950–1953, sep 1999.

[110] Wei Zhao and John C. Wright. Spectral simplification in vibrational spectroscopy using doubly vibrationally enhanced infrared four wave mixing. *Journal of the American Chemical Society*, 121(47):10994–10998, dec 1999.

[111] Nicholas J. Condon and John C. Wright. Doubly vibrationally enhanced four-wave mixing in crotononitrile. *The Journal of Physical Chemistry A*, 109(5):721–729, feb 2005.

[112] Nathan A. Mathew, Stephen B. Block, Lena A. Yurs, Kathryn M. Kornau, Andrei V. Pakoulev, and John C. Wright. Multiply enhanced odd-order wave-mixing spectroscopy. *The Journal of Physical Chemistry A*, 113(48):13562–13569, dec 2009.

[113] Nathan A. Mathew, Lena A. Yurs, Stephen B. Block, Andrei V. Pakoulev, Kathryn M. Kornau, and John C. Wright. Multiple quantum coherence spectroscopy. *The Journal of Physical Chemistry A*, 113(33):9261–9265, aug 2009.

[114] N. A. Mathew, L. A. Yurs, S. B. Block, A. V. Pakoulev, K. M. Kornau, E. L. Sibert, and J. C. Wright. Fully and partially coherent pathways in multiply enhanced odd-order wave-mixing spectroscopy. *Journal of Physical Chemistry A*, 114(2):817–832, 2010.

[115] Eric Jones, Travis Oliphant, Pearu Peterson, et al. SciPy: Open source scientific tools for Python. Accessed: 2018-04-04.

[116] Travis E Oliphant. *A guide to NumPy*. Trelgol Publishing, 2006.

[117] Andrew Collette et al. HDF5 for python. Accessed: 2018-07-28.

[118] John D. Hunter. Matplotlib: A 2d graphics environment. *Computing in Science & Engineering*, 9(3):90–95, 2007.

[119] Pipenv: Python dev workflow for humans. Accessed: 2018-07-28.

[120] Zhenfeng Liu, Hanchi Yan, Kebin Wang, Tingyun Kuang, Jiping Zhang, Lulu Gui, Xiaomin An, and Wenrui Chang. Crystal structure of spinach major light-harvesting complex at 2.72 a resolution. *Nature*, 428(6980):287–292, mar 2004.

[121] K Iriyama, N Ogura, and A Takamiya. A simple method for extraction and partial purification of chlorophyll from plant material, using dioxane. *Journal of biochemistry*, 76(4):901–904, 1974.

[122] Keiji Iriyama and Masahiko Yoshiura. Separation of chlorophyll a and chlorophyll b by column chromatography with sephadex lh-20 or powdered sugar. *Journal of Chromatography*, 177:154–156, 1979.

[123] Richard J. Debus. Evidence from FTIR difference spectroscopy that d1-asp61 influences the water reactions of the oxygen-evolving mn4cao5 cluster of photosystem II. *Biochemistry*, 53(18):2941–2955, apr 2014.

[124] Richard J. Debus. FTIR studies of metal ligands, networks of hydrogen bonds, and water molecules near the active site mn 4 CaO 5 cluster in photosystem II. *Biochimica et Biophysica Acta (BBA) - Bioenergetics*, 1847(1):19–34, jan 2015.

[125] J. Kern, R. Alonso-Mori, R. Tran, J. Hattne, R. J. Gildea, N. Echols, C. Glockner, J. Hellmich, H. Laksmono, R. G. Sierra, B. Lassalle-Kaiser, S. Koroidov, A. Lampe, G. Han, S. Gul, D. DiFiore, D. Milathianaki, A. R. Fry, A. Miahnahri, D. W. Schafer, M. Messerschmidt, M. M. Seibert, J. E. Koglin, D. Sokaras, T.-C. Weng, J. Sellberg, M. J. Latimer, R. W. Grosse-Kunstleve, P. H. Zwart, W. E. White, P. Glatzel, P. D. Adams, M. J. Bogan, G. J. Williams, S. Boutet, J. Messinger, A. Zouni, N. K. Sauter, V. K. Yachandra, U. Bergmann, and J. Yano. Simultaneous femtosecond x-ray spectroscopy and diffraction of photosystem II at room temperature. *Science*, 340(6131):491–495, feb 2013.

[126] Mikhail Askerka, Jimin Wang, David J. Vinyard, Gary W. Brudvig, and Victor S. Batista. S3 state of the o2-evolving complex of photosystem II: Insights from QM/MM, EXAFS, and femtosecond x-ray diffraction. *Biochemistry*, 55(7):981–984, feb 2016.

[127] M. Haumann, C. Müller, P. Liebisch, L. Iuzzolino, J. Dittmer, M. Grabolle, T. Neisius, W. Meyer-Klaucke, and H. Dau. Structural and oxidation state changes of the photosystem II manganese complex in four transitions of the water oxidation cycle (s0→ s1, s1→ s2, s2→ s3, and s3, 4→ s0) characterized by x-ray absorption spectroscopy at 20 k and room temperature†. *Biochemistry*, 44(6):1894–1908, feb 2005.

[128] Pieter Glatzel, Henning Schroeder, Yulia Pushkar, Thaddeus Boron, Shreya Mukherjee, George Christou, Vincent L. Pecoraro, Johannes Messinger, Vittal K. Yachandra, Uwe Bergmann, and Junko Yano. Electronic structural changes of mn in the oxygen-evolving complex of photosystem II during the catalytic cycle. *Inorganic Chemistry*, 52(10):5642–5644, may 2013.

[129] Ravi Pokhrel and Gary W. Brudvig. Oxygen-evolving complex of photosystem II: correlating structure with spectroscopy. *Physical Chemistry Chemical Physics*, 16(24):11812, 2014.

[130] Rhitankar Pal, Christian F. A. Negre, Leslie Vogt, Ravi Pokhrel, Mehmed Z. Ertem, Gary W. Brudvig, and Victor S. Batista. S0-state model of the oxygen-evolving complex of photosystem II. *Biochemistry*, 52(44):7703–7706, oct 2013.

[131] Daniele Bovi, Matteo Capone, Daniele Narzi, and Leonardo Guidoni. Vibrational fingerprints of the mn 4 CaO 5 cluster in photosystem II by mixed quantum-classical molecular dynamics. *Biochimica et Biophysica Acta (BBA) - Bioenergetics*, 1857(10):1669–1677, oct 2016.